

Time development of hadronic showers in a Highly Granular Analog Hadron Calorimeter

Dissertation

zur Erlangung des Doktorgrades
an der Fakultät für Mathematik, Informatik und Naturwissenschaften
Fachbereich Physik
der Universität Hamburg

vorgelegt von
ELDWAN BRIANNE
aus Saint-Malo, Frankreich

Hamburg

2018

Gutachter/innen der Dissertation:	Prof. Dr. Erika Garutti Dr. Katja Krüger
Zusammensetzung der Prüfungskommission:	Prof. Dr. Erika Garutti Dr. Katja Krüger Prof. Dr. Johaness Haller Prof. Dr. Gudrid Moortgat-Pick Prof. Dr. Günter H. W. Sigl
Vorsitzende/r der Prüfungskommission:	Prof. Dr. Günter H. W. Sigl
Datum der Disputation:	03/07/2018
Vorsitzender Fach-Promotionsausschusses PHYSIK:	Prof. Dr. Wolfgang Hansen
Leiter des Fachbereichs PHYSIK:	Prof. Dr. Michael Potthoff
Dekan der Fakultät MIN:	Prof. Dr. Heinrich Graener

Abstract

This thesis presents the study of the time development of hadronic showers in a highly granular hadron calorimeter using data collected by the CALICE Analog Hadron Calorimeter (AHCAL) technological prototype at the Super Proton Synchrotron (SPS) at CERN in July 2015 in μ^- , e^- and hadron beams up to 90 GeV.

Highly granular calorimeters are designed for the concept of Particle Flow Algorithm which aims to measure each individual particle in a jet using the best sub-detector measurement. The Particle Flow approach is a key aspect of the detectors for the International Linear Collider (ILC) which is a future linear lepton collider designed for precision physics studies at a center of mass energy up to 500 GeV.

The CALICE Collaboration is developing highly granular calorimeters for future colliders. The AHCAL is one of the detector concepts based on $30 \times 30 \times 3 \text{ mm}^3$ scintillating tiles read out by Silicon Photomultipliers (SiPM). The SiPM signal is processed by an ASIC (SPIROC2b) capable to measure the amplitude and the time of individual calorimeter hits. A second generation technological prototype of the AHCAL is developed to focus on the full scalability of the detector. The prototype used in this thesis is composed of 14 active layers corresponding to 3744 channels inserted into a steel absorber structure of 4λ depth. For the first time, a large scale prototype has been operated successfully in various beams.

This analysis concentrates on the timing capabilities of the AHCAL prototype. In a first part, the challenging timing calibration procedure, due to the large amount of channels and features of the front-end, is presented. A timing resolution of 5 ns for muons and 8 ns for electron and pion showers has been achieved. In a second part, this thesis shows the study of the time development of hadron showers with the AHCAL prototype by investigating timing correlations with the hit energy, the hit distance to the shower axis and between layers. The results of the testbeam data have been compared to various simulations.

In the last part of this thesis, a study of the effects of timing cuts on calorimeter response, energy resolution and shower topology is presented using a full GEANT4-based simulation of the International Large Detector (ILD) concept. Using the timing information of individual calorimeter hits has the potential to improve pattern recognition and calorimeter energy resolution.

Zusammenfassung

Diese Arbeit präsentiert die Untersuchung der zeitlichen Entwicklung hadronischer Schauer in einem hochgranularen Hadronenkalorimeter unter Verwendung von Daten, die mit dem Technologieprototyp des CALICE Analog Hadron Calorimeter (AHCAL) am Super Proton Synchrotron (SPS) am CERN im Juli 2015 in μ^- -, e^- - und Hadronenstrahlen bis zu 90 GeV aufgezeichnet wurden.

Hochgranulare Kalorimeter wurden für das Konzept des *Particle Flow*-Algorithmus entworfen, bei dem für jedes einzelne Teilchen in einem Jet die beste Sub-Detektor-Messung verwendet wird. Der *Particle Flow*-Ansatz ist ein Schlüsselaspekt der Detektoren für den International Linear Collider (ILC), einen zukünftigen linearen Lepton-Collider, der für Präzisionsphysikstudien bei einer Schwerpunktsenergie von bis zu 500 GeV entworfen wurde.

Die CALICE-Collaboration entwickelt hochgranulare Kalorimeter für zukünftige Collider. Das AHCAL ist eines der Detektorkonzepte, basierend auf $30 \times 30 \times 3 \text{ mm}^3$ szintillierenden Kacheln, die von Silizium-Photomultipliern (SiPM) ausgelesen werden. Das SiPM-Signal wird von einem ASIC (SPIROC2b) verarbeitet, der die Amplitude und die Zeit einzelner Kalorimetertreffer messen kann. Ein technologischer Prototyp der zweiten Generation des AHCAL wurde entwickelt, mit dem Fokus auf der Skalierbarkeit des Detektors. Der in dieser Arbeit verwendete Prototyp besteht aus 14 aktiven Lagen, mit 3744 Kanälen, die in eine Stahlabsorberstruktur von 4λ Tiefe eingesetzt sind. Zum ersten Mal wurde ein großformatiger Prototyp erfolgreich in verschiedenen Teilchen Strahlen betrieben.

Diese Analyse konzentriert sich auf die Fähigkeiten der Zeitmessung des AHCAL-Prototyps. Im ersten Teil wird das Zeitkalibrierungsverfahren vorgestellt, das aufgrund der großen Anzahl von Kanälen und Besonderheiten des Front-Ends anspruchsvoll war. Eine zeitliche Auflösung von 5 ns für Myonen und 8 ns für Elektronen- und Pionschauer wurde erreicht. Im zweiten Teil dieser Dissertation wird die zeitliche Entwicklung von Hadronenschauern mit dem AHCAL-Prototyp untersucht, indem zeitliche Korrelationen mit der Energie eines Treffers, seiner Entfernung zur Schauerachse und zwischen Lagen untersucht werden. Die Ergebnisse der Teststrahlenden wurden mit verschiedenen Simulationen verglichen.

Im letzten Teil dieser Arbeit wird eine Studie über die Auswirkungen von Einschränkungen der Zeit der Kalorimetertreffer, die für die Rekonstruktion verwendet werden, auf die Kalorimeterantwort, die Energieauflösung und die Schauertopologie mit einer vollen, GEANT4-basierten Simulation des International Large Detector (ILD) Konzepts vorgestellt. Die Verwendung der Zeitinformationen der einzelnen Kalorimetertreffer hat das Potenzial, die Mustererkennung und die Energieauflösung des Kalorimeters zu verbessern.

Table of contents

Abstract	iii
Table of contents	v
Introduction	xi
I Theory	1
1 Particle Physics: Theory	3
1.1 The Standard Model of Particle Physics	3
1.1.1 The Standard Model framework	3
1.1.2 Elementary matter particles	4
1.1.3 Fundamental Forces and Mediators	4
1.1.4 Gauge invariance in the electroweak sector	5
1.2 The Higgs Boson	6
1.2.1 The Higgs mechanism	6
1.2.2 Interpretation in the Standard Model	7
1.3 Hadron physics and Jets	8
1.4 Beyond the Standard Model	9
1.4.1 Open questions of the Standard Model	9
II Calorimetry for Future Colliders	13
2 Future e^+e^- linear collider experiments	15
2.1 The case for a lepton collider	16
2.1.1 Higgs Physics	16
2.1.2 Electroweak sector	19
2.1.3 Top mass measurement	19
2.1.4 Beyond the Standard Model	20
2.2 The International Linear Collider (ILC)	20
2.2.1 General Overview	20
2.2.2 Detectors	22
2.3 The International Large Detector (ILD)	23

2.3.1	The ILD Coordinate System	23
2.3.2	The ILD Tracking System	23
2.3.3	The ILD Calorimeter System	24
2.4	The SiD Detector	25
2.5	The Compact Linear Collider (CLIC)	25
3	Calorimetry and the Particle Flow Concept	29
3.1	Particle interaction with matter	29
3.1.1	Electromagnetic showers	29
3.1.2	Interaction of charged heavy particles	32
3.1.3	Hadronic showers	33
3.2	Calorimeters	35
3.2.1	Energy resolution	36
3.2.2	Compensation	36
3.3	The Particle Flow approach	37
3.3.1	The Particle Flow concept	37
3.3.2	Implementation in PandoraPFA	38
4	CALICE Calorimeter concepts	41
4.1	Requirements for the calorimeters in ILD	41
4.2	The CALICE Collaboration	42
4.3	CALICE Electromagnetic Calorimeters	42
4.3.1	Silicon-Tungsten ECAL	42
4.3.2	Scintillator Strip-Tungsten ECAL	44
4.4	Hadronic Calorimeters	45
4.4.1	Digital HCAL	45
4.4.2	Semi-Digital HCAL	45
4.4.3	Analog HCAL	46
5	Simulation and Software tools	55
5.1	Simulation of particle showers	55
5.1.1	Electromagnetic shower models	55
5.1.2	Hadronic shower models	56
5.1.3	GEANT 4 Physics Lists	58
5.2	Software tools	59
5.2.1	ILCSOFT software framework	59
5.2.2	CALICE software framework	59
5.3	AHCAL Detector Geometry implementation and Digitization	59
5.3.1	Geometry implementation	59
5.3.2	Digitization	61

6	Commissioning of the AHCAL technological prototype	63
6.1	Testing of individual SPIROC2B chips	63
6.1.1	DAC Testing	64
6.2	HBU Commissioning procedure	65
6.2.1	Setting the High Voltage	66
6.2.2	First characterization of the SiPM gain	67
6.2.3	Adjustment of the SiPM gain	68
6.2.4	Threshold scan	69
6.3	Noise Measurement in the AHCAL	71
III	Data Analyses	75
7	AHCAL Testbeam setup & Event Selection	77
7.1	Testbeam Configuration	77
7.1.1	Beamline Setup	77
7.1.2	Testbeam Setup	78
7.1.3	Time reference	80
7.2	Dataset and Event Selection	80
7.2.1	Dataset	80
7.2.2	Muon selection	81
7.2.3	Electron Selection	82
7.2.4	Pion Selection	85
7.2.5	Rejection of outlier chips and noisy/dead channels	86
8	Energy Scale Calibration of the AHCAL	91
8.1	Energy Calibration of the AHCAL	91
8.1.1	Pedestal extraction	92
8.1.2	MIP extraction	93
8.2	Results of the energy scale calibration	94
8.2.1	MIP extraction results	94
8.2.2	Uncertainty of the calibration procedure	94
8.2.3	Systematic on the MIP scale	95
8.3	Validation of the simulation	96
8.3.1	Beam profiles	96
8.3.2	MIP Calibration	98
8.3.3	Electrons	98
9	Timing Calibration of the AHCAL	103
9.1	Introduction	103
9.2	Dataset	104
9.3	Slope and pedestal calibration	104
9.4	Calibration of the time reference	106
9.5	Time of the first hit distribution	107

9.5.1	Determination of the time reference offset	107
9.5.2	Time resolution of the AHCAL after calibration	108
9.6	Corrections applied to data	110
9.6.1	Ramp non-linearity correction	110
9.6.2	Time Walk correction	111
9.6.3	Time of first hit for muons after corrections	112
10	Validation of the time calibration	115
10.1	Time of the first hit for electrons	115
10.2	Effect of the number of triggered channels on the time distribution	115
10.3	Time of the first hit after correction	118
10.4	Transportability of the calibration	119
10.5	Estimation of the systematic uncertainty of the time correction on the time of first hit distribution	120
10.6	Systematic uncertainties	121
10.7	Validation of the simulation	122
11	Timing study of hadron showers	127
11.1	Dataset	127
11.2	Time of first hit distribution	127
11.3	Energy dependence of the time of first hit	130
11.4	Radial dependence of the time	132
11.4.1	Time dependence with the shower depth	135
11.5	Time dependence as a function of the layer	136
11.6	Time correlations between modules	138
11.7	Summary and Outlook	142
12	Application of timing cuts in the ILD detector simulation	145
12.1	Simulation and software framework	145
12.1.1	Event Simulation	145
12.2	Event Reconstruction	146
12.2.1	Tracking	146
12.2.2	Calorimeter digitization	146
12.2.3	Pandora PFA	147
12.3	Check of the energy reconstruction	147
12.4	Influence of timing cuts on hadronic showers in the ILD detector	151
12.4.1	Motivation	151
12.4.2	Event Selection	151
12.4.3	Impact of timing cuts on Particle Flow Object reconstruction	152
12.4.4	Impact of timing cuts on calorimeter performance and hadronic showers	153
12.5	Understanding the degradation of the energy resolution with timing cuts	160
12.5.1	Hit Energy spectra in HCAL	162
12.5.2	Influence of timing cuts on hit energy spectra in HCAL	164
12.6	Conclusion and Outlook	164

13 Summary	167
Acknowledgments	171
Appendix A Event selection	173
Appendix B Validation: Additional Plots	175
Appendix C Timing: Additional Plots	179
Appendix D Extraction of noise hits for simulation.	203
Appendix E Estimation of the uncertainty of the time calibration.	205
Appendix F Influence of the number of triggered channels and parametrization in simulation.	207
Appendix G Tables of rejected chips.	209
Appendix H List of dead channels.	211
Appendix I Calibration database	215
List of tables	217
List of figures	219
Acronyms	233
Bibliography	237

Introduction

The *International Linear Collider* (ILC) and the *Compact Linear Collider* (CLIC) are concepts of future lepton colliders. As seen in the past, a lepton collider experiment would be complementary to the results from the *Large Hadron Collider* (LHC) in terms of precision measurements and potential discoveries.

The LHC at CERN is the most energetic particle accelerator ever constructed. It is colliding protons at a center of mass energy up to $\sqrt{s} = 13$ TeV. In 2012, the LHC discovered the *Higgs boson* with the CMS and ATLAS experiments. This marked the accomplishment of a cornerstone of the *Standard Model* of particle physics.

The ILC is planned to collide electrons and positrons at a center of mass energy up to $\sqrt{s} = 500$ GeV. In order to achieve the best possible measurement precision at the ILC, unprecedented detector resolutions are needed. This can be achieved by the concept of *Particle Flow algorithms* (PFAs). The PFA concept aims to combine measurements of the tracking system and the calorimeters by measuring each individual particle in a jet using the best sub-detector measurement. This requires calorimeter systems with an unprecedented *granularity*. The detectors are designed based on the PFA approach in order to achieve the best possible jet energy resolution of around 3-4% [1].

Precision timing measurements have not been a key aspect in hadron calorimeters. However, in order to cope with high-rate collision experiments such as CLIC where bunches are separated by 0.5 ns [2], timing measurements become important. It would permit the separation of out-of-time pile up events and it would reduce fake energy deposits.

In addition, precision timing measurements could act as a *software compensation* method [3]. The hadron calorimeter for the ILC detectors is non-compensating meaning that the response to a hadronic shower is lower than the response to an electromagnetic shower of the same energy. The fluctuations in electromagnetic and hadronic energy fraction in a hadron shower degrade the energy resolution. The time development of a shower is correlated to the energy fluctuations in a hadron shower and therefore, would allow for an event-by-event correction in order to improve the energy resolution of the calorimeter.

This thesis discusses the ongoing development of a highly granular calorimeter within the CALICE collaboration. The work presented in this thesis is based on the analysis of testbeam data collected during the summer of 2015 at CERN with the CALICE analog hadron calorimeter (AHCAL) technological prototype which is a scintillator-based hadron calorimeter using Silicon photomultiplier (SiPM) readout. This thesis is organized as follows.

A recapitulation of the Standard Model of particle physics is given and a short explanation of the Higgs mechanism is presented in Chapter 1, giving the basis for the need of high precision measurements of the Standard Model parameters. It is followed by a description of the International Linear Collider machine and the different detector concepts, the International Large Detector (ILD) and the Silicon Detector (SiD). Furthermore, some of the key aspects of the ILC physics program are presented in Chapter 2. An introduction to

the interactions of particles with matter as well as the principles of calorimetry are presented in Chapter 3. In addition, the Particle Flow concept and its requirements are introduced.

The first and second generation calorimeter prototypes within the CALICE collaboration, with a focus on scintillator-SiPM readout, are introduced and compared in Chapter 4. These calorimeter prototypes have for goal to demonstrate the proof-of-concept of high granularity calorimeters and the scalability of the hardware to a full linear collider detector. The particle shower models in the GEANT 4 simulation software package are presented in Chapter 5 along with the AHCAL simulation geometry model implementation and digitization procedure. This is particularly important to understand the fundamental basis of the simulation shower models as it will be compared to testbeam data. The commissioning procedure of the AHCAL technological prototype is introduced and discussed in Chapter 6.

The testbeam analysis results obtained as part of this thesis are presented in Chapters 7 to 11. The thesis uses testbeam data from the AHCAL technological prototype in the energy range of 10 to 90 GeV, recorded at the Super Proton Synchrotron (SPS) facility at CERN in July 2015. The goals of this analysis are to demonstrate the feasibility of the timing calibration of a full scale hadron calorimeter and its current timing performance in various beams and to improve our understanding of the time development of hadron showers. Firstly, the testbeam setup for this thesis and event selections are described (Chapter 7). Secondly, the energy scale calibration of the AHCAL is performed and the results are discussed (Chapter 8). Thirdly, the timing analysis of the testbeam data is presented. This analysis includes the timing calibration of the full detector and the validation of the calibration with electron data (Chapter 9 and 10). Finally, the analysis of pion showers data is discussed (Chapter 11). The results of this analysis are compared to several GEANT 4 v10.1 physics lists.

Finally, the effects of timing cuts in the hadronic calorimeter of the full ILD detector simulation are investigated and discussed in Chapter 12. The goal of this analysis is to understand the effects of timing cuts on the calorimeter energy response and energy resolution as well as their impact on the spatial development of a hadron shower.

Part I

Theory

Chapter 1

Particle Physics: Theory

In this chapter, the theoretical foundations for this thesis are described. A brief overview of the Standard Model of particle physics (SM) is given in section 1.1. This is followed by a brief description in section 1.2 of the Higgs mechanism and the particle itself, which is one of the corners of the Standard Model. Finally, open-questions of the Standard Model with possible solutions are discussed in section 1.4.

1.1 The Standard Model of Particle Physics

It is difficult to say when particle physics is born. It has its origins in the discovery of the electron by Thomson [4] in 1897 and followed by the scattering experiment of Rutherford [5] in 1909 along with the discovery of radioactivity. This gave rise to the classical model of the atom by Niels Bohr. Following further experiments, it was realized that atoms themselves have an internal structure, and thus leading to the discovery of the nucleons, the proton and the neutron. With energies going higher and higher, more and more particles were discovered. In parallel, a theory that tried to understand radioactivity and the forces emerged. Finally, it was understood that most of the newly discovered particles were composite objects. All sub-atomic particles could be reduced to a small set of *elementary particles* which are known nowadays as the smallest constituents of our universe.

1.1.1 The Standard Model framework

In nature, conservation laws are fundamental laws. Conservation laws are one fundamental base of particle physics and conservation laws are associated to symmetries according to the Noether's theorem [6]. The mathematical framework of the Standard Model is the Quantum Field Theory (QFT). The electromagnetic interaction is described by Quantum electrodynamics (QED), the strong interaction is described by Quantum chromodynamics (QCD) and the weak interaction is described by the weak theory.

In QFT, each elementary particle is described by a field Φ . The interactions (kinematics and dynamics) described by the theory are given by the *Lagrangian density* \mathcal{L} as a function of the field $\Phi(x)$ and its derivatives $\partial_\mu \Phi(x)$.

Symmetries are described by requiring the Lagrangian to be invariant under certain transformations. The

Standard Model theory is based on gauge group theory and can be formulated as

$$SU(3)_C \times SU(2)_L \times U(1)_Y \quad (1.1)$$

where $SU(3)_C$ is for QCD and $SU(2)_L \times U(1)_Y$ for the electroweak theory. The electroweak theory unifies the electromagnetic and weak interactions and is known as the *Glashow-Weinberg-Salam* theory (GWS). These gauge groups are described by the Yang-Mills theory [7].

1.1.2 Elementary matter particles

The Standard Model of particle physics is a theory that describes all elementary particles and their interactions. The SM is divided in different classes of elementary matter particles: the *quarks* and the *leptons* otherwise known as *fermions*. All elementary matter particles have a spin of 1/2. The interactions between particles are mediated by *gauge bosons* (see section 1.1.3).

In the Standard Model, there are six *flavors* of quarks and leptons that are divided into three generations according to their masses and their quantum numbers: the *charge* (Q), the *spin* (S), the *color charge* and the *flavor*. The quarks are divided into two categories: up-type (u, c, t) and down-type quarks (d, s, b) which denote their flavor. Only quarks and gluons (see section 1.1.3) carry a color charge (r, g, b).

The leptons are divided into charged leptons (e^-, μ^-, τ^-) and neutrinos (ν_e, ν_μ, ν_τ). Each lepton has an antiparticle of the same mass and quantum numbers except that they have an opposite sign of charge.

Table 1.1 sums up the fundamental fermions and their properties described in the Standard Model.

Table 1.1 – Elementary fermions and their properties in the Standard Model. The masses are from [8]. The quark masses depend on the calculation scheme.

	Leptons		Quarks	
	charged	neutrino	up-type	down-type
Charge [e]	± 1	0	+2/3	-1/3
Interact weakly	yes	yes	yes	yes
Interact strongly	no	no	yes	yes
1 st generation	e (electron)	ν_e	u (up)	d (down)
Mass [GeV]	5.1×10^{-4}	$< 2 \times 10^{-9}$	$\sim 2.2 \times 10^{-3}$	$\sim 4.7 \times 10^{-3}$
2 nd generation	μ (muon)	ν_μ	c (charm)	s (strange)
Mass [GeV]	0.105	$< 0.19 \times 10^{-3}$	~ 1.28	$\sim 9.6 \times 10^{-2}$
3 rd generation	τ (tau)	ν_τ	t (top)	b (bottom)
Mass [GeV]	1.78	$< 18.2 \times 10^{-3}$	~ 173.1	~ 4.18

1.1.3 Fundamental Forces and Mediators

In Nature, the fundamental forces and interactions are known as:

- The *strong force* which is responsible for the interactions of color charged particles.

- The *electromagnetic* force which is responsible for the interactions between charged particles.
- The *weak force* which is responsible for flavor changing interactions e.g. β -decay.
- The *gravity* which describes interactions between macroscopic and massive objects.

Forces are mediated by *gauge bosons* which are elementary particles of spin 1. The gauge bosons interact with the particles by transferring a discrete amount of energy. Table 1.2 sums up the bosons with their properties described in the Standard Model.

Firstly, the strong force, represented in $SU(3)_C$. The mediators of the strong force are 8 massless gluons (g) which carry a mixture of color and anti-color charges [9].

Secondly, the electromagnetic force is mediated by another massless boson, the photon (γ).

Thirdly, the weak interaction is mediated by three gauge bosons: the electrically charged W^+ and W^- bosons and the neutral Z^0 boson. In the Standard Model, the electromagnetic and weak force are unified in the electroweak theory.

Finally, the gravity is not integrated yet into the Standard Model. It is the weakest force among all forces and it becomes only relevant for macroscopic objects or at very large distances. It is well described by the *general relativity* theory [10], on which astrophysics and cosmology strongly rely. The gravitational force can be neglected for microscopic objects comparing to the other forces.

Table 1.2 – Bosons in the Standard Model. The masses are from [8]. The photon and gluon are assumed to be massless. Gravitation is not considered.

Interaction	Particle	Mass [GeV]	Charge [e]	Spin
Strong	$g \times 8$	0	0	1
Electromagnetic	γ	0	0	1
Weak	$W^{+/-}$	80.385 ± 0.015	± 1	1
	Z^0	91.1876 ± 0.0021	0	
Higgs	H	125.09 ± 0.24	0	0

The last particle to describe is the Higgs Boson (H) which is an elementary particle of spin 0. This boson is one of the cornerstones of the Standard Model. Its properties are shown in table 1.2. The Higgs theory [11, 12] has been formalized by P. Higgs, F. Englert and R. Brout^{†1} in 1964. The predicted Higgs particle has been discovered in 2012 at the Large Hadron Collider [13, 14] with a mass of about 125 GeV and is compatible with the Standard Model.

1.1.4 Gauge invariance in the electroweak sector

In the Standard Model, the Lagrangian \mathcal{L}_D , also known as the *Dirac Lagrangian*, describes a free particle with a spin of 1/2 such as the electron [9]

$$\mathcal{L}_D = i(\hbar c)\bar{\Psi}\gamma^\mu\partial_\mu\Psi - (mc^2)\bar{\Psi}\Psi \quad (1.2)$$

^{†1}Diseased in 2011

where Ψ is a spinor field, γ^μ are the Dirac γ -matrices (four matrices) [15] and m is the mass of the particle. This Lagrangian is invariant under the *global* gauge transformation $\Psi \rightarrow e^{i\theta}\Psi$ with θ being constant (equivalent to a simple phase rotation). However, it is not invariant under a *local* gauge transformation where the phase factor θ is a function of space-time $\theta(x)$.

The local gauge invariance can be restored by adding a new vector field A_μ which follows the local gauge transformation $A_\mu \rightarrow A_\mu + \partial_\mu \lambda$ and by changing the partial derivative ∂_μ with the *covariant derivative* $\mathcal{D}_\mu = \partial_\mu + i \frac{q}{\hbar c} A_\mu$. The local gauge invariant Lagrangian for a free particle of spin 1/2 becomes [9]

$$\mathcal{L}_{QED} = i(\hbar c) \bar{\Psi} \gamma^\mu \mathcal{D}_\mu \Psi - (mc^2) \bar{\Psi} \Psi + (q \bar{\Psi} \gamma^\mu \Psi) A_\mu - \frac{1}{4} F^{\mu\nu} F_{\mu\nu} \quad (1.3)$$

where $F^{\mu\nu} \equiv \partial^\mu A^\nu - \partial^\nu A^\mu$ is the field strength tensor. The term $(q \bar{\Psi} \gamma^\mu \Psi) A_\mu$ describes the interaction between the fermionic spinor field and the new field, which can be identified as the massless photon.

\mathcal{L}_{QED} is invariant under $U(1)$ assuming that the new field is massless ($m_A = 0$). Otherwise, a mass term $m_A^2 A^\mu A_\mu$ needs to be included, which breaks the local gauge symmetry. Evidences [16–18] have shown that the photon is massless, and therefore \mathcal{L}_{QED} describes well the fermions fields interacting with the photon field, known as Quantum Electrodynamics (QED).

A similar approach was done by *Yang-Mills* for the weak interaction. It requires the Lagrangian to be invariant under $SU(2)_L$ local gauge transformation. This is done by changing the partial derivative with a new *covariant derivative* that satisfies the local gauge invariance under $SU(2)_L$. The resulting Lagrangian is in the form [9]

$$\mathcal{L}_{YM} = i(\hbar c) \bar{\Psi} \gamma^\mu \mathcal{D}_\mu \Psi - (mc^2) \bar{\Psi} \Psi + (q \bar{\Psi} \gamma^\mu \mathbf{T} \Psi) \cdot \mathbf{A}_\mu - \frac{1}{4} \mathbf{F}^{\mu\nu} \cdot \mathbf{F}_{\mu\nu}, \quad \Psi = \begin{pmatrix} \Psi_1 \\ \Psi_2 \end{pmatrix} \quad (1.4)$$

where Ψ_1 and Ψ_2 are four-component field spinors, $\mathcal{D}_\mu \equiv \partial_\mu + i \frac{q}{\hbar c} \mathbf{T} \cdot \mathbf{A}_\mu$ is the covariant derivative. \mathbf{T} refers to the Pauli matrices and $\mathbf{A}_\mu = (A_\mu^1, A_\mu^2, A_\mu^3)$ is the new gauge field. This Lagrangian satisfies local gauge symmetry in $SU(2)_L$ only if the new gauge bosons are massless.

However, experimental evidences [19] show that the weak bosons $W^{+/-}$ and Z^0 have large masses (see table 1.2). Therefore, the local gauge symmetry must be broken to include their mass terms in the Lagrangian \mathcal{L}_{YM} . A new concept is needed in order to restore the local gauge symmetry. This is called the *Electroweak Symmetry Breaking* (EWSB) mechanism. It gives rise to the *Higgs mechanism*, which allows all other massive elementary particles to interact with the Higgs field to acquire mass.

1.2 The Higgs Boson

1.2.1 The Higgs mechanism

The electroweak gauge group $SU(2)_L \times U(1)_Y$ does not allow for fermions and bosons to be massive in order to conserve the local symmetry. A new framework is needed in order to give mass to the $W^{+/-}$ and Z^0 bosons while conserving the local gauge symmetry. The electroweak symmetry breaking (EWSB) provides such framework. It postulates that a self-interacting complex scalar field exists (see section 1.2.2) predicting a scalar particle known as the Higgs boson.

In the Standard Model, the Lagrangian for a scalar field Φ of mass m with spin 0 is written as [9]

$$\mathcal{L} = \frac{1}{2}(\partial_\mu \Phi)^\dagger (\partial^\mu \Phi) - \frac{1}{2} \left(\frac{mc}{\hbar} \right)^2 \Phi^2 \quad (1.5)$$

and can be re-written (from classical Lagrangian) as

$$\mathcal{L} = \frac{1}{2}(\partial_\mu \Phi)^\dagger (\partial^\mu \Phi) - V(\Phi) \quad (1.6)$$

where $V(\Phi)$ is the potential term. The potential can be written as:

$$\begin{aligned} V(\Phi) &= \mu^2 (\Phi^* \Phi) + \lambda (\Phi^* \Phi)^2 \\ &= \mu^2 |\Phi|^2 + \lambda |\Phi|^4 \end{aligned} \quad (1.7)$$

where μ and $\lambda > 0$ are real constants. If $\mu^2 > 0$, the field is zero and the Lagrangian is symmetric. It describes a particle of mass μ with a self-interaction term. However, if $\mu^2 < 0$, this induces that the potential has a non-zero field value of $v = \sqrt{-\mu^2/\lambda}$. To circumvent this, a field centered at the vacuum $\eta = \Phi - v$ is introduced. The Lagrangian is then

$$\mathcal{L} = \frac{1}{2}(\partial_\mu \eta)^\dagger (\partial^\mu \eta) - \lambda v^2 \eta^2 + \text{cubic and quadratic terms} \quad (1.8)$$

This Lagrangian describes the kinematics for a scalar particle of mass $m_\eta = \sqrt{2\lambda}v$, the Higgs mass. This describes the principle for the Higgs mechanism for an Abelian² group ($U(1)$).

1.2.2 Interpretation in the Standard Model

The Higgs mechanism can be generalized to a non-Abelian³ group ($SU(2)_L \times U(1)_Y$). In $SU(2)$, the Higgs field is a complex doublet defined as

$$\Phi = \begin{pmatrix} \Phi^+ \\ \Phi^0 \end{pmatrix} = \frac{1}{\sqrt{2}} \begin{pmatrix} \Phi_1 + i\Phi_2 \\ \Phi_3 + i\Phi_4 \end{pmatrix} \quad (1.9)$$

where Φ^+ is the charged complex component and Φ^0 the neutral component. Following the mechanism explain in section 1.2.1, if $\mu^2 < 0$ in equation 1.7, the symmetry is spontaneously broken such as the neutral component of the Higgs field take a non-zero vacuum expectation value. At the ground state, the Higgs field is of the form

$$\Phi_0 = \frac{1}{\sqrt{2}} \begin{pmatrix} 0 \\ v \end{pmatrix} \quad (1.10)$$

The Higgs Lagrangian is

$$\mathcal{L}_{Higgs} = \underbrace{\frac{1}{2}(\mathcal{D}_\mu \Phi)^\dagger (\mathcal{D}^\mu \Phi)}_{\text{Gauge boson mass term}} - \underbrace{V(\Phi)}_{\text{Higgs mass + self-interaction}} \quad (1.11)$$

²More commonly a commutative group i.e $a \cdot b = b \cdot a$

³The counterpart of Abelian groups where commutation is not applicable i.e $a \cdot b \neq b \cdot a$

where the covariant derivative operator of $SU(2)_L \times U(1)_Y$ is $\mathcal{D}_\mu \equiv \partial_\mu + i g \mathbf{T} \cdot \mathbf{W}_\mu + i g' B_\mu Y$ where g and g' are the gauge couplings, \mathbf{W}_μ and B_μ are the gauge fields.

This leads to the $W^{+/-}$ and Z^0 to acquire mass through interaction with the Higgs such as

$$\begin{aligned} m_W &= g \frac{v}{2} \\ m_Z &= \sqrt{g^2 + g'^2} \frac{v}{2} \end{aligned} \quad (1.12)$$

The couplings of the gauge bosons with the Higgs are proportional to the square of the boson mass given by

$$g_{HVV} \propto \frac{m_V^2}{v} \quad (1.13)$$

In quantum mechanics, fermions can be left-handed or right-handed, a property known as the chirality. It is important to make the distinction because the Standard Model treats the chirality differently due to only left-handed fermions (right-handed anti-fermions) interacting with the W boson. In this case, left-handed fermions are doublets and right-handed are singlets. Right-handed neutrinos have never been observed and are not included here. Both types of fermions interact with the Higgs field and acquire masses through the *Yukawa interactions*. The Yukawa Lagrangian is [20]

$$\mathcal{L}_{Yukawa} = -y_{ij}^u \bar{u}_{Ri} \tilde{\Phi}^\dagger Q_{Lj} - y_{ij}^d \bar{d}_{Ri} \Phi^\dagger Q_{Lj} - y_{ij}^l \bar{l}_{Ri} \Phi^\dagger L_{Lj} + \text{h.c.} \quad (1.14)$$

where Q_{Lj} are left-handed quark fields, \bar{u}_{Ri} are right-handed up-type quark fields, \bar{d}_{Ri} are right-handed down-type quark fields, L_{Lj} are the left-handed lepton fields and \bar{l}_{Ri} are the right-handed lepton fields. The term $\tilde{\Phi} = i T_2 \Phi^*$ is the Higgs conjugate. The terms y^u , y^d and y^l are the Yukawa coupling matrices for up-type quarks, down-type quarks and charged leptons respectively. These couplings are free parameters in the Standard Model.

All the couplings of fermions with the Higgs can be predicted and are proportional to the fermion mass and v given by

$$g_{Hff} \propto \frac{m_f}{v} \quad (1.15)$$

The Higgs mass is one of the important free parameters of the Standard Model. A precise measurement of the mass is necessary to validate the Standard Model. The Higgs boson has a large branching ratio decaying to a pair of bottom quarks ($\text{BR}(H \rightarrow b\bar{b}) = 0.58$). However, in hadron colliders such as the Large Hadron Collider (LHC), the ratio signal over background is very low [21] for this channel and a poor mass resolution due to large QCD background and thus makes it very challenging for a precise mass measurement.

Lepton colliders (see chapter 2) can offer a precise measurement of the Higgs Boson properties for example by exploiting the $H \rightarrow b\bar{b}$ channel. This implies the measurement of a final hadronic state. The specifics of hadrons are explained in the following section.

1.3 Hadron physics and Jets

Quarks are fundamental particles of the Standard Model that are governed by the strong interaction. Bound states of quarks forming colorless particles are commonly called *hadrons*. They are categorized as either *mesons*, which are composed of a pair of quark-antiquark, or *baryons* which are composed of three

quarks.

The existence of quarks has been proven experimentally even if no *free* quarks have been observed. This is explained by the *color confinement* in which color charged particles cannot be isolated, and thus quarks cannot be observed directly.

An important aspect of QCD is the *asymptotic freedom*. It means that the strong interaction between quarks and gluons becomes weaker at high energy scales, i.e. at short distances. Asymptotic freedom has the effect that quarks inside a hadron are considered free and are not tightly bounded.

Quarks turn into colorless hadrons through a process called the *hadronization*. This process can only be described phenomenologically via three main axioms: the independent hadronization, the string hadronization [22] and the cluster hadronization [23]. In a simple system of a di-jet production in a e^+e^- annihilation, the $q\bar{q}$ partons move away from the common production vertex. The partons are bounded by a *tube* or *string* that confines both objects. At short distances (<1 fm), the $q\bar{q}$ pair is considered free. As they are colored particles they can radiate gluons. Since gluons carry color charges, they can also emit radiation. This process is known as *parton showering* [24]. Once the distance becomes large enough, the energy stored in the string will be sufficient to produce a new $q\bar{q}'$ pair. This process continues and creates a cascade of new $q\bar{q}$ pairs until the energy is low enough to hadronize the quarks into colorless hadrons. Unstable hadrons decay further into more stable particles that are observed in the detector. This creates a collimated cascade of particles known as a *jet*.

1.4 Beyond the Standard Model

The Standard Model succeeds in describing many experimental results. The current Standard Model is composed of 19 free parameters which are:

- The three leptons masses (m_e, m_μ, m_τ)
- The six quark masses ($m_u, m_d, m_c, m_s, m_b, m_t$)
- The strong gauge coupling constant g_s , the electroweak gauge coupling constants g and g'
- The vacuum expectation value v and the Higgs mass m_H
- The weak mixing angles ($\theta_{12}, \theta_{23}, \theta_{13}$) and the CP phase δ for the flavor-changing weak decays [25]

These parameters have their numerical values determined from experimental data. Nevertheless, there are still open questions that need to be answered, suggesting that the SM is maybe a *low energy* approximation of a higher theory.

1.4.1 Open questions of the Standard Model

Gravity

Gravity is a fundamental force in nature and is described by the theory of general relativity. The Standard Model does not include gravity. Some attempts to unify the SM and general relativity have been proposed by theorists, but they do not provide enough prediction power to be experimentally validated.

Dark Matter

Astrophysics and Cosmology have given evidences for the existence of invisible matter, e.g. from galaxies observations [26], the Cosmological Microwave Background (CMB) [27]. This invisible matter is known as the *dark matter*. Dark matter particles have not been found so far, the interaction of dark matter with EM force and strong force have been ruled out. It is supposed that the coupling of dark matter is only through the weak interaction. New physics beyond the Standard Model is needed to explain the nature of dark matter.

Neutrino masses

No neutrino masses are present in the Standard Model. As there is no right-handed neutrino, neutrinos cannot acquire mass through Yukawa coupling. However, experiments on neutrino oscillations [28] shows that neutrinos have a mass. The mechanism by which neutrinos gain mass is so far unclear.

Hierarchy problem

The Standard Model Higgs boson mass of around 125 GeV is a theoretical challenge known as the hierarchy problem. In the SM, the mass of the Higgs boson gets loop corrections from fermions, gauge bosons and the Higgs itself [29]. If the Standard Model would be valid up to the Plank scale $\Lambda \sim 10^{19}$ GeV, these corrections would make the mass of the Higgs boson very large. To keep the Higgs mass at the electroweak scale (~ 100 GeV), it would require a very fine-tuning, i.e cancellations between the loop corrections and the bare mass. This is considered unnatural.

Asymmetry matter-antimatter

The Standard Model predicts that matter and anti-matter should be in equal amounts in the observable universe. But it is well established that our universe is composed mostly of matter. This *baryon asymmetry* is not explained in the Standard Model. CP violation [30] may be the answer for this asymmetry. It is present in the Standard Model but has only been observed for weak interactions in the quark sector. However, CP violation would not entirely explain the matter-antimatter asymmetry by itself [31].

Numerous theoreticians are extending the Standard Model to answer few of these questions. The simplest approach is to add symmetries to the Lagrangian. This approach is known as *Supersymmetry* (SUSY). Supersymmetry adds super-partners to the Standard Model particles differing by a spin of 1/2, i.e. each fermion has a boson as super-partner and vice-versa.

The Standard Model is so far the most reliable theory describing the elementary objects and the interactions that govern our world. The Higgs boson is one of the cornerstones of the theory, therefore, a very precise measurement of its properties such as mass and couplings are needed. This motivates us to probe the Standard Model deeply and look for any deviations from predictions that would suggest physics beyond the Standard Model. Measurements at hadrons colliders, like the Large Hadron Collider, suggest that if any other particle exists, it would be at a multi-TeV scale. However, the effect of such particles on coupling measurements would be below the percent level. Currently, it is very challenging for the LHC to achieve the level

of precision needed to distinguish theories beyond the Standard Model [\[32\]](#). A lepton collider would be the perfect tool to conduct precision measurements as shown in the next chapter.

Part II

Calorimetry for Future Colliders

Chapter 2

Future e^+e^- linear collider experiments

The Standard Model has been so far a very successful theory in describing physics phenomena up to TeV-scale energies. However, there are still open-questions that the Standard Model fails to answer as discussed in chapter 1.

Currently, the only high energy hadron collider in operation to push the energy frontier is the *Large Hadron Collider* (LHC) at CERN between Switzerland and France. The LHC uses the Large Electron-Positron Collider (LEP) long underground tunnel of 27 km circumference and it is colliding protons at a center-of-mass energy up to $\sqrt{s} = 14$ TeV using superconducting magnets. The LHC is probing the Standard Model to an unprecedented energy scale and searches for new particles beyond the Standard Model. The discovery of the Higgs Boson in 2012 [13, 14] was one of the major milestones of the LHC. The colliding particles are protons that are composite particles. The collision happens at parton level, carrying a fraction of the proton energy of which the energy is not accessible by the experiment. These collisions are very complex and the initial conditions of the collisions are not known and thus, limits the precision of the measurements. On the other hand, lepton colliders provide a clean environment and a known initial state for precision physics.

A limitation of e^+e^- ring colliders is the maximum achievable collision energy which is limited by the energy losses of the particles due to the synchrotron radiation. Due to the energy and mass dependence of the radiation losses ($\sim E^4/m^4$), a trade-off is needed between the radius of the collider and the maximal energy provided to the machine. In order to minimize the power losses by colliding leptons, it is most likely that the next e^+e^- collider will be a linear accelerator to achieve energies near the TeV scale.

There are currently several proposals for future lepton colliders such as the *Compact Linear Collider* (CLIC) [2], the Future Circular Collider (FCC) [33], the Circular Electron Positron Collider (CEPC) [34, 35] and the *International Linear Collider* (ILC) [1]. The most mature project is the ILC which is a polarized lepton collider with a center of mass energy between 250 and 500 GeV upgradable to 1 TeV.

In this chapter, the scientific case for a lepton collider is made in section 2.1. Then a short summary of the ILC machine is given in section 2.2. The two detectors are foreseen to be installed at the ILC interaction point, namely the International Large Detector (ILD) and the Silicon Detector (SiD) are described in section 2.3. All the information provided in this chapter are based on the ILC Technical Design Report (TDR) [1, 20, 36–38] if not stated otherwise.

2.1 The case for a lepton collider

The ILC physics program is complementary to studies done at the LHC. The recent discovery of the Higgs Boson in the 125 GeV range at the LHC, which was for several decades the missing piece of the Standard Model, can be studied with higher precision with the ILC. The probing of the characteristics of the Higgs Boson to a percent level is necessary to validate the current SM and as well in order to be able to observe any deviations to the SM predictions that would be a strong hint for physics beyond the SM. Besides, the ILC would provide many opportunities for the study of new physics, the Z and W Bosons and the top quark. This section will describe few key points of the ILC physics program.

2.1.1 Higgs Physics

The ILC experiment would provide a precise measurement of the Higgs Boson characteristics such as its mass, its full decay width and its coupling to SM particles. At hadron colliders such as the LHC, the Higgs total cross-section is measured under some assumptions. Therefore the measurements of the Higgs properties are model-dependent. The precision on some of the Higgs properties at the LHC is significantly worse than for the ILC [39].

2.1.1.1 Higgs mass, Branching Ratio and coupling measurements

There are two main production modes of the Higgs at the ILC, the *Higgsstrahlung* and *Vector Boson Fusion* (VBF). The *Higgsstrahlung* process is the production of a Higgs Boson in association with a Z Boson. For the VBF mode, either two Z or W Bosons fuse in a Higgs Boson in association with either an electron-positron pair or neutrino-antineutrino pair. The Feymann diagrams of these processes are shown in figure 2.1.

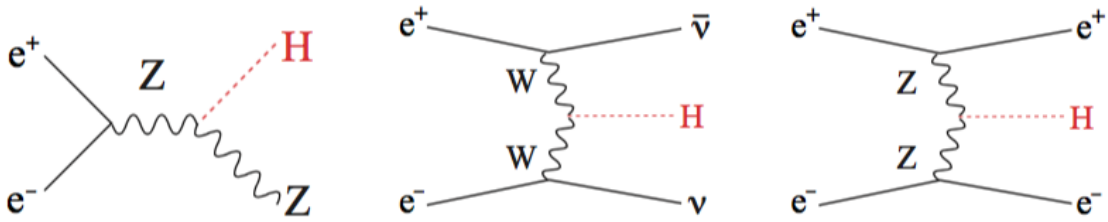


Figure 2.1 – Feymann diagrams for the Higgs production at the ILC at tree level. [20]

At $\sqrt{s} = 250$ GeV, the production cross-section is dominant [40]. At higher energies around $\sqrt{s} = 450$ GeV, the VBF production cross-section starts to dominate. The decay modes of the Higgs and their branching ratio are shown in table 2.1. Massless final states decays are possible through heavy loops (top, WW or ZZ loops).

At the ILC, the initial state of the collision is precisely known, offering a unique method to measure the Higgs mass. The *recoil mass measurement*, in the *Higgsstrahlung* process, aims at reconstructing the Z boson recoiling against the Higgs without the need to reconstruct the Higgs itself, no assumption is made on the decay mode. This enables a model-independent measurement of the Higgs mass, the Higgs couplings and the Higgs full decay width with an unprecedented precision.

Table 2.1 – Decay modes of the Higgs boson and the branching ratio for a SM Higgs boson at $m_H = 125$ GeV []. Others represents $\mu\mu$, $\gamma\gamma$, $Z\gamma$ and invisible.

Decay Mode	Branching Ratio
$H \rightarrow b\bar{b}$	57.7%
$H \rightarrow WW^*$	21.5%
$H \rightarrow ZZ^*$	2.6%
$H \rightarrow gg$	8.6%
$H \rightarrow \tau^+\tau^-$	6.3%
$H \rightarrow c\bar{c}$	2.9%
$H \rightarrow \text{others}$	< 1%

Events where the Z decays to a pair of charged leptons (e^+e^- or $\mu^+\mu^-$) are used due to the excellent tracker resolution of the ILC detectors. The recoil mass m_{recoil} can be calculated as [41]

$$m_{recoil}^2 = (\sqrt{s} - (E_{l^+} + E_{l^-}))^2 - |\mathbf{p}_{l^+} + \mathbf{p}_{l^-}|^2 \quad (2.1)$$

where E_{lj} and \mathbf{p}_{lj} are the energy and momentum of the lepton pair from the Z decay. These events can be selected by constraining the invariant mass of the lepton pair to be consistent with the Z mass. A reconstructed recoil mass distribution for $Zh \rightarrow \mu^+\mu^-X$ is shown in figure 2.2. Combining the results of the $\mu^+\mu^-$ and e^+e^- channels, a statistical precision of 32 MeV on the Higgs mass can be achieved, resulting in an uncertainty of 2.5% on the production cross-section measurement.

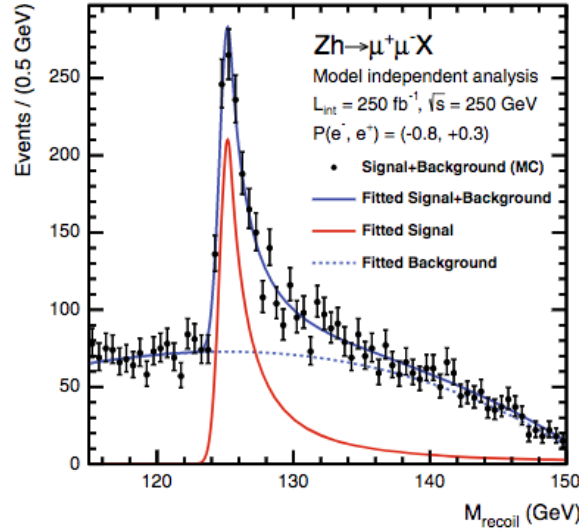


Figure 2.2 – The recoil mass distribution for $Zh \rightarrow \mu^+\mu^-X$ at $\sqrt{s} = 250$ GeV for 250 fb^{-1} integrated luminosity and beam polarisation of (+80%, -30%). Simulated with $m_h = 125$ GeV. [42]

At the ILC, the full Higgsstrahlung inclusive production cross-section is proportional to the square of the

coupling between the Z and Higgs, g_{hZZ}

$$\sigma(e^+e^- \rightarrow Zh) \propto g_{hZZ}^2 \quad (2.2)$$

The branching ratio of a decay channel is expressed as

$$BR(h \rightarrow XX) = \frac{\Gamma(h \rightarrow XX)}{\Gamma_h} \quad (2.3)$$

where Γ_h is the full decay width of the Higgs and $\Gamma(h \rightarrow XX)$ is the partial decay width with $\Gamma(h \rightarrow XX) \propto g_{hXX}^2$.

Typically in a collider, the quantity measured is the event rate of a final state corresponding to the product of the production cross-section and BR. Thus the final state cross-section at the ILC for the Higgsstrahlung and VBF production is expressed as

$$\begin{aligned} \sigma(e^+e^- \rightarrow Zh) \times BR(h \rightarrow XX) &\propto \frac{g_{hZZ}^2 \cdot g_{hXX}^2}{\Gamma_h} \\ \sigma(e^+e^- \rightarrow h\nu_e\nu_e) \times BR(h \rightarrow XX) &\propto \frac{g_{hWW}^2 \cdot g_{hXX}^2}{\Gamma_h} \end{aligned} \quad (2.4)$$

By measuring the inclusive cross-section $\sigma(e^+e^- \rightarrow Zh)$ with the recoil technique, a direct measure of g_{hZZ} is done. A precision of 1.3% can be achieved for this coupling for 250 fb^{-1} integrated luminosity. The coupling g_{hWW} for the same final state of the Higgs (e.g. $h \rightarrow bb$) can be expressed as:

$$g_{hWW}^2 \propto g_{hZZ}^2 \times \frac{\sigma(e^+e^- \rightarrow h\nu_e\nu_e)}{\sigma(e^+e^- \rightarrow Zh)} \quad (2.5)$$

Therefore, it is only needed to measure the branching ratio $BR(h \rightarrow WW^*)$ to determine Γ_h via $\sigma(e^+e^- \rightarrow h\nu_e\nu_e) \times BR(h \rightarrow WW^*) \propto \frac{g_{hWW}^4}{\Gamma_h}$. All inclusive cross-section measurements can be included into a global fit to minimize the uncertainty on Γ_h . Figure 2.3 shows the relative precision achievable for the ILC compared to the LHC. For most of the measurements, the ILC is one order of magnitude more precise than at the LHC and below the percent level precision.

There are different models for physics beyond the Standard Model. These models result in deviations, scaling as $1/\Lambda_{NP}^2$, to the predicted Higgs couplings from the SM generally around few percent level [43]. For example, in a composite Higgs model, a decrease in all the Higgs couplings is expected. Therefore, searching for deviations in the Higgs couplings measurement gives a way to know if the discovered Higgs is from the Standard Model, a composite particle or whether there is more than one Higgs boson.

2.1.1.2 Higgs self-coupling

The trilinear Higgs self-coupling λ determines the shape of the Higgs potential as discussed in chapter 1. It gives an understanding of the nature of the transition from a symmetric state to a broken symmetry state in the electroweak sector [44]. It would give hints about the possibility of CP violation in the Higgs sector and thus information about the origin of baryon-antibaryon asymmetry.

The trilinear coupling can be studied at the ILC via the Higgsstrahlung or VBF production starting at around $\sqrt{s} = 350 \text{ GeV}$. The cross-section maximizes at around $\sqrt{s} = 600 \text{ GeV}$ dominated by the Higgsstrahlung

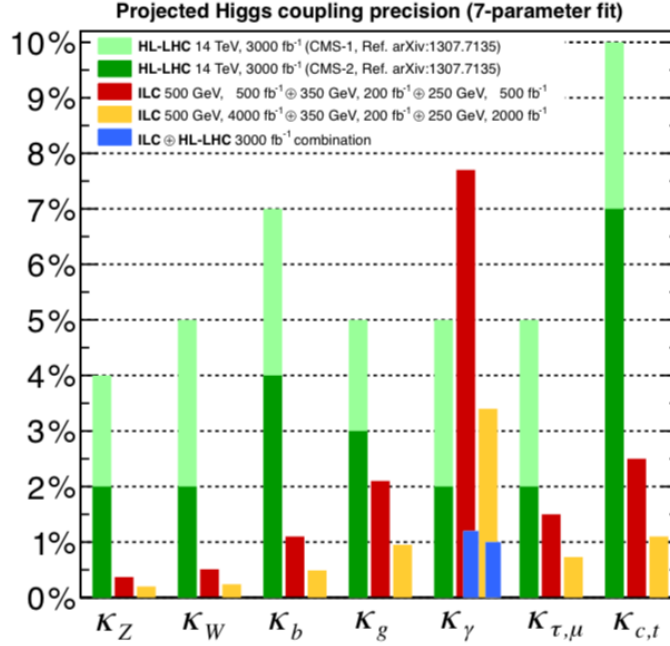


Figure 2.3 – Relative precision of the Higgs couplings extracted for the ILC in a model-dependent analysis. Projections of the achievable precision on the Higgs couplings for the HL-LHC are shown as well in a pessimistic (CMS-1) and optimistic (CMS-2) case on the systematic uncertainties [39].

process. Extensive studies [45, 46] have found that at 500 GeV with 4 ab^{-1} of integrated luminosity combining $H \rightarrow bbbb$ and $H \rightarrow bbWW^*$ channels, a precision of 27% on the Higgs self-coupling can be achieved. At 1 TeV with 8 ab^{-1} and by combining with the 500 GeV measurement, a precision of around 10% can be achieved on the trilinear Higgs self-coupling.

2.1.2 Electroweak sector

The ILC gives access to an unprecedented level of precision for the measurement of W and Z masses, widths and couplings. The production processes $e^+e^- \rightarrow W^+W^-$, $e^+e^- \rightarrow ZZ$, $\gamma\gamma \rightarrow W^+W^-$ and triple boson production $e^+e^- \rightarrow VVV$ can be studied.

Currently, the LHC does not constrain much new physics in the electroweak sector and its reach is limited [47]. Therefore with the ILC, vector boson scattering can be studied at the TeV scale to constrain furthermore the Electroweak (EW) sector and search for deviations in the structure of the EW sector of the SM. Many new physics models beyond the SM predict new couplings to the W and Z bosons, thus mixing effects of the new bosons could be detected by the ILC precision measurements.

2.1.3 Top mass measurement

The top quark is the heaviest particle in the Standard Model with a mass of $173.34 \pm 0.27 \text{ (stat)} \pm 0.71 \text{ (syst) GeV}$ [48]. The top quark was discovered at the Tevatron by the CDF and DØ experiments [49, 50], and has only been studied by hadron colliders so far. The ILC would be the first machine to study the top quark

using a leptonic initial state.

It is the most strongly coupled particle to the Higgs as the coupling is proportional to the mass (see chapter 1). Many parameters of the Standard Model such as the W, Z couplings and Higgs mass are affected by the top mass via radiative corrections. The top quark is therefore expected to be one of the most promising windows to new physics beyond the Standard Model at the TeV energy scale.

The top quark has a very short lifetime (10^{-25} s), and it decays before hadronization thus the top is a "bare" quark. It decays almost exclusively to $t \rightarrow W^+ b$ with the b quark being almost only left-handed polarized. At the ILC, the top quark mass can be measured at the threshold of $\sqrt{s} \sim 2m_t$ as the machine can be tuned in energy. Thus the shape of the top cross-section production can be measured allowing precise measurement of the top mass m_t , width Γ_t and strong coupling constant α_s . Additionally, the initial beam polarization state can be tuned to enhance the cross-section.

Via this method, the top mass is expected to be measured at the ILC with a statistical precision of around 30 MeV but the final mass is mostly dominated by theoretical uncertainties of around 100-200 MeV.

2.1.4 Beyond the Standard Model

One of the central pillar for a lepton collider is the search for new physics beyond the Standard Model. For direct searches, dark matter is of the main interest such as mono-photon searches similar to mono-jet searches at the LHC [51]. The ILC is complementary to the LHC in covering the phase space of dark matter mass, in the sense that the LHC covers high masses while the ILC covers low couplings and high mediator masses [52].

In addition, some regions are not accessible or can be very challenging at the LHC in the case of a degenerate lightest supersymmetric particle (LSP) and the next lightest supersymmetric particle (NLSP) [53]. The ILC could resolve such degenerate spectrum thus allowing the measurement of SUSY parameters in the order of 5% [54].

2.2 The International Linear Collider (ILC)

The design of the International Linear Collider (ILC) has been ongoing for several decades of research and development for linear colliders. The ILC community regroups more than 300 laboratories, institutes and universities worldwide. In this section, a general overview of the ILC machine is given.

2.2.1 General Overview

The ILC is planned to be a 31 km long e^+e^- linear collider to be built in Japan with a baseline design peak luminosity of around $2 \times 10^{34} \text{ cm}^{-2} \text{ s}^{-1}$ and a center-of-mass energy of 500 GeV. An upgrade up to 1 TeV center-of-mass energy and a higher luminosity is possible. However, a staging scenario approach starting at 250 GeV is proposed in [55]. It uses superconducting radio-frequency (SCRF) cavities to accelerate electrons and positrons. The project is currently under discussion between the governments and a decision by the end of 2018 should be reached. A schematic of the ILC layout is shown in figure 2.4.

One of the advantages of the ILC is the polarization of beam particles. A polarization up to 80% for electrons and 30% for positrons can be achieved. The use of opposite sign polarity for the electron and positron beam enables the enhancement of SM rates. On the other hand, the use of same sign polarity for the beams

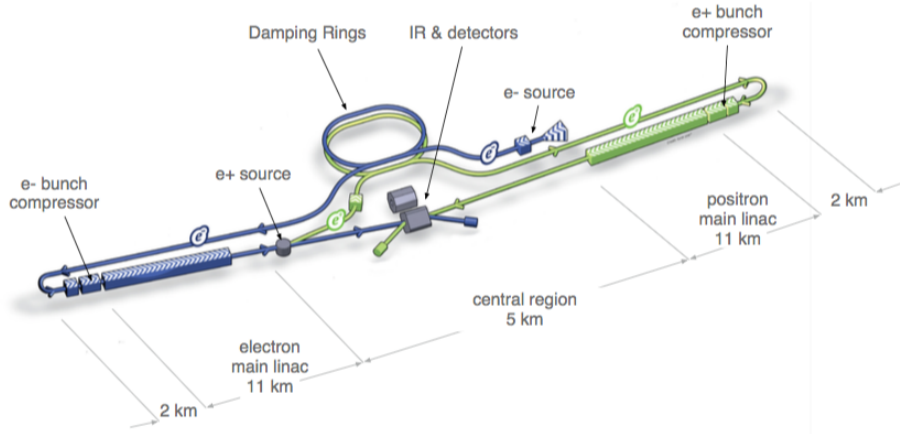


Figure 2.4 – Schematic of the International Linear Collider (not to scale). [1].

suppresses the Standard Model background. The polarization is a crucial feature in the ILC program as explained in section 2.1.

The electron beam is produced by a laser illuminating a GaAs photocathode in a DC electron gun. It provides bunches of electrons that are accelerated to 5 GeV in a SCRF booster before being collected in the damping ring. The damping ring has a circumference of 3.2 km in which bunch trains are formed. The emittance of the beam is then reduced by 5 orders of magnitude down to 20 nm. It is achieved by the succession of normal magnets, superconducting magnets and wiggler magnets. The wiggler magnets cool the beam by damping synchrotron radiation and, thus reducing the beam emittance. The beam structure of the ILC consists of bunch-trains separated by around 200 ms. Each bunch-train contains 1312 bunches with 2×10^{10} particles. Each bunch is separated by 554 ns. A schematic of the beam structure is shown in figure 2.5.

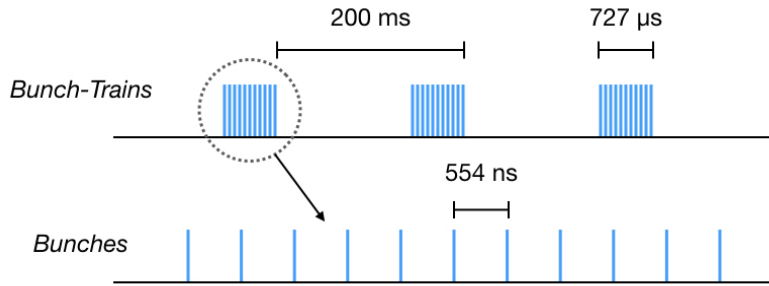


Figure 2.5 – Schematic of beam structure of the ILC operated a design parameters.

The electron beam is then transported by the Ring to Main Linac (RTML), accelerating electrons from 5 GeV to 15 GeV while compressing the bunch-length to few micrometers for the interaction region (IR).

The main linac of the ILC accelerates the electron beam up to 250 GeV by using superconducting RF cavities of niobium as shown in figure 2.6. The cavities are operated at 2 Kelvins housed in cryomodules. The RF power is delivered by a system of Klystrons. The average gradient of the cavities is around $31.5 \frac{MV}{m}$ with a quality factor $Q_0 \geq 10^{10}$. A demonstration of the mass-production and the operation of cryomodules which

represents around 1% of the ILC has been achieved for the synchrotron sources of FLASH and recently the European X-Ray Free Electron Laser (XFEL) [56] based at DESY.



Figure 2.6 – Picture of a nine-cell 1.3 GHz superconducting RF niobium cavity developed for the ILC. [36].

After the acceleration, the electron beam is transported through a superconducting helical undulator which generates photons from 10 to 30 MeV. Then the electron beam is separated from the photon beam and transported by the Beam Delivery System (BDS) to the IR. The BDS is a complex system of different magnets and collimators which focuses the beam down to $474 \text{ nm} \times 5.9 \text{ nm}$ (x and y respectively at $\sqrt{s} = 500 \text{ GeV}$) to reach the luminosity goal of $2 \times 10^{34} \text{ cm}^{-2} \text{ s}^{-1}$.

The photons produced from the electron beam are directed onto a thin ($0.4X_0$) titanium alloy (Ti) target producing electron-positron pairs. The positrons are accelerated to 400 MeV in a first step while the remaining electrons and photons are dumped. Then, in a second step, they are accelerated to 5 GeV by a booster and injected into a damping ring, parallel to the electron ring. From there, the positron beam follows a second beam line that is similar to the electron beam line design and both beams are brought into collision at the IR, where the ILC detectors lie.

2.2.2 Detectors

The extensive ILC physics program (see section 2.1) drives the requirements on the ILC detectors. In order to realize it, significant advances in detector performance are essential and many technological challenges must be overcome.

At the ILC, many physics processes have a hadronic jet final state. The requirement on the relative jet energy resolution at the ILC is driven by the separation of W and Z di-jet final states which is around 3-4%. The current state of the art detectors cannot fulfill this requirement. The *Particle Flow* approach (see section 3.3) is an alternative method to traditional calorimetry that allows for better jet energy resolution. The Particle flow reconstruction requires a highly efficient tracking system and highly granular calorimeters.

At the ILC, two general purpose detector experiments are sharing the interaction region in a push-pull configuration. One detector occupies the IR while the other detector is parked in the detector hall. Both detectors can be moved in and out of the IR periodically every few weeks.

The requirements imposed by the physics program to the ILC detectors are [38]:

- A relative jet energy resolution σ_E/E between 3% to 4% for 100 GeV jets.
- A track momentum resolution σ_p/p^2 below $5 \times 10^{-5} \text{ GeV}^{-1}$.

- An impact parameter resolution below $5\text{ }\mu\text{m} \oplus 10\text{ }\mu\text{m}/p(\text{GeV}/c) \sin^{3/2}(\theta)$ for an excellent flavor tagging (efficiency above 60% for b jets).
- A low angle coverage for hermiticity.

The two detector concepts being developed for the ILC, the *Silicon Detector* (SiD) and the *International Large Detector* (ILD), are designed to fulfill the above requirements. In the following section, the ILD and SiD detector concepts will be briefly described.

2.3 The International Large Detector (ILD)

The ILD detector is a multi-purpose detector. The tracking system and the calorimeter systems are both located within a superconducting solenoid magnet of 3.4 m radius providing a field of 3.5 T parallel to the beam axis. A schematic of the ILD detector is shown in figure 2.7.

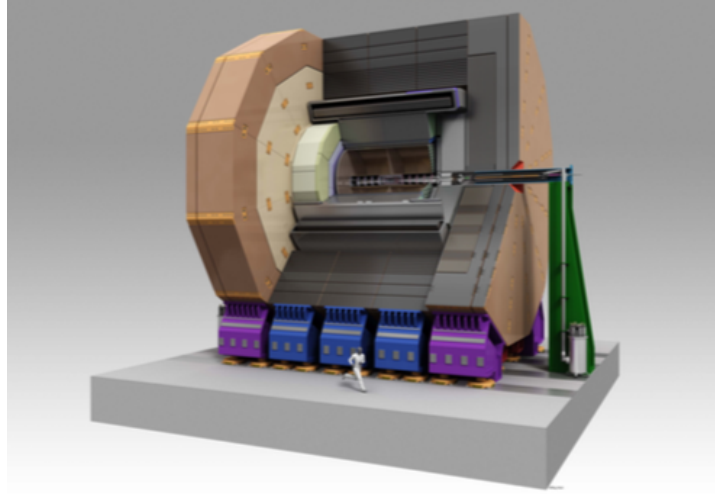


Figure 2.7 – Schematic view of the International Large Detector. [38]

2.3.1 The ILD Coordinate System

The ILD coordinate system [57] is a right-handed Cartesian system with its origin at the nominal ILC interaction point. The z-axis is along the beam direction such as the z-component of the electron beam momentum is positive $p_z^- > 0$. The y-axis is pointing upwards. The x-axis then completes the Cartesian right-handed system.

2.3.2 The ILD Tracking System

The ILD tracking system is composed of multiple sub-detectors. A vertex detector (VTX) is located near the beam pipe surrounded by the main tracker, a Time Projection Chamber (TPC). Additionally, this is supplemented by few layers of silicon tracker between the VTX and the TPC (SET/SIT) and between the TPC and the calorimeters (ETD). Each subsystem is briefly described in the following.

2.3.2.1 Vertex detector (VTX) and Silicon tracking system (FTD/SET/SIT/ETD)

The vertex detector needs to fulfill the requirements of the ILC physics program by delivering an excellent flavor tagging performance of heavy quarks.

The ILD Tracking system consists of a multi-layer pixel vertex detector at the innermost part, at around 1.6 cm of the beam pipe. Different VTX geometries are proposed, a three double layer or a five single layer silicon pixel geometry. Additionally, two layers of silicon strip detector (SIT) are placed around the vertex detector to fill the gap between the VTX and the *Time Projection Chamber* as well as two other layers of silicon strip detector (SET) are installed between the TPC and the calorimeters.

In the forward region, silicon pixel disks and silicon strip disks (FTD) are installed to allow for tracking at low angles. Between the TPC endplate and the calorimeter endcaps, two silicon strip layers (ETD) are installed to improve tracking performance and to provide redundancy between the main tracking volume and the calorimeters.

The VTX offers position hit resolutions of less than $6\mu\text{m}$ [38] with a very low material budget of $0.15\% X_0$ per layer. The SIT and FTD pixel detectors offer similar position hit resolutions with a material budget of $0.65\% X_0$.

While the technology has not been decided yet for the VTX, several technologies are studied: CMOS Pixel Sensors (CPS) [58], Fine Pixel CCDs (FPCCD) [59] and Depleted Field Effect Transistors (DEPFET) [60]. These technologies have the potential to fulfill the requirements of the ILD VTX.

2.3.2.2 Time Projection Chamber (TPC)

The main feature of the ILD tracking system is a large TPC that can provide more than 200 points per track, covering from 330 mm to 1808 mm in radius. The TPC consists of a gas sensitive volume that serves as detection medium. When a charged particle goes through the TPC, it ionizes the gas along its path. The free electrons produced via ionization drift towards the endplates of the TPC by applying an electric field parallel to the beam axis. The endplate detects the drifting electrons using a *Gas Electron Multiplier* (GEM) [61] or a *Micro-Mesh Gaseous Structure* (Micromegas) [62] readout system. These technologies provide the amplification of the drifting electrons and give a two-dimensional position information.

The spatial resolution of the TPC is better than $100\mu\text{m}$ [63] and also offer a double hit resolution in the order of less than 2 mm in $r\phi$. This resolution is worse than what silicon tracking can offer but the TPC presents the advantage of a very low material budget, continuous tracking and excellent reconstruction of the non-pointing tracks from multiple scattering. In addition, the TPC offers the possibility of particle identification via the specific energy loss measurement $\frac{dE}{dx}$ (see subsection 3.1) with a resolution of around 5%.

A combined momentum resolution σ_{p_T}/p_T^2 of $2 \times 10^{-5} \text{ GeV}^{-1}$ has been achieved for high momenta for the ILD tracking system.

2.3.3 The ILD Calorimeter System

The ILD calorimeter system is designed and optimized for *Particle Flow* (see section 3.3). It is aiming to achieve a jet energy resolution σ_E/E of around 3-4 % in the energy range of 45 to 250 GeV. To achieve such goals, an unprecedented 3D granularity for the calorimeters is required combined with an excellent tracking reconstruction. To minimize material budget and optimize track associations to depositions in the

calorimeters, the calorimeters are placed inside the solenoid magnet thus limiting the depth of the calorimeters. The ILD calorimeter system consists of an electromagnetic calorimeter (ECAL) and a hadronic calorimeter (HCAL).

The electromagnetic calorimeter needs to have an unprecedented granularity to fulfill the Particle Flow requirements. It needs to be able to separate showers created by different photons. Additionally, it plays an important role in hadronic shower start identification and separation as a significant fraction of hadron showers start in the ECAL. The baseline ECAL has 30 active layers using silicon-based readout with a 5×5 mm segmentation in a tungsten absorber, allowing a very compact design. The total depth of the ECAL is of 24 radiation length. While the baseline uses silicon, a plastic scintillator strips technology is considered as an option. The two technologies can also be combined to reduce the overall cost of the detector while maintaining the performance.

The hadronic calorimeter measures the energy of hadrons. Following the particle flow approach, only the energy from neutral hadrons is measured in the HCAL, the energy of charged hadrons is measured in the tracker. Therefore, the HCAL needs to provide the necessary topological resolution power to separate charged and neutral hadron showers. The baseline HCAL has 48 active layers in a steel absorber of a depth of 6 nuclear interaction length. Two options are considered for the active layers: scintillator-tile based and gas-based technologies.

In the forward region, additional calorimeters are placed: LumiCal, BeamCal and LHCAL for luminosity monitoring, beamstrahlung measurement and hermiticity at low angles down to 5 mrad.

After the solenoid magnet, an iron yoke returns the magnetic field and is planned to be instrumented with scintillator strips or resistive plate chambers (RPC) to serve as a muon detector and tail catcher for high energy jets.

2.4 The SiD Detector

The SiD detector concept is very similar to the ILD detector. It differs by its size much smaller than ILD, the use of a stronger magnetic field (5 T) and a full silicon tracking system instead of a TPC. The ECAL is also using silicon as active material. Resistive plate chambers (RPCs) with gas as active material were planned to be used for the hadron calorimeter system but a recent change in the baseline design includes now a scintillator-tile hadronic calorimeter. The performance of SiD is very close in numbers to ILD. A representation of the SiD detector is shown in figure 2.8.

2.5 The Compact Linear Collider (CLIC)

Another concept that was aforementioned is the Compact Linear Collider (CLIC) [2, 64]. CLIC is drastically different than the ILC in the design and technology used. CLIC uses normal conducting copper cavities operated at 12 GHz which is much higher than ILC (1.3 GHz). The cavities have a much higher accelerating gradient at around $100 \frac{MV}{m}$. Therefore, a center-of-mass energy up to $\sqrt{s} = 3$ TeV can be achieved while keeping the accelerator compact.

It uses a two-beam operation scheme where a drive beam provides the RF power to accelerate another beam. The beam structure is composed of bunch-trains separated by 20 ns. Each bunch-train consists of 312 bunch-crossings that are separated by 0.5 ns.

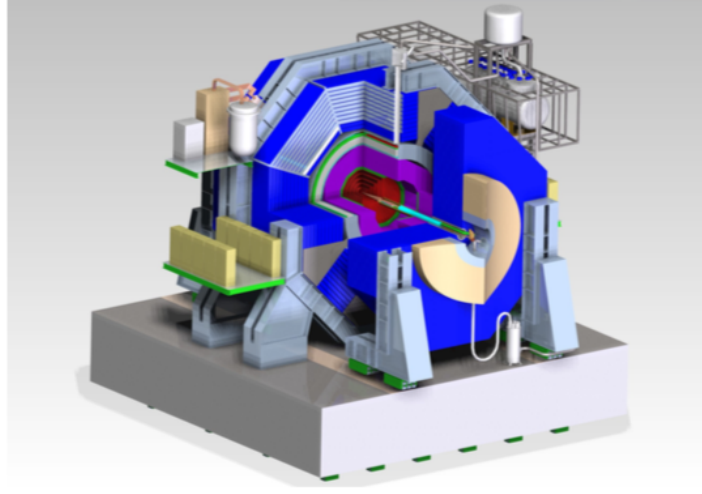


Figure 2.8 – Schematic view of the Silicon Detector. The different sub-detector are shown: tracking (red), ECAL (green), HCAL (violet) and flux return yoke (blue). [38]

The CLIC detectors must meet at minimum the requirements of the ILC detectors. However, they must meet the requirements up to 3 TeV. Therefore, a higher magnetic field of 4 T and a thicker hadron calorimeter (50 active layers corresponding to 7.5 interaction length) using Tungsten as absorbing material is used. In addition, the detectors must be able to operate in the CLIC environment, e.g. 0.5 ns bunch spacing, $\gamma\gamma \rightarrow$ hadrons background. Hence, an excellent time resolution for all detector components is needed.

The CLIC accelerator technology is yet not mature compared to the ILC and still needs several years of R&D before a full CLIC accelerator could be constructed.

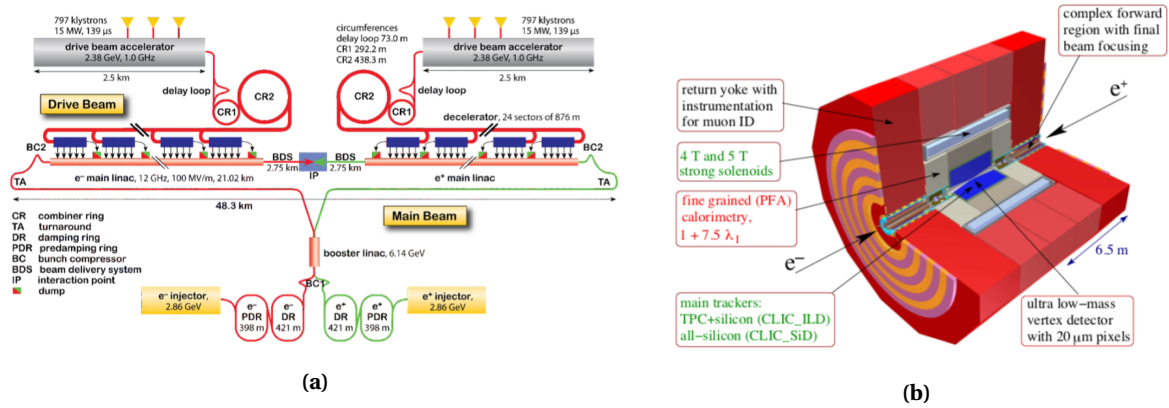


Figure 2.9 – a) Schematic view of the CLIC accelerator at $\sqrt{s} = 3$ TeV [64]. b) Schematic overview of the CLIC detector concepts [65].

As discussed in this chapter, the ILC provides a clean environment combined with advanced detectors that allow for precision physics studies. To fulfill the ILC program, calorimeters are an essential tool in jet

energy measurement and are designed for the Particle Flow approach. The concept of calorimetry and the Particle Flow paradigm are discussed in the next chapter.

Chapter 3

Calorimetry and the Particle Flow Concept

In high energy physics, calorimeters are fundamental tools used to measure the energy of particles. This is done by measuring signals from interactions of high energy particles with atoms in matter. This chapter will give a brief overview of the physics that describes interactions of particles with matter. The modeling of showers is discussed in chapter 5. Additionally, a brief description of the properties of calorimeters and an introduction to the *Particle Flow Concept* which drives the designs of the calorimeters for ILC will be discussed.

3.1 Particle interaction with matter

In this section, a short description of the interaction of particles with matter will be given. This includes electromagnetic showers induced by electrons and photons, the energy loss by heavy charged particles and the development of hadronic showers. Moreover, the consequences of these interactions on calorimetric measurements will be discussed.

3.1.1 Electromagnetic showers

3.1.1.1 Energy loss by electrons/positrons

High energy electrons lose their energy via different processes depending on their kinetic energy. At low energies, below few tens of MeV, electrons (positrons) lose their energy via ionization primarily. However, more processes are contributing such as Bhabha scattering, Møller scattering. At energies above 100 MeV, the principal source of energy loss is from *Bremsstrahlung* photons due to the Coulomb interaction of the electron in the electric field of the nuclei. The emitted photons follow an energy spectrum that falls off as $1/E$ [66]. The different contributions to the electron energy loss as a function of the energy are shown in figure 3.1a. The transition point where the energy losses due to ionization and Bremsstrahlung are roughly equivalent is generally referred to as the critical energy ϵ_c . The critical energy is material dependent and for solids, it can be parametrized as

$$\epsilon_c = \frac{610 \text{ MeV}}{(Z + 1.24)} \quad (3.1)$$

The critical energy for popular material such as iron is around 21 MeV and tungsten around 8 MeV.

3.1.1.2 Energy loss by photons

High energy photons ($> \text{MeV}$) lose their energy via *pair production* where the photon creates an electron-positron pair caused by the nuclear electric field. However for this process, the photon energy needs to be at least the rest mass of the e^+e^- pair ($E_\gamma \geq 2 \times 511 \text{ keV}$). The photon specific cross-sections as a function of the photon energy are shown in figure 3.1b. For energies below the pair production threshold, it is most likely to interact via the *photo-electric effect*. In this process, the photon is absorbed by the atom and an electron is emitted. The excited atom goes back to the ground state by the radiation of Auger electrons or X-rays. Additional processes are contributing to the photon energy loss such as the *Rayleigh* or *Compton* scattering where the photon is scattered coherently or incoherently by an electron of the atom nuclei.

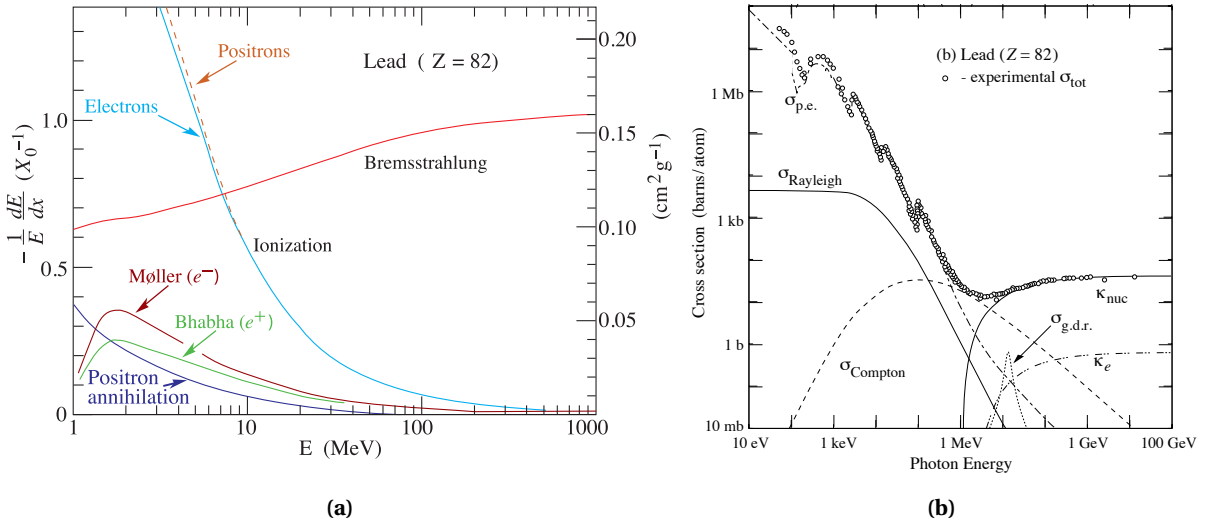


Figure 3.1 – a) Energy loss for electrons in lead as a function of the energy. All the different processes contributing to the electron energy loss are represented. b) Photon total cross-section as function of the photon energy in lead. $\sigma_{p.e.}$ is the photo-electric cross-section, $\sigma_{g.d.r.}$ is the photonuclear cross-section (Giant Dipole Resonance [67]) where the target nucleus is broken up, κ_e is the pair production cross-section in an electron field and κ_{nuc} is the pair production cross-section in a nuclear field [8].

3.1.1.3 Electromagnetic cascades

A cascade initiated by a multi-GeV electron involves all the processes described above. A simple model of the development of electromagnetic shower is shown in figure 3.2. The Bremsstrahlung process plays an important role in electromagnetic cascades. A large number of photons are radiated once the electron enters matter. Most of these photons are very soft and thus will get absorbed by Compton scattering and the photo-electric effect. However, a number of photons have the necessary energy to undergo pair production. These new electrons radiate, in turn, Bremsstrahlung photons creating new branches in the cascade. This results in the multiplication of the number of particles. The number of generated particles in an electron shower of energy E_0 is around $N \approx \frac{E_0}{\epsilon_c}$.

The development of the cascade stops when the average electron energy is around ϵ_c . The longitudinal

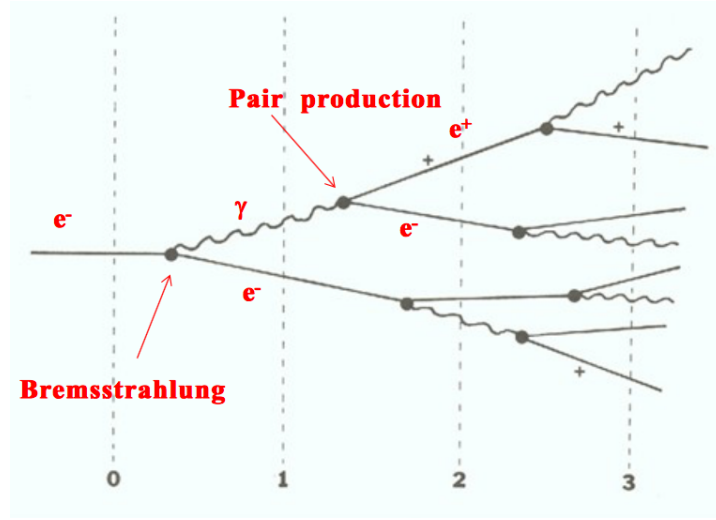


Figure 3.2 – Simple model illustrating the development of an electromagnetic shower. The x-axis represents the depth of the shower in radiation length X_0 . The y-axis represents the lateral development of the shower in Molière radius ρ_M .

depth where this occurs is called the *shower maximum*. The mean shower maximum x is parametrized as

$$\frac{x}{X_0} = \ln\left(\frac{E_0}{\epsilon_c}\right) + C \quad (3.2)$$

where the constant $C = -0.5$ for electron induced showers and $C = 0.5$ for photon induced showers. Therefore it follows a logarithmic dependence on the initial electron energy [66].

The longitudinal containment of the shower scales similarly with $\ln(E_0)$. On average, 95% of the deposited energy of a 10 GeV electron is contained within $14 X_0$ of copper, for a 1 TeV electron, around $22 X_0$ of copper is needed [66].

Typically electromagnetic showers are described by the *radiation length* X_0 for the longitudinal development and by the *Molière radius* ρ_M for the lateral development. The radiation length is defined as the distance over which a high energy electron (positron) loses $(1 - e^{-1}) = 63.2\%$ of its initial energy by Bremsstrahlung. A common parametrization of X_0 as a function of the atomic number Z and the atomic mass number A is [66]

$$X_0 = \frac{716 \times A}{Z(Z+1)\ln(287/\sqrt{Z})} \left[\frac{g}{cm^2} \right] \quad (3.3)$$

For high energy photons, the radiation length is related to the *mean free path* λ_γ of the photon, i.e the typical distance in which the photon travels before undergoing pair production as

$$\lambda_\gamma = \frac{9}{7} X_0 \quad (3.4)$$

The lateral development of an electromagnetic shower is characterized by the Molière radius ρ_M . On average, 90% of the energy of the shower will be contained in a cylinder of radius ρ_M . The Molière radius is

parametrized as [66]

$$\rho_M = 21.2 \text{ MeV} \frac{X_0}{\epsilon_c} \quad (3.5)$$

3.1.2 Interaction of charged heavy particles

As explained above Bremsstrahlung is the main process in which particles lose their energy. But this process is suppressed by the particle mass as $1/m^4$, thus for muons or charged hadrons, ionization is the main process for energy loss. The mean energy loss of a heavy charged particle is given by the Bethe-Bloch formula [66]

$$\left\langle \frac{dE}{dx} \right\rangle = K z^2 \frac{Z}{A} \frac{1}{\beta^2} \left(\frac{1}{2} \ln \frac{2m_e c^2 \beta^2 \gamma^2 T_{max}}{I^2} - \beta^2 - \frac{\delta}{2} \right) \quad (3.6)$$

where T_{max} is the maximum single collision energy transfer, I is the mean excitation energy of the absorber, δ is a correction term for then density effect depending on $\beta\gamma$, K is a constant equals to $4\pi N_A r_e^2 m_e c^2$, β is the particle velocity and γ is the Lorentz factor. The figure 3.3 shows the mean energy loss for muons in copper as function the particle momentum and $\beta\gamma = \frac{p}{mc}$.

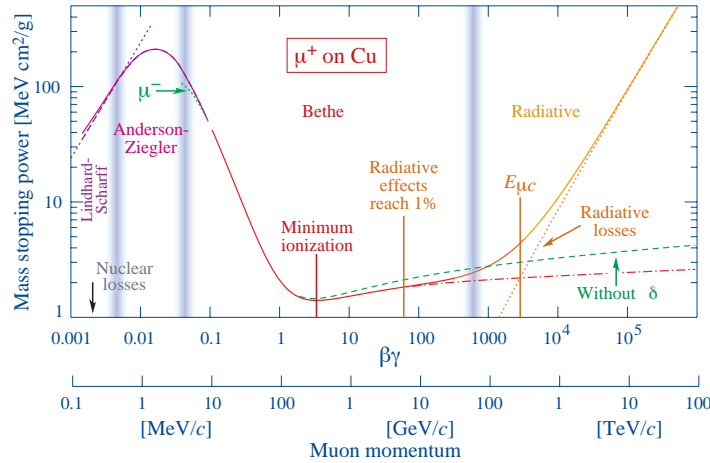


Figure 3.3 – Mean energy loss of muons in copper as a function of particle momentum. Vertical bands indicate boundaries between model transitions [8].

Below 100 GeV, ionization effects dominate in the energy loss and present a broad minimum around 1 GeV ($\beta\gamma \sim 2 - 4$). Particles in that region are generally referred as *Minimum Ionizing Particles* (MIP). Above 100 GeV, radiative effects become more important than ionization.

The energy loss distribution by heavy charged particles in thin materials follows a Landau distribution. However, the most probable value (MPV) for the energy deposition is below the value of the mean energy deposition $\langle \frac{dE}{dx} \rangle$ by around 60% and has a long tail toward high energy losses due to:

- The production of δ -electrons when a significant amount of energy is transferred in a collision
- Bremsstrahlung photons that can initiate small electromagnetic Showers
- Nuclear reactions with the nucleus of the material giving rise to high local energy deposits

The most probable value of the energy loss distribution is less dependent on the momentum of the particle than the mean energy loss $\langle \frac{dE}{dx} \rangle$, therefore the most probable value can be used as a natural energy deposition scale (see chapter 8).

3.1.3 Hadronic showers

Hadrons interact strongly such as many different processes can occur. Afterwards, the products of the interaction can again interact with the absorber material, thus leading to hadronic showers. A representation of the development of a hadronic shower is shown in figure 3.4.

A hadronic shower can be characterized by the *nuclear interaction length* λ_{int} which is defined as the mean free path travelled by a hadron before undergoing an inelastic interaction. Typically, this scale is generally much larger than X_0 , for example, $\lambda_{int}/X_0 \sim 9.5$ in iron. This variable depends on the particle type thus also size as it depends on the inelastic cross-section. The *pion interaction length* λ_π is around 3/2 times larger than the interaction length for protons [66]. Similar to electromagnetic showers, the longitudinal depth of the shower increases logarithmically with the energy of the incoming hadron.

In general, a hadronic shower contains two components, an electromagnetic component and a hadronic component.

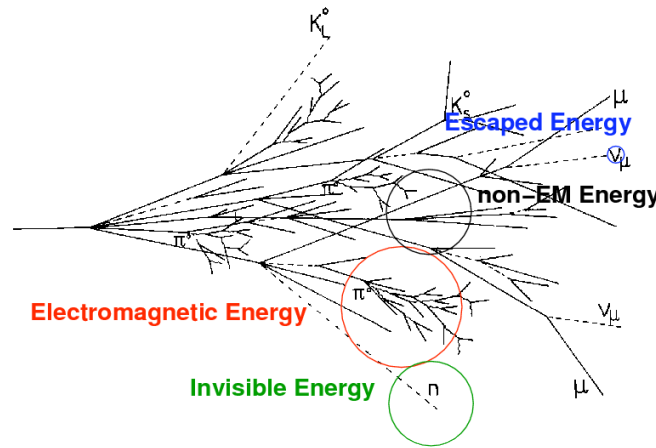


Figure 3.4 – Schematic of a hadronic shower. The different "types" of energy are represented in colors. Electromagnetic energy: decay of π^0 s and η s to γ s. Non-EM energy: ionization by charged hadrons, spallation. Escaped energy: neutrinos from hadron decays. Invisible energy: nuclear binding energy, neutron scattering and capture [68].

3.1.3.1 Electromagnetic component

When a hadron interacts strongly with the medium, it produces a number of secondary particles, in particular, π^0 s and η s, which have a very short life ($\sim 10^{-7}$ s) and decay electromagnetically to photons such as

$$\begin{aligned}\pi^0 &\rightarrow 2\gamma \quad (99\%) \\ \eta &\rightarrow 2\gamma \quad (39\%) \\ \eta &\rightarrow 3\pi^0 \quad (33\%) \\ \eta &\rightarrow \pi^0 + 2\gamma \quad (0.03\%)\end{aligned}$$

Per hadron collision, on average, 1/3 of the available energy will be carried by the electromagnetic component. If the initial energy of the projectile is sufficient, after n generations of reactions, the average electromagnetic fraction $\langle f_{EM} \rangle$ can be parametrized as [66]

$$\langle f_{EM} \rangle = 1 - \left(1 - \frac{1}{3}\right)^n \quad (3.7)$$

However, this is a very simplified model and should be seen only as an upper limit due to other effects (baryon number conservation, ionization and nuclear excitations...) which lower the average electromagnetic fraction. Typically, $\langle f_{EM} \rangle$ increase as a function of the initial particle energy. For example, a 10 GeV pion in copper has $\langle f_{EM} \rangle = 0.38$ and at 1 TeV $\langle f_{EM} \rangle = 0.73$ [66]. However, this is an average electromagnetic fraction, it generally varies strongly from shower to shower.

3.1.3.2 Hadronic component

When a high energy hadron interacts with a nucleus, several processes are possible due to the strong interaction: *spallation*, *evaporation* and *fission*.

Spallation is the most probable interaction. This process can be described in two stages: a fast intra-nuclear cascade involving the constituents of the nucleus and a slow nuclear evaporation. In the first stage, the incoming hadron interacts strongly with the nucleons of the nucleus producing a cascade of new stable and unstable hadrons. The resulting hadrons can then, in turn, interact with a nucleus or they can decay.

The second stage consists of the de-excitation of the nucleus by evaporating free nucleons until the excitation energy is less than the binding energy of the nucleus. This binding energy is often called *invisible energy* as it is lost during the measurement process. Nevertheless, this energy can be regained by using materials with high fission cross-section such as ^{238}U .

During spallation, plenty of neutrons can be released. These neutrons are *invisible* to the calorimeter and scatter through the calorimeter (mean free path \sim cm) until they lost most of their kinetic energy (*thermalization*). Then these neutrons can get captured by a nucleus as the capture cross-section is maximal at rest. This process leads to late energy depositions (\sim min). The excited nucleus emits γ -rays usually to get rid of the excess energy.

Since the *invisible* energy only occurs in hadron showers, this leads to a difference of the calorimeter response between electrons and hadrons of the same energy. This introduces the term of *compensation* that will be described in section 3.2.2.

3.1.3.3 Time development

Electromagnetic cascades develop at the speed of light due to the prompt generation of particles with relativistic energies. However, hadronic cascades have different components which have an impact on the time development of the shower. The electromagnetic component is prompt as an electromagnetic cascade but the hadronic component can be delayed significantly due to nuclear excited states ($\sim \mu\text{s}$) and the release of thermal neutrons ($\sim \mu\text{s-s}$). Thermal neutrons can travel significantly through the detector before being captured by a nucleus and generating a signal in the calorimeter. These effects have an impact on the reconstructed energy and spatial development of the shower due to the time acceptance of the readout electronics.

3.2 Calorimeters

Calorimeters are used to absorb an incident particle and measure the deposited energy. As explained in sections 3.1.1 and 3.1.3, the longitudinal depth of the shower scales logarithmically with the energy of the incoming particle. Thus the energy of a shower can be mostly contained completely with a moderate amount of material, even for very high energy particles. Calorimeters can be separated in two types: *homogenous* and *sampling* calorimeters.

Homogenous calorimeters

In homogenous calorimeters, the complete detector volume is sensitive to particle energy depositions. An example of homogenous calorimeter is the ECAL used by the CMS detector. It uses $PbWO_4$ scintillating crystals of around $2.2 \times 2.2 \times 23 \text{ cm}^3$, these have very short radiation length ($X_0 = 0.85 \text{ cm}$) and Molière Radius ($\rho_M = 2.19 \text{ cm}$) allowing for a compact design. As this calorimeter is homogenous, the entire kinetic energy of an incoming electron or photon can be measured, reducing sampling fluctuations and achieving a very good single particle energy resolution¹ of $\sigma_E/E \approx 2.8\%/\sqrt{E} \oplus 0.3\%$ [69]. In comparison, the BELLE II EM calorimeter achieves an energy resolution of $\sigma_E/E \approx 0.066\%/\sqrt{E} \oplus 1.34\%$ [70] using CsI(Tl) crystals.

Sampling calorimeters

In sampling calorimeters, the calorimeter is divided into a passive medium, the absorber that is made usually of a high-density material, and an active medium that generates the signal to be measured. Sampling calorimeters offer the freedom to chose both the absorber and active material. The absorber can be chosen to minimize the amount of material while still containing most of the energy of the shower. Active materials can be chosen for special purposes, e.g an organic material with high hydrogen content to recover a part of the *invisible energy* by absorbing more neutrons. Also, this allows for optimization of the design and cost. Nevertheless, it has the disadvantage of worse energy resolution than homogenous calorimeters due to sampling fluctuations as only a fraction of the energy of a shower is measured.

A sampling calorimeter can be characterized by its sampling fraction f_{samp} as

$$f_{\text{samp}} = \frac{E_{MIP}^{\text{active}}}{E_{MIP}^{\text{active}} + E_{MIP}^{\text{passive}}} \quad (3.8)$$

¹Explained in 3.2.1.

Usually sampling calorimeters are segmented longitudinally and laterally into small cells in order to provide information about the particle position. An electromagnetic calorimeter (ECAL) is measuring the energy of particles that interact primarily via the electromagnetic interaction, while hadronic calorimeters (HCAL) are designed to measure the energy of particles that interact strongly.

An example of a sampling calorimeter is the HCAL barrel (TileCal) in the ATLAS detector. It consists of iron plates 14 mm thick as absorber and scintillator tiles 3 mm thick as active material. The total depth of the barrel corresponds to 9.7 nuclear interaction length. It is segmented in ϕ and η to provide accurate position measurement. The tiles are coupled to a wavelength shifting fiber that guides the light to two different photomultiplier tubes providing redundancy. It is the central detector for the measurements of single hadrons, jets and missing transverse energy. An energy resolution of $\sigma_E/E \approx 52\%/\sqrt{E} \oplus 3\%$ was achieved for single pions [71]. This is significantly worse compared to the CMS ECAL due to the sampling fluctuations and as well due to the intrinsic fluctuations of hadron showers. It can be compared to the CDF HCAL using scintillator tiles coupled to wavelength shifting fibers and readout by PMTs in which an energy resolution of $\sigma_E/E \approx 80\%/\sqrt{E} \oplus 5\%$ was achieved [72].

3.2.1 Energy resolution

The figure of merit of every calorimeter is the energy resolution. For most calorimeters, the energy resolution σ_E/E can be parametrized as:

$$\frac{\sigma_E}{E} = \frac{a}{\sqrt{E}} \oplus b \oplus \frac{c}{E} \quad (3.9)$$

The first term $\frac{a}{\sqrt{E}}$ is the stochastic term. Assuming that N particles contributed to the signal, the uncertainty follows a Poisson statistic such as $\sigma_N/N = \sqrt{N}/N = 1/\sqrt{N}$. Thus the stochastic term for the energy resolution follow this. Additionally, the sampling fraction f_{samp} adds an additional uncertainty proportional to $\sqrt{1/f_{\text{samp}}}$. For hadronic showers, the fluctuations in the invisible energy also scales as $1/\sqrt{E}$ and the fluctuations in the electromagnetic fraction scales as $1/E^j$ with $j \leq 0.5$. For electromagnetic calorimeter, the stochastic contribution is in the order of few percents for homogenous up to around $10\%/\sqrt{E}$ for sampling calorimeters. Typically, the contribution for hadronic calorimeters is in the order of $60\%/\sqrt{E}$.

The second term b is the constant term. This term is affected by detector inhomogeneities such as calibration uncertainties. This term dominates at high energies and is typically in the order of few percents.

The third term $\frac{c}{E}$ is the noise term. It is energy independent and arises from different effects like the readout electronics. This term dominates at low energies.

3.2.2 Compensation

Due to the invisible energy fraction of a hadron shower, the calorimeter response of a hadron shower of a given energy is typically lower than the calorimeter response of an electromagnetic shower of the same energy. Calorimeters with a response ratio $e/h > 1$ are called *under-compensating* while calorimeters with a response ratio $e/h < 1$ are called *over-compensating*. The e/h ratio decreases with energy due to the electromagnetic fraction increasing with energy.

Homogenous calorimeters have generally a significantly higher ratio $e/h \sim 2$. Sampling calorimeters can be designed to reach compensation ($e/h = 1$). To achieve compensation, either the electromagnetic response can be lowered or the hadronic response can be boosted. A famous example is the ZEUS calorimeter that

used uranium ($Z = 92$) absorbers and plastic scintillator as active material. The thicknesses of the absorber and active material were carefully optimized to reach compensation. In this way, an energy resolution for pions of $\sigma_E/E = 35\%/\sqrt{E} + 2\%$ was achieved with $e/h \sim 1$ [73].

Other methods can be used to achieve compensation:

- *Dual readout* using Cherenkov radiation to estimate the electromagnetic fraction of each event [74].
- *Spacial resolution* in order to identify electromagnetic sub-showers within a hadronic shower and re-weight the whole shower or individual hits of the shower. This has been demonstrated for the H1 experiment which is using the local hit energy density to distinguish electromagnetic sub-showers from hadronic shower depositions [75].

3.3 The Particle Flow approach

Calorimeters are used to measure the energy of single particles and jets. Classically, the energy is reconstructed by summing up all the energy deposits in the electromagnetic and hadronic calorimeters. In this way, typically the stochastic term from equation 3.9 for jets is in the order of $60 - 100\%\sqrt{E}$. This jet energy resolution is far beyond the requirements of the ILC physics program (see chapter 2). A new approach has been developed to solve this issue and its concept is presented in this section.

3.3.1 The Particle Flow concept

Particle Flow is a new approach to calorimetry in order to achieve a jet energy resolution much better than traditional calorimetry approaches (order of twice better). *Particle Flow Algorithms* (PFA) aim to reconstruct the energy of all the individual contributions inside a jet. This was made possible by the significant improvements in tracking detectors and calorimeters over the last decade. A schematic of the Particle Flow concept is shown in figure 3.5.

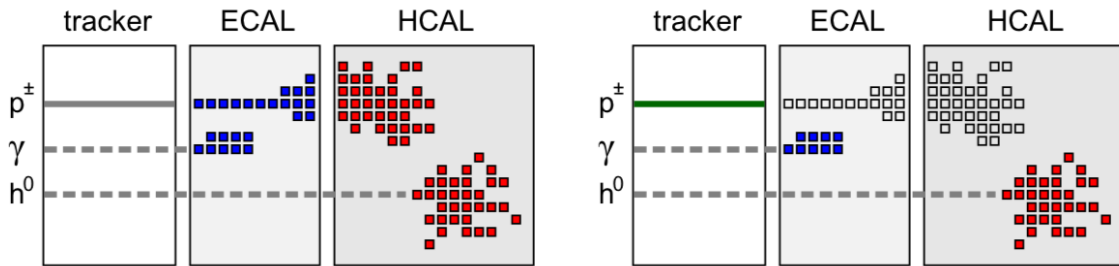


Figure 3.5 – Schematic of the Particle Flow Concept. On the left: Traditional calorimetry, The ECAL and HCAL measure the energy deposited by all particles in a jet (charged particles, photons and neutral particles). The tracker information is not used. On the right: Particle flow approach, The tracker measures all charged particles and the calorimeter information is removed, the ECAL measures the photons and the HCAL measures only neutral particles [76].

On average in a jet, 60% of the energy is carried by charged hadrons, 30% by photons and 10% by neutral hadrons [77]. As hadronic calorimeters have a poor energy resolution ($\sim 60\%/\sqrt{E}$), by a pure calorimetric ap-

proach, 70% of the energy would be poorly measured. Therefore, the poor resolution of the HCAL is dominant in the jet energy resolution.

The Particle Flow reconstruction requires an unprecedented longitudinal and lateral segmentations for the calorimeters in order to distinguish depositions of charged and neutral particles in the calorimeter as well as an excellent tracking system. This approach uses the best sub-detector measurement for each particle in a jet. All charged particles are measured by the tracker due to the excellent tracker resolution, photons are measured in the ECAL and neutral hadrons are measured in the HCAL. In this case, only around 10% of the energy is measured poorly by the HCAL and thus its impact on the jet energy resolution is lessened.

The Particle flow approach at the ILC has the potential to improve the jet energy resolution to around 3-4% in the range of 45 to 250 GeV ($\sim 30\%/\sqrt{E}$). The jet energy resolution can be parametrized as

$$\sigma_{jet} = f_{charged} \cdot \sigma_{Tracker} \oplus f_{\gamma} \cdot \sigma_{ECAL} \oplus f_{neutral} \cdot \sigma_{HCAL} \oplus \sigma_{conf} \oplus \sigma_{leak} \quad (3.10)$$

$\sigma_{Tracker}, \sigma_{ECAL}, \sigma_{HCAL}$ are the energy resolutions of the tracker, ECAL and HCAL respectively, contributing to the jet energy resolution with weighted fractions of the particle type in the event.

σ_{conf} represents the confusion term due to the possibility of wrong assignments of tracks and calorimeter energy depositions. There are three main sources of confusion:

- A part (or all) of the shower from a charged hadron is reconstructed as a neutral cluster. This lead to the double-counting of energy.
- A part (or all) of a neutral shower is associated to a charged shower. This lead to the loss of the energy of the neutral particle, therefore, energy is missing.
- The failure to resolve photons close to a charged hadron track leading to the loss of the photon energy.

The confusion is a limiting factor in Particle Flow calorimetry and starts to dominate for high jet energies due to a high probability of showers overlapping. Other contributions are present such as σ_{leak} that degrade the jet energy resolution due to leakage in the calorimeter and non-instrumented areas.

3.3.2 Implementation in PandoraPFA

Some implementations of PFAs were made in the past like H1 at HERA [78] and up to now in CMS at the LHC [79]. However, these detectors were not designed and optimized for particle flow reconstruction. The ILC detectors are designed in such a way that they offer the best instrumentation for the application of the particle flow concept.

PandoraPFA [80, 81] is an implementation of the Particle Flow Concept for the ILC. It reconstructs individual particles using the information provided by the highly granular calorimeters and the tracker. The algorithm operates in several stages:

- Tracks are categorized based on topology. Kinks, V0s from neutral particle decays, e.g $K_s \rightarrow \pi^+ \pi^-$, are identified and treated separately by the algorithm.
- Calorimeter hits are clustered using a simple cone-based algorithm starting at the front face of the ECAL going to the back of the HCAL. Tracks seeds from the projection of tracks to the front face of the ECAL can be used for the cluster starting point. The clustering algorithm is configured in a way

that it tends to split more the energy deposits than accidentally merging particles in this early stage. The clustering follows certain topological rules and exploits the spatial resolution of the calorimeters to minimize clustering mistakes.

- The calorimeter clusters are associated with tracks. The algorithm compares the cluster energy and track momentum and other properties such as the track direction at the front face of the ECAL and cluster orientation to make the correct associations.
- If the energy of a cluster and the associated momentum of a track don't agree, a statistical re-clustering is performed using different parameters until a better track-cluster compatibility is found.
- The algorithm identifies photons based on shower profile information in order to recover photons that are merged with a charged hadron shower.
- Fragments of hadron showers are identified and the algorithm looks for neutral fragments that are misidentified coming from nearby charged clusters. These fragments are merged into the parent charged cluster and the track-cluster compatibility is evaluated again.
- A Particle Flow Object (PFO) is constructed. Track properties are used for charged particles, the calorimeter information is used for neutral particles.

The details of these stages and possible other stages are described in more details in [80].

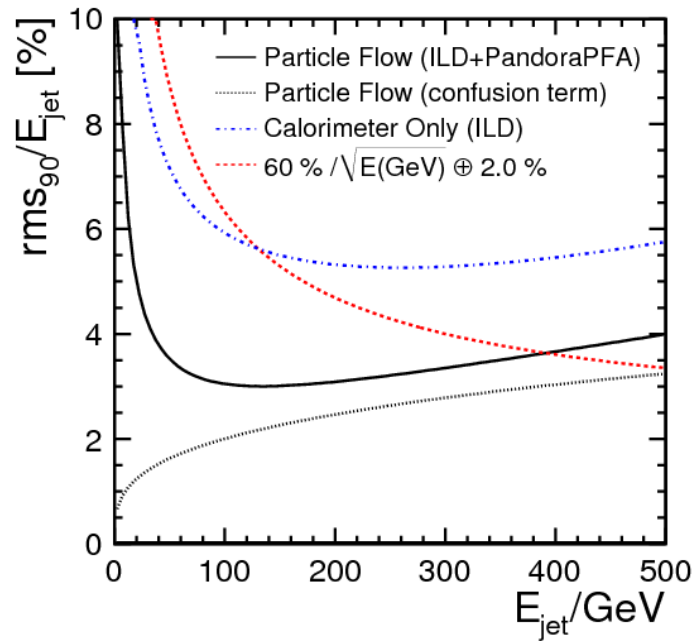


Figure 3.6 – Empirical jet energy resolution as function of the jet energy for PandoraPFA and the ILD detector. The estimated contribution of confusion is represented by the back dotted line. The dotted-dashed blue curve shows the jet energy resolution only from the calorimetric depositions. Moreover, a parametrization of a typical jet energy resolution ($\frac{60\%}{\sqrt{E}} \oplus 2\%$) is shown in red using the traditional calorimetry approach [80].

The jet energy resolution obtained in ILD with Pandora PFA is shown in figure 3.6. The figure shows that the jet resolution obtained is much better than in traditional calorimetry. It also shows that the goal of 3-4% relative jet energy resolution is achieved over a large jet energy range.

As shown in this chapter, jet energy measurements with an excellent resolution can be achieved with the particle flow approach. This approach requires an excellent tracker and highly granular calorimeters. The development of such calorimeters is discussed in the following chapter.

Chapter 4

CALICE Calorimeter concepts

As explained in chapter 2, the ILC provides a clean environment for precision measurements. In many cases, the precision of the measurements is limited by the jet energy resolution, for example in the Higgs mass measurement in the $b\bar{b}$ channel. The jet energy resolution is itself limited by the energy resolution of the calorimeters (see section 3.3). The jet energy resolution achieved by a traditional calorimetry is not sufficient for the ILC. A new approach called the Particle Flow is a promising solution to achieve an unprecedented jet energy resolution. The Particle Flow concept requires an excellent tracker and highly segmented electromagnetic and hadronic calorimeters. The CALICE Collaboration is developing and testing highly granular electromagnetic and hadronic calorimeter concepts for a future linear collider optimized for Particle Flow.

In this chapter, after discussing the requirements for the calorimeters at the ILC in section 4.1, various technology prototypes will be introduced in section 4.3 and 4.4 with a focus on the Analog Hadronic Calorimeter (AHCAL) in section 4.4.3. The detection principle and readout electronics for the AHCAL are introduced in section 4.4.3.1 and 4.4.3.2.

4.1 Requirements for the calorimeters in ILD

The objective for the ILC is to aim for a jet energy resolution of 3-4%. Using traditional calorimetry, this is not achievable. Therefore, the particle flow concept (see section 3.3) was conceived to achieve this goal. With this approach, around 10% of the jet energy is measured in the HCAL with a relatively poor resolution. The particle flow concept imposes requirements on the calorimeters to achieve this goal.

One of the main requirements is the granularity of the calorimeters in order to be able to distinguish energy deposits from different particles. High granularity introduces new challenges that need to be overcome such as the number of readout channels. Each channel needs its dedicated power and signal data lines for configuration and sensor readout. In traditional calorimeters, the number of channels is generally small (~ 100 - 10000) and this approach can be done but in the case of highly granular calorimeters containing millions of channels, it is not feasible. One possibility to solve this is by integrating the front-end electronics on the active layers therefore, reducing the amount of power and data lines going in and out of the detector.

Additionally, other constraints are imposed to the calorimeters by the ILD detector. These constraints include mechanics, power consumption and power dissipation. In order to avoid dead material zones, there is no active cooling considered in ILD between calorimeter absorbers. Thus, this imposes a constraint on the

maximum power dissipation by the front-end electronics on the active layers. To reduce the power consumption and dissipation, the front-end has to take advantage of the ILC beam structure. As shown in section 2.2, ILC bunches are separated by 200 ns with each bunches being around 1 ns long. This leaves 199 ns where there are no collisions therefore, parts of the front-end electronics that are not needed can be switched off to reduce the power consumption and dissipation. This scheme is known as *power-pulsing*.

4.2 The CALICE Collaboration

The CALICE Collaboration is composed of 336 scientists and engineers from 57 institutes and 17 countries who are developing and testing highly granular electromagnetic and hadronic calorimeters. These detector concepts are optimized toward a linear collider environment such as the International Linear Collider (ILC) [1] or Compact Linear Collider (CLIC) [2] but a collaboration with the Large Hadron Collider community for the High-Lumi upgrade (HL-LHC) is ongoing [82].

The CALICE calorimeters are high granularity calorimeters optimized for the use of particle flow algorithms, see section 3.3, providing a very detailed image of physics events and a high spatial resolution to separate nearby showers.

All the calorimeters developed within the collaboration are sampling calorimeters. Several *physics prototypes* were built in the past and tested in testbeam campaigns at DESY, CERN and FNAL [83–87] to demonstrate the performance for energy measurement and particle separation. Three hadron calorimeter prototypes of 1 m³ were conceived using different active material and absorbers as well as different readout schemes.

Nowadays, the CALICE Collaboration focuses on the integration and scalability into a full linear collider detector by designing several new *technological calorimeter prototypes*.

In the following sections, different electromagnetic and hadronic calorimeter concepts will be introduced before focusing on the main topic for this thesis, the CALICE AHCAL.

4.3 CALICE Electromagnetic Calorimeters

The CALICE collaboration is developing two different electromagnetic calorimeters concepts. The goal of the previous prototypes was to prove the performance of such calorimeters for detailed measurements of EM showers. Now engineering prototypes are designed in order to improve the calorimeter design, the integration of the front-end electronics and the readout scheme. In the next subsections, the silicon-based SiECAL and the scintillator-based ScECAL calorimeters using both tungsten as absorber material will be described.

4.3.1 Silicon-Tungsten ECAL

The Silicon-Tungsten ECAL (SiECAL) physics prototype [83] consists of 30 active and absorber layers. The depth of the calorimeter was 24 X_0 achieved by 10 layers of 0.4 X_0 (1.4 mm), followed by 10 layers of 0.8 X_0 (2.8 mm) and 10 more layers of 1.2 X_0 (4.2 mm) thick tungsten absorber plates. Tungsten has a small Molière radius of ~ 9 mm and radiation length ~ 3.5 mm, which allows for a compact design as well as compact electromagnetic showers in order to reduce the probability of overlapping showers.

The sensitive layer is made of high-resistivity silicon wafers 525 μm thick. These are divided into $6 \times 6 \text{ cm}^2$ sensors, segmented into a matrix of $1 \times 1 \text{ cm}^2$ PIN diodes operated in full depletion at around 200 V. The total active area is $18 \times 18 \text{ cm}^2$ per layer. The SiECAL features 9720 channels. Silicon is a technology that has been used for vertex and tracking detectors since decades and can be segmented easily thus making it suitable for highly granular calorimeters. However, in the case of a calorimeter, the area to cover is large which makes this technology expensive in large-scale experiments.

Each very front end board has twelve front-end ASICs (FLC_PHY3) that are mounted on the PCB that amplify the signal. The ASICs are readout by off-detector boards using differential analog lines. A schematic of the prototype is shown in figure 4.1a. The performance of such calorimeter was tested in various beams at DESY and CERN. An energy resolution of $\frac{16.53\%}{\sqrt{E}}$ stochastic term and 1.07% constant term was achieved [88].

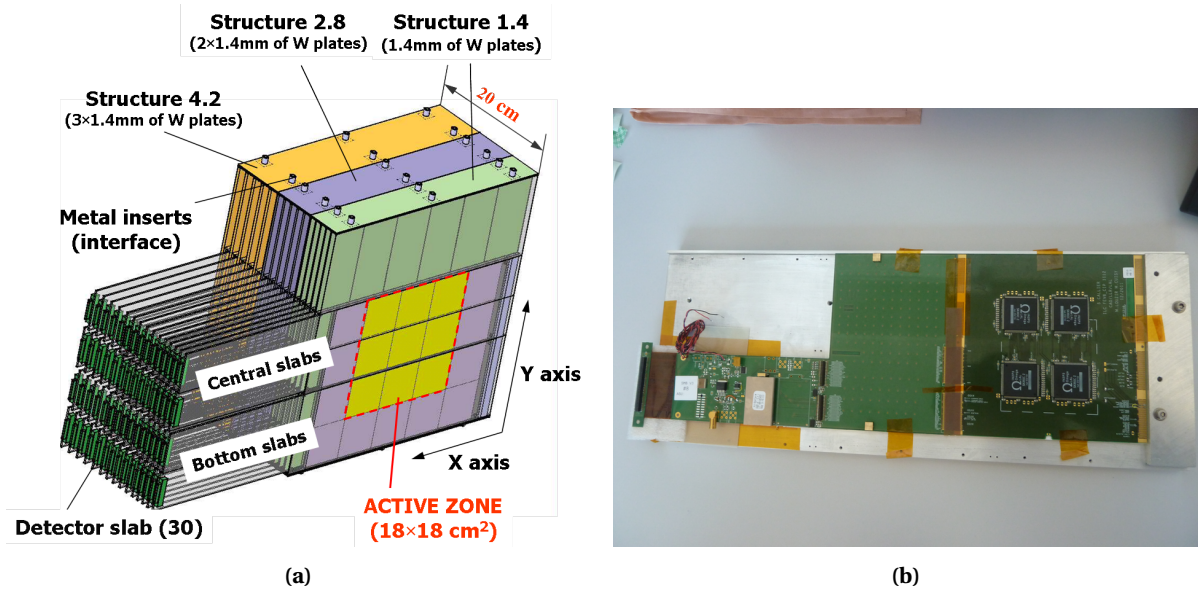


Figure 4.1 – a) The schematics of the SiW-ECAL physics prototype. b) Picture of a layer of the SiW-ECAL technological prototype.

After the validation of the calorimeter concept, a technological SiECAL prototype is being developed focusing on the integration into a full linear collider detector. To do this, modules close to the ILD design are being developed taking into account mass-production requirements and low-power front-end electronics are integrated into the detector volume. The silicon wafers are larger and divided into $9 \times 9 \text{ cm}^2$ sensors. The PIN diode matrix is reduced to $5 \times 5 \text{ mm}^2$ pads to improve the pattern recognition of the calorimeter. New designs of the sensor are also made to minimize dead area at the sensor edge and cross-talk effects.

The front-end is equipped with an ASIC, the SKIROC2 chip [89]. It has 64 channels with adjustable gain charge pre-amplifier, a 12-bit ADC and digital logic. It allows for auto-triggering with an adjustable threshold and it can record the hit time performed on a 12-bit TDC ramp. The SKIROC2 ASIC is designed to match the ILC beam structure (see chapter 2) and thus allows for a power-pulsed mode where electronics are switched off between ILC bunch-trains. This allows a very low power dissipation in the order of 25 μW per channel. A picture of a layer of the technological prototype can be seen in figure 4.1b. The fully assembled layers are inserted into an alveolar absorber structure.

4.3.2 Scintillator Strip-Tungsten ECAL

The Scintillator Strip-Tungsten ECAL (ScECAL) physics prototype [85] consists of 30 layers of scintillator strips and tungsten carbide absorber plates 3.5 mm thick. It exploits the same concept as the AHCAL later discussed in section 4.4.3. The total calorimeter thickness is 266 mm or $21.5 X_0$. The layers have a transverse area of $180 \times 180 \text{ mm}^2$.

Each layer is composed of four rows of 18 scintillator strips of dimensions $45 \times 10 \times 3 \text{ mm}^3$ and the strips are placed orthogonally in consecutive layers. The strips have a Wavelength-shifting Fiber (WLS) inside to guide the scintillation light to a Silicon-Photomultiplier (see section 4.4.3.1). This accounts for 2160 channels in total to be read out. This prototype was tested in various beams, an energy resolution of $\frac{12.6\%}{\sqrt{E}}$ stochastic and 1.6% constant term was demonstrated [85].



Figure 4.2 – a) Photo of the ScECAL physics prototype with the Fe-AHCAL at FNAL. b) Photo of the top side of a layer of the technological ScECAL prototype.

To look forward, a technological prototype is now developed to accommodate the front-end electronics into the layer to reduce the amount of dead material due to cabling. An ECAL Base Unit (EBU) has 144 scintillator strips of dimensions $45 \times 5 \times 2 \text{ mm}^3$. Each EBU has a transverse dimension of $180 \times 180 \text{ mm}^2$. The design of the EBU is derived from the HBU design (see section 4.4.3).

The strips don't have a WLS fiber due to improvements in SiPM technology for the detection of blue light ($\sim 450 \text{ nm}$). Several designs in SiPM and scintillator strip shape are being studied to optimize light collection. Moreover by using a strip splitting algorithm (SSA) [90], an effective granularity of $5 \times 5 \text{ mm}^2$ can be achieved.

In this thesis (see section 7.1.2), two designs were used in testbeam at CERN, a bottom-side readout and a baseline readout design. The former uses 10k pixels surface-mounted SiPMs, the latter uses 1.6k pixels SiPMs placed on the side of the strips. Each SiPM is read out by an ASIC, the SPIROC2B (see section 4.4.3.2). Each layer is equipped with four SPIROC ASICs. Each channel has also an integrated LED calibration system in order to monitor the SiPM gain.

4.4 Hadronic Calorimeters

The CALICE collaboration is developing several hadron calorimeters concepts. The concepts are varying in the granularity from $3 \times 3 \text{ cm}^2$ to $1 \times 1 \text{ cm}^2$ but as well in the precision of the amplitude information. The Digital HCAL and Semi-Digital HCAL calorimeter concepts are using digital information of the amplitude by counting the number of hits on one bit or two bits. The AHCAL calorimeter concept relies on the full analog information of the amplitude. A detailed comparative study of these different calorimeter concepts has been done and can be seen in [91].

4.4.1 Digital HCAL

The Digital Hadron Calorimeter (DHCAL) prototype [92] is a sampling calorimeter based on Resistive Plate Chambers (RPCs) [93] gaseous technology. The DHCAL uses a 1-bit readout system based on the assumption that the deposited energy of a particle is proportional to the number of hits over a given threshold as a first order.

The DHCAL consists of 38 active layers of an active area of $1 \times 1 \text{ m}^2$. The chambers are in a cassette with a front copper plate 2 mm thick and back steel plate 2 mm thick. They are inserted into the same steel absorber structure used by the AHCAL into gaps 1.4 cm wide. A schematic of the cross-section of a DHCAL layer is shown in figure 4.3.

The readout anode of the RPC is segmented into $1 \times 1 \text{ cm}^2$ pads, read out by two front-end boards for each RPC (for a total of 6 boards for a layer) hosting 24 chips each for a total of 144 chips per layer. Each chip reads out 64 pads. The prototype accounts for a total of 350 208 channels.

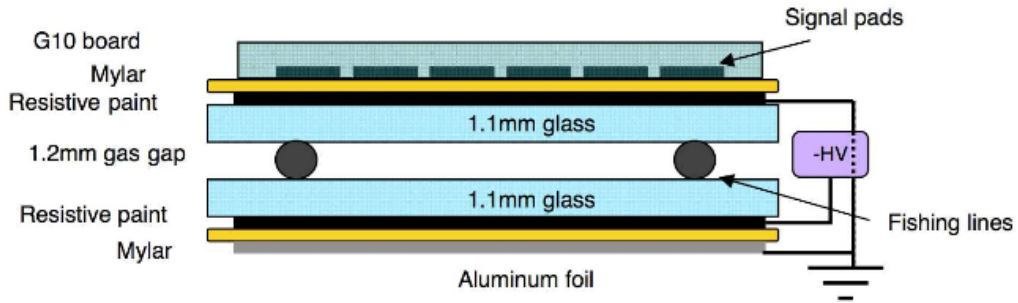


Figure 4.3 – Cross-section of an active RPC layer in the DHCAL prototype. Taken from [87].

This prototype has been used in the testbeam facilities at CERN and Fermilab. A preliminary analysis of testbeam data shows that an energy resolution of $\frac{35.1\%}{\sqrt{E}}$ stochastic and 12.4% constant term has been achieved in a positron beam. An energy resolution of $\frac{64\%}{\sqrt{E}}$ stochastic and 3-4% constant term has been achieved in a pion beam [94]. More details about the DHCAL prototype can be seen in [91].

4.4.2 Semi-Digital HCAL

The Semi-Digital Hadron Calorimeter (SDHCAL) prototype [86] uses also RPCs technology for particle detection. The SDHCAL consists of 48 active layers. Each active layer consists of RPCs with a gap of 1.2 mm

filled with gas and a readout electrode segmented in $1 \times 1 \text{ cm}^2$ pads.

The active layers are inserted into a steel absorber structure of 1.5 cm thick plates. In total, the SDHCAL prototype features 442 368 channels. More detail about the SDHCAL can be found in [86].

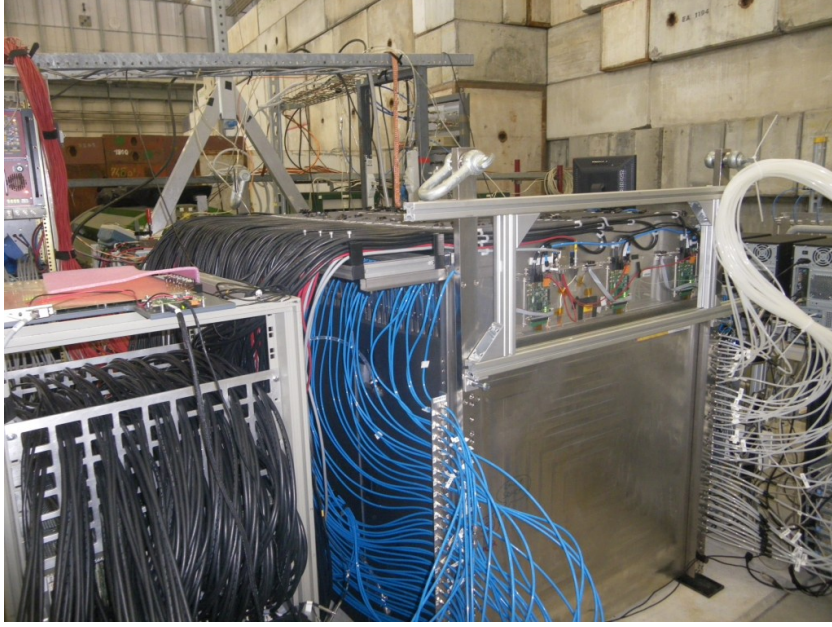


Figure 4.4 – Photo of SDHCAL at CERN in 2012.

The readout is performed by the HARDROC ASIC [95] which can readout up to 64 channels. Instead of using 1-bit readout scheme like the DHCAL, the SDHCAL uses a 3-bit readout system corresponding to three coarse thresholds.

The SDHCAL does not provide direct timing measurement. A timestamp with a precision of 200 ns corresponding to the internal clock of the ASIC can be applied to hits.

The SDHCAL has been tested in various beam types at the CERN SPS facility in 2012. A picture of the prototype is shown in figure 4.4. The first results show an energy resolution that goes from 14.9% at 30 GeV to 9.5% at 80 GeV with pion beams [96].

4.4.3 Analog HCal

The Analog Hadronic calorimeter uses scintillator-based tiles readout by Silicon Photomultipliers. Before discussing about the prototype, a short introduction about Silicon photomultipliers and the readout electronics is presented.

4.4.3.1 Silicon Photomultipliers

Semi-conductors detectors have been used for more than 50 years and are still a major research topic in high energy physics [97–99]. *Silicon photomultipliers* (SiPM) are semi-conductors used to measure light amplitudes down to the single photon. SiPMs are composed of an array of *Avalanche Photodiodes* (APD) pixels operated in Geiger-mode (see below). The pixels are all connected in parallel to a common cathode

and anode. Nowadays, thousands of pixels can be integrated into a few mm^2 area. A picture of a surface-mounted SiPM is shown in figure 4.5.

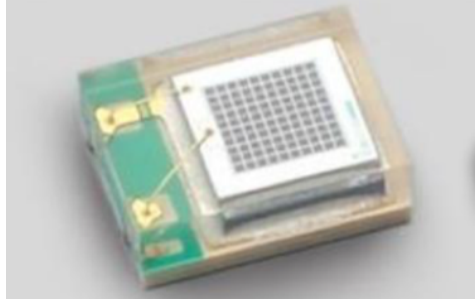


Figure 4.5 – Picture of a surface-mounted SiPM. The picture shows the SiPM package as well the grid of pixels.

Each pixel is operated in reverse bias (V_{bias}), in the order of 30-60 V, larger than the *breakdown voltage* (V_{bd}). When a photon is absorbed, an electron-hole pair is created in the depletion region by the photo-electric effect. This electron is accelerated by the electric field and starts to create a self-sustained avalanche or *Geiger discharge* by impact ionization, rendering the diode conductive. A serial *quenching resistor* (R_q) reduces the effective voltage of the pixel below V_{bd} thus quenching the avalanche. Each pixel deliver a charge Q such as

$$Q = C_{px} \times (V_{bias} - V_{bd}) \quad (4.1)$$

where C_{px} is the capacitance of the pixel which is typically around few pF and depends on the geometry and doping profile of the pixel. $V_{bias} - V_{bd}$ is the over-voltage or excess voltage over the breakdown voltage.

Following this equation, Q characterizes the gain of the SiPM and is proportional to the over-voltage. V_{bd} is temperature dependent, effectively increasing with the temperature. Thus the SiPM gain shows an anti-correlation as a function of the temperature in the range of -1%/K. Similarly, the *quantum efficiency* or *photon detection efficiency* (PDE), the probability to initiate a Geiger discharge, has an inverse correlation with temperature and increases with $V_{bias} - V_{bd}$.

Once an avalanche has stopped, the effective voltage of the pixel can return to V_{bias} with the *recovery time* $R_q \cdot C_{px}$ in the order of hundred nanoseconds before the pixel can fire again. Carriers trapped in defects in the silicon matrix introduce new levels of energy in the conduction band, a release of these carriers causes *afterpulsing* in a period of 50-100 ns after firing.

The measured total charge is the sum of all the fired pixels. With a good uniformity in pixel capacitance and low-noise electronic amplification, the SiPM gain can be measured in-situ by illuminating the SiPM with short and low amplitude light pulses giving a *single-photon spectrum* (SPS) as shown in subsection 6.2.2.

Due to the finite number of pixels and the recovery time of the pixels in the order of several nanoseconds, the response of a SiPM is non-linear and can be at a first order parametrized as

$$N_{fired} \approx N_{total} \times (1 - e^{\frac{-N_\gamma \cdot PDE}{N_{total}}}) \quad (4.2)$$

where N_{total} is the total number of pixels, N_γ is the number of incoming photons and PDE is the photon detection efficiency. This parametrization can describe the data very well at low light levels but can significantly differ with a high number of photons [100].

An avalanche can be initiated by a photon but also free carriers in the depleted layer. The rate of the latter *dark noise* increases with $V_{bias} - V_{bd}$ and the temperature. A dark rate of 100 kHz to several MHz per mm^2 is produced by typical SiPMs. This dark count rate falls dramatically when increasing the threshold of the readout electronics and typically the increase of the threshold by 1 photo-electron amplitude reduces the dark rate by around one order of magnitude.

Geiger avalanches in a pixel can produce photons that can travel to the nearest pixel and trigger an avalanche. This is referred as *optical cross-talk*. This effect is in the order of 3-10% for typical SiPMs and can be mitigated by reducing the operating voltage, adding an optical absorber or trenches between pixels.

In the last decade, significant improvements in the manufacturing of SiPMs have been achieved and they are commercially available. The PDE range has been improved to be sensitive down to near ultraviolet light (300-400 nm) up to infrared light (800-1000 nm). The dark noise rates have been reduced as low as few tens of kHz at room temperature. The introduction of trenches between pixels in the substrate has enabled to reduce the cross-talk probability under 1% [101]. The uniformity improvements within one production batch reduce the need for individual bias adjustment. And finally, SiPMs with a very high number of pixels (≥ 10000) are available, improving the range of linear response and increase the dynamic range but at the detriment of noise rates and PDE.

For the Analog Hadronic Calorimeter, a specific chip, the SPIROC2B has been developed to readout Silicon photomultipliers integrating all the requirements for the ILD detector. The next section will present the chip in details.

4.4.3.2 The SPIROC ASIC

The SPIROC (SiPM Integrated Read-Out Chip) [102] is a dedicated ASIC to readout and digitize the signal of SiPMs. The ASIC needs to satisfy the AHCAL requirements that are:

- Readout and digitization of the SiPM signal.
- Small footprint for integration into the active layers between absorbers.
- Has a low power consumption under $25\mu\text{W}$ per channel to avoid the need for active cooling.
- Operates in the power-pulsing scheme to reduce the power consumption and send the data between bunch-trains.
- Provides individual channel gain and bias voltage adjustment.
- Provides auto-triggering with an adjustable threshold to reduce the data volume.
- Provides timing information of the SiPM signal

The SPIROC ASIC has been developed by the OMEGA group [103] to fulfill the AHCAL requirements. The SPIROC provides the readout for 36 SiPM channels capable to measure the charge and time for each channel. Each channel is equipped with a capacitor-array, called memory-cells, with a depth of 16 events to store the charge and time measurement. A 12-bit Wilkinson ADC is used to digitize the charge and time measurement stored in the capacitor array. The digitized signal is then stored in a RAM buffer.

Each channel can be tuned in bias voltage with an 8-bit Digital to Analog Converter (DAC) corresponding to a voltage range between -4.5V and 0V. Each channel, has a configurable low-noise charge pre-amplifier

gain (between 100 fF to 1500 fF) operating in high gain (HG) or low gain (LG) to cover a high dynamic range between 1 to several thousand photoelectrons.

The time measurement is digitized using a 12-bit Time to Digital Converter (TDC). The SPIROC ASIC has two multiplexed TDC voltage ramp to avoid deadtime between each clock cycle as shown in figure 4.6. The TDC voltage ramp has a designed time resolution of 100 ps if operated in ILC-like conditions (ramp length of 200 ns). In testbeam, the theoretical time resolution is around 1.9 ns (ramp length of 4 μ s).

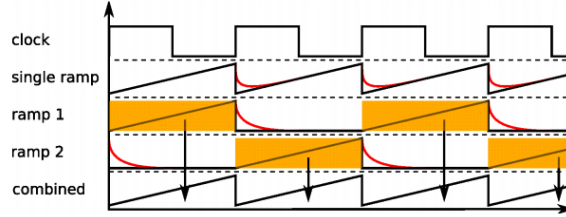


Figure 4.6 – Schematic of the TDC ramps in the SPIROC2B [104].

The chip can be operated in either external trigger mode (ET) or auto-trigger mode (AT). In external trigger, the signal of each cell is sampled synchronously to an external signal. This mode is used to measure the SiPM gain using the integrated LED system of the AHCAL which is described in section 6.2.2. The auto-trigger capabilities of the SPIROC are provided by a fast shaper and a discriminator. The threshold of the discriminator is configurable with a 10-bits DAC and is common to the 36 channels. A 4-bit DAC provides channel-wise threshold adjustment. When a trigger happens, the signal of each cell is compared to a configurable threshold, if the signal is above the threshold, the signal is stored into one memory-cell. In addition, the ASIC provides the information of which channel triggered called a *HitBit*. An external validation trigger can be provided to the ASIC to reduce SiPM noise. The time measurement is stored in another memory-cell when there is a trigger.

Once the 16 memory-cells are filled, no further hits can be stored. Hence, the memory-cells are read-out, digitized and the data is transferred out of the chip. The chip can be operated in power-pulsing mode where parts of the chips not needed in any given state of operation can be switched off. A schematic of the analog part of the SPIROC is shown in figure 4.7.

Several iterations of the chip have been made to fix bugs and improve the provided functionalities. In this thesis, the SPIROC2b has been used for a large AHCAL prototype used in testbeams at DESY and CERN. A new version, the SPIROC2e, is currently used for constructing a cubic meter AHCAL prototype.

4.4.3.3 The AHCAL Prototype

The Analog Hadron Calorimeter (AHCAL) is a sampling calorimeter using scintillator tiles as active material. The absorber structure can be either steel or tungsten. The AHCAL physics prototype [84] consists of 38 active layers inserted in a structure made of steel absorber plates 1 \times 1 m wide and 17.4 mm thick on average or made of tungsten absorber plates around 10 mm thick. The calorimeter has a total depth of 4.28 λ_π (5.3 λ_n). The active layers consist of a steel cassette housing 216, for the 30 first layers, or 141, for the 8 last layers, scintillator tiles connected on a PCB as shown in figure 4.8a. The tiles are 5 mm thick and have different sizes of 3 \times 3, 6 \times 6, 12 \times 12 cm². This accounts for a total of 7608 channels. The light produced in the scintillator is

(HBU), see figure 4.9a, is a 36 cm wide PCB holding four SPIROC2B ASICs for a total of 144 SiPM channels coupled to scintillator tiles of $30 \times 30 \times 3$ mm size to be read out. Up to six HBUs can be connected together to form a *slab*. A full AHCAL layer can be up to three slabs connected in parallel to a common set of readout (DIF), calibration (CALIB) and power modules (PWR). An integrated LED Calibration system [108] can deliver LED light pulses with amplitudes of a few photons up to saturation of the SiPM in order to calibrate and monitor each channel. Several designs of HBU and tiles have been produced to accommodate for soldering pin or surface-mounted (SMD) type SiPMs.

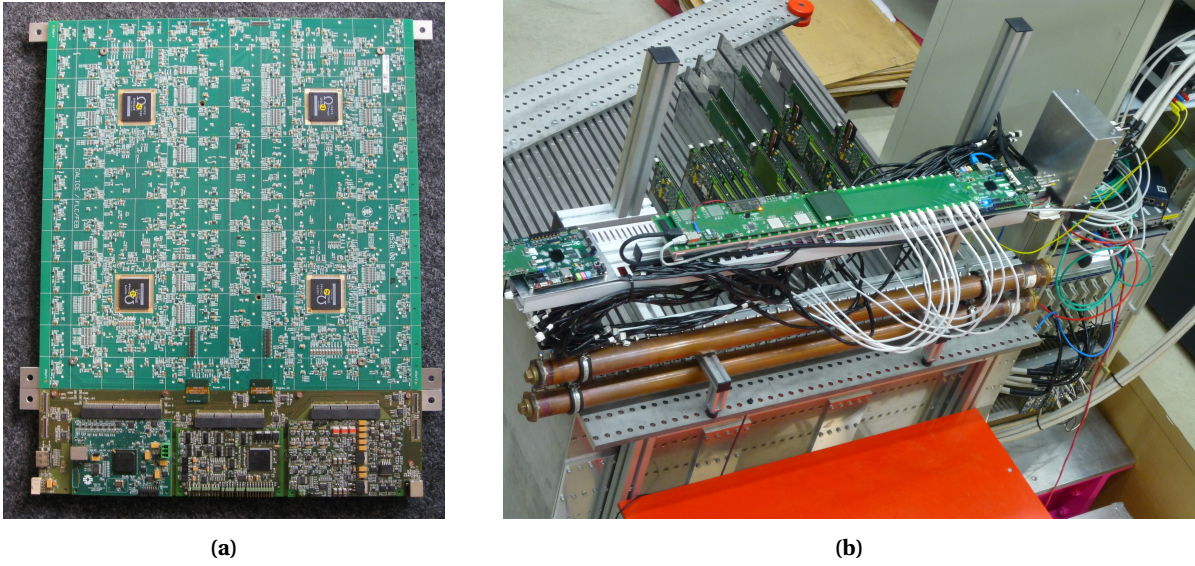


Figure 4.9 – a) Top view of the HBU2 with SPIROC2b. b) Picture of the AHCAL technological prototype in 2015 with several layers inserted.

An important step towards a fully equipped prototype was achieved with the operation of fifteen AHCAL layers in testbeam at the CERN SPS facility in July and August 2015. Various HBU designs with many types of SiPMs from different manufacturers have been used and served as a benchmark for the ongoing development of the scintillator tiles concepts. The active layers were inserted into a steel absorber stack into gaps 9 mm wide with absorber plates that are 1.72 cm thick. The number of channel for this prototype accounts for a total of 3744. A picture of the steel stack with few inserted AHCAL layers is shown in figure 4.9b. The data collected with this prototype is analyzed in this thesis (see from chapter 6 to 11).

This prototype was composed of several different modules. The oldest ones were using a wavelength shifting fiber (WLS) that conducted the light on a SiPM whereas the newest modules were having wrapped tiles in a reflector foil without any WLS fiber inside due to the use of SiPMs that are blue light-sensitive. A picture of AHCAL tiles is shown in figure 4.10.

The current AHCAL DAQ system is fully capable of operating a full scale calorimeter prototype in test-beam in various configurations and is being extended to integrate with other DAQ systems of other detectors (CMS HGCal prototype, Sc/SiECAL prototype...) and testbeam instrumentation (Telescope, Trigger Logic Unit (TLU)...) using the common EUDAQ framework [109–111].

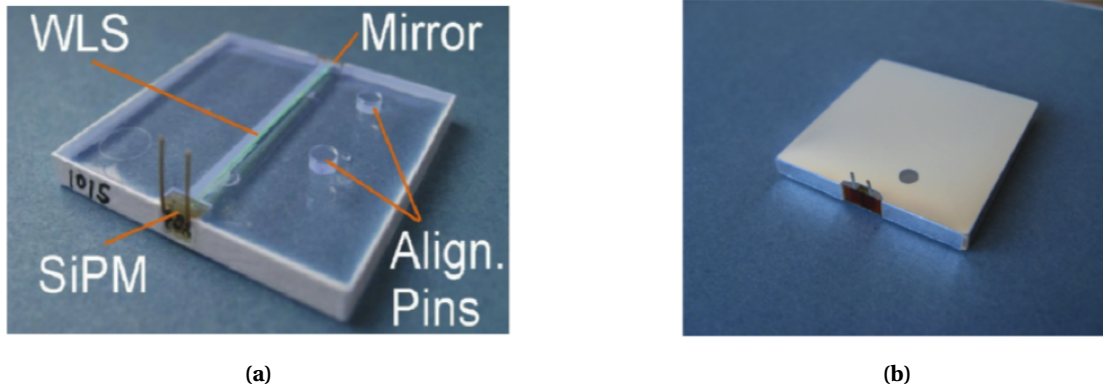


Figure 4.10 – The two different tiles used in the AHCAL technological prototype. The tile on the left is an older version with a WLS fiber and the tile on the right is a new design invented by MPI Munich and adapted by University of Hamburg which is wrapped in reflective foil and has no WLS fiber.

4.4.3.4 Current status of the AHCAL engineering prototype

A first milestone towards a design suitable for mass production has been achieved by the construction of the small prototype of fifteen AHCAL layers in 2016. The goals of this prototype are:

- The validation of the surface mounted tile-SiPM design using a Hamamatsu MPPC with 2700 px and the new HBU design.
- The evaluation of the performance of such calorimeter in electron beams at DESY.
- The operation of the detector in power-pulsing mode and in a magnetic field [112].

In addition, this prototype has been used as backing calorimeter for the CMS HGCAL prototype for the HL-LHC upgrade [113].

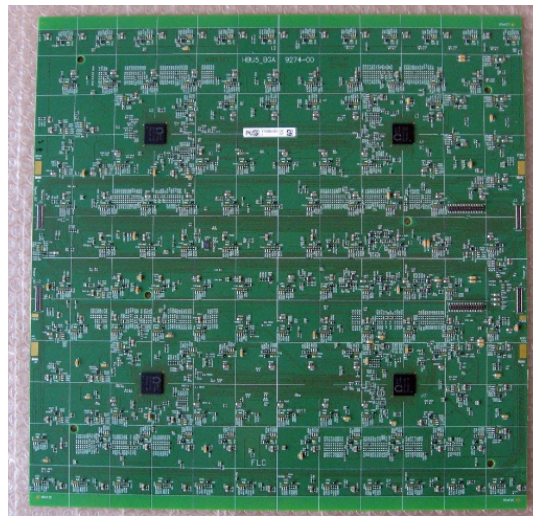


Figure 4.11 – Photo of the top view of the HBU5 with SPIROC2e used for the new AHCAL prototype.

Concerning the assembly of HBU boards, for electric components, this is fully automatized. For the scintillator tiles, the assembly on a mass-production scale is being investigated and is currently being demonstrated for the production batch of HBU boards [114].

The next milestone is the construction and operation of a full calorimeter prototype consisting of 40 2×2 HBU layers equipped with the current surface-mounted MPPCs and tiles, in a steel absorber stack and using the SPIROC2e as front-end electronics, see figure 4.11. It is planned to be operated in power-pulsing mode in various electron and hadron beams at CERN in 2018 [115].

In this chapter, the calorimeter concepts (electromagnetic and hadronic) of the CALICE Collaboration have been described. Concerning the hadronic calorimeters, 3 concepts have been presented. The DHCAL and SDHCAL use RPC gaseous technology to measure a signal on one or three bits readout scheme. The AHCAL uses scintillator-tiles coupled to a SiPM readout system to measure the analog signal of the deposited energy in each cell.

In this thesis, several simulation models are used to compare them with the AHCAL data. Before discussing the analysis and the results, it is important to understand the differences between the simulation models. In the next chapter, the simulation and software tools relevant for this thesis are discussed.

Chapter 5

Simulation and Software tools

In high energy physics as well as in other research areas, simulations are a tool that has become indispensable. They are used to provide model predictions, a guideline for an analysis as well as for optimizing cost and performance of detector designs. In this thesis, the simulations will be used as a guideline for the selection of specific events of the recorded data. An understanding of their functioning is useful and will be described in section 5.1. The software tools and the ILCSoft framework used for this analysis will be described in section 5.2. Finally, the AHCAL simulation model and the digitization procedure will be discussed in section 5.3.

5.1 Simulation of particle showers

The GEANT 4 framework [116] is a common toolkit in particle physics to simulate particle interactions with matter for a wide range of energies. Within this thesis, the simulations of the CALICE calorimeter prototypes and the ILD detector concept are used in conjunction with the MOKKA [117] and DD4HEP [118] framework. These frameworks provide a variety of tools for the implementation of detector geometries. GEANT 4 offers various tools and models to simulate physics processes in particle showers.

5.1.1 Electromagnetic shower models

Electromagnetic showers are generally well understood. This is mainly due to the fact that only electrons, positrons and photons are involved and their interaction with matter is simple as described in section 3.1. All EM interactions are simulated with a standard EM package in GEANT 4 [119]. This package has been extensively compared to many observables measured in calorimeters to a level of $\leq 1\%$ [120].

Recently additions have been made to the GEANT 4 EM physics list by improving the description of ionization processes in the active medium. Then the EM list is used with a suffix `_EMY`. This is needed in order to correctly simulate thin active layers where the detection method is very sensitive to the primary ionization, like in gas detectors such as RPCs. The use of the `_EMY` suffix in the EM physics list is greatly improving the agreement between data and simulation in the RPC based CALICE calorimeter prototypes, the SDHCAL and DHCAL [91]. Many other suffix options are available depending on the type of physics, detector and precision needed for EM processes.

5.1.2 Hadronic shower models

Hadronic showers are more complex in many ways than EM showers mainly due to the compositeness of the projectile as well as the target nucleus. High energy interactions between these lead to a very large phase space in the final state. The interaction is governed by the strong force and generally cannot be solved analytically. Instead, models are used using approximations and parametrizations mainly derived by theory and matched to data. Significant work has been made in the last few years in improving the modelization and accuracy of such models. The CALICE Collaboration has been of a great help in contributing to these improvements [121, 122].

The scale of the interaction in hadronic showers is generally given by the De Broglie wavelength $\lambda_B = h/p$. This simple variable becomes shorter as the particle energy increases thus smaller structures inside a nucleus become more relevant for the description of the interaction. GEANT 4 provides several models that are valid over various energy ranges. These models are described in the following.

5.1.2.1 Intra-Nuclear Cascade Models

For particle energies above a few hundred MeV and below a few GeV, the quark substructure of the nucleus is irrelevant. In this case, the interaction can be described by intra-nuclear cascade models (see figure 5.1). Several models are available in GEANT 4 and will be described in the following.

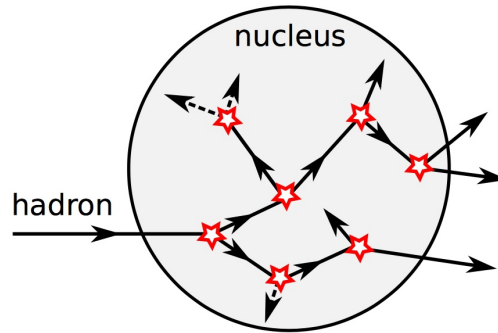


Figure 5.1 – Schematic of the cascade model. The incoming projectile and all secondaries inside the nucleus are tracked and their interaction is calculated until their energy is under a certain threshold or leave the nucleus [76].

Bertini Cascade

The Bertini cascade model [123] consists of the modeling of a nucleus by three concentric spherical shells of approximately constant nucleon density. The nucleons are treated as a degenerated Fermi gas in each shell and all energy levels are filled up to the Fermi energy (E_F). Following the Pauli exclusion principle that products can't be in an occupied state (lowest level filled by the Fermi gas), only secondary nucleons of energy $E > E_F$ can be produced. During the intra-nuclear cascade (INC), the momentum, the type of interaction and the four-momenta of the interaction for each nucleon are calculated until the energy of the tracked nucleon is below 2 MeV. The INC gives rise to excited states of the nucleus and a pre-equilibrium evaporation is com-

puted (emission of proton and neutrons). Then a de-excitation model is applied including Fermi break-up of highly excited light nuclei ($A < 12$), explosion model, fission model and evaporation model until the excitation energy is below 0.1 MeV.

Binary Cascade

The Binary cascade [124] is another approach to model the interaction between a projectile and a target nucleus. The model describes the nucleons with defined position and momentum following the nucleus mass, density distribution and Pauli's exclusion principle. The momentum is chosen randomly between zero and the Fermi momentum ($p_F^{max}(r)$) such that the total momentum of the nucleus is zero (at rest). The model is then treated by steps of excitations and decay into secondary particles emerging from the interaction until the average energy of all participants in the nucleus is below a given threshold (70 MeV). The remaining nucleus is further treated by pre-equilibrium and de-excitation models in GEANT 4. The validity range of this model extends from around 100 MeV up to 10 GeV.

5.1.2.2 String-Parton Cascade Models

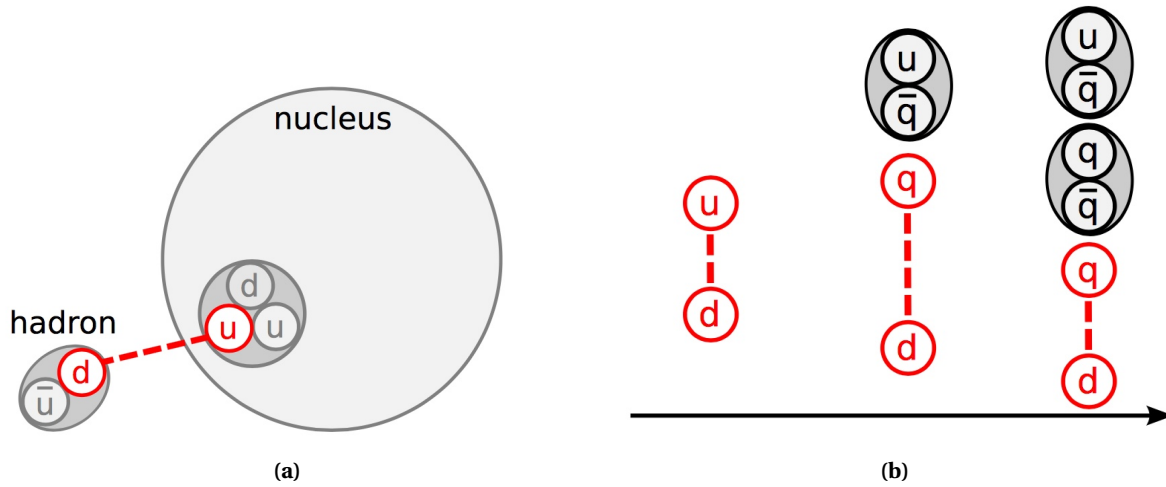


Figure 5.2 – a) The sketch shows the formation of a string between the projectile and one of the quarks inside the nucleus. b) Representation of the fragmentation of the strings via the generation of quark-antiquark pairs into hadrons [76].

The string-parton models [125] are used in GEANT 4 to simulate inelastic scattering of particles with a target nucleus as shown in figures 5.2a and 5.2b. This is used at high energies where INC models break down and where the quark substructure of the nucleons must be taken into account. The model uses string excitation to calculate the scattering. Currently, GEANT 4 provides two different models, the Fritiof model (FTF) and the quark-gluon string model (QGS).

The initial state consists of building the nucleus of individual protons and neutrons. The interaction between the primary particle and the nucleus gives place to one or more excited strings and an excited state nucleus. Quarks are the interacting constituents in the primary particle and the nucleons of the target nucleus.

A string has two endpoints, such that the quark content is defined and carries energy and momentum. The fragmentation of the strings is handled by a longitudinal string fragmentation model and the interaction of secondaries is carried out by cascade models as described in the former paragraph. The de-excitation is then simulated by fragmentation, pre-compound and nuclear de-excitation models natively provided by GEANT 4. The QGS model uses longitudinal strings to represent the momentum transfer and transverse strings for color exchange via Pomerons. In contrary, the FTF model uses an interaction probability calculated based on impact parameter, the center of mass energy, diffractive and elastic cross-sections to form a string. In the next paragraph, the QGS and FTF models are called QGSP and FTFP respectively.

5.1.3 GEANT 4 Physics Lists

GEANT 4 provides several physics lists for simulation that combine different hadron physics models. The physics lists are combinations of models, active in different energy ranges [126]. In this thesis, the physics lists QGSP_BERT and QBBC are used. The validity range of the physics lists is shown in figure 5.3. The former is used in combination with the High-Precision neutron tracking (HP) package. The HP option delivers an increased accuracy in the treatment of neutron interactions below 20 MeV. The QBBC physics list includes also a tracking for neutrons with less precision than the HP package. In addition, the QGSP_BERT physics list uses a parametrized LEP model (based on experimental data) to fill the gap between the transition of cascade models and string-parton models.

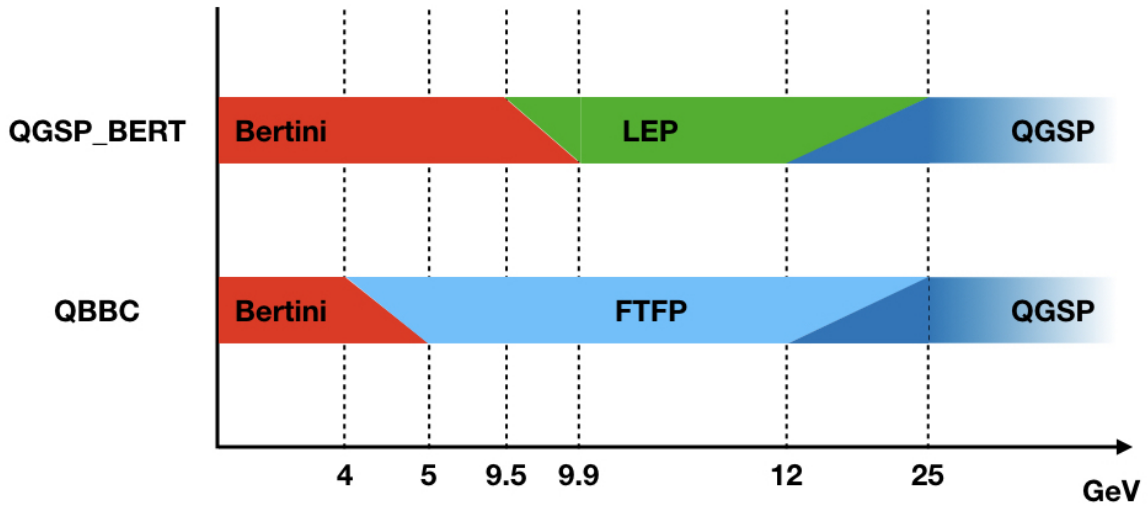


Figure 5.3 – Schematic of the physics list used in GEANT 4 v10.1 for this thesis. The validity range extends above 30 GeV. The diagonal regions represent the overlap region between the different models. The probability to select each model varies linearly between 0 and 100% in the overlap region.

5.2 Software tools

5.2.1 ILCSoft software framework

Various tools developed by the Linear Collider community are grouped in a common software framework called ILCSoft [127]. It provides a complete framework that can be used for Monte-Carlo studies and experiments. As an example, physics studies, ILD detector optimization and performance for the ILC are performed within the ILCSoft framework.

Most of the tools in the framework use an Event Data Model (EMD) named Linear Collider I/O (LCIO) which provides a reliable and performant solution for simulation and analysis studies [128]. With this tool, various detector concepts and analysis can be shared between collaborations such as SiD, ILD, CLIC, FCC.

The ILCSoft framework provides a modular C++ framework named MARLIN for reconstruction and analysis of physics events [129]. MARLIN uses LCIO seamlessly and is configured using XML steering files. MARLIN enables users to develop custom modules for their own and run it along with other already existing modules.

The reconstruction and analysis tools used in this analysis are mostly part of ILCSoft. For this thesis, ILCSoft v01-17-11 was used for simulation, reconstruction and analysis.

5.2.2 CALICE software framework

The CALICE collaboration has developed, since the physics prototypes, a software framework used for the simulation, digitization of simulated data and the calibration of the testbeam data using the MARLIN framework. For this thesis, a software development version (v04-08-03) was used and is available on the DESY svn server [130, 131].

5.3 AHCAL Detector Geometry implementation and Digitization

5.3.1 Geometry implementation

The simulation of the testbeam prototype presented in this thesis (see chapter 7) is based on the MOKKA [132] framework v08-05-01 and the new DD4HEP [133] framework v00-16, which both provide a full GEANT 4 v10.1 based simulation of the detector with detailed geometry and material descriptions. The DD4HEP framework was additionally used in order to validate the new simulation framework for the AHCAL and comparing to the known MOKKA framework. A right-handed coordinate system is used such that the Z-axis points in the beam direction and that the Y-axis is directed upwards. No beamline instrumentation is simulated except scintillator triggers in front of and behind the detector. An additional layer of 5.6 mm of lead (corresponds to $1 X_0$) is added in front of the calorimeter in order to account for missing upstream material. This additional material was determined using the electron data and matching the simulation with the center of gravity distribution in the z-direction (see appendix B).

In the MOKKA framework, this analysis uses the sub-detector models *TBecal4d* for the ScECAL (Scintillator strips with EBUs) and *TBhcal4d* for the AHCAL. In the DD4HEP framework, the detector geometry is provided by a steerable xml file. The distance between the sub-detectors is set to 0 mm. The absorber structure is square-shaped in simulation, on contrary wedge-shape in reality, but it is not expected to have any influence.

The placement of the active layers is the following: 2 single EBU boards, 8 single HBU boards and 4 2×2 HBU boards (in slots 11, 13, 21, 31 of the absorber structure). A schematic can be seen in figure 7.3.

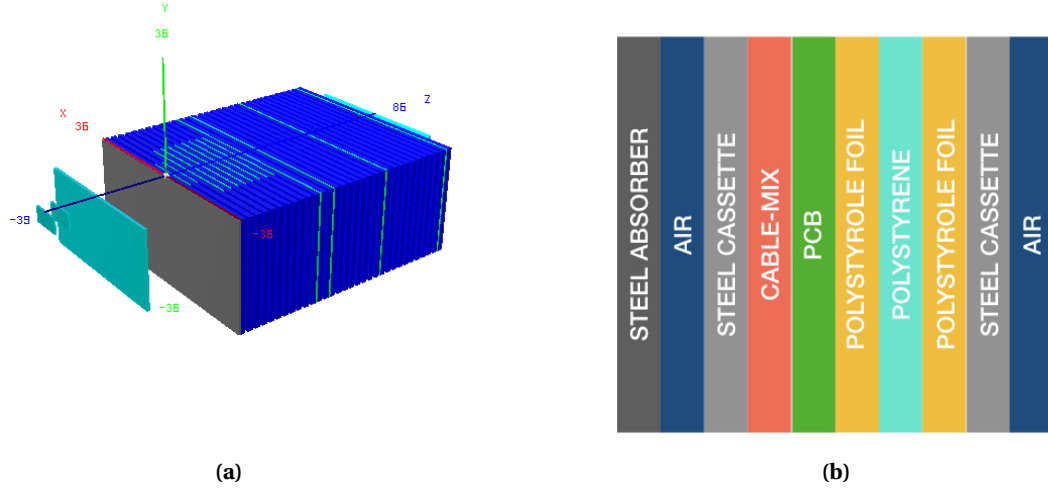


Figure 5.4 – a) DD4hep geometry model of the 2015 testbeam prototype. The dark blue represents the steel absorber structure, the light blue represents the active scintillator layers and the beam instrumentation in front and back of the calorimeter and the dark grey represents the additional lead material to account for missing upstream material. b) Material description of one layer in the MOKKA and DD4HEP simulations of the AHCAL. Dimensions are not to scale.

The material description is shown in table 5.1 for thicknesses and corresponding radiation length and nuclear interaction length. A schematic of the HCAL layer structure can be seen in figure 5.4b. The cable-mix of 1.5 mm, the polystyrole foils of 0.115 mm and the air gaps of 1.285 mm are not listed because of the negligible impact but are present in simulations. A picture of the model in DD4HEP is shown in figure 5.4a. The simulation includes also saturation effects in the scintillator known as the Birk's Law. The saturation appears high ionization densities due to shielding effects of the scintillator material. The implementation of the Birk's Law in GEANT 4 is used and follows the expression

$$\frac{dL}{dx} = \frac{dE}{dx} \times \frac{1}{1 + k_B \frac{dE}{dx}} \quad (5.1)$$

with $\frac{dL}{dx}$ the light yield by unit length and $\frac{dE}{dx}$ the ionization density. The parameter k_B depends on the material and a value of 0.07943 mm/MeV is taken [134]. A check was performed with MOKKA and DD4HEP models with muons and electrons to ensure that the material description in both models is better than 20% (see appendix B).

The beam gun is placed 1 m in front of the calorimeter face for the simulations in this analysis. It is configured to generate single beam particles with a 2% momentum spread, according to the beamline [135], and the beam profile for electrons and pions is extracted from data and applied to simulation. For muon runs, a flat beam covering the full AHCAL is simulated as this is not expected to have an influence on the

Table 5.1 – Material description in MOKKA and DD4HEP simulations of the testbeam setup at CERN in July 2015. The X_0 and λ_n numbers are obtained by the command-line *materialScan* in the DD4HEP framework.

Material	thickness (mm)	X_0	λ_n
steel absorber	17.2	0.977	0.101
steel cassette	0.5	0.028	0.003
PCB	0.7	0.004	0.001
Polystyrene (ECAL/HCAL tile)	2, 3	0.005, 0.007	0.006, 0.009
ECAL layer	26.2	1.044	0.115
HCAL layer	26.2	1.046	0.118
AHCAL	-	33.24	3.54

MIP and time response of the detector. All electron simulations are simulated with GEANT 4 v10.1 using the QGSP_BERT_HP physics list.

Pion showers are simulated using QGSP_BERT, QGSP_BERT_HP and QBBC physics lists. The package *high precision* (_HP) is used in order to understand the differences induced in timing with a precise treatment of the neutrons. The table 5.2 shows the number of single particle events simulated for this thesis.

Table 5.2 – Number of single particle events simulated in MOKKA and DD4HEP for each particle type and energy.

Particle	Energy	# Events
μ^-	150 GeV	1 000 000
e^-	15, 20, 30, 40 GeV	20 000
e^-	10, 50 GeV	200 000
π^-	10, 30, 50, 70, 90 GeV	500 000

5.3.2 Digitization

The digitization of simulated hits is very similar to the one used in the ScECAL and AHCAL physics prototypes [136]. First, the energy deposited in a cell is converted in MIP. This is done in order to have the simulation on the same energy scale (see chapter 8) as the testbeam data once converted. The conversion unit named *MIPtoGeV* is extracted from simulation by projecting 8 GeV muons onto the AHCAL detector and fitting the resulting spectrum of the deposited energy. Motivated by physics, as explained in section 3.1, ideally for a thin active material, the energy deposited follows a Landau distribution. The most probable value (MPV) of this distribution is used as the *MIPtoGeV* factor. For this thesis, a value of 470 keV is used for the AHCAL as shown in figure 5.5 and 309 keV for the ScECAL.

If available, individual calibration factors obtained from data are used to extract the light yield which is needed to model the statistical fluctuations of photons hitting a SiPM [137]. Saturation effects are also included using the number of pixels available on each SiPM type. Most of the tiles used are wrapped with a reflective foil such that crosstalk effects between channels can be neglected. For layers with no wrapping, a default value of 15% for the cross-talk is applied.

Additionally, noise needs to be taken into account for the engineering AHCAL prototype. It is important

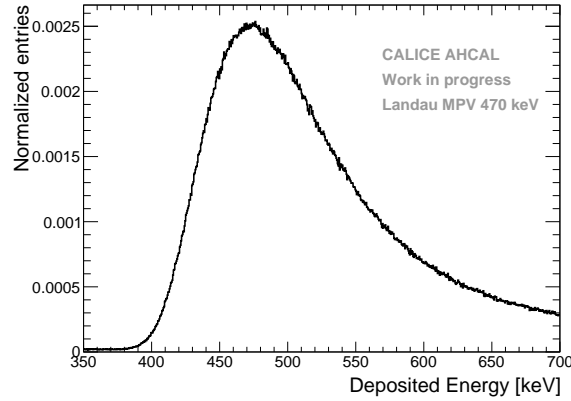


Figure 5.5 – The energy deposited in the AHCAL cells from the raw simulation without any detector effects for 8 GeV muons. The spectrum has been fitted with a Landau distribution and the MPV is extracted as the *MIPtoGeV* factor.

to note that noise is much lower than in the physics prototype but it is important to be taken into account for this thesis as timing is very sensitive to low statistics late tails. Noise is added using muon runs by removing found tracks and keeping remaining hits. This is described in appendix D.

The timing is modeled in the same way as in the SPIROC, the energy from sub-hits in a cell is integrated over a sliding time window of 15 ns, if the energy sum passes the threshold, the time of the simulated sub-hit is used as the time of the hit. In order to simulate detector resolution effects, the time of a hit is smeared with a double Gaussian function with slightly different means and sigmas convoluted with a Gaussian of fixed mean and variable sigma. More details are explained in appendix F.

After digitization, simulated hits have the same format as raw data hits and are then reconstructed using the same software chain as is used for data. To suppress noise, only hits above 0.5 MIP are considered in this analysis in both simulation and data.

In this chapter, the inner details of the simulation models used for this thesis are discussed. The simulation model of the AHCAL is described in details as well as the digitization procedure of simulated AHCAL hits.

Before taking data in testbeam, the detector has to be commissioned. This means that each channel of the detector has to be characterized in terms of the voltage applied on the SiPM, the SiPM gain, the trigger threshold position and the noise of the detector. In the next chapter, the commissioning procedure of the AHCAL is presented.

Chapter 6

Commissioning of the AHCAL technological prototype

Before any beam measurement, all the electronics of the detector has to be characterized. Before the full assembly, each individual ASIC must be tested in order to reject the ones that present bad channels or any other defects. After the assembly, each HBU needs to be characterized. This includes the measurement of the SiPM-tile gain, the trigger threshold and electronic noise. In this chapter, the testing of the ASICs and the commissioning procedure of the AHCAL will be presented.

6.1 Testing of individual SPIROC2B chips

The testing of individual chips prior to the soldering to the HBU board is necessary. This avoids broken chips to be installed and reduces the number of dead channels. In the past, OMEGA was testing the functioning of the SPIROC ASICs and classify it into 3 grades: A, B and C grades. Only A-grades ASICs were used. The testing is done manually for each chip as no fully automatic testing setup was available at the time of testing. This reduces the number of cross-checks done on the chips due to time constraints. The SPIROC2B chip (see section 4.4.3.2) can be tested standalone on a custom made PCB board. The SPIROC2B chip is installed in a special socket and is read-out by an ALTERA FPGA. The board is operated by a Labview software made by the OMEGA group [103].

The board as shown in figure 6.1a contains all the debugging features needed to check the functioning of the chip. The red square represents the input signal for the 36 channels. Generally, a SiPM like-pulse with a fast rising edge (around 1 ns) and a slower falling edge (around 20 ns) is injected into one channel of the chip.

In the blue and yellow square are the output signals. This enables to check via an oscilloscope the output analog signal after the slow shaper, but can only be checked in external trigger mode. This is shown in figure 6.1b, the signal from the SiPM is integrated over a long period (typically 100-200 ns) and it enables to easily sample the signal at the maximum.

In the purple square are the input signals for the FPGA such as the slow clock and external trigger signals. And finally, the green square (above the blue and yellow squares) represents the *trigger threshold* and the channel-wise voltage adjustment *Digital to Analog Converters* (DAC) that can be tested manually or automatically by connecting a Keithley multimeter a serial port on the board.

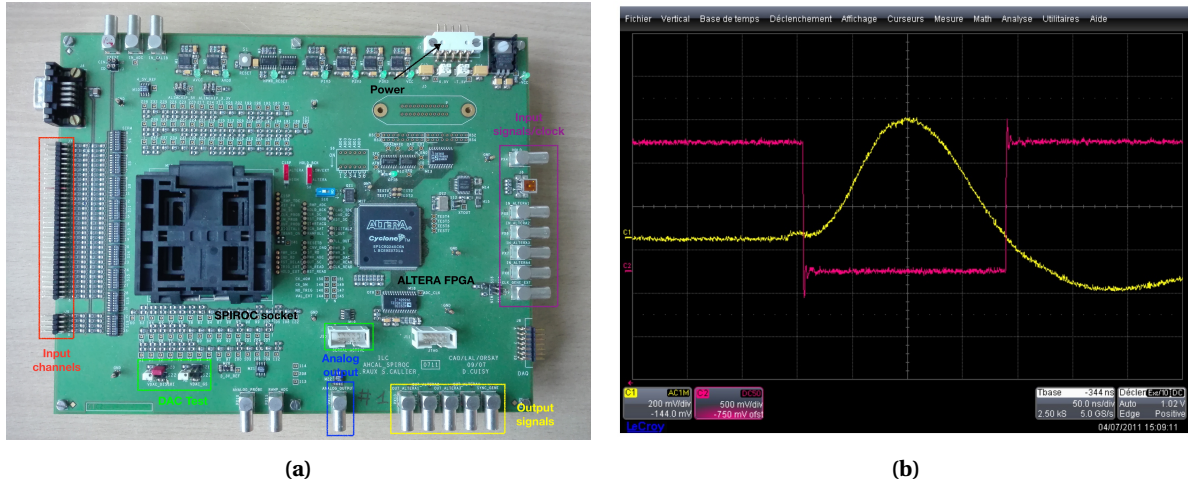


Figure 6.1 – a) Testboard used to test the SPIROC2B chip standalone. The red square represents the 36 input channels of the SPIROC ASIC, the purple square represents the input signals for the ALTERA such as clocks. In yellow and blue squares represent the output signals, analog and digital, of the SPIROC. The green square, above the blue and yellow one, represents the input and output DACs that can be measured automatically via a Keithley multimeter with the Labview software. b) Example of an analog signal outputted by the slow shaper of the SPIROC2B. The signal is represented in yellow. The trigger is represented in red.

In this manual procedure, the vital parts of the chips are tested. This includes to check that all channels are working correctly, that the chip works in both external and auto-trigger modes, that all both the trigger threshold and the voltage adjustment DACs are working and that the digital part converts and sends the data out of the chip. For the testbeam in July 2015, around 60 chips have been tested manually for the modules 12, 13 and 14. The mean time for testing a chip is around ten minutes.

6.1.1 DAC Testing

As the testing procedure is done manually, only the most critical components of the chip are tested. One of this component is called the DAC. Two DACs are present in the SPIROC2b. One is regulating the channel-wise voltage applied to the SiPM (8-bit input DAC) and another is controlling the trigger threshold discriminator (10-bit output DAC) which is common to the 36 channels. In the following, the DAC regulating the voltage channel-wise is referred as the input DAC and the DAC controlling the trigger threshold is referred as the output DAC.

The measurement procedure is done in two parts for the input DAC. First, a simple check is done by measuring the voltage of the channel at a DAC value of 0. If one of the channels presents an unstable voltage, it indicates likely that the input DAC for this channel is broken thus the chip is discarded. If a chip passes the simple check, then the input DAC curve for all channels is measured with a Keithley 2000 multimeter connected to a serial port on the board. The measurement is done automatically using Labview. The time required is around 1-2 minutes per chip.

The output of the measurement is a list containing the DAC value (from 0 to 128) and the associated voltage. The reconstructed input DAC curve is shown in figure 6.2a. One can notice that the spread channel-to-channel for the input DAC increases with the value. The spread is around 10 mV at a value of 0 and goes up to 200 mV at a value of 128. For older generation SiPMs, fine voltage adjustment was needed to reduce

the spread in gain due to a widespread in breakdown voltages [138]. For newer generation SiPMs and new produced modules, the spread in breakdown voltage is very small (less than 100 mV) and, therefore no voltage adjustment is needed anymore. For the testbeam in this thesis, a DAC value of 0 was chosen where the spread is minimal.

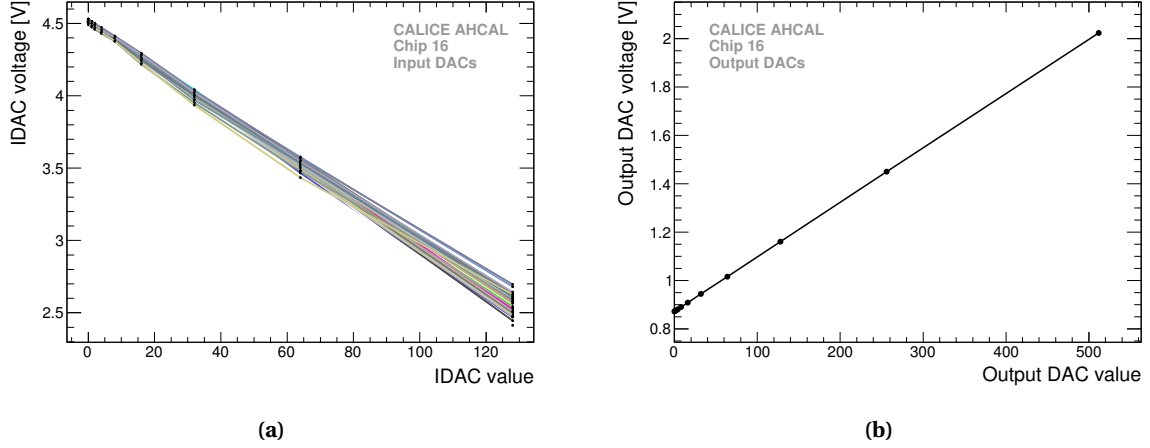


Figure 6.2 – a) Reconstructed input DAC curves of the 36 channels for the Chip 16 of the tested batch. b) Reconstructed output DAC curve for same tested chip.

For the output DAC, a Keithley 2000 multimeter is connected to a second serial port on the board and measures the output DAC automatically using Labview. The output of the measurement is a list containing the output DAC value from 0 to 512 and the associated voltage. The reconstructed curve is shown in figure 6.2b. The output DAC for this chip has a linear behavior as expected. If any other behavior was observed, the chip was discarded.

Around 60 chips were tested with a yield of 84%. There is no obvious common cause for failure (digital part not working, no response to slow control programming, broken input DAC...). The time to test a chip manually is around 10 minutes. A new testing board has been designed by DESY and the University of Wuppertal in order to automatize the testing procedure of individual BGA-packaged chips [139] and to reduce the time needed for the testing procedure. This new board has been commissioned in July 2017 and it is being used currently for the next generation AHCAL prototype to test around 650 chips.

6.2 HBU Commissioning procedure

The commissioning procedure of the detector was done in July/August 2014 for a testbeam that was planned in October/November 2014 at the CERN PS facility. The same boards were used during the testbeams in 2015. A picture of the setup used in this thesis is shown in figure 7.3. Before the assembly of the detector into the absorber stack, each individual HBU needs to be tested. This test is done in order to characterize the full board. The procedure involved these steps:

- The setup of the Power Board voltage to deliver the high voltage to the SiPM and the setup the input DAC value.

- A first characterization of the board by measuring the SiPM gain at nominal settings.
- An iterative adjustment of the pre-amplifier gain to reach the targeted SiPM gain.
- A threshold scan measurement.
- A noise measurement.

A full detailed report can be found in [138]. The following subsections will describe each point in more detail. The module 3 and modules 12 to 14 (13 HBUs) were fully commissioned. The modules 4 to 11 (11 HBUs) have already been calibrated in the past and they used the same pre-configured settings. Only a cross-check was performed for these modules. The modules 1 and 2, the ECAL boards (EBUs), were commissioned separately due to high noise and very low gain.

6.2.1 Setting the High Voltage

Table 6.1 – List of the different SiPMs used in the CALICE AHCAL in July 2015.

Module	Producer	Model	Area (mm ²)	Pitch (μm)	WLS Fibre	Read-out type	N_{px} [10 ³]
1	Hamamatsu	S12571_010P	1 × 1	10	no	Bottom	10
2	Hamamatsu	S10362-11-025O	1 × 1	25	no	Side	1.6
3	Hamamatsu	S12571-025P	1 × 1	25	no	SMD	1.6
4-5	Ketek	N/A	2.25 × 2.25	18	no	Side	12
6-10	CPTA	CPTA	1.28 × 1.28	40	yes	Side	0.8
11-12	Ketek (UHH)	PM1125NS-SB0	1.2 × 1.2	25	no	Side	2.3
13-14	SenSL	MicroFB-10020-SMT	1 × 1	20	no	Side	1.3

An AHCAL board (HBU) has 144 channels, each equipped with a plastic tile-SiPM. To achieve a certain light yield, i.e the number of fired pixels per MIP, the SiPM must be operated above a specific voltage called the breakdown voltage V_{Br} (see section 4.4.3.1). This voltage has been measured for a couple of SiPMs. For newer generation SiPMs, it is given by the manufacturer where batches of SiPMs are placed in bags with a certain V_{Br} and the lower/upper limits are indicated. The table 6.1 shows the SiPMs used during the testbeam at CERN in July 2015. The variation of the breakdown voltage is in the order of hundreds of millivolts between SiPMs of the same type.

The SiPMs are operated between 2.5 to 5 V over the breakdown voltage depending on the type. The high voltage that is set on the power board V_{PB} is determined by the distribution of the SiPM bias voltages of each HBU taking into account a safe margin for the voltage adjustment with the input DAC. Then, the input DAC for each channel is calculated to have the targeted SiPM bias voltage. This made the procedure very laborious and time-taking [138].

As the quality of SiPMs has increased drastically in the last few years, the need for individual channel-wise voltage is reduced. This simplifies the procedure to $V_{PB}[V] = V_{Br} + V_{overvoltage} - V_{IDAC}$ where V_{IDAC} is fixed and common to all channels. V_{IDAC} is typically in the order of -4.5 V to 4 V with a spread of around 10 mV between channels (see section 6.1.1). The table 6.2 sums up the voltages applied.

Table 6.2 – List of breakdown and operating voltages applied to each SiPM types. V_{op} represents $V_{Br} + V_{overvoltage}$. V_{PB} is the voltage applied to the power board.

SiPM type #	V_{Br}	V_{op}	V_{PB}
Hamamatsu (S12571_010P - S10362-11-025O)	~ 65 V	~ 70 V	~ 75.8 V
Hamamatsu (S12571-025P)	~ 65 V	~ 67 V	~ 70.66 V
CPTA (Modules 6-10)	~ 35-45 V	~ 37-50 V	~ 40.1 - 51.7 V
Ketek (Modules 4-5)	~ 28 V	~ 32 V	~ 36.95 - 37.02 V
UHH Ketek (Modules 11-12)	~ 27 V	~ 29.55 - 30.05 V	~ 32.98 - 34.49 V
SenSL (Modules 13-14)	~ 25 V	~ 27.39 - 27.39 V	~ 32.10 - 32.11 V

6.2.2 First characterization of the SiPM gain

In this section, the SiPM gain is related to the ADC value between the two first peaks of a single pixel spectrum where individual pixels, in a relatively small number (~10-15 pixels), are fired by an integrated LED system. This value is proportional to the high voltage applied to the SiPM and can be also modified by adjusting a feedback capacitor of the SPIROC2B high gain pre-amplifier.

Before starting the gain measurement procedure, a scan of the hold time, referred as a holdscan in the following, needs to be performed. The hold time is the time delay between the trigger and the sampling of the signal after the slow shaper. This time needs to be chosen in order to sample the maximum of the signal. The procedure aims to reconstruct the signal shape after the slow shaper by injecting a fixed amplitude signal using the integrated LED system to all the channels while repeating this for several hold time values from 0 to 60 ns.

Only channels where the integral of the curve is above 6000 are chosen. This is done to reject channels presenting a curve too flat that would make the determination of the hold time difficult. The results for a typical chip are shown in figure 6.3a. The hold time value is chosen where the maximum of the signal is.

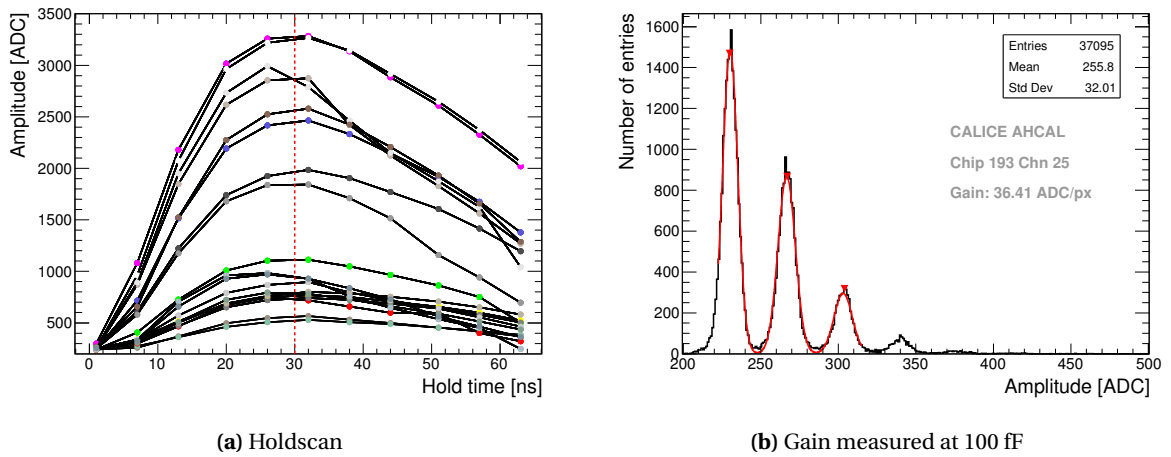


Figure 6.3 – **a)** Reconstructed signal shape for several channels of Chip 174 on HBU_2_15 (Module 11). Only channels where the integral of the holdscan curve is over 6000 are shown. The dotted red line represent the hold time chosen for this board. **b)** Single pixel spectrum of a single channel. The fit is done by a multi-Gaussian where the distance between the 1st and 2nd peaks is the fitted SiPM gain.

After this, a first characterization of the gain can be done at nominal settings using a pre-amplifier value of 100 fF. For this, all channels are illuminated by the integrated LED system with a certain range of LED voltage in steps of 100 mV in order to characterize all channels due to variations in response due to LED light, tiles, SiPM. For modules 4 to 11, a range of 10-15 voltages is needed. Due to improvements in the integrated LED calibration system design, SiPM quality and tile quality, a much smaller range can be used (3-5 voltages) for the modules 3 and 12 to 14. A typical example of a single pixel spectrum at 100 fF can be seen in figure 6.3b.

6.2.3 Adjustment of the SiPM gain

The goal of this procedure is to fit the dynamic range of the SPIROC2B in ADC to the number of pixels on the SiPM to avoid any ADC saturation before SiPM saturation. ADC saturation would mean that information is lost and as well that the full range of pixels on the SiPM would be not used. This calculation is still approximate due to several unknown variables such as the number of effective pixels of a SiPM and the calibration factor between the high gain and the low gain for each channel called the intercalibration factor but this procedure gives a good order of magnitude for the target gain.

The targeted gain is calculated by:

$$G_{target}[ADC] = \frac{ADC_{max}}{N_{px}[px]} \quad (6.1)$$

where G_{target} is the value targeted for gain, ADC_{max} is the maximum ADC range and N_{px} the number of pixels on the SiPM. The maximum ADC range is calculated as follows

$$ADC_{max} = ADC_{12bits} \times IC_{HG/LG} \quad (6.2)$$

where $ADC_{12bits} = 4096$ and $IC_{HG/LG}$ is the high/low gain intercalibration factor. By design, it should have a value of 10. A conservative number of $ADC_{12bits} = 3600$ is taken due to the variation of $IC_{HG/LG}$ between 8-12 and the pedestal value, i.e the ADC level corresponding to no signal, at around 250 ADC. This gives an approximated range of $ADC_{max} = 3600 \times 10 = 36000$ ADC.

The formula 6.1 is competing with the dynamic range to measure the energy:

$$E_{max}[MIP] = \frac{ADC_{max}}{LY \times G_{target}} \quad (6.3)$$

where E_{max} is the maximum energy hit that can be measured in MIP and LY is the light yield corresponding to the number of pixels fired by a MIP. This means that a higher target gain yields a lower maximum hit energy for a fixed light yield. This is generally treated in a way that the maximum hit energy is determined from simulation to avoid loss of information thus giving G_{target} . However, G_{target} needs to be high enough in order to monitor the detector stability during data taking, thus giving a limit on the minimum gain possible. Therefore, a trade-off between the maximum hit energy and the gain is done to fulfill these criteriums. For this thesis, a dynamic range of around 120 MIP was chosen based on simulations. The table 6.3 sums up the assumed light yield and the target gains for each board type.

The Ketek SiPMs with 12k pixels are operated in different modes for calibration and physics data due to the very high number of pixels. The calibration mode is the operation at nominal settings of 100 fF and the physics mode is operated at the maximum pre-amplifier feedback capacitor value of 1500 fF. This is needed

in order to fit the SiPM dynamic range into the ADC range. A gain measurement at 1500 fF is not possible with the current electronics due to very small gain (around 6-7 ADC/px), therefore an approximate intercalibration factor between both modes of around 7 has to be used later on in the energy scale calibration (see chapter 8).

Table 6.3 – List of the targeted gains for each module type.

Type #	LY [px/MIP]	G_{target} [ADC]
Hamamatsu (S12571-025P)	~ 32	~ 11
CPTA	~ 13	~ 22
Ketek	~ 20	~ 40 (calib) - 6 (physics)
UHH Ketek	~ 17	~ 16
SenSL	~ 13	~ 24

The pre-amplifier feedback capacitor value can be calculated using the figure 6.4a to achieve the targeted gain. In principle, this curve needs to be measured for each channel but due to many improvements in the measurement procedure, LED light uniformity, SiPM gain and uniformity, this curve gives a very good approximation. For the example that is shown in figure 6.3b, the calculation gives a value of 675 fF that needs to be used to reach a gain of 12 ADC/px.

The gain measurement procedure described in section 6.2.2 is then performed with the calculated pre-amplifier capacitor feedback. The result of the gain fit is shown in figure 6.4b for the example from above. It shows a gain very close to the target gain. This procedure is iterated until the targeted gain is reached. Most of the time, only one more iteration was needed due to the granularity of the pre-amplifier capacitance.

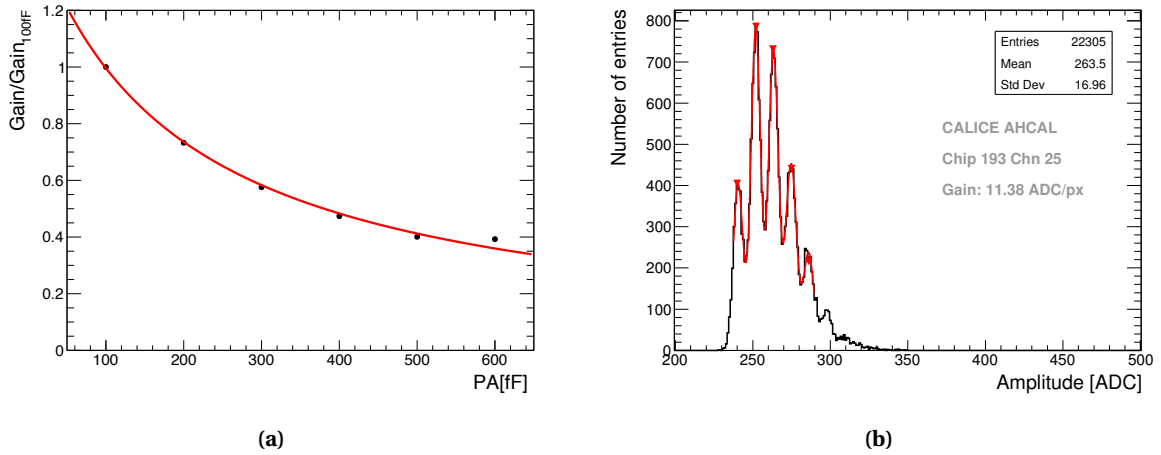


Figure 6.4 – a) Generic dependence of the gain as function of the pre-amplifier capacitance used to determine the value of the pre-amplifier feedback capacitor to use. b) Results of the gain fit for the same channel as shown above after adjustment of the pre-amplifier feedback capacitor from 100 fF to 675 fF.

6.2.4 Threshold scan

The SPIROC2B offers the possibility of setting a global trigger threshold (10-bit range) as well as an individual channel-wise threshold (4-bit range) in auto-trigger operation. The channel-wise threshold cannot be

used currently as it induces a shift on the global threshold. The trigger threshold needs to be setup properly in order to avoid loss of information if set too high or being overwhelmed by noise events if set too low. The goal of this method is to get a good first estimate (to an order of 5-10%) of the needed value for the trigger threshold in a quick and efficient way. Further adjustments in testbeam will depend on beam rates and noise conditions. A more complete description of the procedure can be found in [137] and [140].

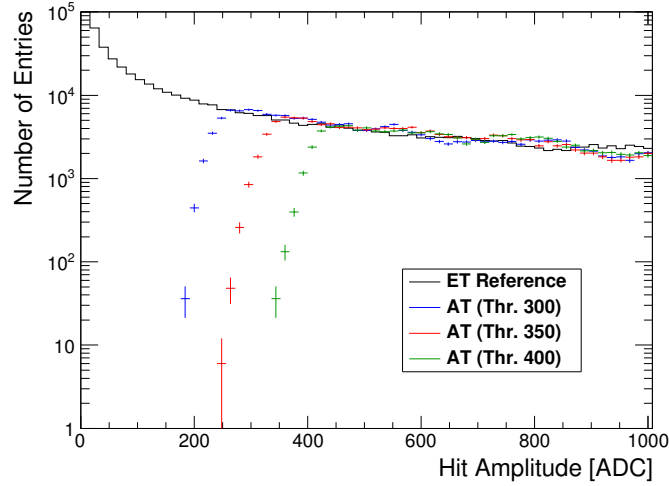


Figure 6.5 – ET reference spectrum and AT spectra of a single channel for different trigger threshold values of 300, 350 and 400. One can notice a clear dependence of the trigger position as a function of the threshold value.

The procedure utilizes the integrated LED calibration system to record a number of runs with increasing LED amplitude. For each LED amplitude, a run is taken in external trigger (ET) and then immediately followed by runs in auto-trigger (AT) with different trigger threshold configurations. This is done to ensure comparable LED amplitudes between the two runs as the LED amplitude is not stable over time. Next, the ADC of all ET runs are summed up into an histogram and the same is done for all AT runs for each trigger threshold value. An example of the spectra obtained for a single channel for three different thresholds is shown in figure 6.5. It shows a clear dependence of the trigger threshold position as expected.

By dividing the ET reference spectrum with the AT spectrum, an efficiency curve is obtained for each trigger threshold configuration. This efficiency curve can be fitted with an *error function* $erf(x)$ of parameters σ and μ for the width and position. An example of the fit for a single channel and trigger threshold configuration is shown in figure 6.6a. The efficiency is normalized to 1 due to the measurement method. The statistical uncertainty on the trigger position is around 1% which is well below the needed accuracy. The fit is repeated for each trigger threshold configuration and the dependence of the trigger position as a function of the threshold parameter can be drawn (see figure 6.6b). The dependence of the trigger position on the threshold parameter is linear as expected.

This method was performed on 14 fully equipped HBUs [140]. The dependence of the trigger position on the threshold parameter was obtained for most channels. The trigger threshold for each channel is then determined at 0.5 MIP using the linear dependence, for this, an assumption of the MIP value for each channel is made based on the target light yield and gain as no MIP measurement was available at the time. The trigger threshold per chip to use is the minimum trigger threshold extracted for all the 36 channels.

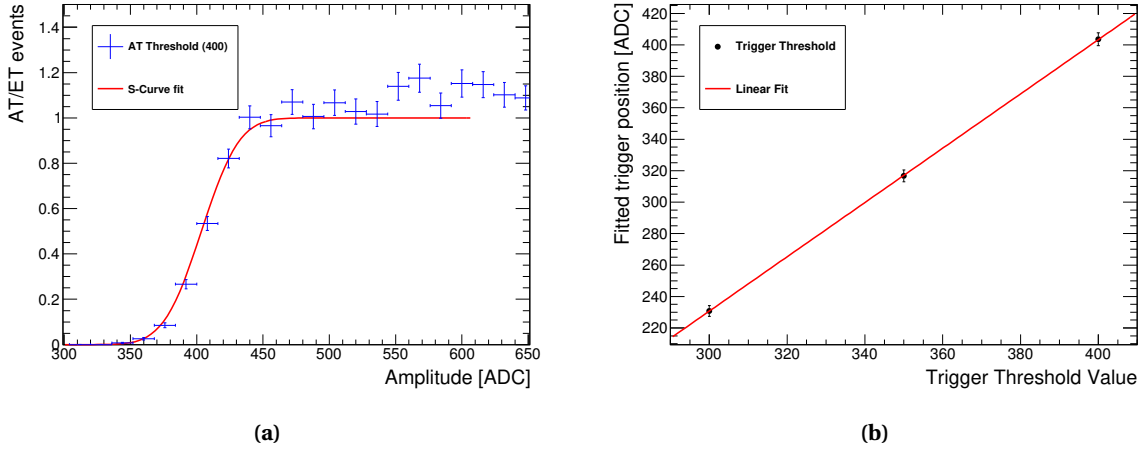


Figure 6.6 – **a)** Trigger efficiency S-Curve fit for a typical channel at a trigger threshold of 400. $\mu = 403.542 \pm 4.04538$. **b)** Extracted trigger threshold positions as a function of the trigger threshold value. One can observe a linear behavior.

6.3 Noise Measurement in the AHCAL

A noise measurement is needed and is a measurement that gives additional information on the trigger threshold. As explained above, the setting of the trigger threshold is very crucial. If the threshold is set too low, a noisy channel could overflow the whole detector thus reducing the readout efficiency. Noise measurements have already been done in the past for 4 HBU boards in 2012 [141]. This method is a proof-of-concept that seems to fulfill the requirement of characterizing the noise as a function of the threshold position for all the channels or a chip at once. The needed accuracy is also here not so crucial in order to keep the threshold in the acceptable range of 0.5 MIP. This method enables us to have an idea of the noise level at a certain trigger threshold and especially to understand the evolution of noise as a function of the trigger threshold. This measurement method utilizes the fact that SiPM noise should follow a Poisson distribution. Moreover, to eliminate the dependence of the SiPM noise as a function of the temperature, the measurement is performed in a climate chamber at a temperature of 25 degrees Celsius.

Each measurement is taken in auto-trigger mode for different time windows (T), from 1 ms to 30 ms, for different values of the trigger threshold from 200 to 250. Each measurement is done 200 times (readout cycles). For each cycle, the number of filled memory cells is put into a histogram per chip. It is checked that the bin 15 of the histogram, i.e corresponding to the memory cell 16, is not filled otherwise the chip would be automatically read out. This is done to ensure that the measurement is stopped at exactly the end of the time window and not before. In a next step, each histogram is fitted with a Poisson distribution. A typical example of a chip can be seen in figure 6.7a. The most probable value (MPV) λ_{mem} of the Poisson distribution gives the most probable number of memory cells filled per chip for a specific trigger threshold value and time window T .

This can then be converted into a noise rate as $Noise\ Rate = \frac{\lambda_{mem}}{T}$ and filled into an histogram per chip for each trigger threshold value. The mean value of the noise rate per chip for each trigger threshold value is used to plot the noise rate as a function of the trigger threshold value for each chip. The figure 6.7b shows the results obtained for a typical board.

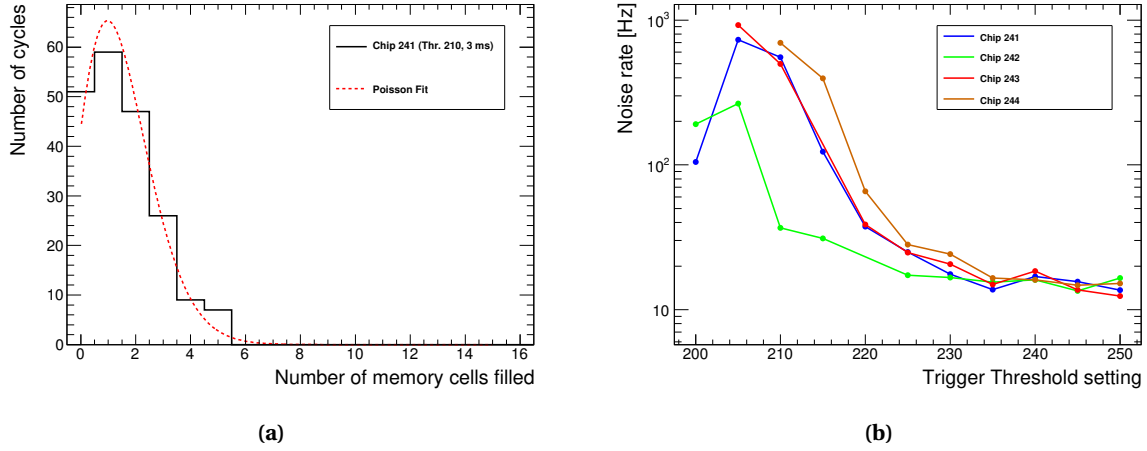


Figure 6.7 – a) Observed histogram of the number of memory cells filled per cycle for a typical chip with a trigger threshold of 210 and a time window T of 3 ms. $\lambda_{mem} = 1.5 \pm 0.1$. b) Extracted noise rate as a function of the trigger threshold setting for a full board.

The figure 6.7b shows that noise decreases fast with increasing threshold until a plateau is reached. This plateau is the ideal area to set the threshold as the curve is quite constant. The fact that the curve is constant as a function of the threshold may indicate that a large signal, e.g. cosmics, limits the noise measurement in this region. However, the rate seems compatible with noise only. In this figure, a threshold between 230 and 240 was chosen. As this method is complementary to the threshold scan, the region can be compared to where is the threshold put in terms of MIP value. For this board, a threshold of 230-240 corresponds to about a threshold 0.2-0.25 MIP which is well below 0.5 MIP and thus safe.

This method is very complementary to the threshold scan and can be used to set a trigger threshold for all chips that allows for a stable operation of the detector. It does not rely on a very precise measurement and has been shown to work well for all chips. Moreover, this method requires only minimal additional time to the commissioning procedure. A full understanding of the position of the trigger threshold relative to 0.5 MIP would greatly improve the data taking efficiency of future AHCAL engineering prototypes.

This chapter presents the ASIC testing and commissioning procedure for the AHCAL technological prototype performed during the summer of 2014. First, around 60 chips have been tested manually with a yield of 84% to be equipped on new HBU boards. The testing procedure aims at reducing the number of dead channels by testing crucial features of the chip. The time to test each ASIC is around 10 minutes.

The commissioning of AHCAL boards is divided into several procedures described in this chapter. In total, three EBU and 24 HBU boards have been commissioned in the year 2014-2015. The total time for the procedure varies between one hour, for the new generation boards, to 7-8 hours depending on the LED amplitude range needed. In the future, the commissioning procedure can be improved by the calibration of the HBU in a cosmic-stand providing a reliable cross-check along the production before a full calibration in testbeam.

After the commissioning, a fully assembled AHCAL prototype was placed in various beams at the CERN SPS facilities during the summer of 2015. In the following chapters, an analysis of the collected testbeam data

focused on the time development of hadronic showers is presented.

Part III

Data Analyses

Chapter 7

AHCAL Testbeam setup & Event Selection

The experimental data used in this thesis has been collected in a testbeam campaign at the SPS facility at CERN in July 2015 with the AHCAL technological prototype described in section 4.4.3.

The main topic of this thesis is the study of the *time development of hadronic showers* and the study of the *effects of timing cuts* in a hadronic calorimeter. The analysis is divided into several parts. In the first part, the energy scale calibration of the AHCAL prototype is presented in chapter 8. In the second part, the timing calibration of the AHCAL is presented in chapter 9. In a third part, the cross-check of the time calibration and the validation of the simulation is shown in chapter 10. Finally, the analysis of the recorded pion data is described in chapter 11.

This chapter discusses the setup of the testbeam first before presenting the selected dataset for this analysis, the selection of the triggers needed for this analysis as time reference and the selection criteria for each dataset of muons, electrons and pions.

The key results presented in this thesis are being approved by the CALICE Collaboration and are soon to be published as *CALICE Analysis Note 061: Timing of hadron showers in the CALICE Analog Hadronic Calorimeter prototype using steel absorber* (CAN-061) [142]. The analysis in this thesis is the first of its kind to such a system level and enters new territories for high granular calorimeters.

7.1 Testbeam Configuration

7.1.1 Beamline Setup

During the summer of 2015, the CALICE collaboration performed several testbeam campaigns with the AHCAL technological prototype. The detector was installed in the beamline H2 in the SPS North Area at CERN [135]. This beamline is equipped with wire chambers and scintillators that provide information on the beam position and number of particles. The wire chamber information would have been useful in order to simulate correctly the beam profile. Unfortunately, this information could not be recorded with the AHCAL data acquisition system. The information available about the amount of material upstream of the detector until the last momentum selection magnet is limited thus the simulation of the beamline is simplified.

A Cherenkov detector (at around 100 m upstream) was available to tag incoming particles. These detectors take advantage of the fact that, a particle that traverses a medium faster than the speed of light in that

medium will generate a cone of Cherenkov light. The opening angle of the cone is proportional to the particle mass [143]. The Cherenkov detector at this beamline offered the possibility to set a threshold for particle tagging. This is particularly needed to tag possible contaminating electrons in a pion beam. The tagging signal from the Cherenkov detector was provided directly to several AHCAL channels.

For the production of particles, a primary high-intensity proton beam (around 10^{12} protons per burst) of 400 GeV impinges on a target. From this, a secondary beam is produced containing various particle types and energies.

A muon beam can be obtained from the decay of a collimated pion beam which is stopped by a collimator before the last bending magnet.

For electrons, a neutral beam of photons is directed to a lead target to generate electrons from gamma conversion, producing a very pure electron beam. Another possibility is to impinge a charged beam onto a secondary target and filter the beam with an absorber. But this has the disadvantage of low rates at low energy and possible contamination of the electron beam with pions [135].

For pions, the momentum is selected via a set of collimators and magnets. Due to the decay of π_0 (conversion of the photons into the absorber filter) and the acceptance of the beamline, a contamination of the pion beam with electrons is possible at low momentum (< 20 GeV).

7.1.2 Testbeam Setup

In July 2015, the AHCAL detector was using the full EUDET steel stack [144] with 48 iron absorber plates. In the stack, 14 active modules were installed. The two first modules consist of single ECAL Base Units (EBUs) with 4×36 cells of 4.5×0.5 cm² size (ECAL). The ECAL cells of both modules are oriented parallel to the x-axis. The next eight modules consist of single HCAL Base Units (HBUs) with 12×12 cells of 3×3 cm² size (HCAL). The first 10 modules correspond to a depth of around $10 X_0$ ($\sim 1 \lambda_\pi$). These modules are mainly used as a shower start finder. The last four modules consist of 2 by 2 HBUs providing information about the development of pion showers at different depths. The detector was placed on a movable stage in order to be able to move the detector position relative to the beam for muon calibration runs. A simplified view of the beamline configuration is shown in figure 7.1.

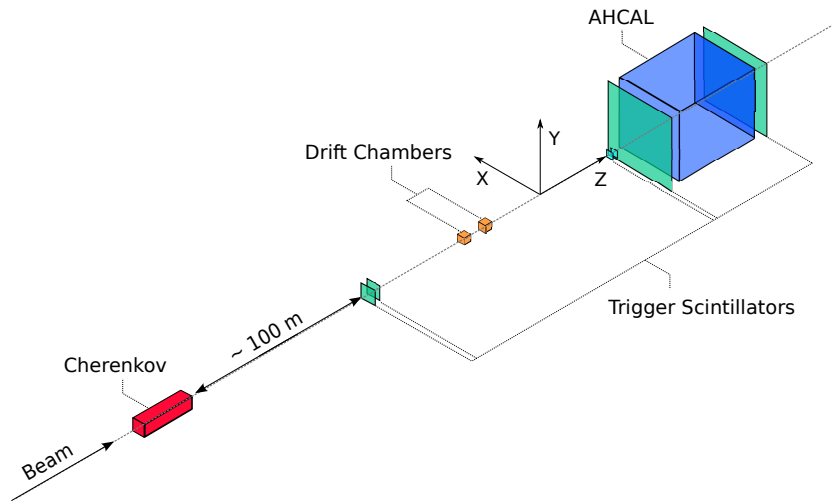


Figure 7.1 – Sketch view of the beamline setup at the CERN SPS H2 beamline in July 2015.

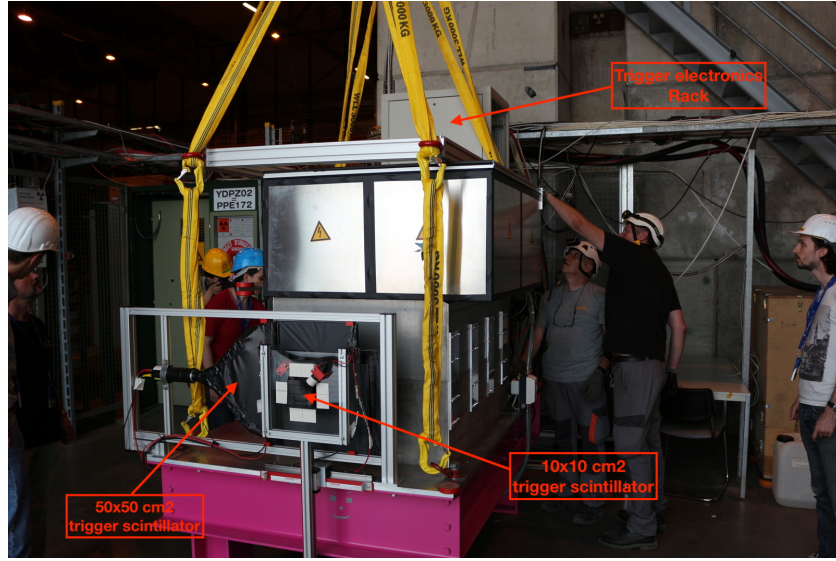


Figure 7.2 – Photo of the AHCAL detector during the installation in the testbeam area.

The beam instrumentation consisted of two $10 \times 10 \text{ cm}^2$ scintillator plates in front of the calorimeter, and two $50 \times 50 \text{ cm}^2$ scintillator plates, one placed in front of the calorimeter and one placed at the back of the calorimeter as shown in figure 7.2. They are read-out by photomultiplier tubes. The coincidence of the $50 \times 50 \text{ cm}^2$ scintillator plates was used for the muon runs and the coincidence of the $10 \times 10 \text{ cm}^2$ scintillator plates is used for the electron and pion runs as a trigger signal.

Additionally, the coincidence signal from the scintillator was provided directly to several channels of the AHCAL in order to provide a reference time information of the trigger which is important for the timing study presented in this thesis. A simplified view of the layer structure of the AHCAL is shown in figure 7.3.

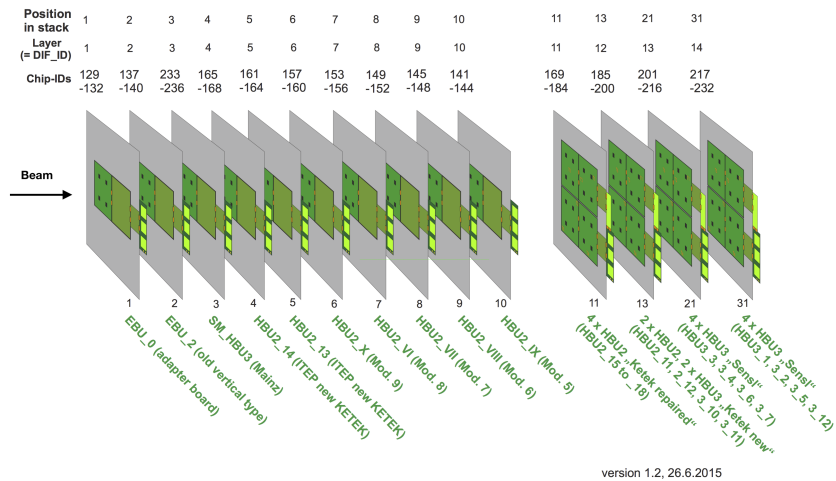


Figure 7.3 – Simplified view of the detector layout used in July 2015.

7.1.3 Time reference

The scintillator plates were used as a time reference signal. Both types of scintillator are connected to a discriminator and a gate for coincidence in order to provide a validation signal to the readout chip (see section 4.4.3.2).

When a coincidence happens, a signal of $4\ \mu\text{s}$ length with a fast rising edge of around 1 ns, is generated with an amplitude of around 100 mV that is used as a time reference. This signal is provided *directly to six AHCAL channels* for redundancy. The list of the AHCAL channels used as a reference time is shown in table 7.1. No other external time reference was available.

Table 7.1 – List of AHCAL channels used as time reference for this analysis.

Layer #	Chip Number	Channel	Comments	Name
11	169	29	noisy	T ₁₁
11	177	23	broken	-
12	185	29	-	T ₁₂
13	201	29	-	T ₁₃
13	211	6	broken	-
14	217	23	-	T ₁₄

In the following analysis, the time reference signals T₁₂, T₁₃ and T₁₄ are used. The channels are determined to be noisy or broken by looking at the energy spectra of these channels. Broken channels result in an empty energy spectrum and noisy channels are showing two energy peaks, one near the pedestal and another at the expected energy value. The channel T₁₁ is not used as it presented a very low efficiency due to noise.

7.2 Dataset and Event Selection

The selections presented in this section are based on simulated data. Beforehand, the simulation has been carefully validated and represents within 10-20% the data in muon and electron beam. More details can be seen in section 8.3.

7.2.1 Dataset

During the campaign at the CERN SPS facility in July 2015, firstly, muon runs were taken at beam energies of 50 GeV and 150 GeV for calibrating the detector. Secondly, several electron runs were taken at beam energies between 10 GeV and 50 GeV to study the electromagnetic response of the calorimeter. Finally, the pion runs were taken at beam energies between 10 GeV and 90 GeV.

The table 7.2 sums up the datasets taken in different beams. The number of events shown in the table is the total number of recorded events including single noise hit events.

Table 7.2 – List of runs taken at SPS in July 2015. The number of event specified in the table are including single noise hit events.

Particle	Energy	Runs	# Events
μ^-	50 GeV	24016-24204	120,887,651
	150 GeV	24623-24662	15,534,328
e^-	10 GeV	24531-24576	38,028,438
	15 GeV	24507-24527	7,701,325
	20 GeV	24479-24504	10,498,554
	30 GeV	24454-24475	3,382,943
	40 GeV	24420-24448	2,665,843
	50 GeV	24404-24419	5,933,995
π^-	10 GeV	24266-24272, 24300-24317, 24381-24397	24,311,420
	20 GeV	24398-24400	N/A ¹
	30 GeV	24259-24299, 24319-24380	10,120,753
	50 GeV	24212-24254, 24325-24357, 24580-24612	10,704,661
	70 GeV	24219-24242, 24365-24374	8,885,407
	90 GeV	24233-24287, 24331-24364	7,955,604

7.2.2 Muon selection

7.2.2.1 Pre-selection

A clean selection of MIP-like particles is needed in order to obtain and cross-check the energy scale calibration of the AHCAL (see chapter 8) and as well performing the timing calibration of the detector (see chapter 9) at a single cell level. A simple pre-selection was performed on the muon dataset designed to select MIP-like particles going through the AHCAL. In a second step, a track selection was performed to retain only MIP-like particle as explained in section 7.2.2.2.

The pre-selection is based on the energy weighted center of gravity along the beam axis $cog_Z = \frac{\sum_i E_i z_i}{\sum_i E_i}$ and the number of hits n_{Hits} . A MIP-like particle should, in principle, deposit the same energy in each layer of the calorimeter thus cog_Z should be roughly centered in the calorimeter in the z coordinate. In addition, the number of hits should be around 1 per layer for a MIP-like particle plus the number of noise hits expected in the detector, therefore explaining a cut at $n_{Hits} = 20$.

The distribution in the plane $cog_Z:n_{Hits}$ shown in figure 7.4 is obtained from simulated 150 GeV muons, electrons and pions. The applied pre-selection is represented by the black box. The pre-selection removes few muon events, as well as it discards electrons greatly and rejects also a large fraction of pions. The pre-selection efficiency is 99.4% for muons, 0% for electrons and 13.3% for pions.

7.2.2.2 Selection

By looking at the spectrum of the number of hits per event, it is estimated that around 30% of the events in the muon runs are contaminated by pions.

¹Not analysed due to limited dataset.

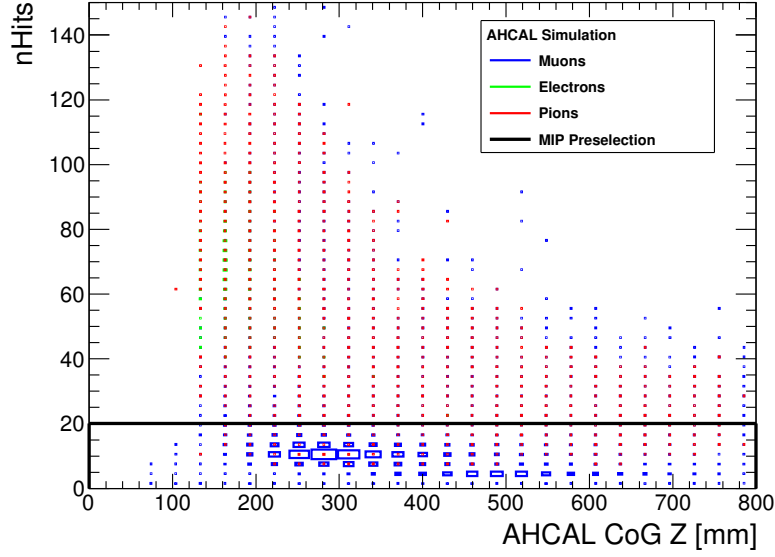


Figure 7.4 – Event distribution in $cogZ : n_{Hits}$ plane. The size of each box represents the number of events in each bin. The black box represents the space-phase covered by the pre-selection.

The MIP selection was designed to efficiently select muons and reject late pion showers. For this, a MIP track finder has been developed based on previous work [137]. This algorithm is designed to select MIP-like particle tracks in the AHCAL detector and remove pion showers.

The algorithm selects AHCAL towers of hits in the same $x : y$ position and it rejects AHCAL towers that contain less than a certain number of hits. In order to select muons or punch-through pions, a straight track of at least 7 hits is required in the whole AHCAL. This assumes that the calorimeter was perfectly perpendicular to the beam, therefore any tilted tracks would be missed. In addition, to reject late pion showers, no more than 2 hits are allowed per layer to account for some flexibility with noise hits.

The distributions of the maximum number of hits in a layer and the number of hits of a track are shown in figures 7.5a and 7.5b for simulated samples of 150 GeV muons, electrons and pions after pre-selection. The MIP track finder was performed in two steps for the inner part of the detector of 12×12 tiles and the outer part for the big modules (modules 11 to 14, Outer BL) in order to calibrate the outer channels of these modules. The figure 7.5a shows that a cut of two hits per layer is optimal in order to reject pions without affecting muons too much.

The selection efficiency is 72.5% for muons. This selection results in a contamination of 0% for electrons and 5.6% for pions. The selection reduces further the pion contamination and the remaining pion fraction is compatible with the fraction of pions traversing the AHCAL without hard interaction. An overview of the MIP selection cuts is given in table A.1.

7.2.3 Electron Selection

The electron selection is done to extract single electron showers contained in the AHCAL. These events are needed to validate the timing behavior in simulation as well as the detector simulation model as explained in chapter 10. It is important to have a clean sample of electrons to cross-check the timing calibration. For

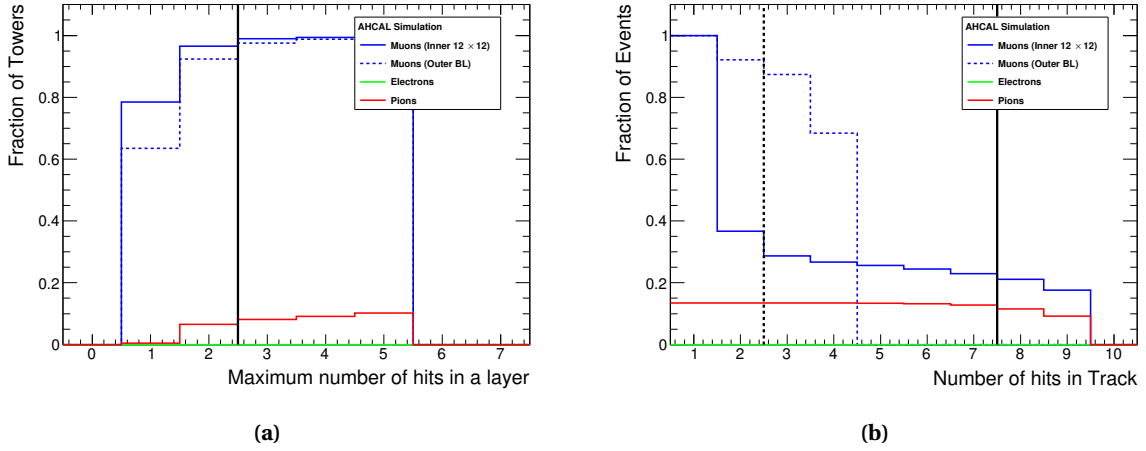


Figure 7.5 – a) Distribution of number of hits in a layer normalized to the number of events for simulated muons at 150 GeV, electrons and pions at 50 GeV. The black line represents the cut of the maximum allowed number of hits in a layer applied for the MIP selection. b) Distribution of the number of hits in a track normalized to the number of events for simulated muons at 150 GeV, electrons and pions at 50 GeV. A AHCAL tower size cut of 7 hits for the inner 12×12 tiles and a AHCAL tower size of 2 hits for the modules 11 to 14 on the outer tiles (Outer BL) were chosen.

the selection, an *Event Quality* pre-selection is done using the beam instrumentation and layer information. Events with a Cherenkov tag (only applied to data) are used. The distributions of the energy deposit in the first three AHCAL layers ($E_3 + E_4 + E_5$) are shown in figures 7.6a and 7.6b for simulated muon, electron and pion beams. In order to suppress muons and pions, $E_3 + E_4 + E_5$ must be over 10 MIPs.

In a next step, the electron selection is performed. Usually, one could use a shower start algorithm to select electrons that interact in the first layers of the calorimeter and reject pions efficiently [137]. However, the first ECAL modules (see section 4.3.2) can't be used because of high noise and the detector is partially equipped with active layers. This would greatly influence the performance of such algorithm, therefore, an alternative selection is needed.

A cut on the number of hits per event (n_{Hits}) versus the center of gravity in z (CoG_Z) is done. It is shown in figures 7.6c and 7.6d. The box cut in the figures does not induce any bias for the timing study in this thesis, it would only reduce the event statistics. In addition, the number of hits in an electron shower is proportional to the shower energy, thus this cut is energy dependent.

Finally, a cut on the energy deposited in the last two layers relative to the energy deposited in the calorimeter ($(E_{13} + E_{14})/(\Sigma E)$) is done. The distributions are shown in figures 7.6e and 7.6f. This cut is required to be under 1% to reject pion showers and to contain the electron shower.

Additionally, to reduce transverse leakage, the shower center of gravity in X and Y needs to be within -90 mm and 90 mm. This cut is wider than the trigger scintillator but has no significant impact. The selection efficiencies for muon, electron and pion beams are shown in table 7.3 for different beam energies from 10 GeV to 50 GeV. The detailed selection cuts are summarized in appendix table A.2.

One can notice from table 7.3 that a significant fraction of pions is present at low beam energies (10 to 20 GeV). But as explained in section 7.1.1 for the production of electrons, it is with confidence that there is no pion contamination in the data [145]. Thus no additional cut is needed.

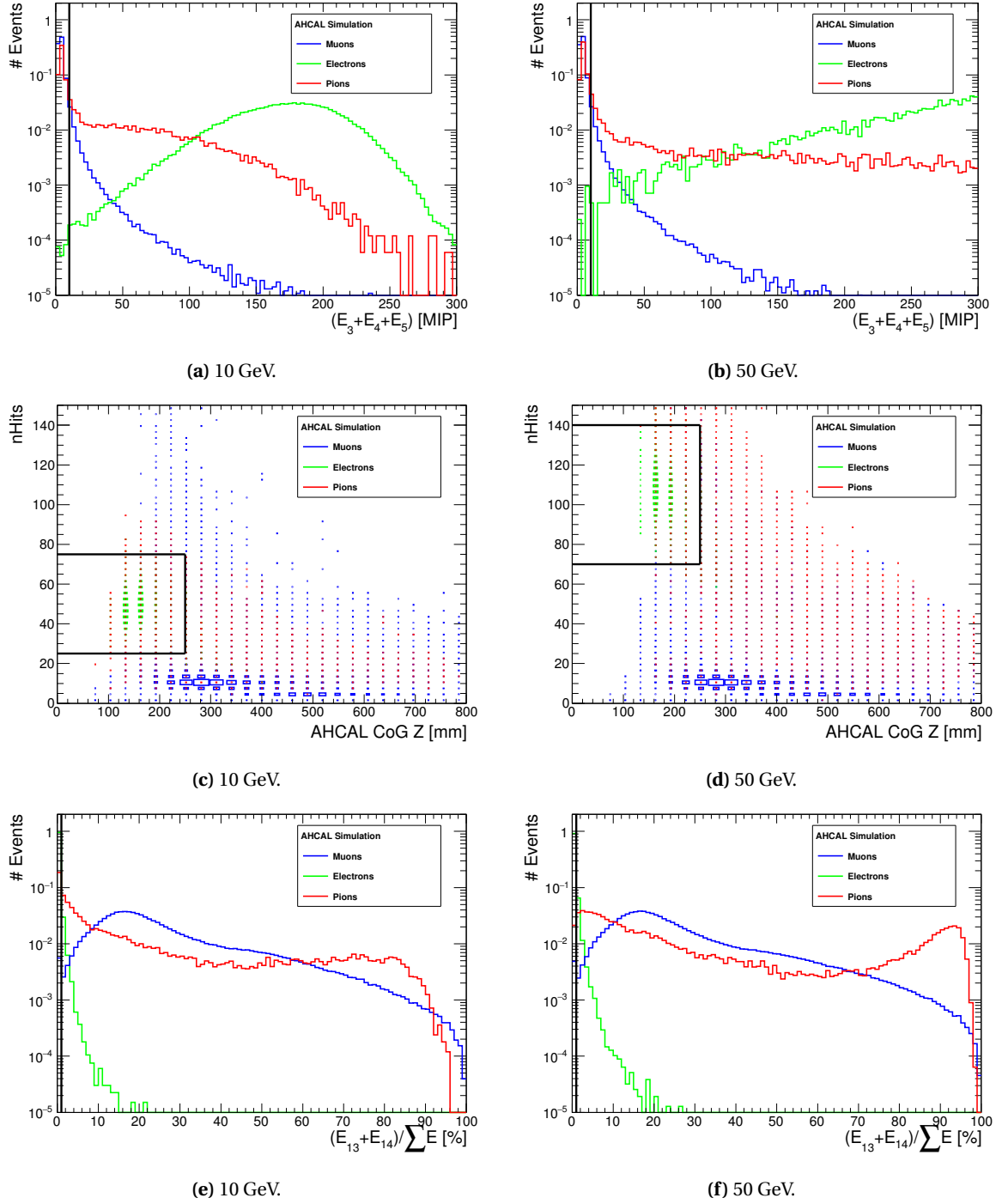


Figure 7.6 – Distribution of the variables used in the electron selection of simulated electron and pion beams between 10 and 50 GeV. The muons are simulated at 150 GeV. These plots were used to determine the best selection criteria for electrons.

Table 7.3 – Efficiency of the electron selection for simulated electrons, muons and pions for energies between 10 and 50 GeV. The efficiency is defined as the number of events after selection divided by the number of events before selection. It is estimated from Monte-Carlo and does not included the Cherenkov efficiency.

Beam Energy	ϵ_μ	ϵ_e	ϵ_π
10 GeV	<0.1%	96%	15.9%
15 GeV	<0.1%	95.7%	10.1%
20 GeV	<0.1%	95.2%	6.3%
30 GeV	<0.1%	93.9%	2.3%
40 GeV	<0.1%	92.7%	1.2%
50 GeV	<0.1%	91.5%	1.1%

7.2.4 Pion Selection

The goal of the pion selection is to reject punch-through pions, muons and possible electron contamination as these events would be instantaneous (see section 3.1.3.3). An *Event Quality* pre-selection is performed using the Cherenkov information. The events without a Cherenkov tag are selected. This is only applied to data. The pion selection is based on the same variables as the electron selection: $cog_Z : n_{Hits}$ plane, $(E_{13} + E_{14})/\Sigma E$ and additionally the number of hits in two first AHCAL layers ($N_3 + N_4$).

Firstly, the distribution of events in the $cog_Z : n_{Hits}$ plane is shown in figures 7.8c and 7.8d for muon, electron and pion beam energies for 10 GeV to 90 GeV. The number of hits required per event needs to be over 20 to reject most muons or punch-through pions without cutting on the center of gravity in z in order not to bias the start of the pion shower.

Secondly, the distributions of the energy fraction deposited in the two last AHCAL layers are shown in figures 7.8e and 7.8f. This variable must be over 1% in order to ensure that pion showered and reject electrons. Finally, the distributions of the number of hits in the two first AHCAL layers is shown in figure 7.8a and 7.8b. The number of hits in the two first AHCAL layers must be under 5 to mitigate possible particle contamination from electrons.

The selection efficiencies for muon, electron and pions beams for different beam energies between 10 and 90 GeV are shown in table 7.4. At 10 GeV, one can observe a low pion selection efficiency that is due to the fact less energy is deposited in the last two layers of the AHCAL thus reducing the number of selected pion events.

Table 7.4 – Efficiency of the pion selection for beam energies between 10 and 90 GeV. The efficiency is defined as the number of events after selection divided by the number of events before selection. It is estimated from Monte-Carlo and does not included the Cherenkov efficiency.

Beam Energy	ϵ_μ	ϵ_e	ϵ_π
10 GeV	<0.1%	<0.1%	29.9%
30 GeV	0.9%	<0.1%	50.3%
50 GeV	0.9%	<0.1%	51.1%
70 GeV	0.9%	<0.1%	51%
90 GeV	0.9%	<0.1%	50.2%

In addition, multiple particle events were observed in the data as shown in figure 7.7. As no beam instrumentation could be used for rejecting these events, a rejection method based on the hit time information was developed.

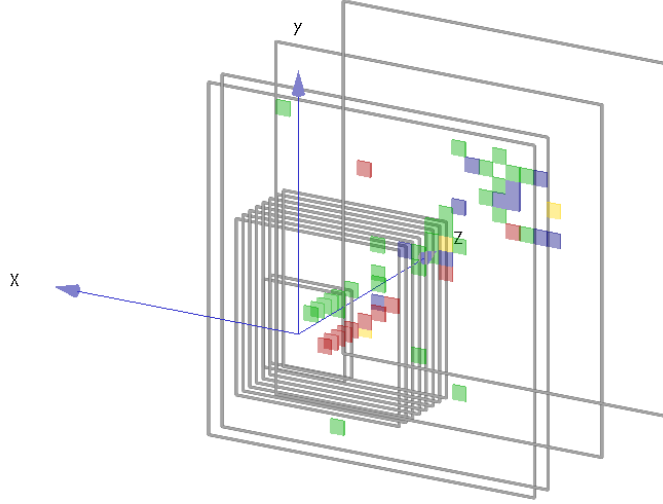


Figure 7.7 – Multi-particle event in the 50 GeV pion data sample. The colors represent the time of the hit: green < 5 ns, blue 5 ns to 15 ns, yellow 15 ns to 35, orange 35 ns to 50 ns and red > 50 ns. One can observe an additional late muon going through the detector.

The method is the following: all the hits in an event are placed and ordered in time; Then for each hit after 50 ns, a timing window of 30 ns is used. The number of hits in that window are counted. If the number of hits is larger than 5, it is classified as a *late cluster*. The event is rejected if there is at least one late cluster. This method works because if an event has several particles, the time reference of the event is generated by the first particle. Therefore, the second particle will have all the hits late relative to the time reference and thus the event will be rejected.

The method is based on data in order to remove multi-particle events. The multi-particle event rejection has been checked on simulated data and affects the selection between <0.1% up to 2% from 10 to 90 GeV pions. These multi-particle events are greatly suppressed in data. The number of events removed varies between 0.1% and 1% depending on the beam energy. Due to the calorimeter not being fully equipped thus providing limited information, some contamination may remain in the data.

A detailed description of the selection cuts is shown in appendix table A.3.

7.2.5 Rejection of outlier chips and noisy/dead channels

A careful check of the hit time distribution (see chapter 9) for each chip has been performed to reject any outlier. For all the data collected, the module 11 is rejected due to a likely problem with the electronics (see section 9.3). For the muon data, a single chip (157) shows a strange behavior likely because the input DAC on this chip is broken resulting in an unstable voltage applied to the SiPM.

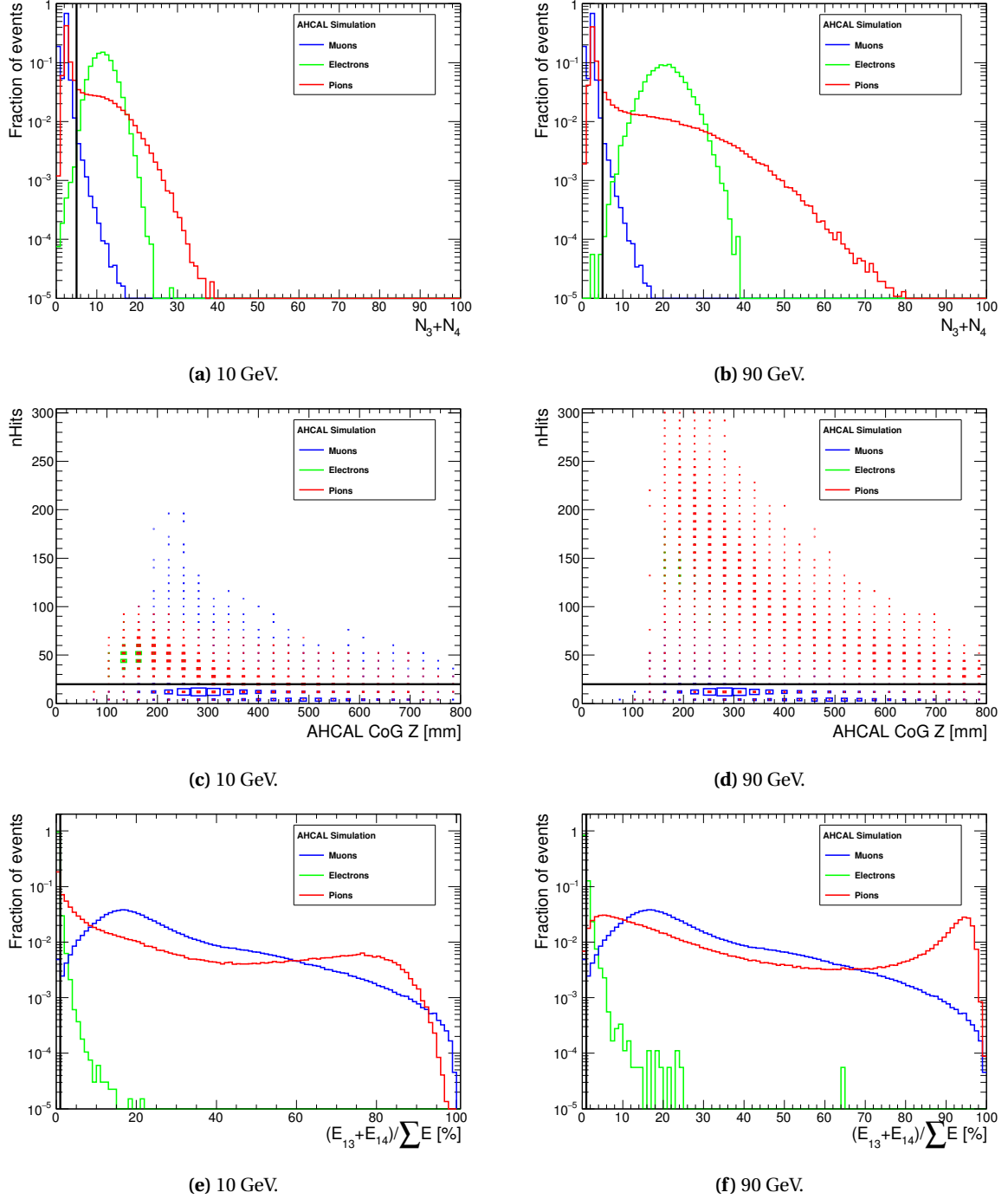


Figure 7.8 – Distribution of the variables used in the pion selection for simulated muon, electron and pion beams between 10 and 90 GeV. These plots were used to determine the best selection criteria for pions.

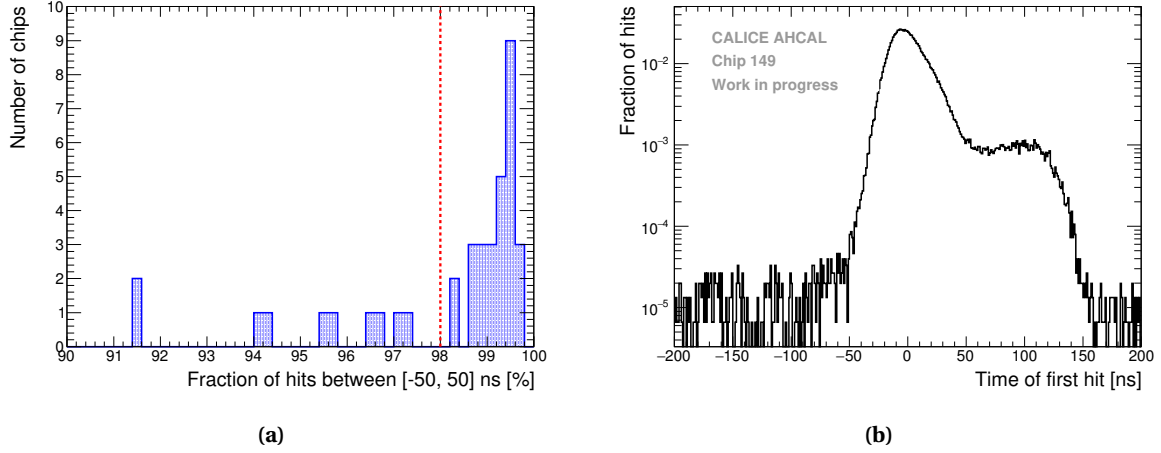


Figure 7.9 – a) Distribution of the variable R_{chip} for 50 GeV electrons for all chips. Each entry corresponds to a chip. The red line represent the cut applied to reject bad chips. b) Example of a typical bad chip that is rejected with this method (Chip 149).

For the electron data, the variable R_{chip} was used to determine bad behaving chips and it is calculated as

$$R_{chip} = \frac{1}{N_{total}} |N_{50ns}^{200ns} - N_{-200ns}^{50ns}| \quad (7.1)$$

where N_{total} is the total number of entries, N_{50ns}^{200ns} is the number of entries between 50 ns and 200 ns and N_{-200ns}^{50ns} is the number of entries between -200 ns and 50 ns. The variable is minimum when most of the hits in the chip are outside of the core of the time distribution between -50 and 50 ns. If R is below 98%, the chip is rejected. With this method, 20 chips are rejected.

For the pion data, applying the same method as for electrons is not possible due to a late tail to higher time related to delayed energy depositions from neutrons. The same chips as for electrons were rejected but in addition, each chip time distribution after correction was manually checked. The chips that presented an abnormal shape such as double peaks were discarded. Hence, 16 chips are additionally rejected. This leaves 44 chips in the pion analysis. A detailed table of the rejected chips can be seen in appendix G.

For this analysis, noisy and dead channels, as well as channels where any calibration value could not be determined was rejected (see appendix H).

The datasets used for this thesis, the selection criteria for each beam type have been presented. MIP-like particles can be selected efficiently at more than 70%. The electron selection has an efficiency of more than 90% at all electron beam energies. The pion selection selects pions with an efficiency over 50% for all pion energies except for 10 GeV where the selection efficiency is around 30%. Multi-particle events in the pion data is observed. A method using the hit time information is used to mitigate these events. Up to 1% of events can be removed. To be able to do a meaningful comparison of the data to simulations, accurate data calibration factors and a realistic AHCAL simulation model are essential. In the next chapter, the energy scale calibration of the AHCAL prototype and the validation of the AHCAL simulation model is presented.

Chapter 8

Energy Scale Calibration of the AHCAL

The AHCAL was installed at the SPS CERN facilities in July 2015 in order to provide energy and time measurements of electromagnetic and hadronic showers. The data recorded in each cell of the calorimeter is measured in ADC counts. Channel-to-channel differences in light yield and SiPM gain make difficult channel-to-channel comparisons using this scale. Therefore, all channels have to be scaled to a common physical energy unit that suppresses these differences. For the AHCAL, the Minimum Ionizing Particle or MIP unit is chosen. This unit relates to the cell energy in a well understood physical process.

The conversion requires a calibration of each cell of the calorimeter which is by itself a challenge due to the high number of readout channels. For this thesis, 3744 channels have to be calibrated. Due to the AHCAL boards (see section 7.1.2) equipped with various types of SiPMs, the procedure needs to be automatic and robust to extract the calibration constant for each channel.

In this chapter, the first section will describe the procedure for the AHCAL energy scale calibration. The second section will present the results of the energy scale calibration as well as a comparison with simulation to validate the calibration. In this thesis, only the calibration of the energy scale of the detector was performed. A dedicated analysis of the performance of the detector is being performed in parallel [145, 146].

8.1 Energy Calibration of the AHCAL

The energy deposited by a charged particle in a single AHCAL cell follows approximatively a Landau distribution (see section 3.1) but due to the electronic noise, the resulting response is convoluted with a Gaussian distribution. The maximum of the Landau-Gaussian convolution density function is defined as the MIP constant (M_i) for the i -th channel. The conversion to the MIP energy scale for a AHCAL cell is expressed as:

$$E_i = \frac{(A_i - P_i) \times IC_i}{\frac{M_i}{ICP_i}} \quad (8.1)$$

where E_i is the calibrated amplitude in MIP, A_i is the measured amplitude in ADC, P_i is the pedestal in ADC, ICP_i is the intercalibration factor between calibration and physics mode specific to the layers 4 and 5 (see section 6.2.3), IC_i is the intercalibration factor between High/Low gain (see section 4.4.3.2) and M_i is the MIP constant of the i -th channel in $\frac{ADC}{MIP}$. SiPMs have a finite number of pixel thus their signal saturates for a high number of scintillation photons. One can correct the hit energy for the saturation effect with the

following formula:

$$E_i = \frac{f_{unsat}^i((A_i - P_i) \times \frac{IC_i \times ICP_i}{G_i})}{LY_i} \quad (8.2)$$

where f_{unsat}^i is the inverse SiPM saturation function (see section 4.4.3.1) and $LY_i = \frac{M_i}{G_i}$ is the light yield of the i -th channel.

8.1.1 Pedestal extraction

The baseline or pedestal needs to be subtracted to the signal to obtain the MIP calibration constant for each channel. The pedestal value for each channel is extracted from the data taking muon runs. In order to be consistent, the pedestal value is extracted in the same running mode as the recorded data, i.e. in auto-trigger (AT) [141, 147].

The pedestal distribution of a typical AHCAL channel is shown in figure 8.1. A histogram is filled with the ADC value per readout cycle. This is only done for channels where the HitBit is not set (see section 4.4.3.2). The extraction of the pedestal value is performed in an iterative way due to a high energy tail that is not yet understood and could come from an inefficiency in the trigger threshold.

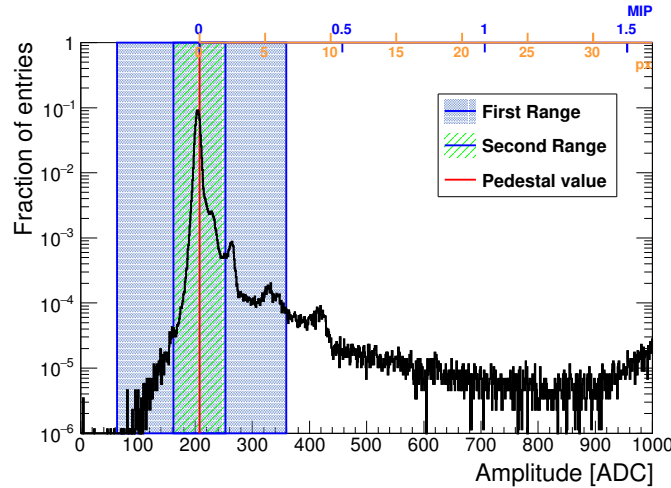


Figure 8.1 – Typical pedestal distribution of a channel in auto-trigger mode. The different colored boxed represent the iterative procedure to extract the pedestal value marked with the red line. The upper x-axis shows the corresponding ADC value in terms of MIP and pixels.

The SiPM noise contributes to the pedestal value as shown by the additional peaks next to the main peak in the figure 8.1. Considering a Poisson statistic, one to three pixels could be fired due to the dark noise and cross-talk. The range to determine the pedestal value then needs to be in the same order of magnitude. For this, the histogram x-axis range is reduced in the range of 3 RMS around the mean. It is done iteratively two times. Then the mean of the histogram is taken as the pedestal value. This is done for each channel and memory-cell.

However, the CALICE database structure, containing the main calibration constants, is currently designed to store the pedestal constant for each channel only (not memory-cell). Therefore, a mean over all memory cells is computed per channel and used in the data reconstruction. The difference between the mean pedestal

and the memory cell wise pedestal is shown in figure 8.2. The RMS of the distribution is around 21 ADC which corresponds to an uncertainty of about 4% on the MIP constant, assuming a typical MIP calibration value of 500 ADC. This error is dominating in the MIP constant uncertainty.

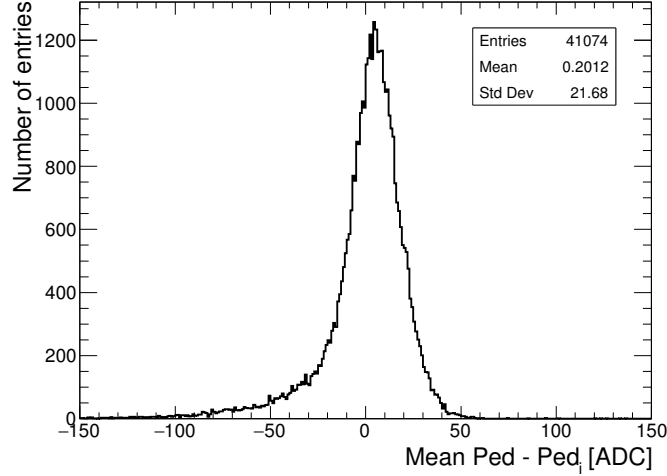


Figure 8.2 – Distribution of the difference between the mean pedestal to the memory-cell wise pedestal per channel.

8.1.2 MIP extraction

After the pedestal calibration, the extraction of the MIP calibration constant for each channel can be performed. As the detector was equipped with various types of SiPM and boards designs, the extraction procedure needs to be automatic and robust. In order to reduce the number of noise hits in the hit energy spectra of each cell that would lead to unstable fits and wrong MIP calibration constants, a MIP track selection has been performed (see section 7.2.2.2).

The fitting procedure is very sensitive to the initial parameters of the fit and can be quite difficult with the variety of SiPM and tiles in the AHCAL. To ensure a good fit, an iterative fitting procedure is performed. A more precise and detailed description of the fitting procedure can be found in [147, 148].

Only channels with more than 1000 entries are considered to obtain a reliable fit. The parameters in the fit are: the area of the hit energy distribution, the width of the convoluted Gaussian, the most probable value (MPV) of the Landau distribution and the width of the Landau distribution. The spectrum of the hit energy is fitted with a Landau-Gaussian convolution function for each channel and the maximum of this convoluted function is taken as the MIP constant. A typical example of a single channel fit can be seen in figure 8.3. The fit result has been verified channel-by-channel for all the channels of the detector.

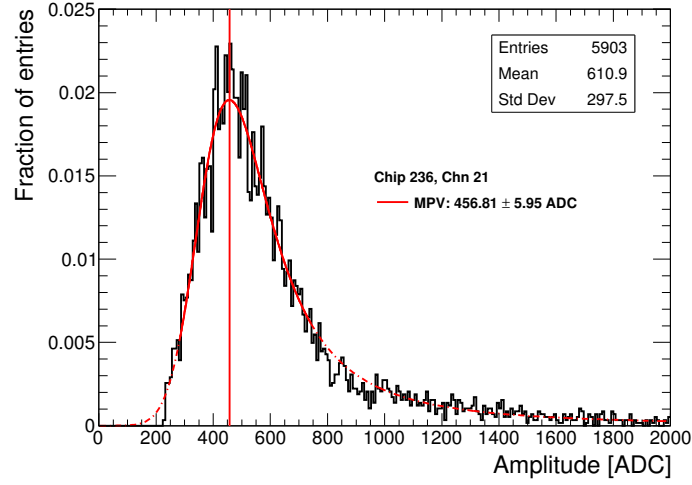


Figure 8.3 – Typical energy distribution in a single channel of the AHCAL with the data collected in July 2015 at CERN. The convoluted function is represented in red with the extracted MIP constant for this channel showed by the vertical red line.

8.2 Results of the energy scale calibration

8.2.1 MIP extraction results

In the muon data recorded in July 2015, the MIP calibration constant of 72% of the 3744 channels is determined. The remaining 28% of the channels do not provide enough or usable information to perform a fit, this includes the outer channels (outside of the inner 12×12 tiles) of the layers 11 to 14 that don't have enough statistics. In order to have a MIP calibration value for these outer channels, the results are combined with MIP calibration values obtained from previous testbeams performed in April and May 2015 at DESY with the layers 11 to 14.

Additionally, if a channel does not have a MIP calibration value, the mean of the MIP constant distribution of a chip or a layer is used. 85% of the detector channels (3171 channels) have been calibrated, excluding dead and noisy channels (see appendix H).

The results of the extracted MIP values are shown in table 8.1 and are regrouped by SiPM types. The results are well compatible with previous work [147] although there is a slight difference in the number of fitted channels that may come from the differences in the event selection and the extraction procedure.

8.2.2 Uncertainty of the calibration procedure

It is necessary to evaluate the uncertainty of the calibration procedure. The figure 8.4 shows the relative error $\frac{\Delta MIP_i}{MIP_i}$ for all the fitted channels of the detector. The relative error on the MIP calibration value, for most of the channels, is in the expected range of 1% to 3% and it is compatible with previous results [147]. However, some higher values can be seen due to the layers 1 and 2 where difficulties were met due to a high noise and low SiPM gain.

Table 8.1 – Table containing the results of the extraction of the MIP calibration constants. The results are regrouped by SiPM type. $\langle \text{MIP} \rangle$ is the mean of the MIP calibration constant distribution per SiPM type. RMS is the standard deviation of MIP calibration constant distribution per SiPM type. Dead and noisy channels are rejected.

Layer #	$\langle \text{MIP} \rangle$ [ADC]	RMS [ADC]	N_{fitted}
1-2	66.72	35.54	172
3	501.71	50.4	142
4-5	796.54	113.12	265
6-10	250.99	62.72	414
11-12	285.85	62.83	1069
13-14	307.73	58.96	1109

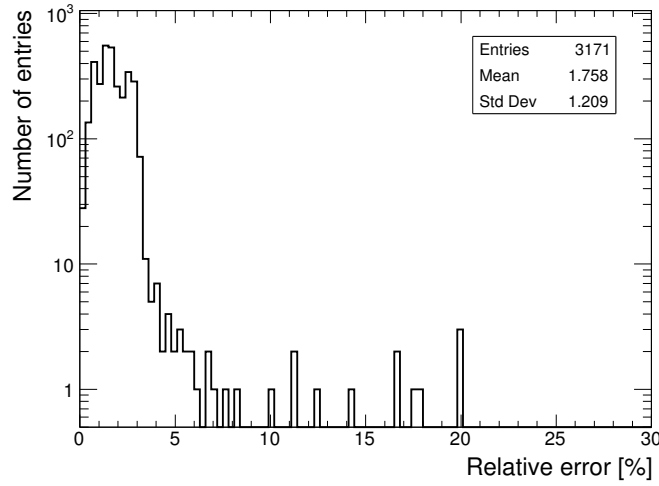


Figure 8.4 – Relative error $\frac{\Delta \text{MIP}_i}{\text{MIP}_i}$ for the 3171 detector channels in the AHCAL. The right tail comes from the layers 1 and 2 where difficulties are met for the determination of the MIP constant.

8.2.3 Systematic on the MIP scale

The MIP constant value is sensitive to temperature and temporal variations. A systematic error on the MIP energy scale can be derived by dividing the data muon sample into two sub-samples by even or odd run number. It will take into account the uncertainty on the MIP calibration but as well temperature and temporal variations. Each sub-sample is fitted using the same fitting procedure as described in section 8.1.2. The results of the MIP fit for each sub-samples are shown in figure 8.5.

The sub-samples are very similar with a shift in the mean value of less than 1%. A slight shoulder is present to higher MIP values though the mean is still very close to unity. By looking at the mean of the RMS of the distributions, a systematic uncertainty of around 3.6% on the MIP energy scale can be derived. This systematic uncertainty can then be used in the timing analysis described in the next chapters.

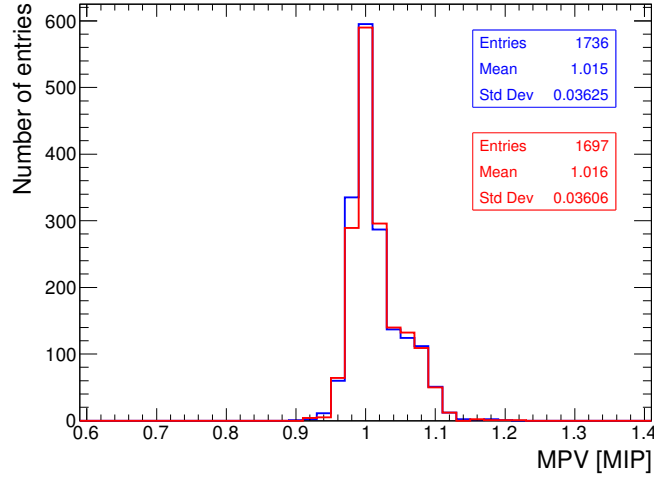


Figure 8.5 – MPV fitted value in MIP for the two muon sub-samples. Even runs are in blue, odd runs are in red.

8.3 Validation of the simulation

The MIP scale is crucial to the timing studies, that the simulation is validated in the following text in order to ensure its description of the data. This section first describes cross-checks performed to validate the cell-wise energy calibration in data and simulation. Then, the AHCAL simulation and digitization model are validated by comparing electromagnetic shower observables from data to simulation. Comparisons using electromagnetic interactions within the AHCAL are preferred as these interactions should be well described in simulations and are less subject to modeling uncertainties than hadronic showers.

8.3.1 Beam profiles

To simulate beam particles, the simulation is using the position and width of a particle gun as parameter. It has to be placed in x, y directions such that the beam sizes of the experiment are modeled. This is done to guaranty that the same cells of the detector are hit in data and simulation. Otherwise, this would result in a significant bias in the comparison of data and simulation. In the z-direction, the beam gun needs to be put as close as possible to the detector to avoid beam broadening by scattering on air molecules.

The best method to estimate the beam profile for data would be to analyze the beam profile provided by the wired chambers. Unfortunately, this data could not be added to the AHCAL data acquisition system. As a workaround, the mean and RMS of the center of gravity distributions in x and y are used to estimate the beam size instead. This does not reflect the true positions since both positions are biased by dead and noisy channels. The center of gravity is calculated as the following:

$$CoG_x[mm] = \frac{\sum_i E_i x_i}{\sum_i E_i} \quad , \quad CoG_y[mm] = \frac{\sum_i E_i y_i}{\sum_i E_i} \quad \text{and} \quad CoG_z[mm] = \frac{\sum_i E_i z_i}{\sum_i E_i} \quad (8.3)$$

where E_i is the energy of the i-th hit and x_i and y_i are the x and y position of the i-th hit.

For muon runs, a flat beam profile with a half-width of 20 cm is configured in the simulation. A perfect representation of the beam profile for muons is not expected to have an impact on the MIP response in the

simulation.

For electron runs, the distribution of the center of gravity in x and y directions are used as an estimate of the beam profile. The figure 8.6 shows the beam profiles in the x and y directions in data and simulation for 10 GeV electrons. The agreement looks good between data and simulation. This has been check for all energies. The agreement gets worse for higher electrons energies that may be due to a contamination from lower energy electrons [145]. In addition, at higher energy, the beam looks less gaussian-like and the shape in simulation can't be simulated perfectly.

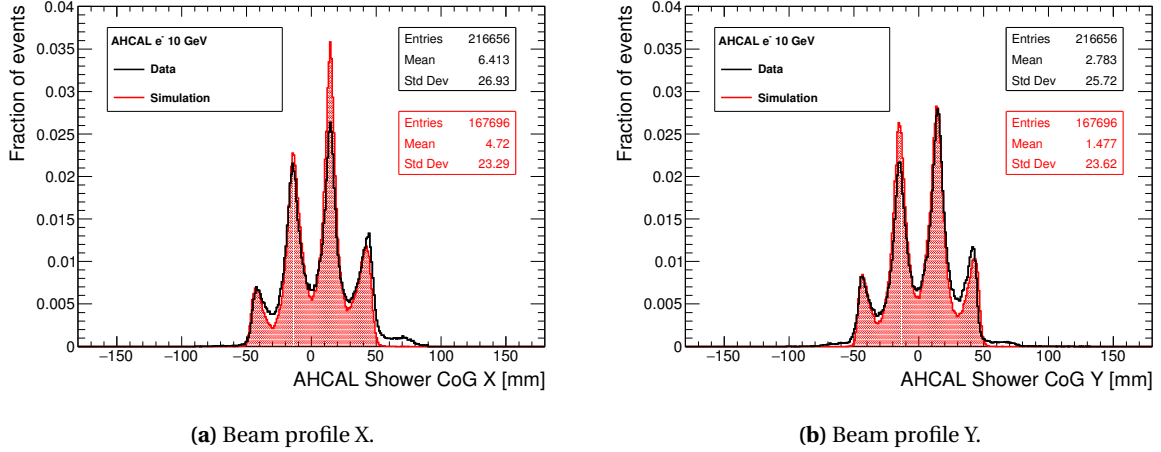


Figure 8.6 – Beam profiles for 10 GeV electrons in data and simulation. Simulated with QGSP_BERT_HP using GEANT 4 v10.1.

For pion runs, the same method as for electron runs is used. The figures 8.7 show the beam profiles in the x and y-direction in data and simulation for 10 GeV pions. The agreement looks quite good for 10 GeV, with only a slight difference that is visible in the y-direction. The beam profiles have been checked also for all energies with the same conclusion.

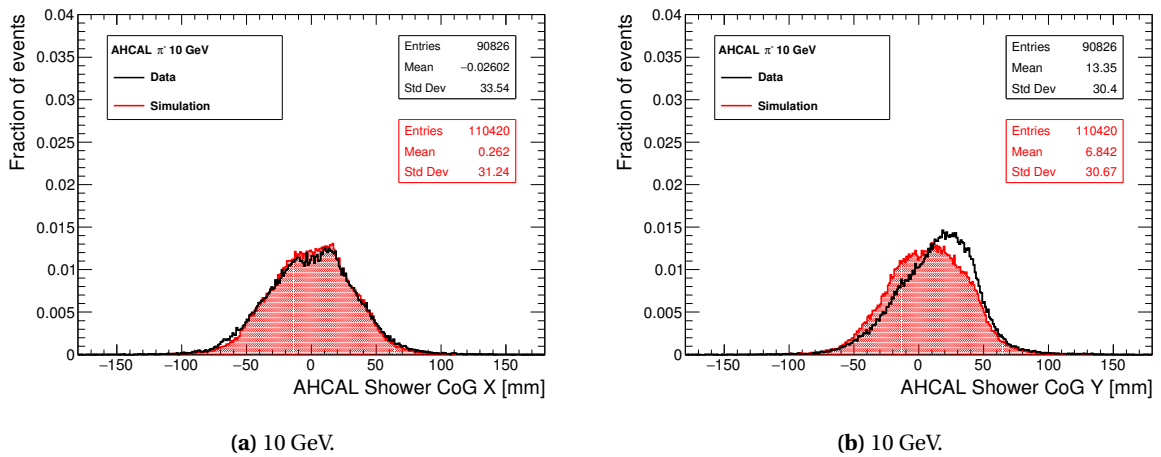


Figure 8.7 – Beam profiles for 10 GeV pions in data and simulation. Simulated with QGSP_BERT_HP using GEANT 4 v10.1

Additional beam profiles can be seen in appendix B. The particle gun configurations used to reproduce

the data runs in this thesis are shown in table 8.2.

Table 8.2 – Settings of the particle gun in simulation used to reproduce the beam profile of the data runs used in this thesis.

Type	Energy [GeV]	σ_E [GeV]	μ_x [mm]	μ_y [mm]	RMS_x [mm]	RMS_y [mm]
e^-	10	0.2	7.5	3.2	29.2	27.5
e^-	15	0.3	5.6	2.9	28.0	26.2
e^-	20	0.4	2.1	-0.3	27.0	26.1
e^-	30	0.6	-4.6	18.5	23.8	21.9
e^-	40	0.8	-2.8	11.3	24.7	25.5
e^-	50	1	-18.4	5.8	28.2	28.9
π^-	10	0.2	-0.3	14.8	34.6	29.8
π^-	30	0.6	7.7	-1.9	28.3	26.4
π^-	50	1	10.1	14.0	19.6	17.1
π^-	70	1.4	21.9	-14.5	28.8	28.6
π^-	90	1.8	3.2	2.8	23.7	23.5

8.3.2 MIP Calibration

The MIP calibration defines the energy scale of the energy depositions measured in the AHCAL. It is needed to carefully validate the MIP calibration in data and in simulation in order to be able to compare results.

Applying the MIP selection on the muon runs results in energy depositions of single MIP amplitudes for all channels. The comparison of the MIP spectrum for the whole AHCAL between data and simulation is shown in figure 8.8a. The shape of the hit energy spectrum matches relatively well. The data appears slightly wider than for simulation because of the channel-by-channel mis-calibrations that are not modeled in the simulation. Figure 8.8b shows the mean energy deposition per layer. The simulation reproduces the data within 3-4%. This comparison validates the simulation at the lowest hit energies.

The figure 8.9 shows the distribution of the extracted MIP calibration constant for single channels in data and simulation. Ideally, the distribution should peak at the unity for all channels. But in practice, due to the fitting procedure uncertainty, mis-calibrations and statistic limitation, it results in a widening of the distribution. Both data and simulation give a mean value reasonably close to unity indicating a good average calibration at the cell level of the AHCAL. The higher values to the right that appear in the data have been checked and all channels present a good fit.

8.3.3 Electrons

Electromagnetic showers are used to validate further the simulation. As the physics of electron showers are very well understood and can be simulated with great accuracy, it is used as a tool to validate the detector geometry, especially concerning the material composition as well as the general calibration. Besides noise and beam profiles, the influence of cross-talk has a significant impact due to the higher energy deposited.

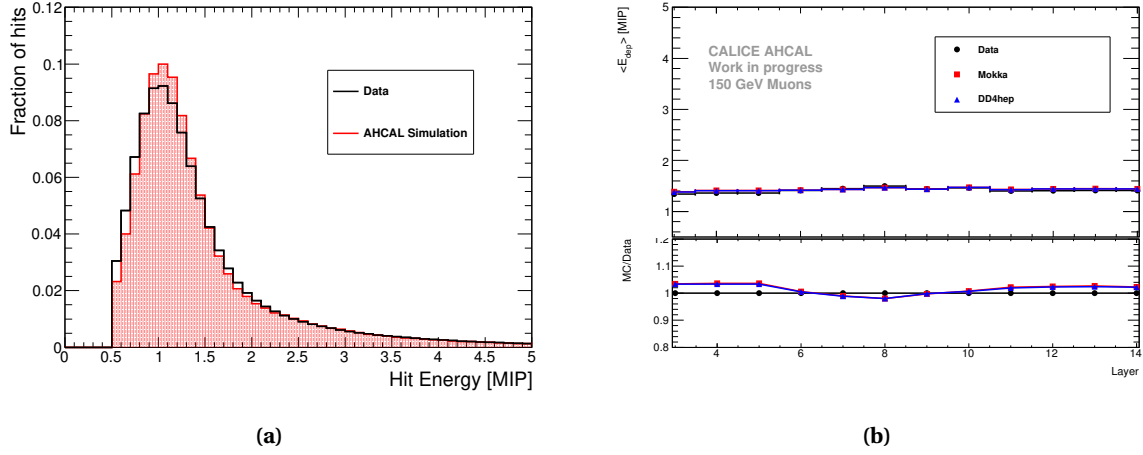


Figure 8.8 – a) Hit Energy Spectra for the complete AHCAL for muon like-track hits for both data and simulation. b) Longitudinal mean energy profile for muon like-track hits in data and simulations.

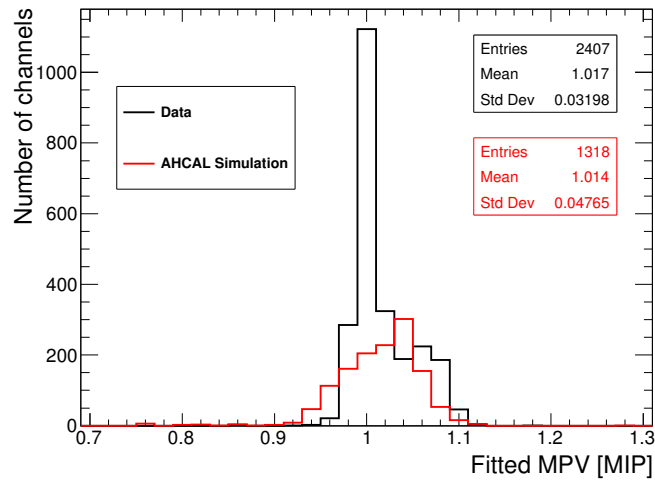


Figure 8.9 – Distribution of the fitted MIP value in single channels of the AHCAL for data and simulation.

In addition, the SiPM saturation unfolding of high energy cells is very important as generally electrons deposit in few cells all their energy. Unfortunately, no saturation curves are available and only estimations of the necessary parameters are used. However, in this thesis, the energy deposited in a single cell is only relevant at low energies (from 0.5 to few MIPs) where the response of the SiPM is linear. Therefore, the SiPM saturation unfolding is not used. Only saturation of the hit energy is performed on the simulation as hits from the data are obtained saturated.

The figure 8.10 shows the hit energy spectra for 10 GeV and 50 GeV electron showers in data and simulation. Hit energies up to 60 MIPs are described by the simulation up to 10-30%. A difference is noticeable around 20 MIPs because of overestimated intercalibration factors between high gain hits and low gain hits that shift the hit energy to slightly higher values. For 10 GeV, the simulation is underestimating the hit energy by a large factor over 60 MIPs. It is similar at higher beam energies. At 50 GeV, the region between 120 to 220 MIPs is overestimated by the simulation. The underestimation in simulation of the hit energy comes from an incorrect value of the number of effective pixels used in the saturation function (see equation 4.2) to saturate hits in the simulation. This number is too small thus saturating the simulation to lower hit energies. The description of the shape of the hit energy spectra is influenced by the formula of saturation function used [100] and the figure shows that for energies between 100 and 200 MIPs, the current function is not good enough to describe well the shape of the observed hit energy spectra in data.

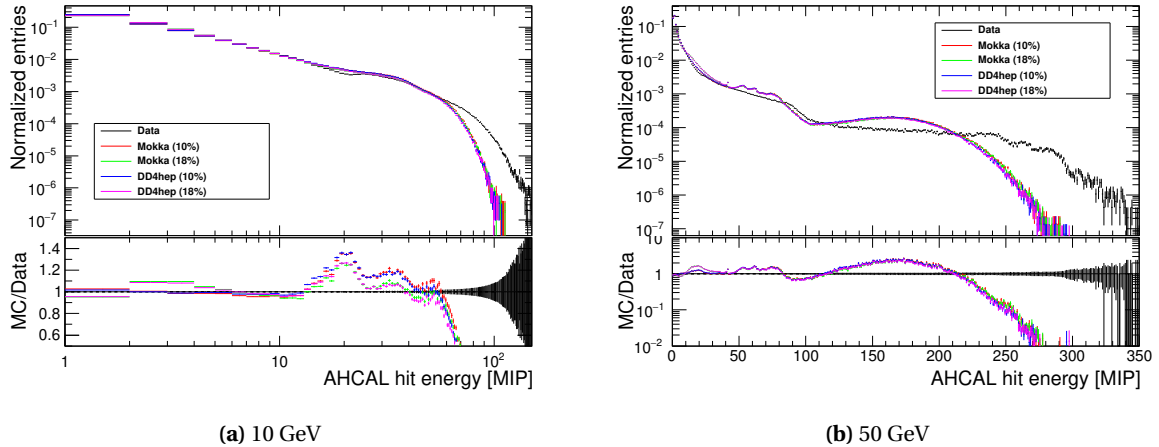


Figure 8.10 – Electron hit energy spectra for data and simulation for 10 and 50 GeV beam energies. The different colors corresponds to the variation of the cross-talk parameter in the simulations between 10% and 18%.

Figure 8.11a shows the mean energy sum $\langle E_{sum} \rangle$ and figure 8.11b shows the mean number of hits $\langle nHits \rangle$ as a function of the electron beam energy between 10 and 50 GeV in data and simulation with different cross-talk parameters. The mean is obtained from the mean of the distribution, no fit is performed. The visible energy for data agrees within the simulations for 10, 15 and 20 GeV electron energy and seems to agree better with the 10% cross-talk simulations. For higher energies, the data deviates significantly to lower values due to the presence of the long tail left of the distribution that the simulations cannot describe (see appendix B). The curve does not look linear as one would expect, this is probably due to saturation effects that are not corrected.

The number of hits is well described in the simulations but agrees better with 10% cross-talk at low ener-

gies and with the 18% cross-talk at higher energies. However, the data cannot be described for both distributions at once in either simulation with a global cross-talk parameter.

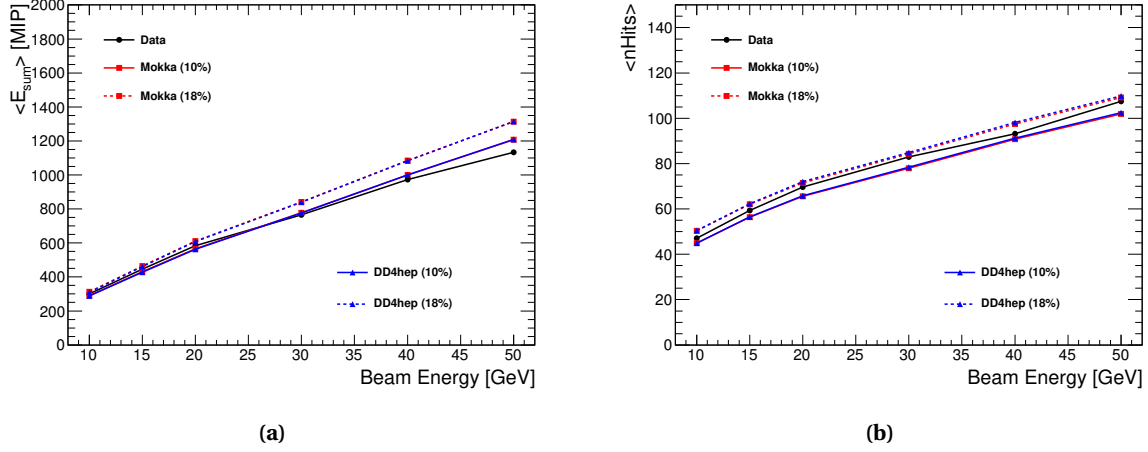


Figure 8.11 – a) Comparison of the mean energy sum in the AHCAL as function of the beam energy for electron data and simulations with different cross-talk parameters. Simulated with QGSP_BERT_HP in GEANT 4 v10.1. b) Comparison of the mean number of hits in the AHCAL as function of the beam energy for electron data and simulations with different cross-talk parameters. Simulated with QGSP_BERT_HP in GEANT 4 v10.1.

The precision of the detector simulation for electrons is limited by the cross-talk simulation. For energies above 20 GeV, the possible contamination with low energy electrons in the data limits as well the agreement between data and simulation. A deeper investigation on the energy aspect of the data is carried out in parallel of this analysis [145]. The description of electromagnetic showers in simulations is satisfactory for the study of the time development of hadron showers.

The MIP calibration procedure was explained and developed in order to accommodate to such high number of channels as well as the diversity in SiPM types and tile designs. In this way, 85% of the 3744 channels in the detector have their MIP constant determined. An error around 1-3% is made on the MIP constant value with the current fitting method which is in the order of magnitude expected due to the limited statistics. In order to validate the calibration and the simulation model, a comparison of the MIP calibrated value have been made at the single channel level. Data and simulation are in a good agreement with less than 1% deviation. The simulation appears narrower due to channel-wise mis-calibrations not being modelled. A systematic uncertainty of 3.6% on the MIP energy scale has been determined due to run-by-run, time and environmental variations.

The simulation has been validated to the lowest hit energies as well as with electromagnetic showers. The simulation reproduces the data between 10-30% which is good enough for the study presented in this thesis as interesting hits below 10 MIPs are important. Before studying the time development of hadronic showers, the time of a hit recorded in data needs to be calibrated. The timing calibration of the AHCAL prototype is presented in the next chapter.

Chapter 9

Timing Calibration of the AHCAL

9.1 Introduction

As explained in section 3.1.2, muons interact primarily via ionization. This process is instantaneous and therefore muons are a good candidate to perform the timing calibration of the AHCAL. Similarly, electrons can be used for the timing calibration and cross-checks as electromagnetic showers are quasi-instantaneous. On the contrary, the pion data cannot be used for this purpose due to delayed energy depositions in hadron showers.

The time information provided by the SPIROC in the data is in TDC units (see section 4.4.3.2). Similar to the ADC scale, it would be difficult to compare directly channels using the TDC unit. The TDC information needs to be interpreted into a common unit of time, the nanosecond. The TDC information of each channel can be converted into nanoseconds following the simple schematic shown in figure 9.1.

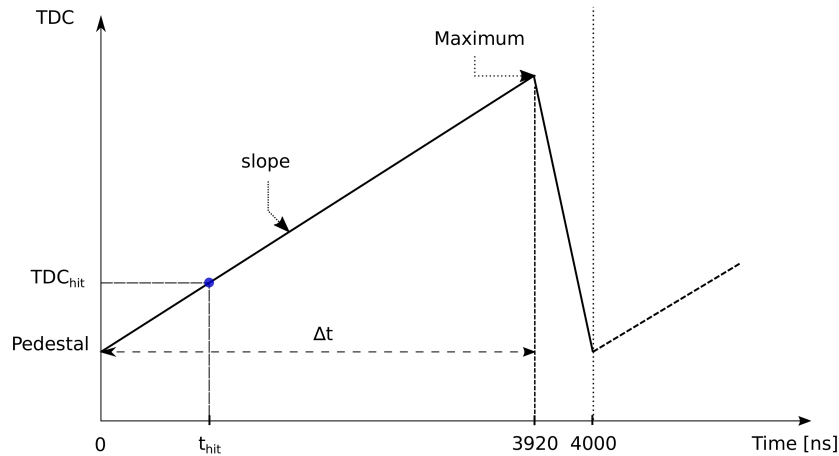


Figure 9.1 – Schematic of the TDC ramp in the SPIROC used in testbeam with a slow clock of 250 kHz. The slope of the ramp is $s = (Max - Ped)/\Delta t$. The time of the hit is then calculated as the following: $t_{Hit} = 1/s \times (TDC_{Hit} - Ped)$.

In order to determine the ramp slope, the starting point or pedestal of the ramp and the endpoint of the ramp are measured. Since the SPIROC2B has two TDC ramps, each defined by a bunch-crossing (BXID)

parity (even or odd), two slopes need to be extracted per chip. In addition, each channel can store up to 16 events called memory-cell. Each memory-cell is different thus 16 calibration values or pedestal are needed per channel. The extraction of the slope and the determination of the pedestal is explained in section 9.3.

Then the data and the time reference of the trigger can be converted into nanosecond using the determined parameters (see section 9.4). This is done in order to be able to compare them. Ideally, the time difference between the time reference and the data should be a δ peak at 0 ns. In reality, this δ peak is smeared by the time resolution introduced by the front-end electronics (see section 9.5).

Additionally, possible electronics effects can be corrected in order to improve the time resolution. For this study, two effects are corrected, the non-linearity of the TDC ramp (see section 9.6.1) and the time-walk effect (see section 9.6.2). In the following, the hit time of a channel is referred to as *the time of the first hit* because only the first hit per channel is registered during a bunch-crossing (multiple hits could occur in a channel but only the first one is kept by the SPIROC2b).

9.2 Dataset

In this chapter, the muon dataset shown in section 7.2.1 is used for the timing calibration of the AHCAL. The table 9.1 summarizes the runs and datasets used. Raw events are considered if the reference signals T_{12} , T_{13} and T_{14} are present in the event (see section 7.1.3). N_{3T_0} is the number of events after the selection on the time reference (see section 9.4) or electron selection (see section 7.2.3). $N_{sel.}$ is the number of events after the selection on the error of the time reference that is explained in section 9.4.

Table 9.1 – Table with the number of events selected for the muon and electron data for the timing calibration.

Runs	Energy	Particle Type	N_{3T_0}	$N_{sel.}$	$\frac{N_{sel.}}{N_{3T_0}}$
24016-24663	50-150 GeV	μ^-	1851536	836796	45.2%
24528-24577	10 GeV	e^-	268275	216656	80.8%
24510-24520	15 GeV	e^-	108092	90395	83.6%
24486-24504	20 GeV	e^-	130232	110161	84.6%
24460-24470	30 GeV	e^-	82202	69692	84.8%
24427-24435	40 GeV	e^-	65901	55660	84.5%
24405-24419	50 GeV	e^-	123422	104030	84.3%

9.3 Slope and pedestal calibration

To reconstruct the time of the first hit in a channel, the TDC value measured needs to be converted into nanoseconds. The slope is calculated as

$$s [\text{TDC/ns}] = \frac{b - a}{3920} \quad (9.1)$$

where s is the TDC ramp slope, b is the endpoint of the TDC ramp and a is the start point of the TDC ramp that is referred to in the following as pedestal. The total length of the ramp is 3920 ns instead of the expected value of 4000 ns due to a deadtime of around 2% [149] induced by the multiplexer that switches between the

two ramps. This deadtime is assumed to be the same for all chips. This section will describe the method used to extract the slope of the TDC ramp.

At a first order, the slope of the TDC ramp is assumed to be linear. The parameters a and b are extracted from the TDC spectrum per chip (combining all channels) and BXID parity using only the first memory-cell as shown in figure 9.2a. The TDC ramp slope does not depend on the memory-cell as the memory-cell only introduce an offset on the parameters a and b . A total of 208 slopes have to be extracted for the testbeam setup.

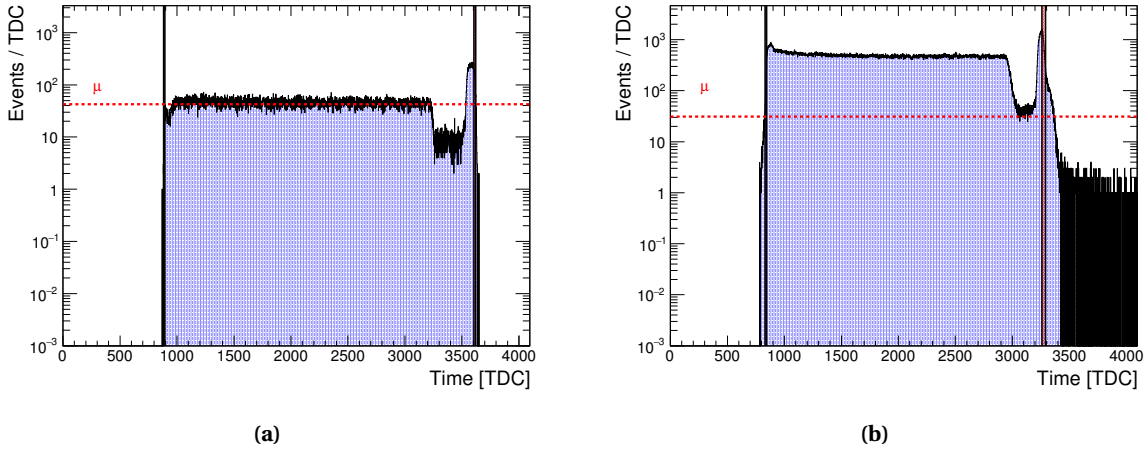


Figure 9.2 – a) TDC spectrum of a typical chip (all channels). The black lines indicate the fitted Max and Pedestal parameters for this chip. The extracted parameters are $1/s = 1.44 \pm 0.01$ ns/TDC, $a = 888 \pm 5$ TDC and $b = 3613 \pm 8$ TDC. b) TDC spectrum of a bad chip on module 11. The chip 175 on this module is presenting a long tail to high TDC values. The reason is not understood but present on all chips on that module.

The extraction of the parameters a and b is done by detecting the edges of the TDC spectrum. A threshold μ is used to extract a . This threshold corresponds to the mean of the vertical axis of the TDC spectrum. The parameter a is extracted as the value of the first bin above 30% of the threshold μ . The endpoint of the ramp is extracted as the value of the last bin above 50% of the maximum bin content of the TDC spectrum. The start point and the endpoint of the ramp are not extracted as the first and the last bin of the TDC spectrum, because the extraction technique needs to be robust against outliers and strange spectra such as the one shown in figure 9.2b.

An estimation of the uncertainties of the method has been performed. This is done to evaluate the precision of the extraction method. The uncertainty on the parameter a is done by varying the 30% threshold value by the uncertainty of μ . Similarly for the parameter b , the uncertainty is done by varying by 1/3 of the maximum bin content. More details about the estimation of the calibration uncertainties is described in the appendix E.

The extracted values for the inverse of the slope are shown in figure 9.3. They are in the expected range of 1.6 ns per TDC bin due to the limited dynamic range provided by the chip, around 2500 TDC bins for 4 μ s.

Once the ramp slope has been extracted for each chip and BXID parity, the time of a hit in the i -th channel can then be calculated as

$$t_i [\text{ns}] = 1/s \times (\text{TDC}_i - \text{Ped}) \quad (9.2)$$

where t_i is the time of the i -th channel, s is the ramp slope, TDC_i is the TDC value of the i -th channel and

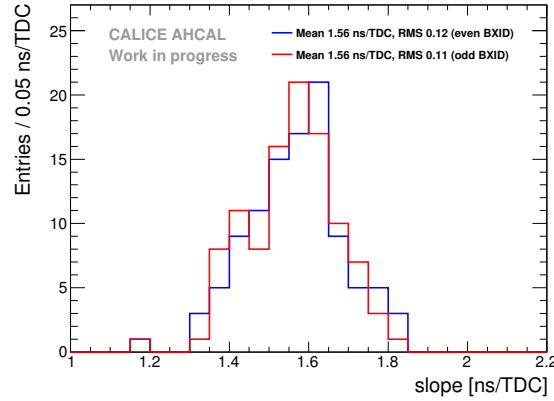


Figure 9.3 – Distribution of the inverse of the slope for even and odd bunch-crossing IDs. $\mu_{odd} = 1.564$ ns/TDC, $RMS_{odd} = 0.121$, $\mu_{even} = 1.556$ ns/TDC, $RMS_{even} = 0.113$. In total, 208 TDC slopes were extracted.

Ped is the TDC pedestal value of the i -th channel for the first memory-cell without taking into account the BXID parity that is extracted using the same method as above. In principle, one would need to perform this conversion using memory-cell-wise pedestals, however due to a limitation on the available statistics, only the first memory cell is taken into account. Any time offsets that are induced by the other memory-cells and the BXID parity are corrected in a later stage (see section 9.5).

9.4 Calibration of the time reference

To reconstruct the time of the first hit in a channel, the measured time of a hit needs to be compared to the time of a reference trigger. The channels recording the signal from the trigger scintillators (see section 7.1.3) are calibrated using the same method as described in section 9.3. With the addition that the pedestal value is extracted for all memory cells, possible due to the high statistics, to guarantee the most accurate result.

Events are selected by requiring that T_{12} , T_{13} and T_{14} are present in the event in a certain amplitude range as shown in table A.4 to reject noise hits from these channels. These channels receive the trigger coincidence signal at the same time, and therefore a timing correction is applied to ensure that they match in time. This is done to remove any effect induced by the front-end electronics.

A 2^{nd} order polynomial correction of the time of $(T_{12} - T_{14})$ and $(T_{13} - T_{14})$ as a function of T_{12} and T_{13} respectively is done. This correction is equivalent to a non-linearity correction of T_{12} and T_{13} relative to T_{14} similar to the procedure shown in section 9.6.1. In this case, T_{14} is not corrected for non-linearity. Ideally, the difference between T_{12} and T_{13} to T_{14} should be a Gaussian distribution centered at 0 ns. The figure 9.4a shows the difference $(T_{12} - T_{14})$ before correction in blue and after correction in red.

The correction is needed due to the fact that a different value of the pedestal is needed for each BXID parity which was not expected. The resulting RMS of the reference triggers is around 4-5 ns.

In a next step, to reduce the uncertainty of the time reference, the time reference T_{ref} and its associated uncertainty σ_{ref} are calculated following the equations 9.3 and 9.4. A cut of 4 ns is performed on σ_{ref} to reject events with a too large uncertainty on the time of the trigger reference as shown in figure 9.4b. This cut was chosen in order to minimize the error on the time without while keeping most of the event statistics. The mean uncertainty of the time reference is around 1.30 ns which is compatible with previous results [150]. This

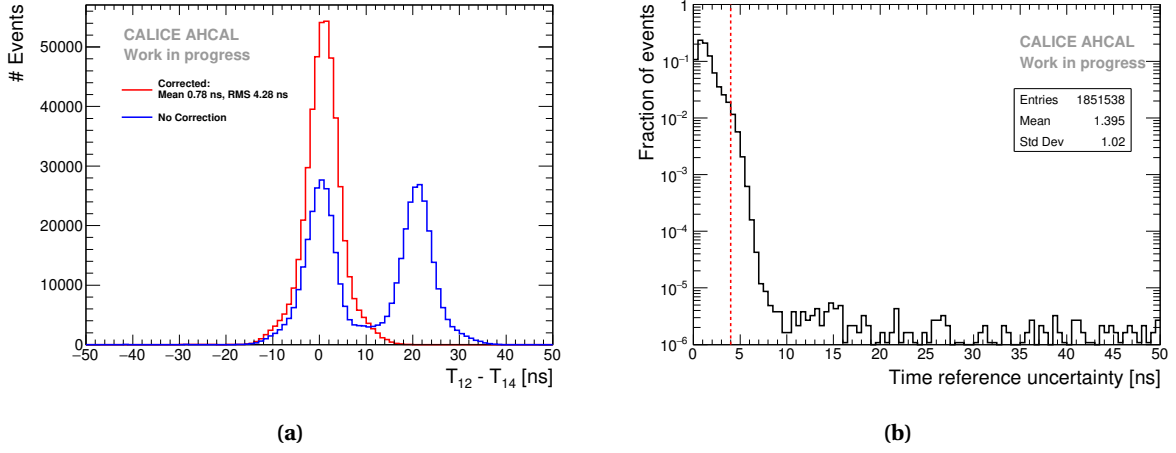


Figure 9.4 – **a)** Time difference between the trigger channels before and after correction for T_{12} and T_{14} . $\mu = 10.6$ ns, $RMS = 11.6$ ns, $\mu_{corrected} = 0.9$ ns, $RMS_{corrected} = 4.8$ ns. The two visible peaks in blue are due to pedestal values being different dependent of the bunch-crossing parity. **b)** Distribution of the uncertainty σ_{ref} . The red line represents the cut of 4 ns.

resolution from the time reference contributes to the final timing resolution obtained. Finally, only events with a calibrated time value between 500 and 3500 ns were considered to avoid TDC ramp edge effects.

$$T_{ref} = \frac{T_{12} + T_{13} + T_{14}}{3} \quad (9.3)$$

$$\sigma_{ref}^2 = \frac{(T_{12} - T_{ref})^2 + (T_{13} - T_{ref})^2 + (T_{14} - T_{ref})^2}{6} \quad (9.4)$$

9.5 Time of the first hit distribution

9.5.1 Determination of the time reference offset

The time reference of the trigger is delayed compared to the muon passing through the detector because of cabling and the trigger electronics logic. Therefore, the time offset of the time reference is determined from data. Muons are instantaneous particles thus the time of the first hit distribution for each channel, memory cell and BXID should peak at 0 ns.

A shifting procedure of the time of the hit relative to the time reference for each channel, memory-cell and BXID parity is performed. This is done to take into account the delay time of the trigger due to cabling and the trigger electronics as well as possible differences in channel pedestals. Only memory-cells containing more than 100 events are considered. The histogram range of the time of the hit relative to the time reference is reduced iteratively until the RMS of the distribution is under 10 ns. This value was chosen because it corresponds to around 3 sigmas of the time reference uncertainty. The mean of the histogram is then used as the time offset value. An example of a single channel is shown in figure 9.5a.

Then a second step is done to correct for a possible mis-calibration of the time offset in the first step. Non-prompt events are rejected if there is less than 4 hits in the range -20 ns to 20 ns. This was necessary in order to reduce the impact of noise on the time offset and ensure a good calibration of the time offset

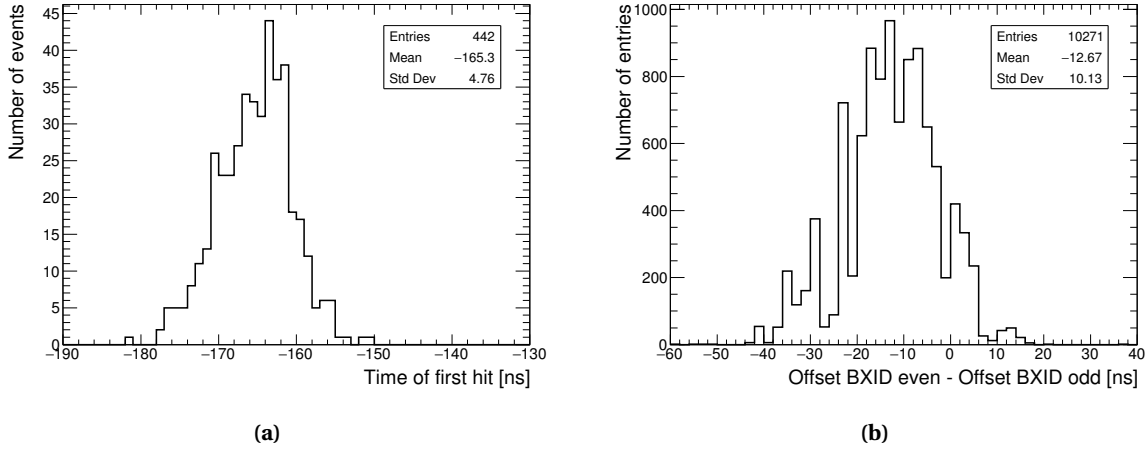


Figure 9.5 – **a)** Time of first hit distribution for a single channel (Chip 236, Chn 21, Mem 01, BXID 1). An offset of -165.3 ns is determined for this channel. **b)** Distribution of the difference of offsets extracted for even and odd BXID for each channel and memory-cell. A mean time offset difference of 12 ns is visible between even and odd BXID.

for all channels. Then the time offset is extracted again using the same method as described above with the non-prompt events removed.

In total, 21040 individual offsets are extracted from data. The mean value of the time offset is around -150 ns which is around the expected value considering the cabling length and the trigger logic delay. Individual offsets have to be extracted for each BXID parity and memory-cell for the pedestal as shown in figure 9.5b.

9.5.2 Time resolution of the AHCAL after calibration

After the time calibration, the time of the first hit $T_{chn} - T_{ref}$ is obtained combining all channels as shown in figure 9.6a. The time resolution (RMS) is around 5.65 ns. The time distribution is obtained by combining all layers excluding layer 11 and by just applying the time calibration on the data. This is far from the desired time resolution of 1 ns. In addition, an asymmetry can be seen in the time distribution to the left. Some improvements are still possible as described in the following sections.

It is expected that the time distribution should follow a Gaussian distribution. However, no fit is performed because of the asymmetry of the time distribution. But a comparison between a Gaussian fit to extract the σ and the RMS of the time distribution is done for each layer as shown in figure 9.6b. All layers are very similar in terms of time resolution and Gaussian-like. The layer 6 and 10 present a worse time resolution that may be due to the bad quality of these boards. The discrepancy observed for the layer 11 is most likely due to an electronic problem in the TDC voltage ramp of all the chips on that layer. All calibration values, channel-wise and chip-wise time distributions on this layer have been investigated manually and all channels present a large tail to high time value. The reason is not clear and identified.

In order to know what time resolution could be expected without the influence of the electronics, a small MC toy study has been done. Firstly, a GEANT 4 simulation of the propagation of photons generated by a muon within an AHCAL tile is done [101]. The simulation gives the distribution of the arrival time of the photons on the SiPM. Secondly, the MC toy generates a random number of fired pixels for each event from a Landau distribution with a MPV corresponding to a light yield of 15 pixels. Each generated photon is assigned

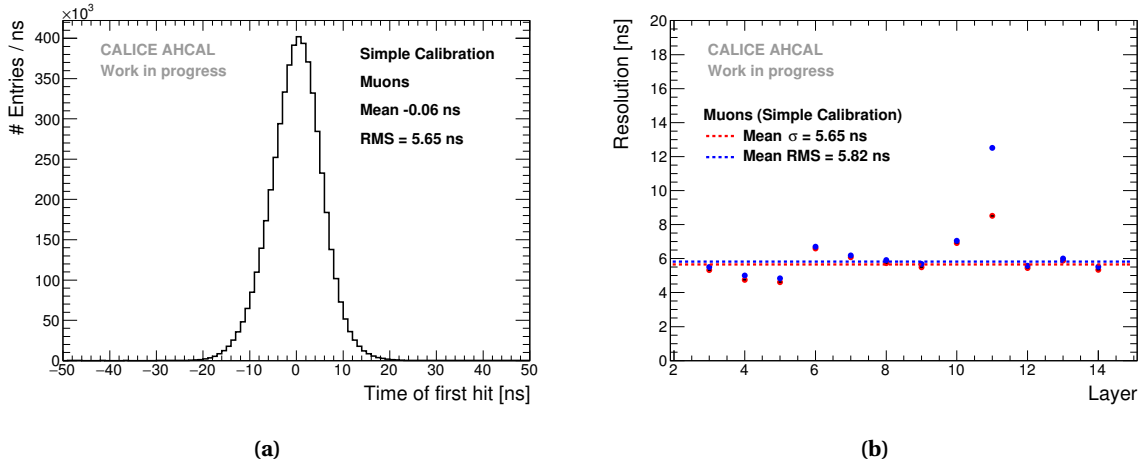


Figure 9.6 – a) Time of the first hit distribution of the AHCAL after the time calibration. $\mu = -0.06$ ns , RMS = 5.65 ns. The distribution is asymmetric to the left. b) Time resolution for all layers in the AHCAL. The mean RMS time resolution is represented by the blue line. The sigma resolution of each layer is obtained from a Gaussian fit. Mean $\sigma = 5.65$ ns, Mean RMS = 5.82 ns.

an arrival time randomly from the distribution of the time of arrival obtained from the simulation. The photons are then sorted by time of arrival from the earliest to the latest and the time of the 5th photon is taken as it corresponds to the threshold of 0.3 MIP of the AHCAL. The MC toy is repeated 100 000 times.

The distribution of the time of arrival of the 5th photon is shown in figure 9.7a. The time resolution from the propagation is then around 0.9 ns which is much smaller than the obtained time resolution. This gives confidence that the time resolution obtained is dominated by the electronics. In addition, it is expected that with a higher number of fired pixels, like for electromagnetic showers, that the time resolution from the propagation decreases. This is confirmed by the figure 9.7b.

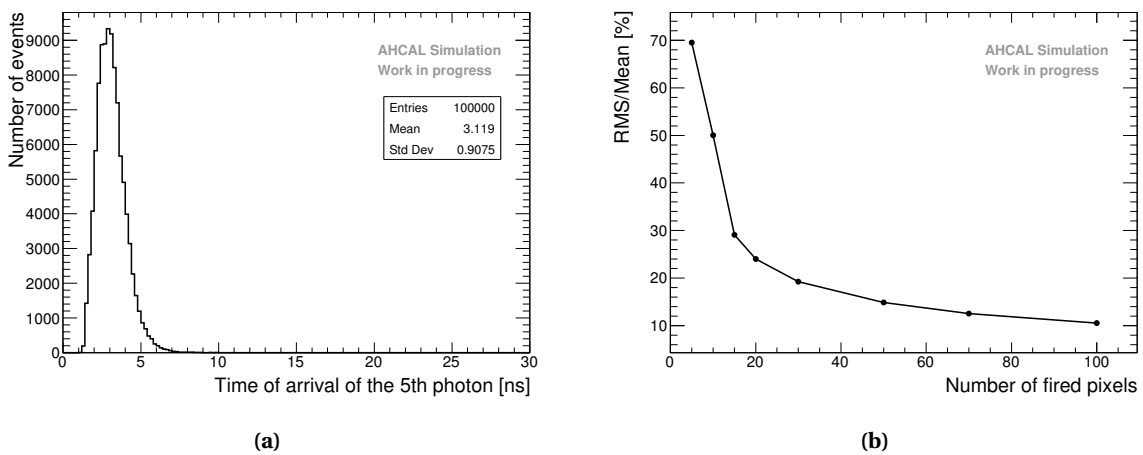


Figure 9.7 – a) Distribution of the time of arrival of the 5th photon for a light yield of 15 pixels per MIP. b) RMS/Mean of the time of arrival of the 5th photon as a function of the number of fired pixels. As expected, the RMS/Mean decreases with a higher number of fired pixels.

9.6 Corrections applied to data

9.6.1 Ramp non-linearity correction

The time calibration relies on the linearity of the TDC voltage ramp in the *SPIROC2B*. This assumption is not entirely reliable as described in [149, 151]. The voltage slope shows a slight kink around the middle thus leading to a non-linear ramp. For this, a correction of the non-linearity is applied. Since the time reference is determined from a non-linear TDC ramp and it can't be corrected due to the lack of external time reference, the position of $T_{hit} - T_{ref}$ on the ramp is actually corrected here.

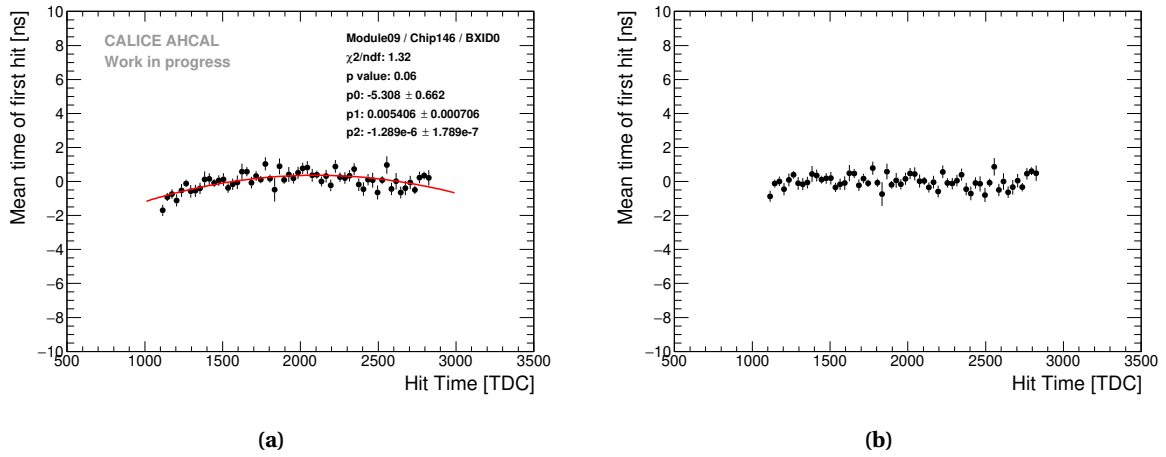


Figure 9.8 – **a)** Quadratic fit of chip 146 (BXID even) on layer 9. The graph is slightly curved showing that this chip presents a non-linear TDC ramp. **b)** Profile for chip 146 on layer 9 after the non-linearity correction of the ramp. The correction parameters are applied on the data to cross-check the quality of the correction. The curve flattens with the non-linearity correction applied.

By investigating the time of the first hit (T_{fH}) for each chip and BXID parity as a function of the TDC value of the hit, the shape of the graph indicates how reliable is the assumption of a linear ramp. If the ramp would be perfectly linear, one would obtain a flat graph. To correct for the non-linearity of the ramp, a 2^{nd} order polynomial is used for each chip and BXID as shown in figure 9.8a. This fit function is an assumption as in reality, the correct underlying fit function is unknown. This also assumes that the fit function is similar for all chips which is known to be not entirely true. However, this fit function describes relatively well the data for most of the chips. The time correction needed can be in the order of few nanoseconds. The figure 9.8b shows the time of first hit as a function of the TDC value of the hit after the non-linearity correction. As expected, the curve looks much flatter after the non-linearity correction.

The non-linearity correction results in an improvement in the timing resolution (RMS) of the AHCAL by about 5.1% (from 5.65 to 5.36 ns) as shown in figure 9.9a. Looking at each layer, as shown in figure 9.9b, the time resolution decrease by the same amount.

However, the asymmetry of the time distribution remains. This effect has been investigated and appears for all layers and chips. It may be due to the time reference channels because the non-linearity of the TDC ramp for these channels cannot be corrected without an external time reference. This has been investigated by looking at the time of first hit distribution in bins of the mean TDC value of the time reference. It has been observed, for all layers, that the time distribution asymmetry increases as a function of the TDC value of the

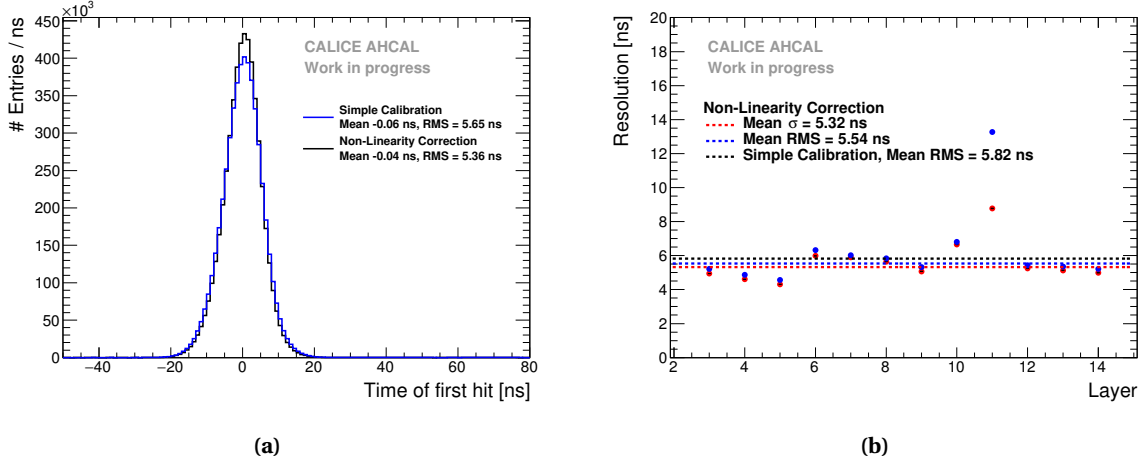


Figure 9.9 – a) Time of the first hit distribution of the AHCAL before the non-linearity correction in black and after in blue. The non-linearity correction improves the time resolution by around 5.1%. b) Time resolution for all layers in the AHCAL. A comparison of the RMS after the simple calibration is shown with the black dashed line.

time reference.

9.6.2 Time Walk correction

The time-walk effect is due to the presence of an energy threshold that induces a time shift between a small amplitude signal and a high amplitude signal. Small amplitude signals will systematically trigger at a later time than high amplitude signals for a shaper that makes the signals peak at the same time. A time correction can be determined by looking at the time of the first hit as a function of the amplitude of the hit. This may be particularly relevant for late energy depositions in hadron showers that comes generally from neutrons depositing little energy in the calorimeter.

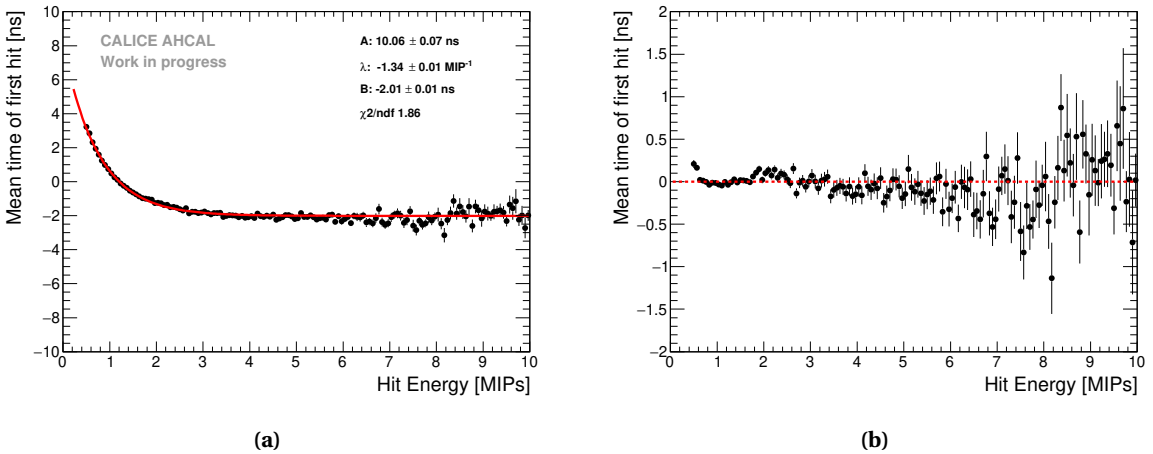


Figure 9.10 – a) Time of first hit as a function of the hit energy. A difference up to 6 ns is seen between small and large amplitudes. Time-walk correction extracted from data. The fit function is of the form $A \times e^{-\lambda x} + B$. b) Time of first hit as a function of the hit energy after correction showing a spread of less than 1 ns.

The correction is assumed to be the same for all the chips, independent threshold value of each chip, because hits are cut at 0.5 MIP. Thresholds of most of the chips were set to similar values, which was far below 0.5 MIP. It has been verified and no significant differences in the shape of the curve are seen between different chips. An exponential fit in the form $A \times e^{-\lambda x} + B$ is applied to the data to extract the parameters which are needed to correct the time walk effect as shown in figure 9.10a. The residuals after correction, shown in figure 9.10b, are under one nanosecond.

9.6.3 Time of first hit for muons after corrections

Figure 9.11a shows the time of first hit distribution for muons after the time-walk correction. An improvement of around 3% is achieved on the time resolution of the AHCAL. The figure 9.11b shows the time resolution obtained for all the layers in the AHCAL. The obtained time resolution is around 5.2 ns RMS. The asymmetry of the distribution will be taken into account in the simulation by parametrizing the time distribution with a double Gaussian function.

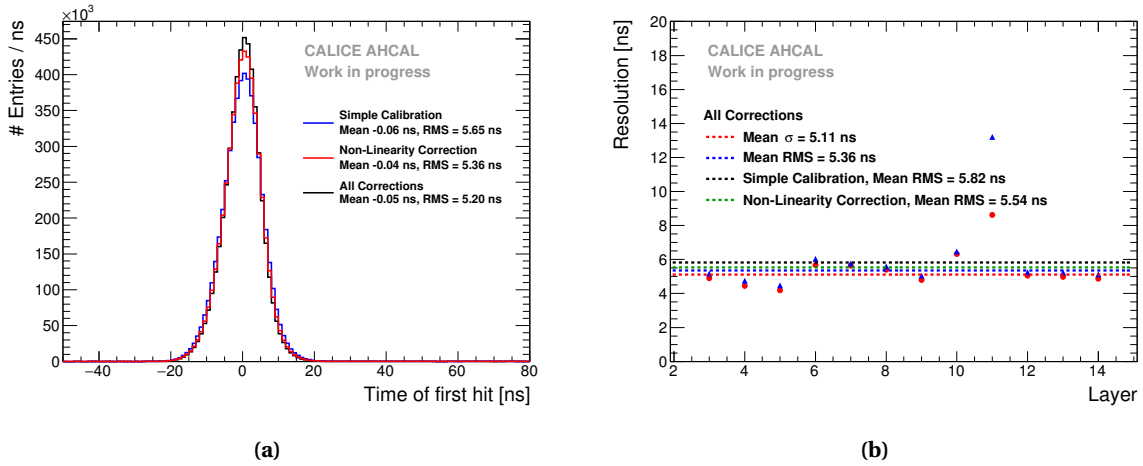


Figure 9.11 – a) Time of the first hit for muons after the simple calibration in blue, after the non-linearity correction in red and after all corrections in black. Each correction improves the time resolution. b) Time resolution obtained for each layer in the AHCAL. A comparison of the RMS after the simple calibration and the non-linearity correction is shown with the black and green dashed lines.

The timing calibration of the AHCAL was performed using the recorded muon data. The TDC ramp slope determination, the calibration of the time reference and the different corrections applied to data have been explained. After a simple timing calibration, a time resolution of around 5.6 ns is achieved. After correcting the non-linearity of the TDC ramp, an improvement of around 5.1% is visible on the time resolution (5.4 ns). Finally, after correcting for the time-walk effect, an improvement of 3% is achieved on the time resolution. After all corrections, the time resolution of the AHCAL is around 5.2 ns.

Before investigating hadronic showers, the calibration must be cross-checked and the simulation of the hit times must be validated. Electromagnetic showers are quasi-instantaneous and, in addition, they have a higher number of hits in the detector compared to muons as well as higher hit energies, and therefore are the

perfect tool to perform the cross-check of the calibration. The cross-check of the calibration is discussed in the next chapter.

Chapter 10

Validation of the time calibration

It is necessary to perform a validation of the timing calibration (see chapter 9). The recorded electron data is used because electromagnetic showers are quasi-instantaneous and thus are perfect to validate the time calibration. The electron dataset used in this study is selected based on criteria described in section 7.2.3. The same calibration constants and correction constants determined from the muon data are applied to the electron data.

10.1 Time of the first hit for electrons

The time of the first hit for 20 GeV electrons after the timing calibration with the calibration constants obtained from the muon data is shown in figure 10.1. In addition, the distribution is compared to the time distribution from the muon data. It is expected to obtain a similar or better time resolution for electrons compared to muons.

The peak of the electron time distribution in figure 10.1 is shifted to the left by around 10 ns. This time offset is expected due to a change in the trigger configuration (see section 7.1.2). This offset is consistent with the difference between the trigger configurations in cable length to route the trigger signal.

However, the time distribution of electrons presents a large tail to the right and is much wider than the one for muons. This is not expected first and this could be related to the number of hits which is much higher in an electromagnetic shower than from a muon and as well that the deposited energy in a single cell can be over 100 MIPs (see figure 8.10).

10.2 Effect of the number of triggered channels on the time distribution

For the energy measurement, there is a known and well understood feature of the SPIROC chip [138], that induces a shift in the baseline of the ADC signal for large pre-amplifier loads, i.e. for large charges on the SPIROC input channels. This feature may be also present for the timing measurement. Since it is a priori not clear if the effect depends on the number of triggered channels *in a chip* or the energy sum *in a chip*, the time correction has been checked using both variables. It turned out that the time correction as a function of the number of triggered channels over 0.5 MIP in a chip gives better results than the time correction as a function of the energy sum in a chip. This is not totally understood why.

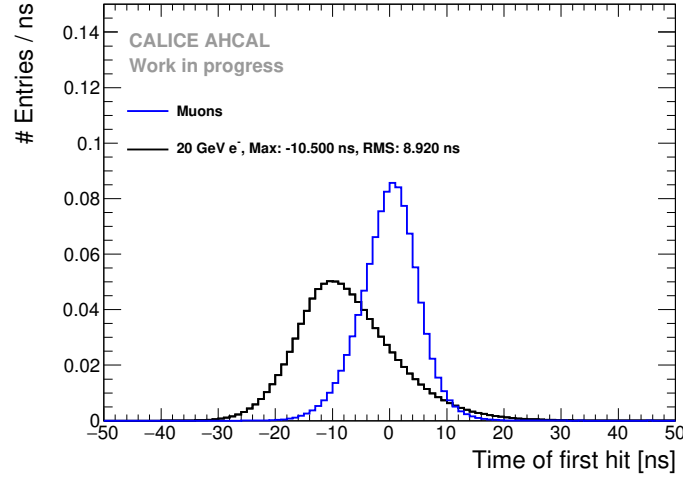


Figure 10.1 – Time of the first hit distribution for 20 GeV electrons after applying the calibration constants extracted from the muon data. The blue distribution represents the time of first hit distribution obtained with muons.

The mean time of first hit as a function of the number of triggered channels over 0.5 MIP in a chip is shown in figure 10.2a. A time shift up to 20-40 ns can be seen depending on the number of triggered channels in a chip. The cause of the observed effect is most likely due to an element in the chip called a *delay box* that gets unstable with a high charge going through the chip. This chip element is responsible for the hold signal of the TDC ramp in the chip. The hold signal is delayed, and thus a higher TDC ramp value than the one expected is sampled.

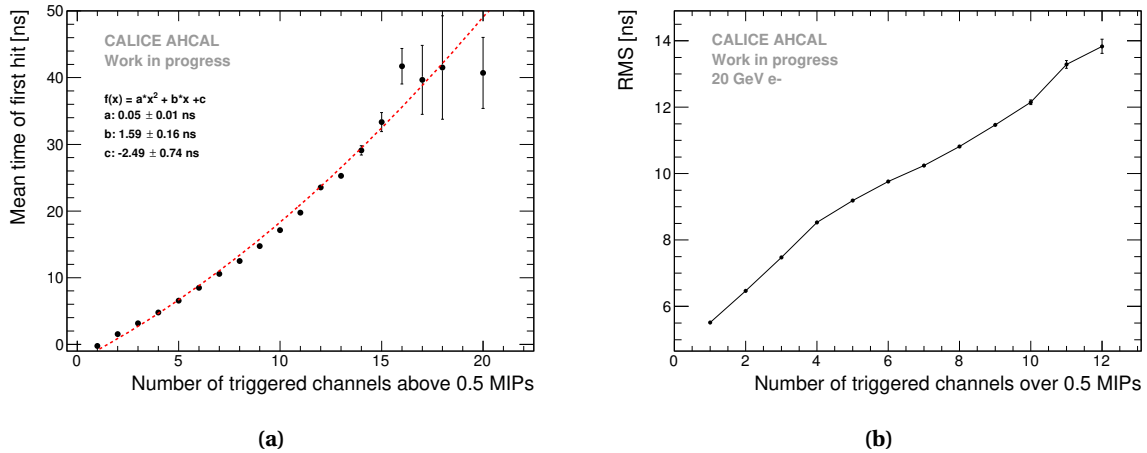


Figure 10.2 – **a)** Mean time of the first hit as a function of the number of triggered channels above 0.5 MIP in a chip. The mean time shifts upwards with the increase of triggered channels leading to large tails in the time distribution. A second order polynomial fit is done for the time correction shown by the red dashed line. **b)** The RMS of the time of first hit distribution as a function of the number of triggered channels above 0.5 MIP in a chip for 20 GeV electrons. The RMS of the time distribution can increase up to 10-15 ns for a high number of triggered channels in a chip.

The time correction parameters are determined by a 2nd order polynomial fit to the data as shown by the red line in the figure 10.2a. In order to determine a reliable time correction, the time correction parameters are determined by combining all the electron data. A priori, this effect should not be dependent on the beam energy. However, a dependence is seen (see section 10.5) and shows that the effect is not totally understood. Therefore, the differences are treated as systematic uncertainty. This effect may be chip-dependent and the parameters for the correction may differ from chip to chip. However, the limited amount of data does not allow to determine a correction function for each chip. Therefore, a global function is used to correct the time in the data.

Figure 10.3 shows the residuals of the mean time of first hit as a function of the number of triggered channels above 0.5 MIP in a chip ($N_{trig/chip}$) after the correction. The correction has been applied to all electron samples separately in order to evaluate the systematic uncertainty of the correction. Three ranges in $N_{trig/chip}$ have been defined delimited by the red lines to estimate the uncertainty. To not overestimate the uncertainty, half of the residual envelope is taken as uncertainty. For $0 < N_{trig/chip} < 5$, a systematic uncertainty of 2 ns is taken, For $5 \leq N_{trig/chip} < 12$, a systematic uncertainty of 5 ns is taken and finally for $N_{trig/chip} \geq 12$, a systematic of 7 ns is taken. Finally, the uncertainty for the mean time of the first hit is computed *for each bin of energy and radius* by weighting according to the fraction of hits in each of the three regions following equation 10.1. As the uncertainties in the three ranges are correlated, a conservative way is to add linearly the uncertainties.

$$\sigma = n_1 \times \sigma_1 + n_2 \times \sigma_2 + n_3 \times \sigma_3 \quad (10.1)$$

with $\sigma_1 = 2$ ns, $\sigma_2 = 5$ ns, $\sigma_3 = 7$ ns, n_1 the fraction of hits for the i-th bin in the region $0 < N_{trig/chip} < 5$, n_2 the fraction of hits for the i-th bin in the region $5 \leq N_{trig/chip} < 12$ and n_3 the fraction of hits for the i-th bin in the region $N_{trig/chip} \geq 12$ and such as $n_1 + n_2 + n_3$ is equal to one in the i-th bin.

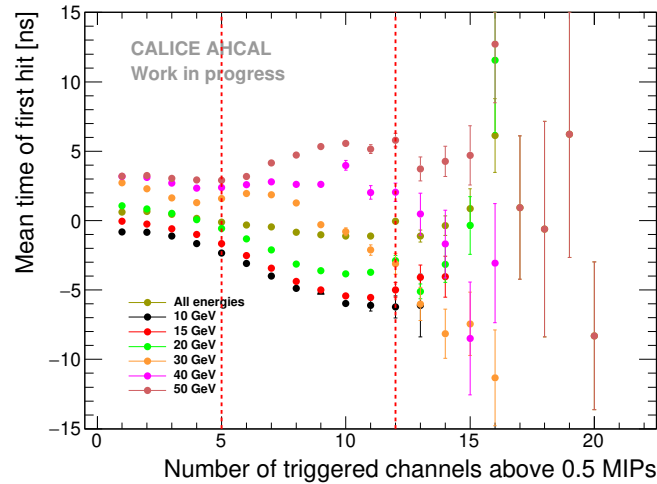


Figure 10.3 – Residuals of the mean time of the first hit as a function of the number of triggered channels above 0.5 MIP in a chip after correction. The correction has been applied to all electron samples separately to evaluate the systematic uncertainty. The vertical red lines delimit the three sections used for the systematic uncertainty.

The figure 10.2b shows the RMS of the time distribution increasing with the number of triggered channels over 0.5 MIP in a chip. As expected, if a single channel in a chip triggers, the RMS of the time distribution (~ 5.5 ns) is close to the time resolution for muons as shown in figure 10.2b.

The time resolution (RMS) of the AHCAL is expected to be slightly dependent on the electron beam profile that affects directly the number of triggered channels in a chip. In addition, as the time resolution (RMS) of the AHCAL is dependent on the number of triggered channels in a chip, i.e the number of hits in the calorimeter, it is expected that the time resolution increases as a function of the electron beam energy as the number of hits in a EM shower is proportional to its energy.

10.3 Time of the first hit after correction

The distribution of the time of the first hit for 20 GeV electrons is shown in figure 10.4a before and after the time correction as a function of the number of triggered channels in a chip. The correction improves the RMS of the distribution by around 10%, as well as the distribution appears more Gaussian-like.

However, there is still a discrepancy of around 54.6% from the time resolution obtained from muons (see section 9.6.3). This is because the RMS of the time distribution increases as a function of the number of triggered channels in a chip (see figure 10.2b). The increase of the RMS can't be corrected unlike the mean of the time distribution.

The increase of the width of the time distribution is parametrized from data for the simulation. More details about the parametrization implementation in the simulation are given in the appendix F.

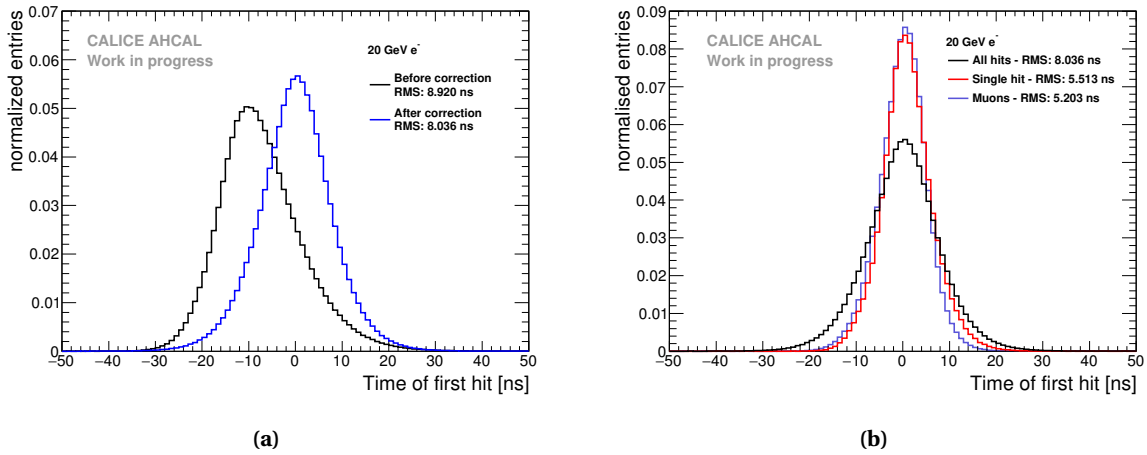


Figure 10.4 – a) Time of the first hit distribution for 20 GeV electrons after the number of triggered channel in a chip correction. **b)** Comparison of time distribution of 20 GeV electrons and muons. The electron time distribution is very similar to the muon time distribution when only a single channel triggers in a chip.

A comparison of the time distribution from electrons and from muons has been done in order to further cross-check the calibration (see figure 10.4b). The time resolution from electrons is very similar to the time resolution from muons when only a single channel triggers in a chip. The difference in time resolution is around 6% (5.51 ns (e^-), 5.2 ns (μ^-)).

All electron runs have been carefully checked to validate the timing calibration. The figure 10.5 shows the comparison of the time distribution from electrons between 10 GeV to 50 GeV beam energies. The mean of

the time distributions is very similar. The RMS of the time distributions increases as expected and it varies between 7.94 ns at 10 GeV and 8.88 ns at 50 GeV corresponding to an increase of 11.8%. A large deviation from the 20 GeV electron time distribution for energies above is visible after 20-30 ns. This may be due to slight differences in beam profile for each beam energy, the increase of the time resolution for higher beam energies and the time correction as a function of the number of triggered channels in a chip that is not perfect. However, within 3 sigmas, the time distributions differ up to 10-20%. In addition, a similar effect is visible for negative times, thus different noise levels due to different beam rates might also play a role.

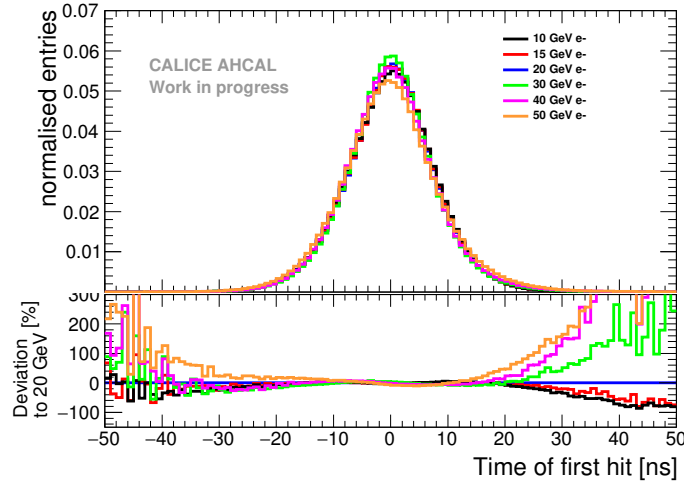


Figure 10.5 – Comparison of the time of first hit distribution for electron beam energies between 10 GeV and 50 GeV. The bottom plots shows the relative difference to the 20 GeV electron time distribution.

10.4 Transportability of the calibration

A check on the validity of the calibration for other data-taking periods has been performed on another dataset from a testbeam at DESY II in May 2016. The goal is to understand the transportability of the time calibration. The setup was composed of the same layers 11 to 14 used at CERN in July 2015. In order to have enough hits in all layers, an aluminum absorber of $3 X_0$ was placed in front of the detector in a 3 GeV electron beam.

The same time calibration constants determined from the CERN muon and electron data were used, except that a re-calibration of the time reference triggers (T_0) and the trigger time offset was necessary. This is due to different setups in the cabling and trigger electronics. For this setup, only two T_0 channels on the layer 14 were working properly.

Figure 10.6 shows the distribution of the time of first hits for layer 12 to 14, the layer 11 is ignored as the same behavior seen in the CERN dataset is also seen for this dataset, for all hits in black and for events with only single hits per chip in blue. The time distribution is compared to the time distribution for the layers 12 to 14 of 10 GeV electrons recorded at CERN in July 2015.

The time resolution is around 6.9 ns which is very slightly worse than ($\sim 6\%$ difference) the time resolution using the same layers at the CERN testbeam. This difference seen in time resolution can be related to the

slightly worse (around 4%) time reference resolution.

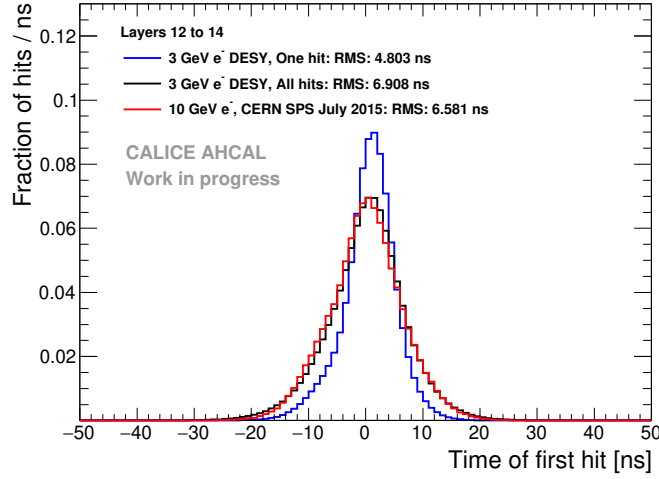


Figure 10.6 – Time of the first hit distribution for 3 GeV electron showers at the DESY II testbeam in May 2016 combining layers 12 to 14 in black. The blue distribution is the time of first hit in the case of events in which only single hits in a chip are taken. The red distribution is the time of first hit for the same layers in 10 GeV electrons collected at the CERN SPS in July 2015.

We can learn from this study, that the time calibration constants determined in a specific dataset can also be used for another dataset. The timing calibration values depend mainly on hardware and not so much on the environment.

10.5 Estimation of the systematic uncertainty of the time correction on the time of first hit distribution

A global correction is used for the time correction as a function of the number of triggered channels. A priori, it is not clear if the time correction is chip-dependent and it could not be verified. Therefore, a systematic uncertainty of the time correction on the time of first hit distribution needs to be estimated.

A study has been done to estimate this uncertainty by looking at the time distribution for events where the center of gravity of the shower is in one of the four center tiles of the detector. The four center tiles are chosen due to the higher event rate. This gives four different time distributions that can be compared and that can help to estimate the impact of the time correction as a function of the number of triggered channels in a chip in different sections of the detector. This has been performed for electron beam energies of 10 GeV and 50 GeV.

The figure 10.7a and 10.7b show the time distribution for events with the center of gravity in each one of the four tiles for 10 GeV and 50 GeV electron beam energies respectively. For both beam energies, the mean of the time distributions are very similar and are close to 0 ns. The RMS of the time distributions varies between 7.12 ns and 7.45 ns at 10 GeV and between 8.1 ns and 8.8 ns at 50 GeV. The mean deviation from the top left tile is shown in black line in the bottom plots. A relative deviation over 30% to the top left tile can be seen in the region over 30 ns and under -30 ns. The mean deviation curve in figure 10.7b is taken as a systematic

uncertainty on the bin content in the data truncated in the region from -30 ns to 30 ns. Outside of this region, a systematic uncertainty of 50% on the bin content is taken.

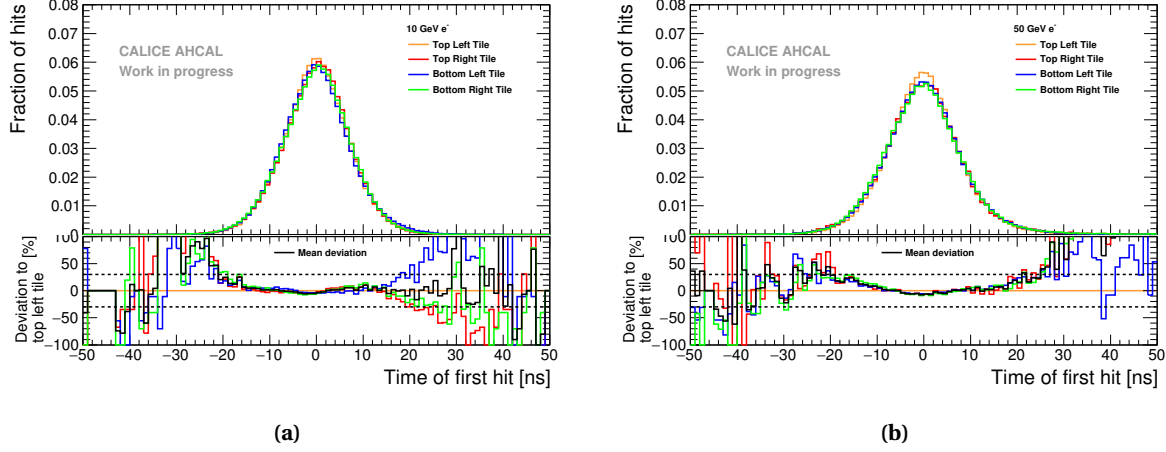


Figure 10.7 – Time of the first hit distribution for events where the center of gravity of the shower is in the four center tiles for 10 GeV electrons on the left and 50 GeV electrons on the right. Under each figure, the deviation of each time distribution to the top left tile is shown. The mean deviation of the time distributions is shown in a black line. The dashed black line represents a 30% deviation relative to the top left tile time distribution.

10.6 Systematic uncertainties

For a significant assessment of differences observed between data and simulations, systematic uncertainties must be evaluated. Several possible sources were identified. The following sources of systematic uncertainty are taken into account for data:

- **Non-Linearity correction:** A non-linearity correction (see section 9.6.1) is determined from data with a limited accuracy lead to a systematic uncertainty. The residuals of the correction give a systematic uncertainty at the level of 0.2 ns.
- **Time walk correction:** Similarly to the non-linearity correction of the data, the systematic uncertainty obtained from the residuals of the time walk correction (see section 9.6.2) is in the order of 0.2 ns.
- **Number of triggered channels correction:** The correction for the number of triggered channels over 0.5 MIP in a chip results in a residual on the mean time of the first hit (see section 10.2). The systematic uncertainty varies between 2 to 3.9 ns. For the time of first hit distribution, a systematic uncertainty is applied bin-by-bin for electrons and pions in the region of -30 ns to 30 ns. Outside of this region, a systematic uncertainty of 50% is taken (see section 10.5). This systematic error is the most dominant over all other uncertainties. A similar method is used to evaluate the systematic uncertainty on the RMS of the time distribution which varies between 1.2 ns and 2 ns.
- **AHCAL energy scale:** The energy scale of the AHCAL was determined using the muon dataset (see chapter 8). A systematic uncertainty on the MIP scale of around 3.6% was derived by dividing the muon sample in odd and even run numbers and by looking at the average spread of the fitted MIP value for

both subsamples. This is converted to an uncertainty in time using the mean time of first hit as a function of the hit energy using the QGSP_BERT_HP physics list. At 0.5 MIP, this results in an uncertainty of 0.1 ns. For hits above 1 MIP, the uncertainty is below 0.05 ns.

The following systematic uncertainties are taken into account for the simulation:

- **Global time smearing parameters:** A global time smearing parametrization is used from muon data to smear the time in simulation. A bin-by-bin systematic uncertainty is applied to the time of first hit distribution to take into account the difference with a layer-wise time smearing parametrization.
- **Number of triggered channels in a chip parametrization:** A smearing parametrization of the width of the time distribution as a function of the number of triggered channels in a chip is obtained from the electron dataset. An error band on the width was obtained by comparing all electron energies (see appendix F). This is applied to simulation for the systematic uncertainty on the RMS of the time distribution.
- **Determination of the offset to $t = 0$:** For simulation, the time shift per layer is calculated using a time of flight correction $T_{of} = \frac{z_{layer}}{c}$ with c the speed of light and z_{layer} the z position of a layer. For this, an uncertainty of 3 mm corresponding to the scintillator thickness is taken in z corresponding to 0.01 ns uncertainty in timing.
- **Cross-talk:** No measurement for optical cross-talk between tiles is available and from previous measurements with the AHCAL physics prototype, it varies between 10% and 18% [152]. The cross-talk value induces a different number of hits in the detector thus has an impact on the width of the time of first hit distribution. The variation of this parameter in the simulation for the layers 4 to 10 is used for systematics.
- **Absolute number of events:** In the pion data, some possible contamination from multi-particle events (mainly muons) may be present still after the selection. Thus, the number of true pion events is not known. The cluster time rejection method (see section 7.2.4) rejects up to 1% of multi-particle events in the data. A conservative uncertainty of 10% on the data normalization is assigned to each bin when comparing data to simulation for the absolute time of first hit distribution.

The systematic uncertainties are added in quadrature for the full systematic uncertainty assuming no correlation between uncertainties. For the mean time of the first hit as a function of the hit energy and as a function of the hit distance to the shower center of gravity, the systematic uncertainty is resulting at 0.3 ns for muons and between 2 to 4 ns for electrons and pions. The table 10.1 sums up the systematic uncertainties used in the analysis.

10.7 Validation of the simulation

The simulation is validated by comparing the recorded muon and electron data to simulations. The timing resolution is extracted from muon data runs by fitting a double Gaussian to the data in the range [-50 ns, 50 ns] and is used to smear the timing of simulated calorimeter hits. For the sake of simplifying the time smearing in the simulation, a global smearing parametrization is done. The table 10.2 summarizes up the parameters used.

Table 10.1 – Summary of systematic uncertainties.

Uncertainty source	Full uncertainty
Non-linearity correction	0.2 ns (data)
Time-walk correction	0.2 ns (data)
Number of triggered channels correction	2 - 3.9 ns (mean) / 1.2 - 2 (RMS) / bin-wise (e/ π) (data)
Energy Scale	0.05-0.1 ns (data)
Time of flight offset	0.01 ns (MC)
Cross-talk parameter	10-18% (MC)
Global time smearing parameters	bin-wise (MC)
Number of triggered channels in a chip parametrization	bin-wise (MC)
Multi-particle events	10% (π) (data)
Resulting systematic uncertainties per distribution (data)	
data-MC ToFH distribution	bin-wise (e) - bin-wise + 10% (π)
data-MC vs hit energy	0.3 ns (μ) - 1.8 to 3 ns (e/ π)
data-MC vs hit distance to shower CoG	0.3 ns (μ) - 1.8 to 3 ns (e/ π)
data-MC vs hit depth	0.3 ns (μ) - 1.8 to 3 ns (e/ π)

Table 10.2 – Timing resolution extracted with a double Gaussian fit from muon data used for simulation.

α_1	μ_1 [ns]	σ_1 [ns]	α_2	μ_2 [ns]	σ_2 [ns]
0.607352	-0.699095	5.85891	0.391041	0.945274	3.4012

The comparison of the time of first hit distribution for muons between data and simulations is shown in figure 10.8. The comparison shows that in the range of -20 ns to 20 ns, data and simulation agree well within the uncertainties. In this range, the smearing with a double Gaussian in the simulation reproduces well the data. However, outside this range, the simulation underestimates the tails. This is probably caused by the noise implementation in simulation that does not perfectly reproduce the data. The time of distribution has been checked layer-by-layer and compared to simulations. Similar, the agreement between data and simulations is best in the range of -20 ns to 20 ns and the tails are not perfectly reproduced in simulation.

To further validate the simulation, a comparison with electron data has been done. In addition to the muon resolution, a parametrization of the increase of the width of the time distribution as a function of the number of triggered channels in a chip above 0.5 MIPs is added in simulation (see appendix F). The figure 10.9a shows the comparison of the time of first hit distribution for 10 GeV electrons in data and simulation. The errors bars in the simulation are obtained by varying the cross-talk parameter between 10% and 18%, taking into account the global time smearing parametrization uncertainty and from the uncertainty of the parametrization of the increase of the width of the time distribution as a function of the number of triggered channels in a chip. The last uncertainty is dominant over the other uncertainties.

The simulation is systematically narrower than data. This is caused by the simulation having fewer hits in a chip than data which can be seen in figure 10.9b. The simulation is generally 10% to 20% lower than data in the region of 6 to 10 hits per chip. Overall, the simulation describes well the data within statistical

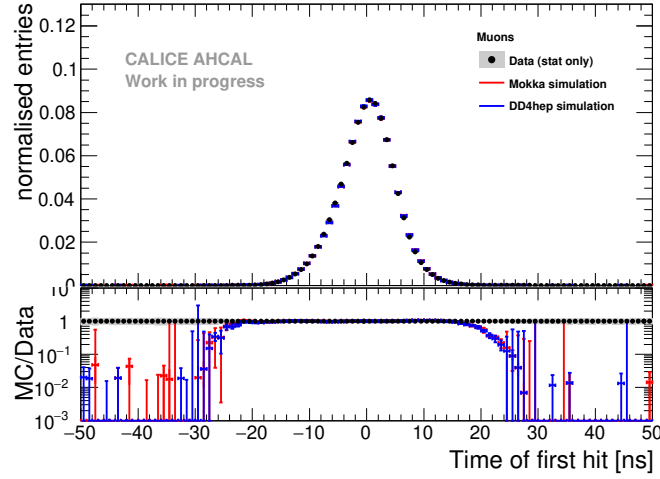


Figure 10.8 – Time of first hit distribution for muons in data and simulation between -50 and 50 ns. The grey area represents the statistical uncertainty of the data. The error bars of the simulation are obtained by varying the cross-talk parameter between 10% and 18% and taking into account the error of a global time smearing parametrization.

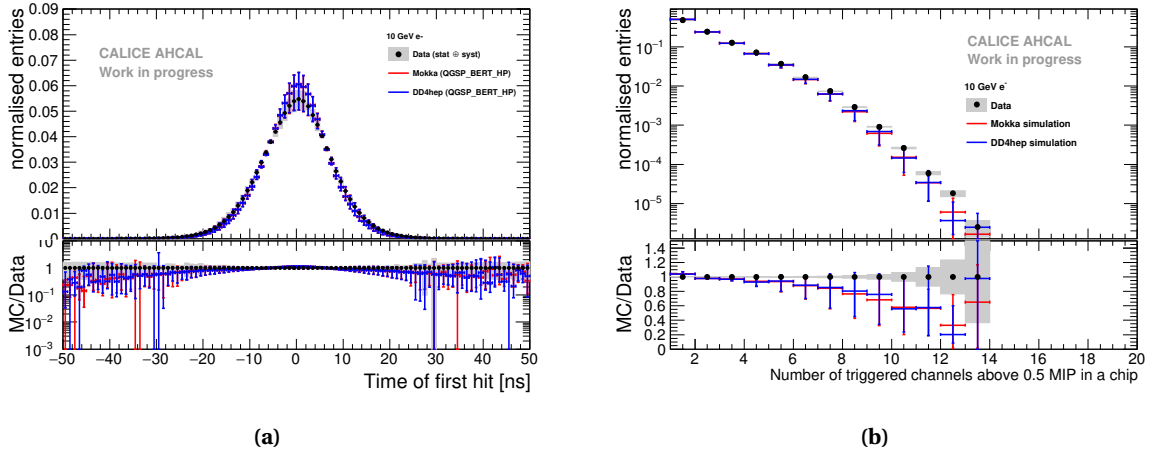


Figure 10.9 – **a)** Comparison of the time of first hit between data and simulations for 10 GeV electrons. The grey area represents the statistical and systematical error of the data. Error bars in simulation are obtained by varying the cross-talk parameter between 10% and 18% and with the uncertainty on parametrization of the width of the time distribution as a function of the number of triggered channels in a chip. **b)** Comparison of the number of triggered channels per chip between data and MC for 10 GeV electrons. The grey area represents the statistical error of the data. Error bars in simulation are obtained by varying the cross-talk parameter between 10% and 18%.

and systematic uncertainties in the central region of -30 ns to 30 ns for all energies. The error bars in the simulation is due to the parametrization of the increase of the width. However, the description of the tails of the time of first hit distribution in the simulation are well underestimated. As for muons, this is probably due to the description of the noise in the simulation that does not perfectly reproduce the data. The time of first hit distributions and the distribution of the number of triggered channels per chip have been checked for all energies and they can be seen in [appendix C](#).

In this chapter, the timing analysis of the recorded electron data has been presented. A time resolution (RMS) for the AHCAL in electron beams is obtained between 7.8 ns at 10 GeV beam energy and 8.5 ns at 50 GeV beam energy. An increase of the width of the time distribution as a function of the number of triggered channels in a chip is observed in the electron data. This electronic effect has been parametrized and it is used as an input to tune the simulation in order to reflect the data.

The AHCAL timing simulation has been validated by comparing the simulated time distributions to data using muons and electrons. Overall, the simulation reproduces the data within 20% in the range of -30 ns to 30 ns. In addition, the simulation underestimates highly the tails of the distribution that is due to an imperfect implementation of noise hits in the simulation.

However, the simulation is in good enough agreement with data that the time of hadron showers can be studied. In the next chapter, the timing analysis of pion showers and comparisons to simulation will be presented.

Chapter 11

Timing study of hadron showers

In this chapter, the recorded pion data is compared to GEANT 4 v10.1 simulations using different hadronic models as explained in chapter 5. Just as a reminder, the hit time of a channel is referred to as *the time of the first hit* because only the first hit per channel is registered during a bunch-crossing (multiple hits could occur in a channel but only the first one is kept by the SPIROC2b).

11.1 Dataset

The pion dataset used in this study is selected based on criteria described in section 7.2.4. The same time calibration constants and corrections determined from muons and electrons is applied to the pion data. The table 11.1 summarizes the runs and datasets used for the pion analysis. N_{3T_0} is the number of events after the selection on the time reference (see section 9.4). $N_{sel.}$ is the number of events after the cut on the error of the time reference.

Table 11.1 – Table with the number of events selected in the pion dataset for the timing study.

Runs	Energy	Particle Type	N_{3T_0}	$N_{sel.}$	$\frac{N_{sel.}}{N_{3T_0}}$
24306-24317 24381-24397	10 GeV	π^-	425517	349012	82%
24578-24612	50 GeV	π^-	1183790	1007889	85.1%
24339-24342	70 GeV	π^-	142813	122376	85.7%
24223-24238 24273-24287 24331-24336 24358-24364	90 GeV	π^-	466927	395884	84.8%

11.2 Time of first hit distribution

Inside a hadronic shower, absorber materials with a high atomic number Z , thus containing a high number of neutrons, are expected to release a high number of evaporation neutrons. These neutrons then will

deposit energy by two different mechanisms with different time scales relative to the first hard interaction.

First, the elastic scattering of neutrons in the active material especially with high hydrogen content will play a role at a few nanoseconds to tens of nanoseconds time scale, whereas neutron capture in the absorber material at the interface with the active material will contribute to several hundred or thousands of nanoseconds timescale due to the relatively long time of flight of thermal neutrons and the lifetime of such atomic states. Thus it is expected that hadronic showers will present an increase in the late component, i.e an increase in the right tail of the time distribution, compared to muons or electrons time distributions.

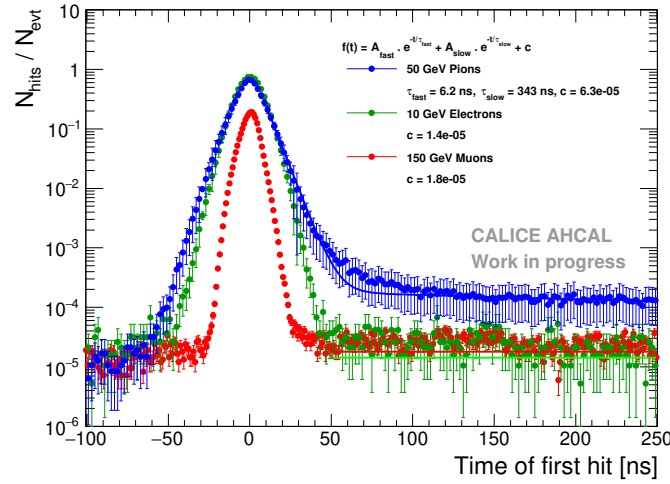


Figure 11.1 – Time of first hit for muons, electrons and pions in steel absorber in a range of -100 to 250 ns. The histograms are normalized to the number of events where at least one hit was identified. The errors bars are statistical and systematic uncertainties. The lines represent the fit to the data as explained in the text.

Figure 11.1 shows the time of first hit for muons, 10 GeV electrons and 50 GeV pions. Energy depositions from muons and electrons are instantaneous within a certain time window centered around 0 ns that is determined by the intrinsic time resolution of the detector. Some isolated hits are present in the tails most likely caused by SiPM thermal noise. This gives an idea of the noise level as well as the rejection of noise in the analysis.

The fraction of hits n_{Late}/n_{Core} , with n_{Late} the number of hits between 50 ns and 2 μ s and n_{Core} the number of hits between -50 and 50 ns, is around 1.76% for muons, 0.32% for electrons and about 1.41% for pions. The noise level is similar on the left side of the time distribution for muons, electrons and pions giving confidence that the right tail observed in the pion data is coming from physics and not noise.

The pion time distribution presents a higher tail between 30 to 50 ns than the electron time distribution. In order to characterize the distribution, a model of the sum of two exponentials and a constant, similar to the T3B experiment [153] is applied following the equation 11.1:

$$\frac{1}{N} \frac{dN}{dt} = A_{fast} \times e^{-\frac{t}{\tau_{fast}}} + A_{slow} \times e^{-\frac{t}{\tau_{slow}}} + c \quad (11.1)$$

where A_{fast}, τ_{fast} and A_{slow}, τ_{slow} are the amplitudes and decays times of the modeled fast and slow component of the hadronic shower. Since the fit is performed on several orders of magnitudes, the fit is performed in several steps. Firstly, the constant is fitted between 500 ns and 2 μ s. Then, a new histogram of

the time of hits hit is made subtracting the noise floor. Secondly, the slow component is fitted between 90 ns and 2 μ s. Then, the parameter of the slow component is fixed and then the fast component is fitted between 10 ns to 2 μ s.

With this procedure, a fast component of 6.21 ± 0.30 ns and a slow component of 343 ± 39 ns are fitted. The time constant of the fast component is in the same order of magnitude as given by T3B of 8 ns and is interpreted by the energy deposition of evaporation of neutrons in the active medium. But due to the time resolution of the AHCAL being in the same order of magnitude, it is difficult to confirm this origin.

However, the time constant of the slow component is very different than in the T3B experiment (around 80 ns in steel). This may be due to the contribution of SiPM noise that reduces the sensitivity to this slow component in the shower, and the contribution of multi-particle events. One can remark that this model may be incomplete as the fitting function does match well the data in the transition region of 50 to 100 ns. The table 11.2 sums up the fitted results.

Table 11.2 – Summary of the fit results in figure 11.1.

Parameter	Muon	Electron	Pion
τ_{fast} [ns]	-	-	6.21 ± 0.30
τ_{slow} [ns]	-	-	343 ± 39
c	$(1.79 \pm 0.01) \times 10^{-5}$	$(1.43 \pm 0.04) \times 10^{-5}$	$(6.33 \pm 0.15) \times 10^{-5}$

Figure 11.2 shows the time distribution of first hits compared with three different physics lists for 50 GeV pions. Additional distributions for higher pion beam energies are shown in appendix C. For the core of the distribution under 50 ns, overall, all physics lists describe relatively well the data within the systematics.

The QGSP_BERT_HP and QBBC physics list reproduces relatively well the distribution within the systematic uncertainty. For all time of first hit distributions, the QGSP_BERT physics list without the high-precision neutron treatment, too much late shower activity is predicted by around a factor 5.

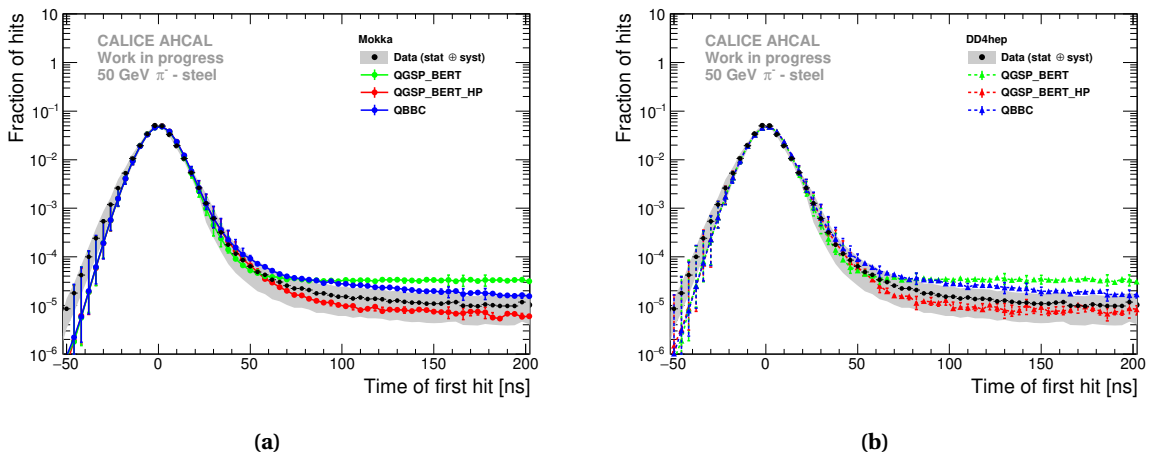


Figure 11.2 – Comparison of the time of first hit distribution for 50 GeV pions in data and three different physics list for Mokka (left) and DD4HEP (right) simulations. The grey and color bands shows the statistical and systematic uncertainties.

11.3 Energy dependence of the time of first hit

The dependence of the time of first hit as a function of the hit energy has been studied in the following. It is expected that there is no hit energy dependence for muon and electron beams as these are quasi-instantaneous. On the other hand, for pions, it is expected that low energy hits in the calorimeter are delayed, mostly coming from neutron signals.

The mean time of the first hit taken in a time window of -50 ns to 200 ns as a function of the hit energy is shown in figure 11.3a for muon, electron and pion beams. For muons and electrons, no dependence on energy is observed as expected, all hits are instantaneous independent of their energy. For 10 GeV pions, a delay of 2-3 ns at 0.5 MIP is observed and decreases down to 0-1 ns above 1 MIP. For higher pion energies, the mean time of the first hit decreases between 0.5 and 1.5 MIP then increases for hit energies above 1.5 MIPs. This is not expected, thus individual distributions have been checked. An example is shown in figure 11.3b for 90 GeV pions. After 1.5 MIP, the time distribution gets wider and the maximum of the distribution is de-centered slightly from 0 ns, therefore explaining the increase of the mean time of the first hit for hit energies over 1.5 MIP. This may be coming from an imperfect time correction as a function of the number of triggered channels in a chip (see section 10.2) as mostly high energy hits are coming from the electromagnetic core of the hadronic shower.

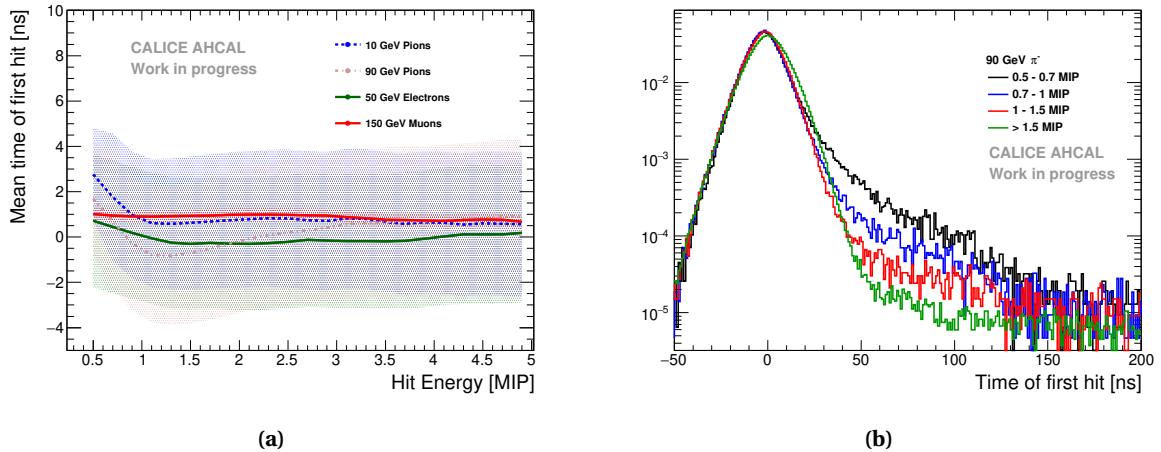


Figure 11.3 – On the left, the mean time of first hit as a function of the hit energy for muons, electrons and pions in steel absorber taken in a range of -50 to 200 ns. The bands represent the systematic uncertainty. On the right, the time distribution for 90 GeV pions for different hit energy ranges.

Figures 11.4a and 11.4b show the comparison of the mean time of first hit as a function of the hit energy in data and simulations for 10 GeV and 90 GeV pions. For other pion beam energies and the DD4HEP simulation, the figures are available in appendix C. For all energies, the simulation reproduces the data within the systematics. However, firstly, a difference is visible between the QGSP_BERT and QGSP_BERT_HP physics lists mainly between hit energies of 1-3 MIPs but, in general, the difference is smaller than the systematic uncertainty on the data. Secondly, the QGSP_BERT and QBBC physics lists are very similar over the full hit energy range. Finally, all models show an increase of the mean time of first hit at small hit energies with higher beam energy. The data does not reflect this.

Then the dependence of the RMS of the time distribution as a function of the hit energy has been studied.

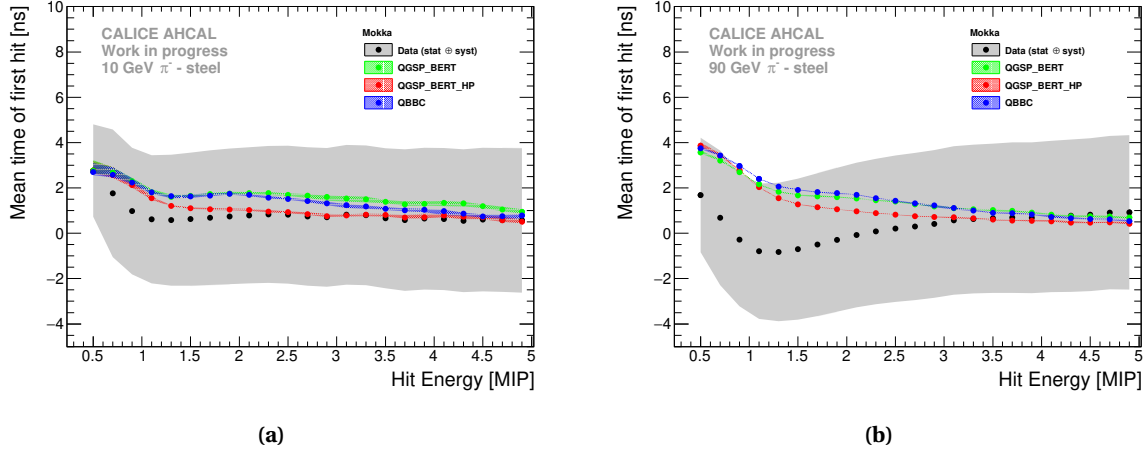


Figure 11.4 – Comparison of the mean time of the first hit as a function of the hit energy in data and MOKKA simulation for 10 GeV and 90 GeV pions. The grey and color bands show the statistical and systematic uncertainties.

It is expected that the RMS of the time distribution is bigger at low hit energies coming mostly from slow neutrons and then decreases for higher hit energies. The figure 11.5a shows the RMS of the time distribution as a function of the hit energy for muons, electrons and pions. As expected, the RMS is bigger at low hit energy and reaches a plateau at high hit energies. The RMS varies from 12-16 ns at 0.5 MIP, to 10-13 ns at 1 MIP and above.

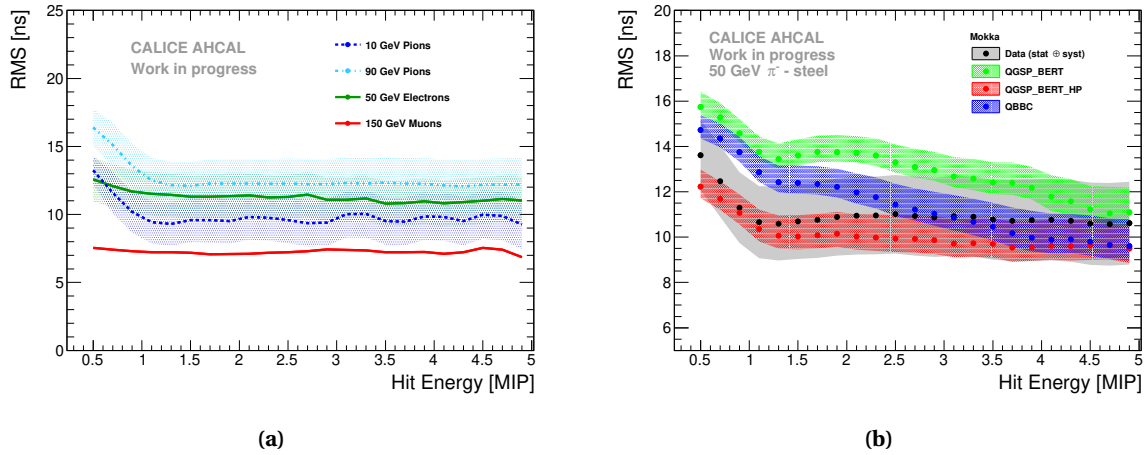


Figure 11.5 – a) The RMS of the time distribution as a function of the hit energy for muons, electrons and pions in steel absorber taken in a range of -50 to 200 ns. The systematics are shown by the color bands. b) Comparison between data and simulation of the RMS of the time distribution as a function of the hit energy. The color bands show the statistical and systematic uncertainty.

It has been compared to simulations as shown in figure 11.5b for 50 GeV pions. The QGSP_BERT_HP and QBBC physics list agrees relatively well with the data within the systematic uncertainty, while QGSP_BERT tends to over-estimate the RMS for hit energies below 3 MIPs by around 2 ns. Additional comparison plots for other pion energies can be seen in appendix C.

This comparison study seems to confirm that low energy hits are responsible for delayed energy depositions in the calorimeter, most likely due to low energy neutrons from capture and spallation processes. Higher energy deposits occur mostly in the prompt part of the hadron shower.

11.4 Radial dependence of the time

The prompt component of a hadron shower is dominated by EM sub-showers and relativistic particles, whereas the delayed component is coming from mostly evaporation and spallation low energy neutrons. It is expected that the former is concentrated near the shower axis, while the latter, is spread out laterally as these neutrons can travel far away in the calorimeter before interacting.

This is investigated by looking at the mean time of first hit as a function of the hit distance to the shower center of gravity defined in the x-y plane of the calorimeter. For the muon data, the hit position in the detector relative to (0,0) is used. The mean time of the first hit as a function of the hit distance to the shower center of gravity is shown in figure 11.6a for the modules 3 to 10 and in figure 11.6b the modules 11 to 14 separately. The layers needed to be separated because of a decrease of the mean time of first hit at the distance where there is a transition between a single HBU (modules 3 to 10, up to 1λ) and a 2 by 2 HBU (modules 11 to 14, after 1λ). This is thought that this effect may be related to the starting point of the pion shower. This is investigated in more details in section 11.4.1.

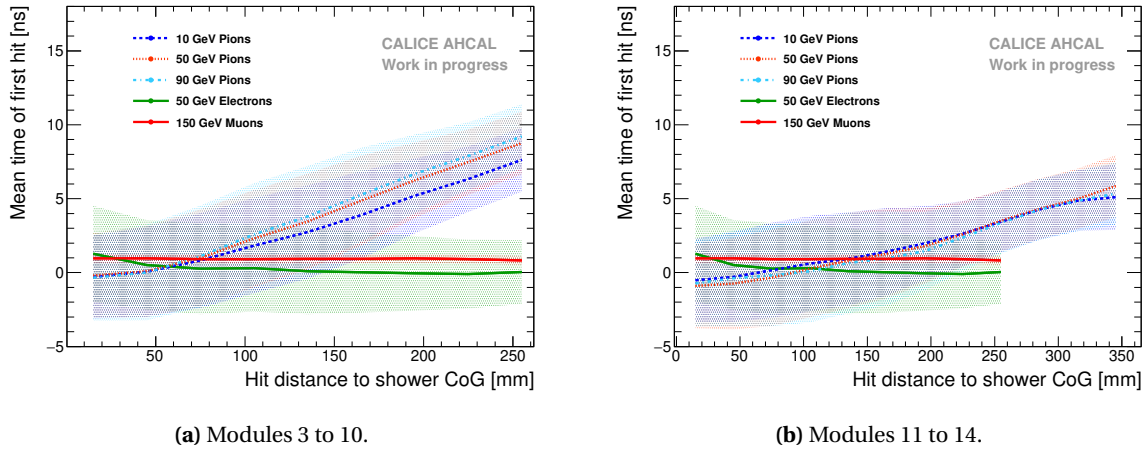


Figure 11.6 – The mean time of first hit for muon, electron and pion beams. The left plot shows the mean time dependency for the modules 3 to 10 and the right for the modules 11 to 14. The reason for the separation is described in the text. The systematics are shown by the color bands.

For muons and electrons, the mean time of the first hit does not vary with the increase of radius as expected as the time calibration forces the mean to 0 ns. On the contrary for hadronic showers, it shows an increase of the mean time of the first hit as a function of the hit distance to the shower axis. As well, there is no dependence on the energy of the shower. However, the modules 3 to 10 present a steeper slope by around 50% than for the modules 11 to 14 (from ~ 1 ns per tile to ~ 0.5 ns per tile).

Nevertheless, the observation is consistent with the expectation of the core of the shower depositing promptly most of the energy via EM sub-showers and relativistic particles near the shower axis. This is followed by a hadronic halo which contributes to delayed signals that may be from mainly neutron-induced

processes. For the modules 3 to 10, the mean time of first hit varies between 0 ns at small radius and 9 ns at 22-23 cm. For the modules 11 to 14, it varies between 0 ns near the shower axis, 4 ns at 25 cm and 6 ns at 35 cm.

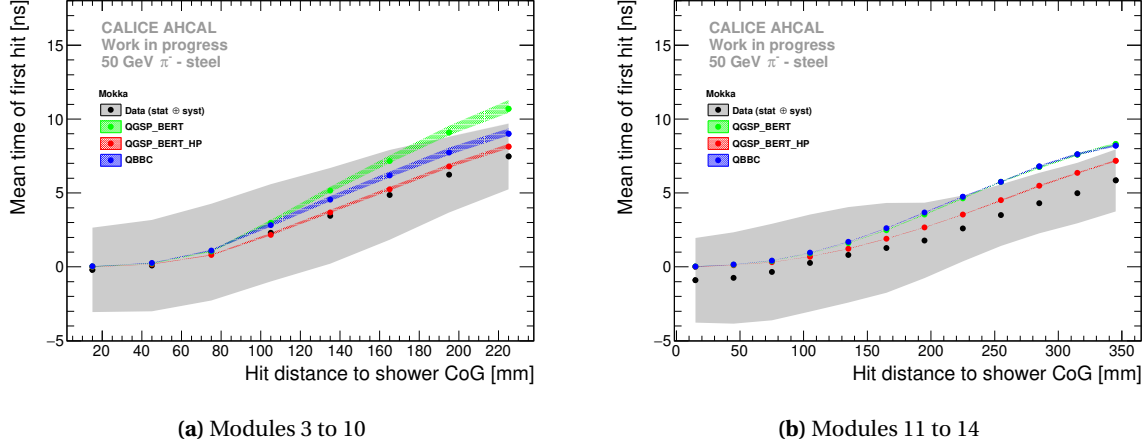


Figure 11.7 – Comparison of the mean time of first hit as a function of the hit distance to the shower axis in data and MOKKA simulation for 50 GeV pion for the modules 3 to 10 on the left and for modules 11 to 14 on the right. The grey and color bands shows the systematics.

The radial dependence of the time of first hit of 50 GeV pion showers is compared to simulations as shown in figure 11.7. For other energies and simulations, the figures can be seen in appendix C. For the modules 3 to 10, the QBBC and QGSP_BERT_HP physics lists reproduce well the data within systematics. The QGSP_BERT physics list agrees well under a 10 cm distance and then starts to deviate from data up to 4-6 ns at 23 cm. Concerning the modules 11 to 14, over the full energy range, the QGSP_BERT_HP physics list agrees the best with the data. The QBBC and QGSP_BERT physics lists agree with data up to around a 10 cm distance and then both lie above the data for higher distances, varying between few ns to 3-4 ns between 17 cm to 35 cm distance. This study shows that without the precision neutron tracking in simulation, too many late energy depositions are created that are spread far away from the shower axis.

Then, the dependency of the RMS of the time distribution as a function of the distance of the hit to the center of gravity of the shower has been studied. The figure 11.8 shows the dependency of the RMS as a function of hit radius for data for both types of modules. The data shows an increase of the RMS for higher hit radius for both types of modules as expected. The muons and electrons show a flat dependency of the RMS as for pions, an increase of the RMS from 5 ns at 0 mm to 20-25 ns at 250 mm is seen for modules 3 to 10 and an increase from 10 ns at 0 mm to 15-20 ns at 350 mm for modules 11 to 14.

The figure 11.9 shows the comparison between data and simulation for 50 GeV pions. For modules 3 to 10, the QGSP_BERT_HP and QBBC physics lists agree relatively well with the data. QGSP_BERT over-estimates the RMS at large hit radius by around 8-10 ns. For modules 11 to 14, all physics lists agree well with data up to a radius of around 100 mm. However, at larger hit radius, QGSP_BERT_HP under-estimates the RMS by around 2 ns while QBBC over-estimates it by around 1-2 ns. Similarly to modules 3 to 10, QGSP_BERT over-estimates greatly the RMS by around 8 ns. Other pion energies have been compared to simulation and they can be seen in appendix C.

This confirms that without the proper treatment of the neutrons, the amount of late deposition is over-

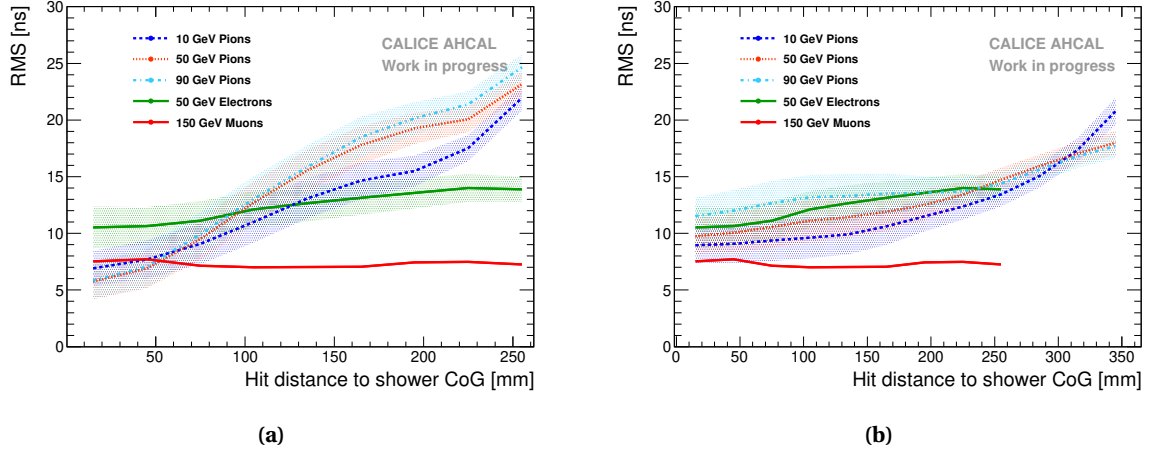


Figure 11.8 – Dependency of the RMS as a function of the hit distance to the shower axis in data for muons, electrons and pions. On the left for the modules 3 to 10. On the right, for modules 11 to 14. The systematics are shown by the color bands.

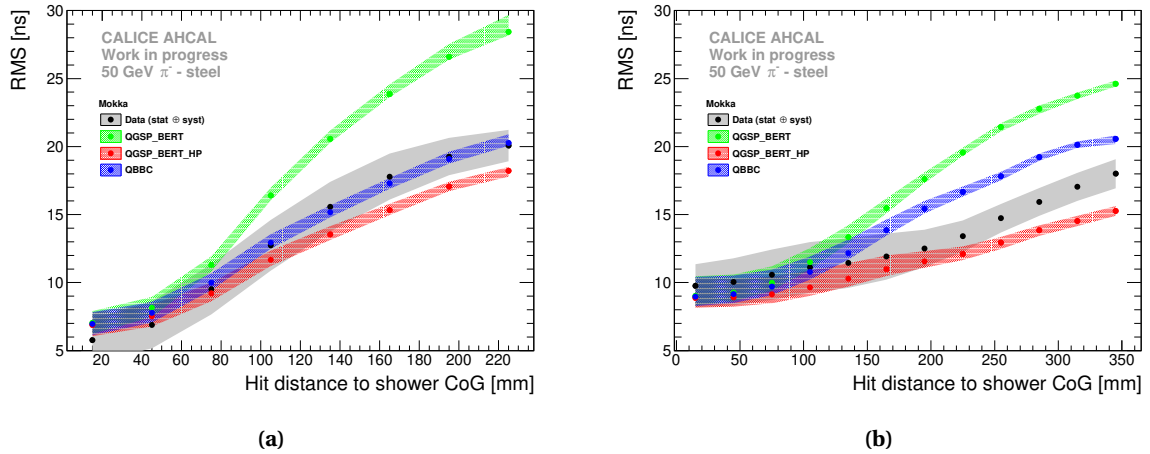


Figure 11.9 – Comparison of the RMS as a function of the hit distance to the shower axis in MOKKA simulation for 50 GeV pion for the modules 3 to 10 on the left and for modules 11 to 14 on the right. The color bands show the statistical and systematic uncertainty.

estimated for hit far away from the center of the shower.

11.4.1 Time dependence with the shower depth

The dependence of the mean time of first hit as a function of the hit distance to the center of gravity of the shower for different modules, i.e. corresponding to different shower depths, is shown in figure 11.10a. One can notice that there is a dependency of the slope of the curve as a function of the module. Module 3 shows a much steeper slope of around 1.8 ns per tile than for the module 14 at 0.6 ns per tile. The observed dependency can be explained by that for the first modules is that the late component could come from the Albedo effect [154] and backscattered neutrons. However, for the last modules, one expects more hits but in average it does not mean that the hits are later. In a hadron shower, MIP-like particles can be generated following a hard interaction in the first modules, these particles then are travelling and scattered to the back at around the speed of light thus explaining why the mean time of first hit can decrease at higher radius. This is confirmed by the simulation with the QGSP_BERT_HP physics list as shown in figure 11.10b. In simulation, the module 3 shows a slope of around 1.7 ns per tile and the module 14 show a slope of 0.5 ns per tile which is well compatible with the observation in data.

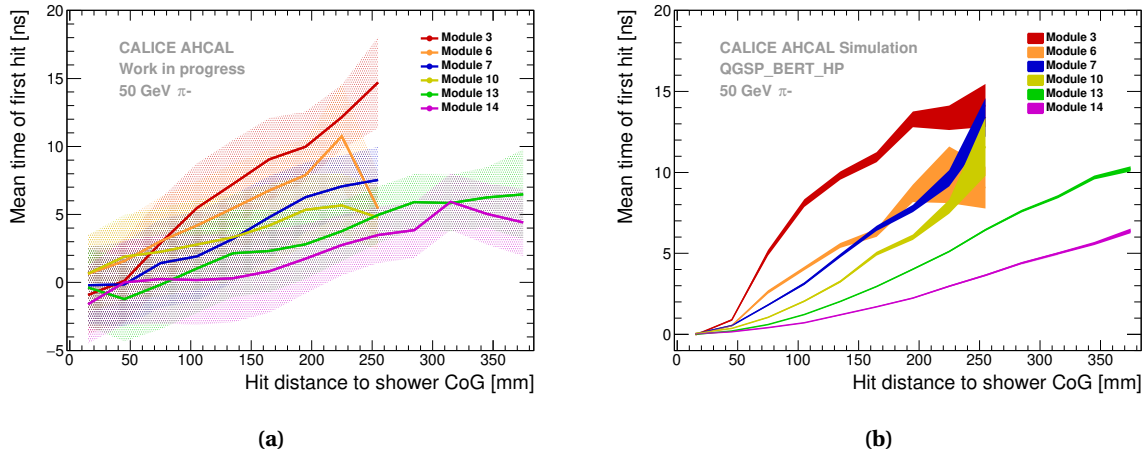


Figure 11.10 – Mean time of first hit as a function of the hit distance to the center of gravity for 50 GeV pions for different modules. On the left, it is shown for data. On the right, it is shown for simulation using the QGSP_BERT_HP physics list. Both figures show the same behavior with a decrease of the curve slope for deeper layers in the calorimeter.

To understand this effect, the mean time of first hit as a function of the hit distance to the shower axis is investigated at a constant distance between a layer and the first hard interaction (FHI) layer. To do this, the shower start finder algorithm is based on previous work [155] in order to find the layer of the first hard interaction. However, slight modifications had to be done due to the fact that some of the layers in the front of the detector show a bad performance with many non-working channels.

The basics of the algorithm is to find the primary pion track and to determine the shower start layer. To determine the shower start layer s_{layer} , the number of hits $n_{Hits}^{i,i+1}$ in the layer i and $i+1$ is counted. If $n_{Hits}^{i,i+1} > 6$, the shower is considered started between layer i and $i+1$. To determine the correct layer, the energy sum between layer i , $i+1$, $i+2$ and $i+3$ are checked in order to determine the correct layer for the start of the shower. In the case of a layer is identified as the FHI, a cross-check on the length of the primary track is

made. The length of the primary track is required to be over three hits. The performance of the algorithm is evaluated by looking at the difference between the reconstructed layer of the FHI and the Monte-Carlo truth information on the start of the shower. This is shown in figure 11.11. The performance of the algorithm is good enough in order to get a good estimate of the FHI layer but it has a small tendency to reconstruct the FHI at a deeper layer.

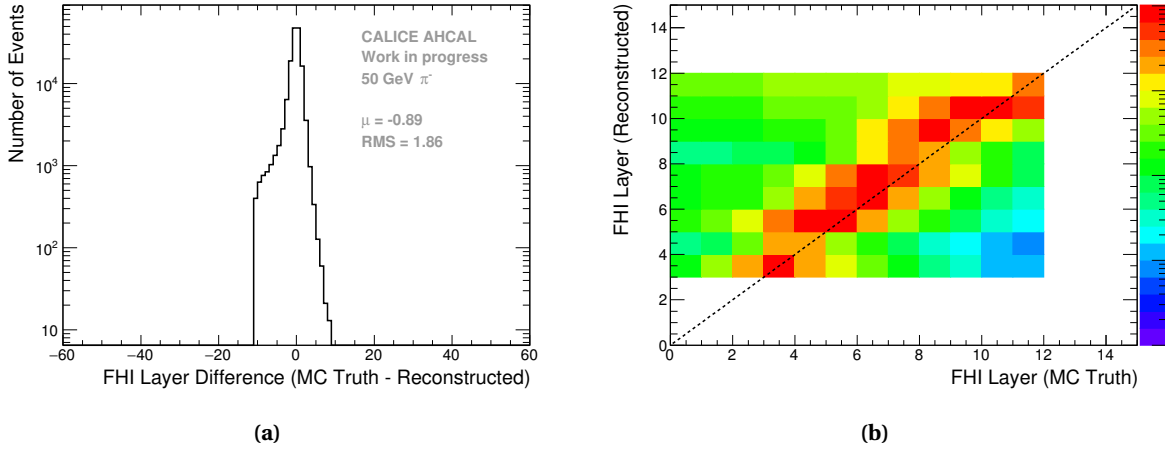


Figure 11.11 – Performance of the FHI algorithm in the AHCAL detector. The left plot shows the difference between the reconstructed FHI layer and the MC truth. The distribution is slightly de-centered at -0.81 with a RMS of 1.87. The right plot shows the correlation between the reconstructed FHI layer and the MC truth. The black line represent a guide for a perfect correlation.

It is expected, at a constant distance between the reconstructed FHI layer and a layer, that there will be the same dependence of the mean time of the hit as a function of the hit distance to the shower axis because in this way, the same part of the shower is sampled. Or that inversely, looking at a fixed layer, the expected behavior would be a change in the slope of the mean time of first hit as a function of the hit distance to the shower axis for different reconstructed FHI layer. The figures 11.12a and 11.13a are an attempt for this study.

The data shows that by fixing the distance between the reconstructed FHI layer and a layer, the mean time of first hit displays the same slope within the systematic uncertainties. On the other hand, by looking at a fixed layer, which is in this case the layer 10, it seems that there is a trend of an increase of the curve slope as a function of the reconstructed FHI layer within the systematics. However, because of many layers not working well, it is difficult to find a different comparable configuration to confirm the observation made. In addition, a reduction of the systematic uncertainty is needed. This has been checked in simulation with the QGSP_BERT_HP physics list as shown in figures 11.12b and 11.13b. The simulation agrees well with the observation made in the data.

11.5 Time dependence as a function of the layer

Hadronic showers develop as well longitudinally, therefore the longitudinal dependence of the mean time of the first hit as a function of the layer was studied. It is expected that the further you are in the calorimeter that more low energy neutrons contribute to the energy deposition thus enhancing the late tail. The figure 11.14a shown the mean time of first hit as a function of the layer for muon, electron and pion beams.

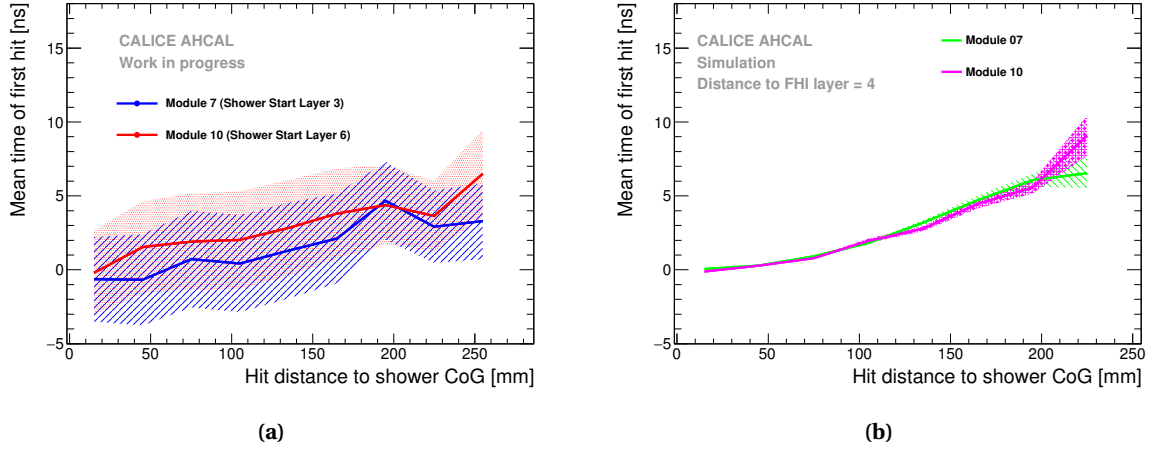


Figure 11.12 – Mean time of first hit as a function of the hit distance to the shower axis for 50 GeV pions for a fixed distance of 4 between the reconstructed FHI layer and a layer. The left plot shows the radial timing profile of modules 7 and 10 in data. The right plots shows the radial timing profile for the same layers in simulation with the QGSP_BERT_HP physics list.

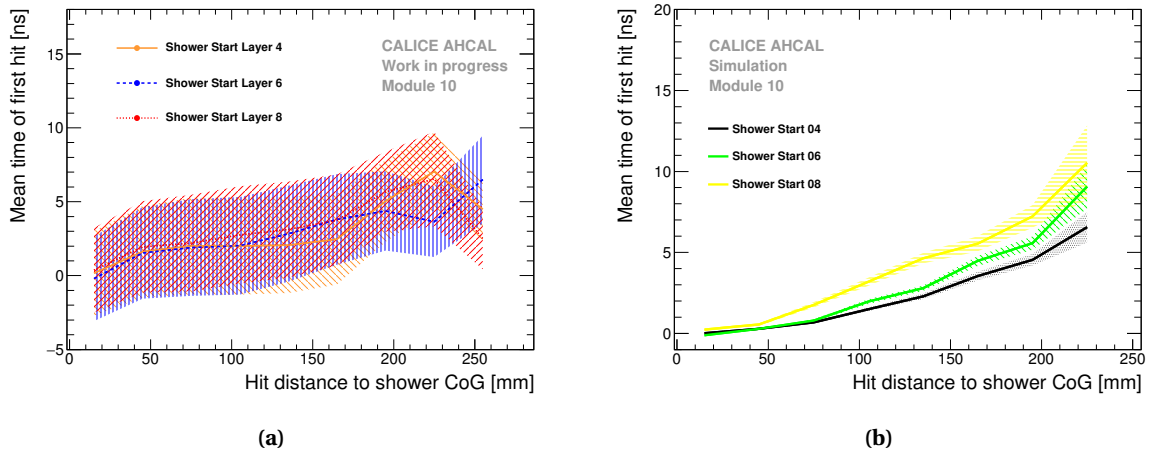


Figure 11.13 – Mean time of the first hit as a function of the hit distance to the shower axis for 50 GeV pions for different reconstructed FHI layers. In data on the left and in simulation with the QGSP_BERT_HP physics list on the right.

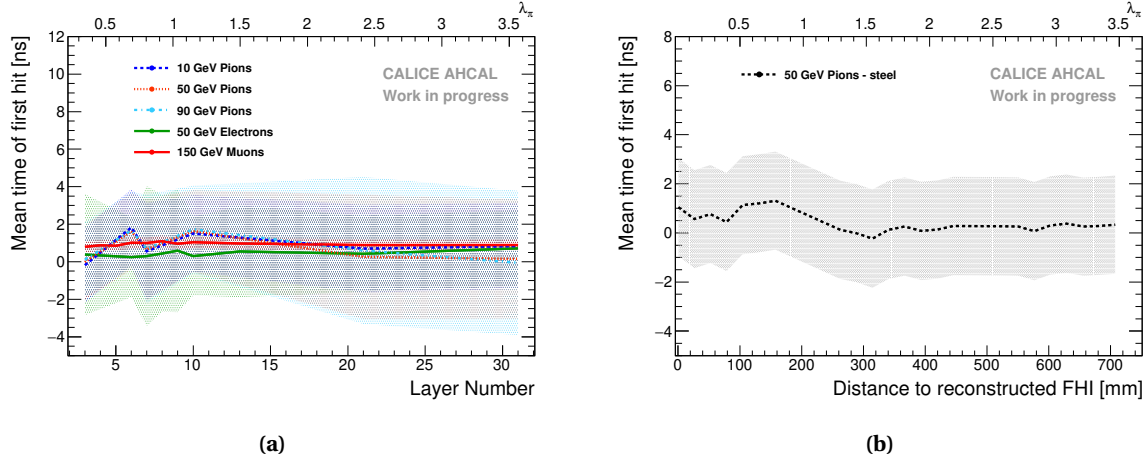


Figure 11.14 – The left plot shows the mean time of the first hit as a function of the layer for muon, electron and pion beams. The right plot shows the mean time of the first hit as a function of the distance to the reconstructed FHI layer for 50 GeV pions.

In data, no increase of the mean time is observed as a function of the layer and as well no beam energy dependence is visible. This may be due to the late component that is suppressed by the high time resolution of the AHCAL and the systematic uncertainty. An attempt was made to get a better sensitivity by looking at the mean time of first hit as a function of the distance to the reconstructed FHI layer as shown in figure 11.14b. However, the figure still shows a flat distribution centered around 0 ns.

The longitudinal timing profile was also compared to simulations. The mean time of first hit is compatible with a flat distribution around 0 ns for all models. The timing resolution of the AHCAL may be too high in order to be sensitive to any small changes of the mean time over the calorimeter depth. To check this, the simulation with the QGSP_BERT_HP physics list without time smearing is shown in figure 11.15b. It shows that there is an increase of the mean time of first hit as a function of the layer in the order of 1 ns and confirms that due to the electronics time resolution this is not visible in data.

Secondly, the dependence of the RMS of the time distribution as a function of the layer has been studied. It is expected the RMS of the time distribution increases for deeper layers in the calorimeter due to the contribution to neutrons. The figure 11.16a shows the RMS as a function of the layer for muons and pions. As expected, the RMS increases from around 8 ns for the first layers to 12-14 ns for the deeper layers for pions and the RMS stays constants for muons.

It has been compared to simulation as shown in figure 11.16b for 50 GeV pions. The QGSP_BERT_HP and QBBC physics lists reproduce well the data while QGSP_BERT over-estimates the RMS by around 2-3 ns except for the last layer where all physics lists agree with the data. The increase of the RMS of the time distribution could come from an increase of the late contribution from slow neutrons. More comparisons between data and simulation for other pion energies can be seen in appendix C.

11.6 Time correlations between modules

The advantage of this studied prototype over T3B is the possibility to investigate time correlations between modules. For this study, the data below 50 ns is ignored as only the tail of the timing distributions is

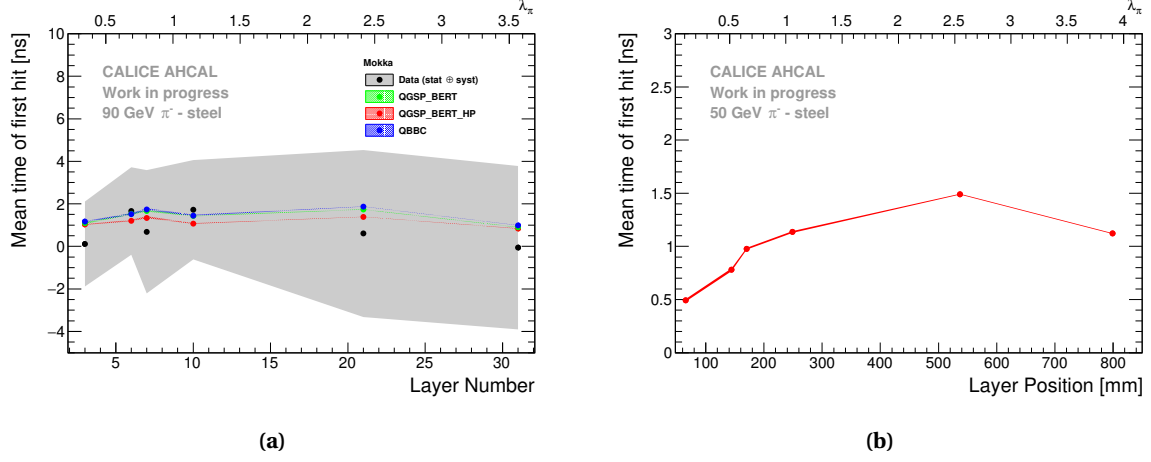


Figure 11.15 – On the left, comparison of the mean time of first hit as a function of the layer in data and Mokka simulation for 90 GeV pions. The grey and color bands show the systematics. On the right, mean time of first hit as a function of the layer for 50 GeV pions in simulation with the QGSP_BERT_HP physics list with no time smearing.

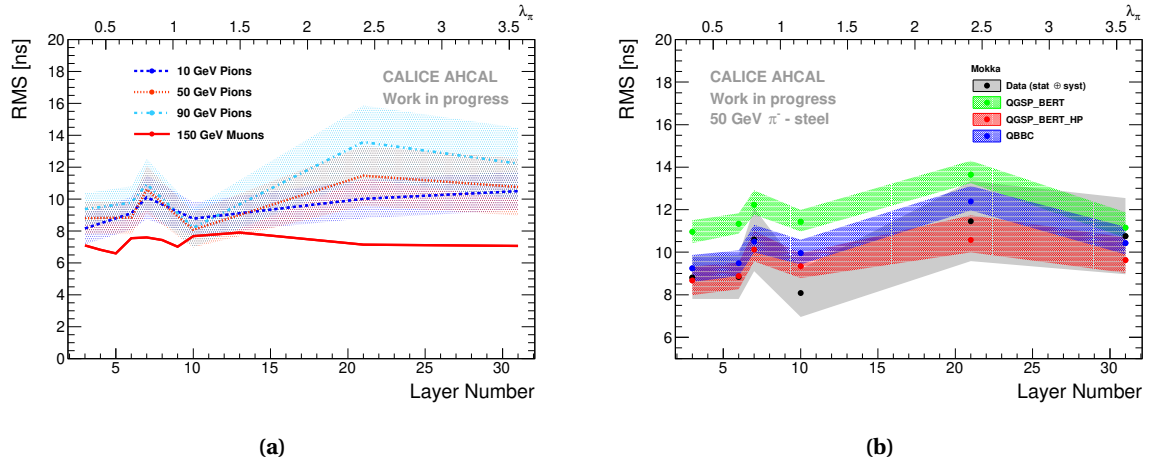


Figure 11.16 – a) The RMS of the time distribution as a function of the layer for muons and pions in steel absorber taken in a range of -50 to 200 ns. b) Comparison between data and simulation of the RMS of the time distribution as a function of the layer. The color bands show the statistical and systematic uncertainty.

investigated.

The procedure is done by looking at each hit in module i and checking in module $i + 1$ for a hit within a distance of 60 mm in the $x : y$ plane. If a hit is found, both times are plotted against each other. If more than one hit is found in module $i + 1$ within a radial distance of 60 mm, the closest in the $x : y$ plane is taken.

Two types of correlations were investigated, short and long. For the short correlation, the modules 6 and 7 were chosen, separated by $1 X_0$ or $0.1 \lambda_\pi$. As for the long, the modules 13 and 14 were selected, separated by $10 X_0$ or $1 \lambda_\pi$. These were chosen due to the fact that few layers were working properly. It is expected that EM sub-showers can lead to a correlation of hit times for the modules 6 and 7, while the modules 13 and 14 are far apart, and therefore would show less or no correlation of hit times. One could expect that a long correlation of hit times is possible due to the production of relativistic MIP-like particles in a hadron shower. However, these particles are produced immediately after the first hard interaction and travel at the speed of light to the back of the calorimeter. A distance of $1 \lambda_\pi$ corresponds to around 0.8 ns assuming that they travel at around 90% of the speed of light and don't interact. Thus a correlation could be only visible within the first nanoseconds thus no correlation should be visible for hit times later than 50 ns. The hit times correlation is shown in figure 11.17 for the 50 GeV dataset.

The figures show that a correlation is visible in the data for both cases. To quantify this, the following ratio is calculated

$$R = \frac{\int_{50ns}^{2\mu s} \int_{50ns}^{2\mu s} \frac{dN_i(t)}{dt_i} \frac{dN_j(t)}{dt_j} dt_i dt_j}{N_{tot}} \quad (11.2)$$

where N_{tot} is the total number of entries in the histogram and the nominator is the number of entries between 50 ns and $2 \mu s$ in the red box of the above figures.

The results show that 18.19% of the entries are in the red box region for the short correlation. This may come from EM sub-showers in the hadron shower. For the long correlation, 3.24% of the entries are in the red box region.

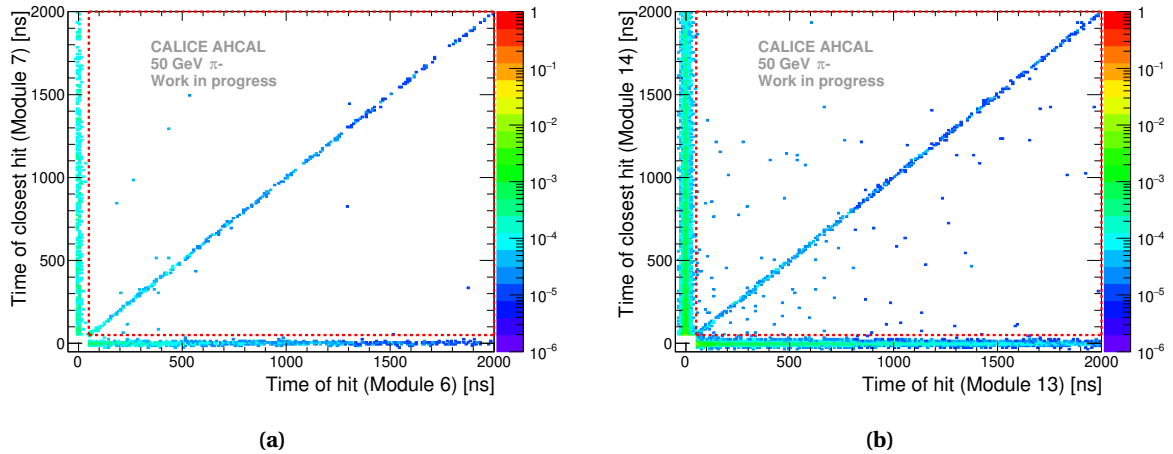


Figure 11.17 – The left plot shows the time correlation between modules 6 and 7 separated by $1 X_0$. The right plot shows the time correlation for modules 13 and 14 separated by $1 \lambda_\pi$. Each bin is normalized to the number of entries in the 2D histogram. The red box represent the region of interest. Both plots show a visible time correlation.

This was compared to simulation using the QGSP_BERT_HP physics lists as shown in figures 11.18. The

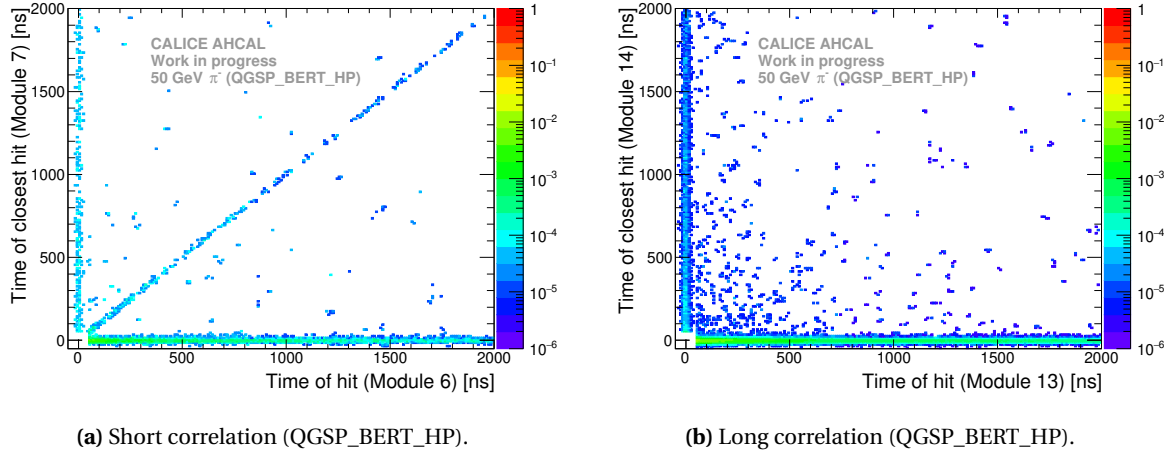


Figure 11.18 – Hit timing correlations between modules 6 and 7 and modules 13 and 14 in the MOKKA simulation with QGSP_BERT_HP for 50 GeV pions. Each bin is normalized to the total number of entries in the 2D histogram.

figures for simulations with other physics lists can be seen in appendix C. In the same way, the number of correlated time hits was calculated and it is summarized in table 11.3. The choice of the physics list is irrelevant for this observable as all physics lists give the same result within 0.1% maximum. Furthermore, the DD4HEP simulation has slightly less correlated hits, around 1%, at a short range than in the MOKKA simulation which is not understood.

Comparing data and simulations, there is a large discrepancy for the short range correlation with an absolute difference of around 15%. For the long correlation, the numbers also differ by around 3% points. The reason for the discrepancy between data and simulation is not clear though it may come from the selection of the data that may be not good enough to reject multi-particle events as shown figure 7.7, therefore providing more correlated hits than observed in simulation. More data, especially with a better detector to be sure to reject multi-particle events, is required in order to understand the origin of such correlations.

Table 11.3 – Table with fraction of entries in the red box region as calculated with equation 11.2. The top is for MOKKA simulations, the bottom is for DD4HEP simulations. The quoted errors are only statistical errors.

Type	Short correlation [%]	Long correlation [%]
Data	18.19 ± 0.93	3.25 ± 0.12
QGSP_BERT	4.08 ± 0.14	0.65 ± 0.02
	3.01 ± 0.14	0.68 ± 0.02
QGSP_BERT_HP	4.10 ± 0.14	0.67 ± 0.02
	3.06 ± 0.14	0.71 ± 0.02
QBBC	4.09 ± 0.14	0.66 ± 0.02
	3.02 ± 0.14	0.69 ± 0.02

11.7 Summary and Outlook

The understanding of the time structure of hadronic showers and the level of accuracy reflected in GEANT 4 simulations is highly relevant for calorimeters at future (linear) collider experiments. This can be applied for conditions with a high level of background such as $\gamma\gamma \rightarrow$ hadrons or high repetition rates experiments to remove out-of-time pile-up events.

A testbeam at the SPS facility at CERN in July 2015 was focused to enhance the knowledge of the time development of hadronic showers. The AHCAL technological prototype, close to the ILD detector design, was equipped with 14 layers inserted in a steel absorber and using scintillator tiles as active material readout by SiPMs to provide radial and longitudinal sampling of showers with a high granularity and a ns-scale time resolution. For the first time, time study of hadronic showers was done which such granular calorimeters using integrated readout electronics.

Energy scale calibration: In chapter 8, the energy scale calibration of the AHCAL was presented. 85% of the AHCAL detector channels have been calibrated to a precision of around 1.7%. The validation studies of the simulation concluded that a good average energy calibration is achieved at the cell level. In addition, the simulation has been further validated with electromagnetic showers and it showed that the data is well reproduced at a level of 10-20% precision in terms of hit energy up to 60 MIPs, energy sum and number of hits.

Time calibration of the AHCAL: In chapter 9, the time calibration procedure of the AHCAL was presented. More than 20000 constants have been determined from data. A time resolution of 5.65 ns for muons is achieved after a simple time calibration of the AHCAL. However, several effects from the front-end electronics can be corrected. The non-linearity correction, related to the non-linearity of the TDC ramp in the ASIC, improves the time resolution by around 5% and the time-walk correction, related to the slow shaper in the ASIC that delays low amplitude signals, improves the time resolution further by 3%. In the end, a time resolution of the order of 5 ns is achieved for minimum ionizing particles.

Validation of the time calibration: In chapter 10, the timing calibration was cross-checked with the electron dataset recorded at CERN and the timing simulation has been validated. It was expected that a time resolution in the same order of magnitude or better than the time resolution obtained for MIPs would be achieved. However, due to the readout electronics that affect the time resolution as a function of the number of triggered channels in a chip, the time resolution for electrons is worse with a value between 7.5 to 8.2 ns for beam energies between 10 and 50 GeV. This effect has been parametrized from data and implemented in the time smearing for the simulation. The simulation reproduces the data within 10-20% for all electron beam energies. However, the tails of the time distribution are not well reproduced due to an imperfect implementation of noise hits. Nevertheless, this is considered good enough for looking at the time development of pion showers.

Timing of hadron showers: In chapter 11, the timing of hadronic showers was studied. Firstly, the absolute time of first hit distribution has been investigated. The data shows a clear tail to late hits compared to muon and electron time distributions. A comparison with simulation has been done for pion beam energies between 10 GeV and 90 GeV. The comparison showed that the QGSP_BERT_HP and QBBC physics lists agree

well with the data. However, the QGSP_BERT physics list overestimates the amount of hits in the late tail by around a factor 5.

Secondly, the energy dependence of the hit time has been studied. The data shows that late hits are concentrated at low hit energies below 1 MIP in iron. The comparison with simulation agrees with the data within the systematics uncertainty.

Thirdly, the radial dependence of the hit time has been investigated. This dependence has been looked at separately for modules 3 to 10 (single HBU) and modules 11 to 14 (2 by 2 HBU) due to a decrease of the mean hit time at the transition radius between the two type of modules. This has been studied in more details and concluded that this feature may be due to a dependence as a function of the start of the shower that showed that the radial dependence of the mean time of first hit decreases with deeper layers. The simulation reflects this feature as well. Anyhow, the data shows that late hits are mostly at a great distance from the shower axis, while prompt hits from electromagnetic sub-showers and relativistic hadrons are predominant near the shower axis. A comparison between data and simulation has been carried out and showed that the QGSP_BERT_HP physics list agrees well with the data but the QBBC and QGSP_BERT physics lists agree with the data up to a hit distance to the shower axis of 100-150 mm and for higher hit distances to the shower axis, these physics lists tend to overestimate the late depositions by 1-3 ns.

Fourthly, the longitudinal dependence of the hit time has been studied. This study concluded that there is no visible dependence for all beam energies. This is due to the timing resolution of the AHCAL that is too high. The simulation without time smearing shows that an increase of the mean time of around 1-1.5 ns is visible as a function of the layer.

Finally, timing correlations between modules have been investigated. Short range ($1 X_0$ separation) and long range ($10 X_0$ or 1λ separation) have been looked at. Time correlations are visible at short range as well as long range in different proportions in the data. In addition, a comparison of detailed simulations with data has been performed. It shows that in general, time correlations are reproduced in simulation but the amount of hits in data and simulation differ quite significantly. This may be due to the selection of the data that does not reject efficiently multi-particle events. More data and investigations to understand the origin such time correlations are needed.

Furthermore, the time resolution achieved in testbeam does not reflect the time resolution that could be accessible in an ILC running mode due to a different frequency of the slow clock (250 kHz in testbeam compared to 5 MHz at the ILC). By extrapolation, assuming that the time resolution scales linearly with the frequency of the slow clock, a time resolution of the order of 1 ns could be obtained in an ILC running scenario. The use of timing information could be a powerful tool to have to help in separating nearby showers in case of very busy events, for example in a ttH event. Timing information could also be used in a software compensation way by using timing bins differentiating electromagnetic sub-showers or relativistic hadrons and the hadronic late component, and weight each individual hit energy to improve the calorimeter energy resolution.

Chapter 12

Application of timing cuts in the ILD detector simulation

Chapter 11 showed that hadronic showers have several components in their time development. Early hit times come most likely from the electromagnetic core of the shower and relativistic hadrons and the late hit times coming from neutrons and late processes in the de-excitation of nuclear states. Hit times could then be used in order to separate the electromagnetic part of the shower from the hadronic part and therefore could be a tool to improve the pattern recognition in particle flow and as well improve the calorimeter energy resolution. This chapter will look at the application of timing cuts for the ILD detector and its impact on hadronic showers.

In this chapter, a study of timing cuts on hadronic shower is performed. The goal of this study is to assess the influence of timing cuts on the properties of hadronic showers as for example the width of the shower as well as the needed time resolution. In the section 12.1, the detector and software framework used in this study will be briefly presented. In section 12.2.3, the influence of timing cuts will be discussed. The study will be divided into 2 parts, the first part assuming a perfect time resolution (see section 12.4) and the second part assuming time resolution for different scenarios (see section 12.4.4.2).

12.1 Simulation and software framework

12.1.1 Event Simulation

In this step, the simulation of the interactions of the particles in the detector and the signals that they produce in the sensitive material is done using GEANT 4. GEANT 4 provides models for particle-matter interactions as explained in section 5.1.

A full GEANT 4 simulation of the ILD detector is implemented in the MOKKA framework and is included in ILCSoft. The MOKKA framework provides a realistic description of the ILD sub-detectors including mechanical support structures, gaps and other non-instrumented material such as electronics and cabling. For this study, the ILCSoft version v01-17-11 is used (with MOKKA v08-05 and GEANT 4 v10.01).

As presented in section 2.3, various technologies are considered for the ILD detector. In this study, the

ILD detector version ILD_o1_v05 is used. This version uses the Silicon Tungsten electromagnetic calorimeter and the Analog HCAL hadronic calorimeter.

The simulation of events is performed by using a particle gun to shoot particles, K_L^0 for this study, with a fixed energy in different regions of the detector by randomly varying the angles θ and ϕ of the gun (see ILD coordinates in section 2.3). To model hadronic showers, the QGSP_BERT_HP physics list is used as this physics list reflects the best the late neutron component of hadron shower. The output of the simulation provides a LCIO file containing collections of the tracking hits and simulated calorimeter hits. This file is reconstructed with the MARLIN framework.

12.2 Event Reconstruction

The reconstruction is done on simulated data in order to implement detector electronic effects to obtain similar signals from a real experiment. The reconstruction of an event is mainly done by track finding and pattern recognition. The reconstruction is generally done in several stages in a way that the output of one stage can be used latter on for another stage. The output of the reconstruction is a collection of particle flow objects (PFOs) that contains information on the measured particle in the detector. The ILCSOFT framework with MARLIN are used for the reconstruction of events.

12.2.1 Tracking

Generally, in the first step, track fitting is performed on each individual tracking detector. Track segments are identified by pattern recognition algorithms. A track fitting is performed using the track segments with a Kalman filter [156, 157] to identify trajectories of charged particles. Each track contains origin, direction, charge and momentum of the particle.

12.2.2 Calorimeter digitization

In a next step, simulated calorimeter hits are digitized. This is done as part of the *ILDCaloDigi* processor [158]. This MARLIN processor digitizes ECAL and HCAL simulated hits to obtain a realistic hit measurement by implementing technology specific effects for scintillator-SiPM readout and silicon readout. This processor can apply thresholds in hit energy and hit timing, simulation dead cells, mis-calibrations per cell and a gaussian electronic noise contribution [137].

Relevant for this thesis, the timing of hits is obtained following these steps:

- For each simulated hits, sub-hit contributions are looped over.
- Sub-hits are added if $t_{min} < t_{subhit} - t_{ToF} < t_{cut}$, where t_{min} is the minimum time window with a default value of -1 ns, t_{cut} is the maximum time window with a default value of 100 ns and $t_{ToF} = r_{hit}/c$ is a time of flight correction and it is a simple assumption that the hit originates from the detector origin.
- A digitized calorimeter hit is created with the energy sum of all sub-hits in the time window and with a time corresponding to the earliest sub-hit time.

This procedure is done in order to simulate the time acceptance of the readout electronics. This modelization of timing is very simplified as in reality the electronics are shaping the signal with a certain shaping time and

register the time of the first contribution over the threshold (default is 0.5 MIP) as explained in section 5.3.2. The smearing of the time hit (only performed on HCAL hits) is done adding a smearing contribution t_{smear} to the digitized calorimeter hit where t_{smear} is obtained by randomly picking up a value using a normalized Gaussian centered at 0 ns with a steerable timing resolution σ_t .

12.2.3 Pandora PFA

Finally, fitted tracks and digitized calorimeter hits are used to form Particle Flow Objects (PFO) using the particle flow approach. PandoraPFA [80] is the Particle Flow algorithm used for Linear Colliders as explained in chapter 3.3. It uses a complex multi-stage process but basically, calorimeter hits are clustered and associated to tracks (if any). Then a re-clustering step is merging or splitting clusters in order to match the track energy if any. If the right criteria are matched, it forms a PFO which contains information about the reconstructed objects.

The timing of hits is registered in a very simplified way as explained in section 12.2.2. Different time windows ranging from 1 ns to 100 ns are used. This is done to evaluate the effects of such timing window on the reconstruction of hadronic showers. To generate hadronic showers almost exclusively inside the hadronic calorimeter, neutral kaons particles (K_L^0) are used with energies ranging from 5 GeV to 90 GeV, corresponding typically to the energy range of particles inside a jet of energies between 50 to 250 GeV. The kaons are projected exclusively inside the barrel at a direction (0.5, 0.5, 0.1) corresponding to the middle of an ILD HCAL stave at angles θ between 0 and 35 degrees and ϕ up to 360 degrees. This is done to avoid the barrel-endcap transition and keep the generic nature of the results. The QGSP_BERT_HP physics list is used to simulate hadronic showers.

12.3 Check of the energy reconstruction

Before studying the effect of timing on hadrons showers, it is important to check the energy reconstruction of the ILD detector with the initially provided calibration constants. The energy is initially reconstructed by scaling the hit energy of calorimeters with various constants. The main important ones are:

- A constant used for converting the energy from GeV to MIP. For the HCAL, the constant is *CalibHCALMIP* and is equal to 497.5 keV/MIP.
- The light yield constant used to convert MIP to pixels. For the HCAL, this constant is equal to 15 pixels per MIP.
- A constant used for the scaling of the reconstructed hit energy due to the sampling fraction of the calorimeters. For example, the *CalibrHCALBarrel* constant is responsible for the sampling fraction in the HCAL barrel and is equal to 50.8262.

In a next step, the digitized hits are passed on to PandoraPFA. Several energy reconstruction schemes can be done with PandoraPFA:

- Simple energy reconstruction: The energy of all hits belonging to a cluster are added.
- Energy truncation: The energy of a cell is truncated when it is over 1 GeV [159].

- Software compensation (SC): the EM and HAD component of a shower are weighted to correct for non-compensation nature of the AHCAL [159].
- Non-linearity correction (NLC): a correction is applied to the cluster energy to account for non-linearity effects introduced by PandoraPFA.

However, the calibration constants used by PandoraPFA need to be prior calibrated. The calibration procedure is explained in [160]. To cross-check the energy calibration, the calorimeter linearity and energy resolution have been investigated. Both have been looked at the hit level, i.e. before PandoraPFA and at the cluster level, i.e. after PandoraPFA. The same procedure as described in *Pandora Analysis* package is used to determine the energy resolution defined as $\text{RMS}_{90}/\text{Mean}_{90}$. RMS_{90} and Mean_{90} are from a Gaussian fit in the smallest range of total reconstructed energy which contains 90% of all events. This makes the energy resolution from single particles directly comparable to the energy resolution of the CALICE AHCAL [106, 159], which is determined from Gaussian fits to the reconstructed energy. Only events in the barrel ($|\cos\theta| < 0.7$) and with a single reconstructed Particle Flow Object (PFO) are selected for this cross-check.

Figures 12.1 and 12.2 show the linearity and resolution curves for different cases, in all cases, the reconstructed energy is obtained by summing up the energy of all calorimeter hits. The blue and black curves, representing the cases where software compensation or energy truncation are used, are similar as well as the green and red curves, representing the case where the energy truncation and the non-linearity correction are used after a recalibration of the PandoraPFA calibration constants has been performed. This is because the energy reconstruction scheme does not affect the calorimeter hit energy. The blue and black curves deviate from linearity due to mis-calibrated hit energy scaling constants. The linearity curve varies between -5% and 5% and also crosses the line $x = y$ which if corrected would degrade the energy resolution. The red and green curves are obtained after the recalibration of the hit energy scaling constants therefore differ from the blue and black curves. The non-linearity correction does not have an effect on the reconstructed energy because it is only applied to clusters. The linearity fluctuates between -10% and 0% but does not cross the line $x = y$. Looking at the energy resolution, all the curves are very similar. The recalibration of the scaling constants improves slightly the energy resolution by around 1%. This cross-check shows that the hit energy scaling constants have a large influence ($\sim 5\%$) on the energy linearity of the calorimeter. However, the effect is relatively small ($\sim 1\%$) on the energy resolution of the calorimeter.

Figures 12.3 and 12.4 shows the linearity and resolution curves for different energy reconstruction schemes after PandoraPFA. By comparing these figures to the one shown above, it enables to understand the effects of the different energy reconstruction schemes in PandoraPFA. The reconstructed energy is the energy of the reconstructed PFO. For the linearity curve, the red and black lines in the case of energy truncation reconstruction scheme are similar and show a non-linearity especially at high energies between -10% and 2%. It shows that the energy truncation introduces a non-linearity effect on the energy reconstruction. The difference between the curves could be related to the difference of the hit energy scaling constant. However, it has a small effect around 1-2% that may come from the clustering step in PandoraPFA. The green curve in the case of energy truncation and non-linearity correction reconstruction scheme shows a linear behavior. The blue curve in the case of software compensation reconstruction scheme deviates from the linearity by around 10%. This is believed to be related to the software compensation weights applied in the reconstruction scheme that were not optimized for this ILD model. Regarding the resolution curves, a very small rise ($\sim 1-2\%$) of the resolution at high energies of the black, red and green curves is visible. As expected, a degradation of the

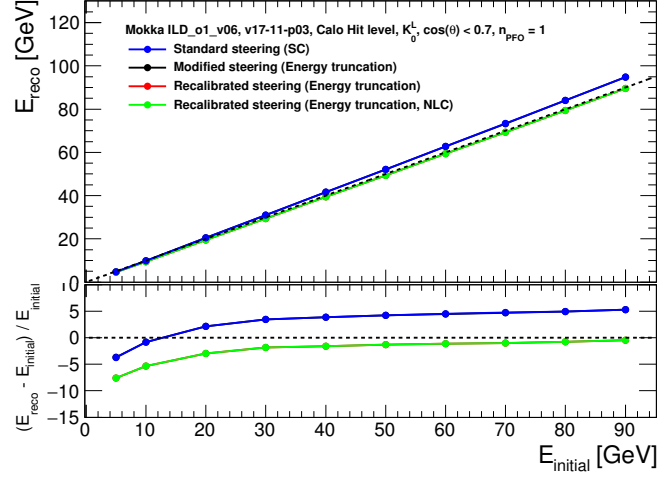


Figure 12.1 – Mean reconstructed energy E_{reco} for 5 to 90 GeV K_L^0 as a function of the simulated energy $E_{initial}$. The reconstructed energy is the sum of all calibrated hit energies. The bottom plot shows the relative deviation from linearity. Error bars represent the statistical uncertainty. The black and blue curves represent the cases where software compensation or energy truncation reconstruction scheme is used and are the same. The red and green curve are the same, representing the case where the energy truncation and the non-linearity correction reconstruction scheme are used after a recalibration of the PandoraPFA calibration constants has been performed.

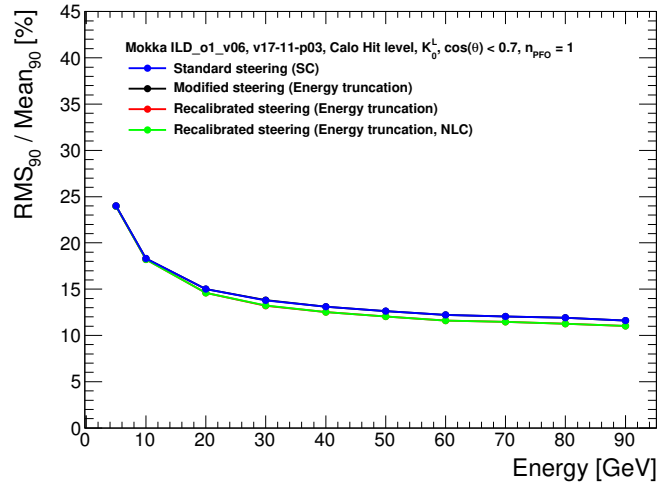


Figure 12.2 – Relative energy resolution $RMS_{90}/Mean_{90}$ as a function of the energy. Error bars represent the statistical uncertainty. The black and blue curves are the same and the red and green curve are the same.

energy resolution is observed where the non-linearity correction is applied. In the software compensation reconstruction scheme, a slight change in the curve can be seen at 50 GeV. This is correlated with the change of the curve slope in the linearity plot.

Despite that the energy linearity is not perfect, the energy reconstruction, after the recalibration of the different constants used in the reconstruction, is good enough to study the impact of timing cuts on hadronic showers. In the following analysis, the different hadronic shower variables will be obtained at the individual hit level. This is done in order to avoid clustering effects from PandoraPFA.

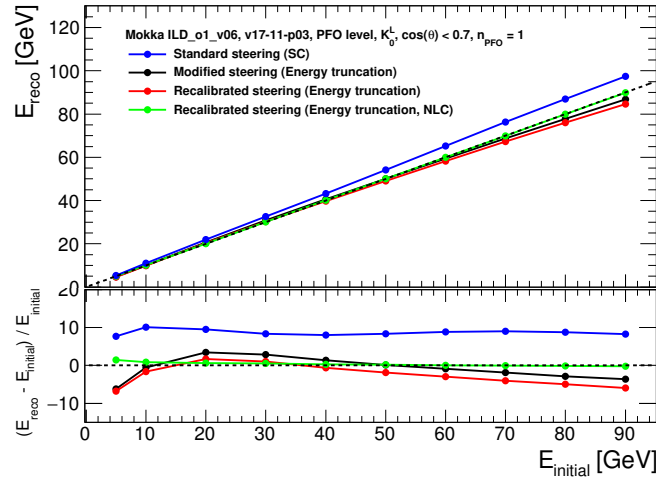


Figure 12.3 – Mean PFO reconstructed energy E_{reco} for 5 to 90 GeV K_L^0 as a function of the simulated energy $E_{initial}$ for different energy reconstruction schemes. The bottom plot shows the relative deviation from linearity. Error bars represent the statistical uncertainty.

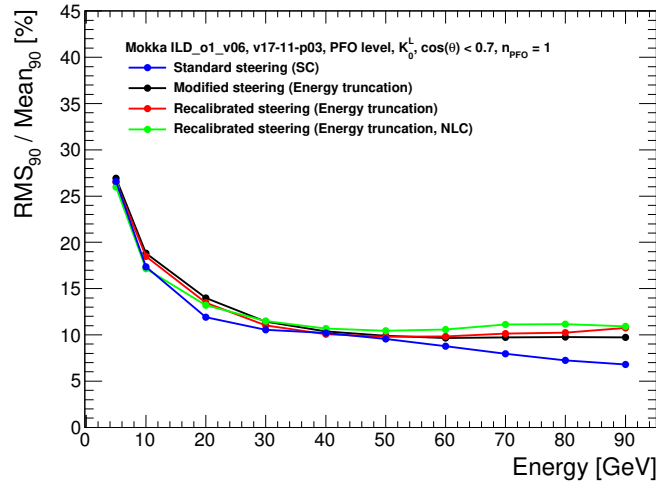


Figure 12.4 – Relative PFO energy resolution $RMS_{90}/Mean_{90}$ as a function of the energy for different energy reconstruction schemes. Error bars represent the statistical uncertainty.

12.4 Influence of timing cuts on hadronic showers in the ILD detector

12.4.1 Motivation

To illustrate typical topological situation, the figure 12.5 shows the momenta distribution and distances of two classes of events: for jets representative of heavy boson decay near production threshold $e^+e^- \rightarrow Z/\gamma \rightarrow q\bar{q}$ with $q = u, d, s$ and for heavy boosted jets with a more complex event topology $e^+e^- \rightarrow W^+W^- \rightarrow q\bar{q}q\bar{q}$ where q is a quark. They show that typically the momentum spectrum is dominated by low momenta below 10-20 GeV while the minimal distance (measured at the front face of the SiW-ECAL) between a charged and neutral hadron changes greatly depending of the center of mass energy.

In the case of the production of a Z boson near threshold, the mean distance is around 180 mm thus in this context, showers are well separated. However at higher energies where density is higher, typical distances of 50 mm need to be resolved. This situation can become relevant in the contribution of confusion to the jet energy resolution. In this case, the use of timing information could help to separate nearby showers and improve the pattern recognition.

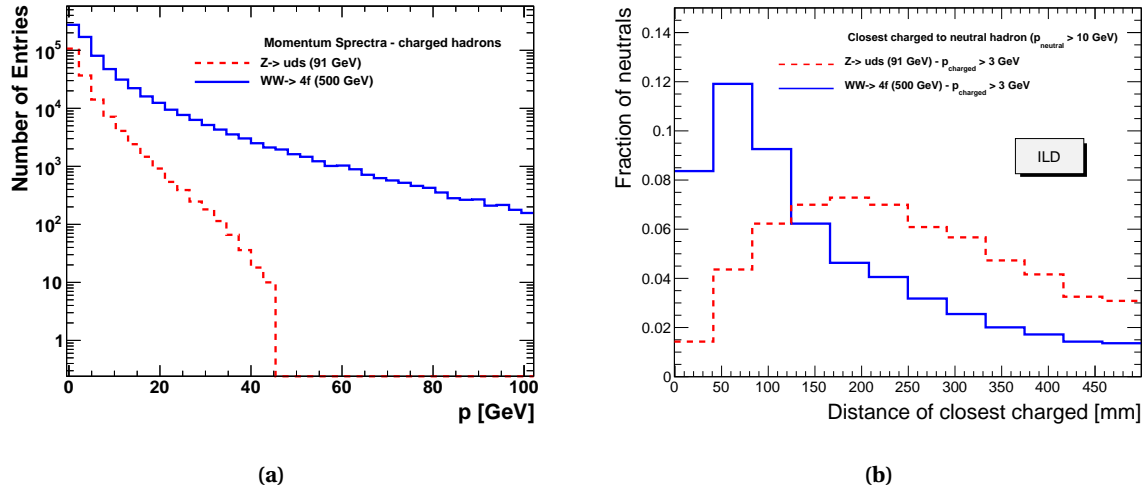


Figure 12.5 – **a)** Momentum distribution for charged particles in simulated $e^+e^- \rightarrow Z/\gamma \rightarrow q\bar{q}$ with $q = u, d, s$ at $\sqrt{s} = 91$ GeV and $e^+e^- \rightarrow W^+W^- \rightarrow q\bar{q}q\bar{q}$ where q is a quark at $\sqrt{s} = 500$ GeV. **b)** Distribution of distances to the closest charged track for neutral particles produced in $Z/\gamma \rightarrow q\bar{q}$ and $W^+W^- \rightarrow q\bar{q}q\bar{q}$ processes measured at the front face of the electromagnetic calorimeter in the ILD detector.

In this section, the effect of timing cuts on hadronic showers is investigated. The study was performed using the ILCSoft framework for reconstruction. In order to study the effect of timing on hadronic shower properties, the initial study was performed assuming a perfect timing resolution (i.e. the timing information is the Monte-Carlo truth). In a following step, several timing resolutions were used to assess different scenarios.

12.4.2 Event Selection

In this analysis, events are selected similar as in [106] and based on the following criteria:

- A single Particle Flow Object (PFO) is reconstructed (except for section 12.4.3).

- The reconstructed particle must be in the barrel region such as $|\cos\theta| < 0.7$.
- The ratio of E_{ECAL}/E_{total} is under 5% to ensure that the shower is mostly in the HCAL.
- The start of the shower must be inside the first 5 HCAL layers in order to have the shower mostly in the HCAL and reduce the effect of leakage.

In the following analysis, the timing cut is defined such as the calorimeter hits are rejected if $t_{hit} - t_{ToF} > t_{cut}$ (see section 12.2.2 for the definition of t_{hit} and t_{ToF}).

12.4.3 Impact of timing cuts on Particle Flow Object reconstruction

Firstly, the impact of timing cuts on the number of reconstructed particles was investigated. The figure 12.6a shows the number of reconstructed PFO per event for different timing cuts. The figure shows that up to four, five PFOs can be reconstructed in a single event. These events are primarily due to small shower fragments that are not correctly associated with the main cluster. In addition, the figure demonstrates that timing cuts reduce the number of events reconstructed with more than one PFO. It is expected because timing cuts would likely remove shower fragments that are not associated with the main cluster and therefore reconstruct fewer events with more than one PFO. Furthermore, the impact has been studied for all energies between 5 GeV and 90 GeV. Figure 12.6b shows the number of events reconstructed with a single PFO relative to the default configuration with 100 ns timing cut. Timing cuts increase the fraction of reconstructed events containing a single PFO over all energies between 10-25%.

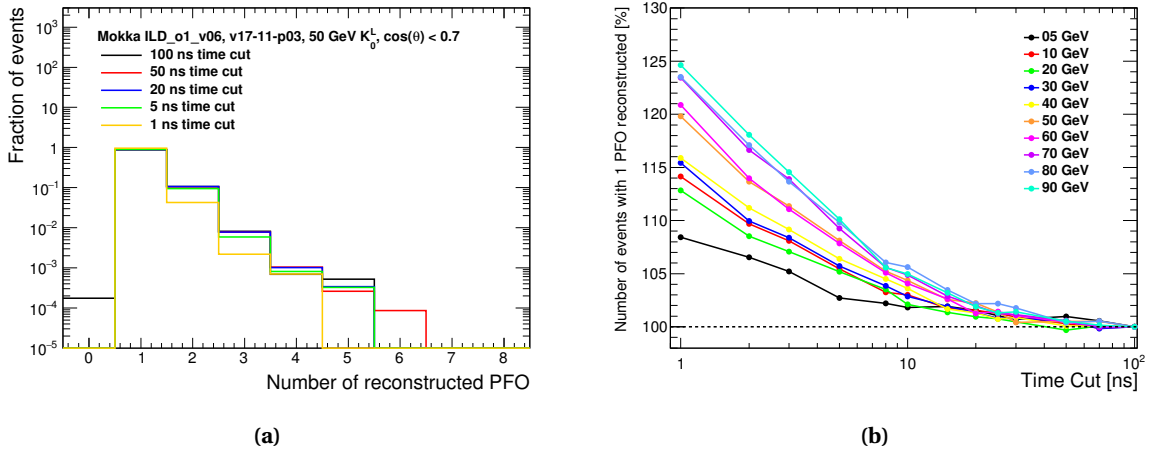


Figure 12.6 – a) Distribution of the number of PFO reconstructed per event for 50 GeV K_L^0 in the ILD barrel for different timing cuts. It shows that timing cuts indeed improves the number of events reconstructed with a single PFO but as well a large tail is present. The use of timing cuts reduces slightly the tail of the distribution. **b)** Number of events reconstructed with only a single PFO normalized to the number of events in the case of 100 ns. It shows a relative increase with a lower timing cut, up to 10-25% more events are reconstructed with a single PFO using a 1 ns timing cut.

To understand more into details what happens, the figures 12.7a and 12.7b show the energy distribution and the distance of the second most energetic cluster to the main cluster for events where more than one PFO is reconstructed for 50 GeV K_L^0 for different timing cuts of 100 ns and 1 ns.

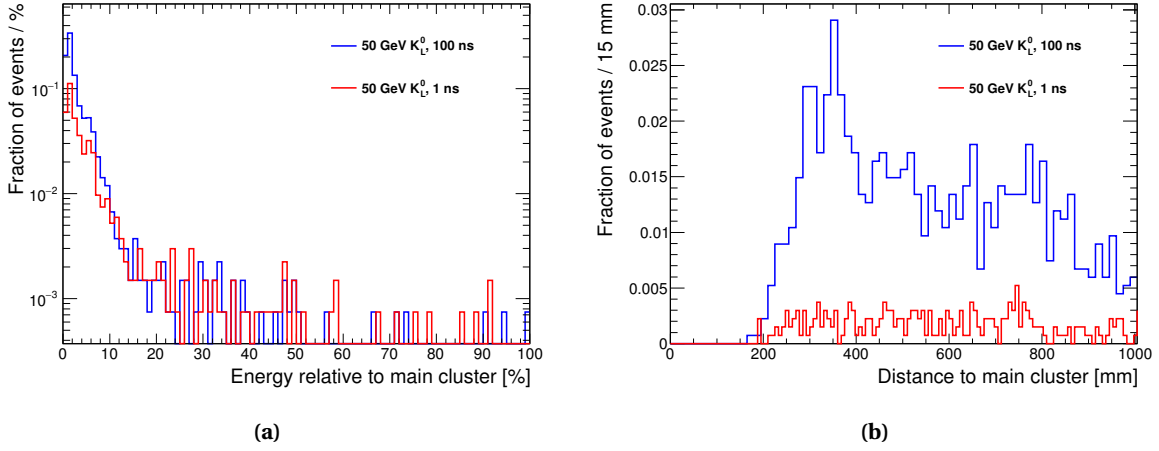


Figure 12.7 – a) Normalized energy distribution of 2^{nd} most energetic cluster. One can see that most of the entries are below few percents. b) Normalized distance to main PFO of 2^{nd} most energetic cluster. The distribution peaks in the region 25-30 cm.

The figures show that the second most energetic cluster has mostly an energy below few percents of the main cluster energy, over 97% of the entries are below 20% of the main cluster energy. The mean distance of this second cluster is around 25-30 cm from the main cluster with around 22% of entries below 40 cm and is comprised of a long tail to higher distances. This is visible for both timing cuts of 100 ns and 1 ns. This tells us that mainly the split cluster has little energy compared to the main cluster and is situated at around 7 to 10 AHCAL tiles away from the main cluster which is far enough to not be recombined by PandoraPFA with the main cluster. These clusters may be coming from low energy neutrons traveling through the calorimeter. This explains that by introducing a timing cut more events are reconstructed with a single PFO. As shown in chapter 11, low energy neutrons are correlated with low energy deposition and late depositions far away from the shower axis and are removed with a timing cut below few tens of nanoseconds.

12.4.4 Impact of timing cuts on calorimeter performance and hadronic showers

12.4.4.1 Assuming perfect time resolution

The following section presents results of timing cuts on the calorimeter performance and hadronic showers assuming a perfect time resolution. To avoid any clustering effects, the study was performed at the calorimeter hit level. The reconstructed energy is obtained by summing up the energy of all hits in the calorimeters. In addition, several shower observables were studied as a function of the timing cut for energies from 5 GeV to 90 GeV K_L^0 . The different time cuts used are: 1, 2, 3, 5, 8, 10, 15, 20, 25, 30, 50, 70 and 100 ns.

The figures 12.8 and 12.9 show the effect of the timing cuts on the calorimeter response and energy resolution. The response decreases and energy resolution gets degraded for lower timing cuts. The response degrades as much as 10% at high energies for a 1 ns timing cut. This would effectively mean that with a harder timing cut, more hits of the shower are removed but without affecting much the total shower energy.

The figure 12.9 shows the relative impact on the calorimeter energy resolution as a function of the energy for different timing cuts. The energy resolution is very little affected by a cut of above 20 ns. Then for a cut

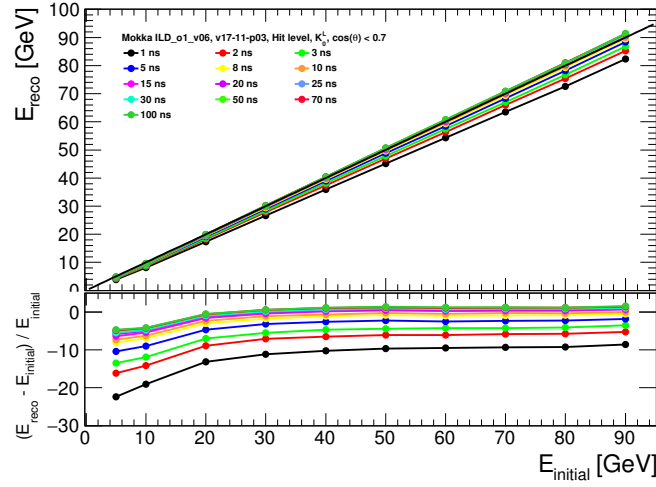


Figure 12.8 – The top plot shows the reconstructed energy E_{reco} as a function of the initial particle energy $E_{initial}$ for different timing cuts assuming a perfect time resolution. The bottom plot represent the relative deviation to the line $x = y$ for the different time cuts.

under 20 ns, the resolution starts to degrade slowly relatively in the same way for all energies. A hard cut of 1 ns will degrade greatly the energy resolution by around 20-30% relative to 100 ns. The degradation of the energy resolution comes mostly from an increase of the constant term. Naively, ones would expect that if for example randomly 10% of the shower energy is removed in average that then the resolution would behave as \sqrt{E} and would degrade by around 6% from a statistical point of view. However, timing cuts do not remove hits randomly. There is a bias to remove late hits which are mostly coming from the hadronic component of the shower. As in hadronic showers, the electromagnetic and hadronic fraction of the shower is fluctuating a lot on an event-by-event basis this may affect the energy resolution much more. To understand this effect, a similar study as in [106] has been performed in section 12.5. The figure 12.10 shows the fraction of energy of the shower as a function of the timing cut. It shows that 99% of the shower energy is deposited within 15 ns. Thus, up to a timing cut of around 15 ns, the energy resolution should not be degraded which is compatible with the observation in figure 12.9.

The figure 12.11 shows a K_L^0 radial shower profile at 50 GeV. For the calculation of the radial profile, the energy within each radial bin of 3 cm width is summed up and normalized to the bin area. The average energy deposit per area is displayed as a function of the distance to the shower main axis. Almost all the shower energy is contained in a circle of few centimeter radius. The influence of timing cuts is highly visible in the tail of the distribution corresponding to the halo of the shower while they have little influence on the energy deposited in the core of the shower. A cut at 1 ns reduces up to 30% the radial shower profile above 30-40 cm. In addition, an increase of energy in the two first bins of the distribution is visible. This effect is related to a displacement of the center of gravity as a function of the timing cut because outer hits of the shower are removed. This was verified by calculating the distance relative to a fixed reference, i.e the endpoint of the MC particle, instead of the center of gravity. In this case, it has been observed that timing cuts remove only part of the distribution tail without affecting the two first bin of the distribution.

The shower width is calculated as the mean distance of all the hits to the shower main axis according to

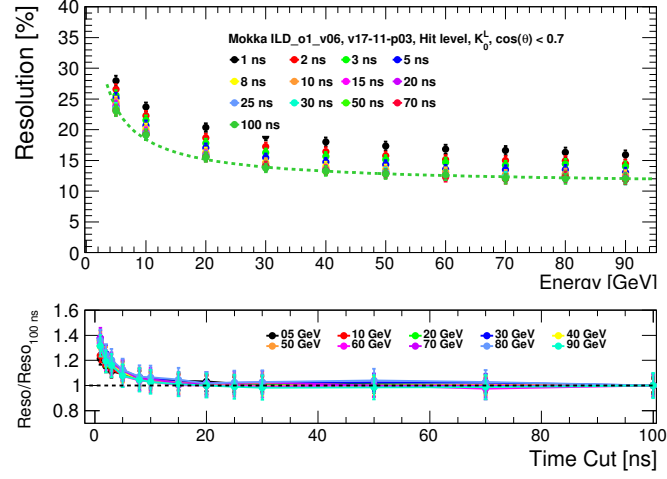


Figure 12.9 – The top plot illustrates the relative energy resolution ($\frac{\sigma_E}{E}$) at single particle level for different timing cuts. The green line is a fit performed at 100 ns of the form $\frac{\sigma_E}{E} = \frac{a}{\sqrt{E}} \oplus b$ where a is the stochastic term ($46.73\% \pm 2.03$) and b the constant term ($10.99\% \pm 0.41$). The bottom plot shows the relative change of the energy resolution compared to 100 ns as a function of the timing cut for each particle energy. The error bars represent the statistical uncertainty.

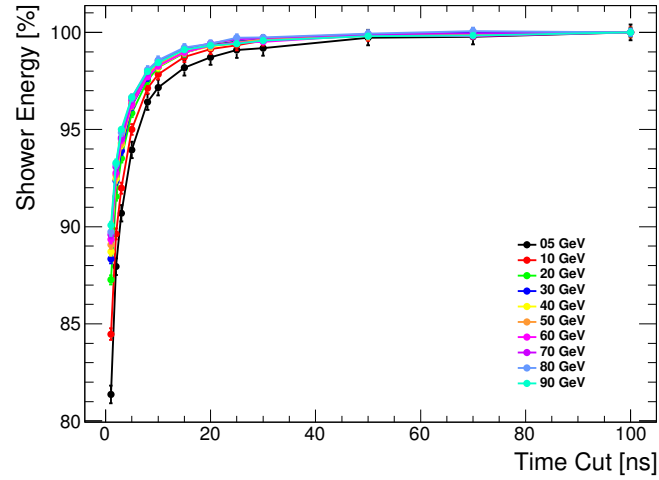


Figure 12.10 – Fraction of the total shower energy as a function of the timing cut. The fraction is defined such as the shower energy at a 100 ns timing cut is 100%.

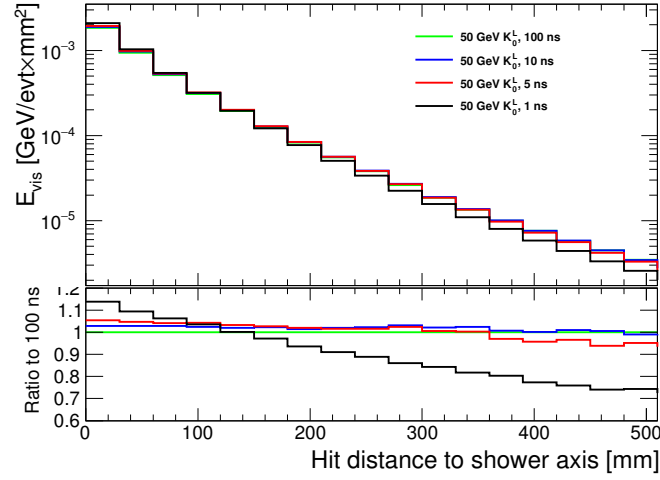


Figure 12.11 – The top plot shows the radial profile of a 50 GeV hadronic shower overlaid for different timing cuts. The bottom plot shows the ratio of the histograms to 100 ns radial profile.

the formula:

$$w = \sqrt{\frac{\sum_i E_i \times r_i^2}{\sum_i E_i}} \quad (12.1)$$

where E_i is the energy of the i -th hit and r_i is the distance of the i -th hit to the cluster main axis.

The figures 12.12a and 12.12b show the shower width for different particle energies as a function of the timing cut. It shows that a timing cut of 1 ns can reduce the shower width by around 40-50%. One can observe also that the shower width at 5 and 10 GeV are behaving differently than for higher energies. This may come from the transition from the Bertini model (BERT) to the quark string gluon model (QGSP) in the physics list in this energy range. Looking at the shower width in absolute value, hadronic showers are slightly wider at lower energies with a mean width of ~ 125 mm for 10 GeV and ~ 115 mm for 90 GeV. This may be related to the fact that the electromagnetic fraction in a hadronic shower increases with energy. Therefore, the mean shower width is reduced because the hits close to the shower axis carry most of the energy. In general, all energies behave in a rather similar manner.

Finally, it is interesting to look at the gain in the reduction of the shower width compared to the loss in energy resolution. Reducing the shower width by applying timing cuts could help to improve the pattern recognition in PandoraPFA. The figure 12.13 shows the resolution loss as a function of the shower width for different K_L^0 energies and different timing cuts. The bottom plot shows that the gain in shower width is behaving in the same way for all energies. The shower width is reduced and the resolution gets slowly degraded for tighter timing cuts. The main point here is that the gain in shower width is great, up to 40% decrease in shower width, compared to the loss in energy resolution which is around 4-6% (absolute) that could be recovered in a next step after pattern recognition.

To conclude, this study shows that the use of timing cuts give a great advantage in order to improve pattern recognition without degrading too much the energy resolution of a hadronic shower. A timing cut up to 15 ns does not degrade the energy resolution and would reduce the shower width by around 10%. A cut below 15 ns starts to degrade heavily the energy resolution and reduce as well the shower width. The needed time resolution depends on the aim for the use of timing. A cut at 25 ns like the LHC looks good enough. However,

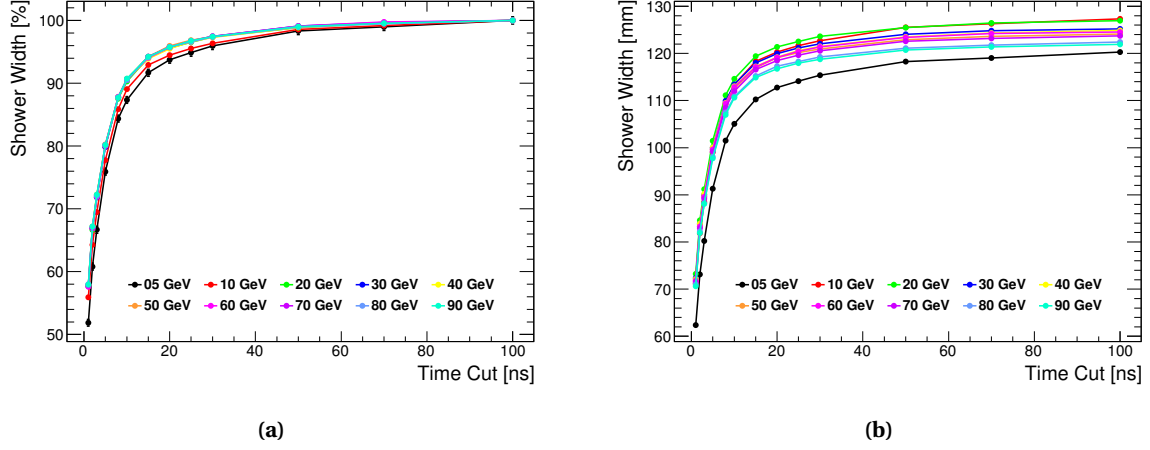


Figure 12.12 – a) Mean shower width as a function of the timing cut for different K_L^0 energies between 5 GeV and 90 GeV. The y-axis has been normalized to the shower width at 100 ns. The shower width decreases steadily as a function of the timing cut, indicating that the shower gets narrower. b) Mean shower width in mm as a function of the timing cut for different K_L^0 energies between 5 GeV and 90 GeV. Under 20 ns, the shower width is very similar indicating the core of the shower is fairly identical for all energies.

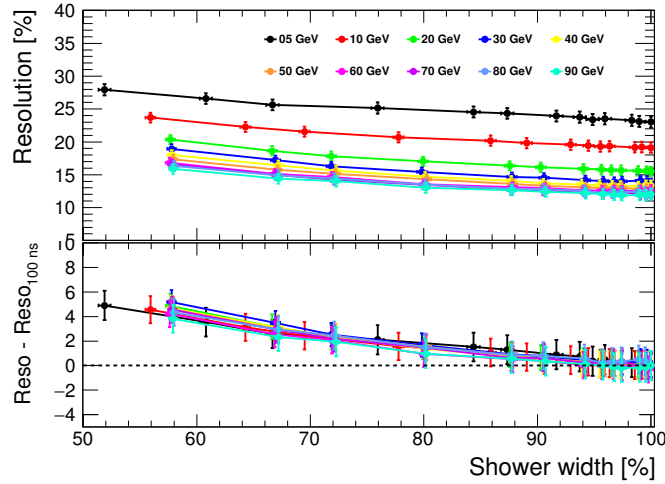


Figure 12.13 – The top plot shows the energy resolution as a function of the relative shower width for different particle energies. Each point represents a timing cut from 1 ns to 100 ns from left to right. The bottom plot shows the absolute loss of resolution as a function of the relative shower width.

in order to locate the electromagnetic core of the shower, a much lower timing cut is needed thus the time resolution must be better. This study assumes a perfect timing resolution which does not reflect the reality. In the next section, different time resolutions were assumed based on the current knowledge on the timing resolution of the foreseen front-end electronics.

12.4.4.2 In a realistic scenario

In this section, a similar study is performed as in previous section 12.4. Instead, it assumes realistic time resolutions based on the current electronic technology. The table 12.1 sums up the investigated time resolutions. The same selection is applied as in the previous section.

Table 12.1 – Assumption on the time resolution of the front-end electronics for different scenarios.

Scenario	Time resolution (ns)
Testbeam	8
Scenario 1	1
Scenario 2	0.4

The testbeam resolution is the time resolution obtained with the current AHCAL technological prototype as shown in section 10.3. The Scenario 1 is an assumption on the ideal time resolution which is in the order of the timescale of the development of hadronic showers therefore around 1 ns. And finally, the Scenario 2 is the time resolution which is obtained by assuming a linear extrapolation from the testbeam time resolution by using a faster slow clock of 5 MHz instead of 250 kHz (20 times faster) although this is probably an optimistic scenario.

Looking at the impact on calorimeter response and energy resolution, the figures 12.14a and 12.14b show that a time resolution in the order of sub-nanosecond does not affect much the response and energy resolution. The figures 12.15a and 12.15b show that for a time resolution in the nanosecond order, the response and energy resolution does not get affected much also. However, for a cut below 1-2 ns, it will start to degrade the response rapidly, up to 35-40%. The resolution gets affected as well up to 35-50% (relative to 100 ns). The figures 12.16a and 12.16b show that for the 8 ns timing resolution, the response and resolution get heavily degraded by timing cuts below 10-20 ns, up to 55-60% for the response and around 50-60% (relative to 100 ns) for the energy resolution.

The energy resolution as a function of the shower width is shown in figures 12.17a, 12.17b and 12.17c for different K_L^0 energies and different timing cuts assuming the timing resolutions shown in table 12.1. In figure 12.17a, the loss of resolution is comparable when assuming a perfect time resolution while gaining up to 40-50% in shower width. A sub-nanosecond scale time resolution does not have much impact whatever the timing cut applied. In figure 12.17b, the energy resolution gets degraded by around 2% (absolute) for the same decrease of 40-50% in shower width. This loss in energy resolution is acceptable even with a tight timing cut and could be recovered in a later stage by adding few hits around the core of the shower to the identified main cluster. In figure 12.17c, the same loss in resolution of 2% (absolute) would only yield a reduction of 30% in the shower width and corresponds to a timing cut of around 10 ns.

From these figures, we can conclude that for a timing resolution of around 1 ns or better, the calorimeter linearity and energy resolution does not get affected much by timing cuts around 5-10 ns. This can be

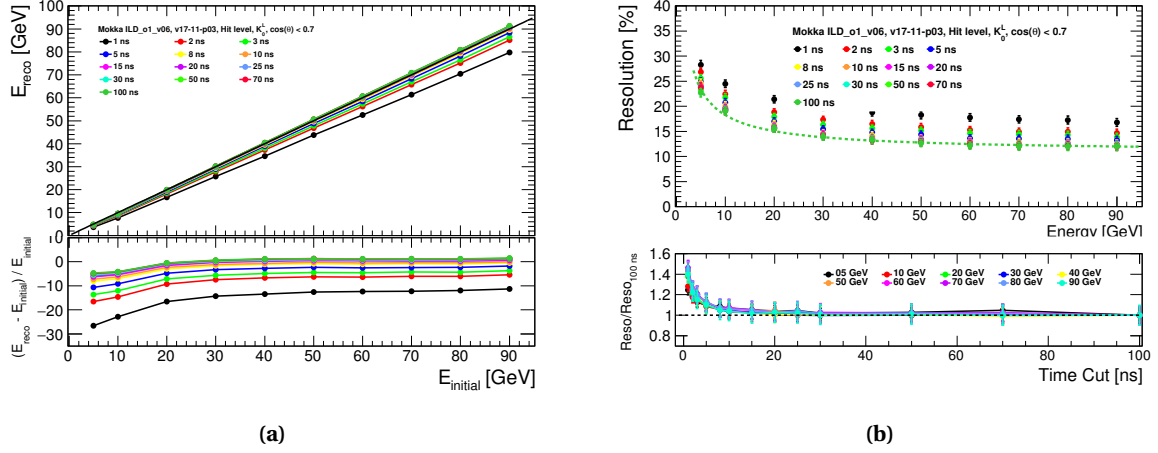


Figure 12.14 – a) The top plot shows the reconstructed energy E_{reco} as a function of the initial particle energy $E_{initial}$ for different timing cuts assuming a time resolution of 0.4 ns. The bottom plot represent the relative deviation to the line $x = y$ for the different time cuts. b) Energy resolution curves for 0.4 ns time resolution. The plot represents the relative energy resolution $\frac{\sigma_E}{E}$ for kaons from 5 to 90 GeV for each timing cut. The green line is a fit applied to 100 ns timing cut of the typical form $\frac{\sigma_E}{E} = \frac{a}{\sqrt{E}} \oplus b$.

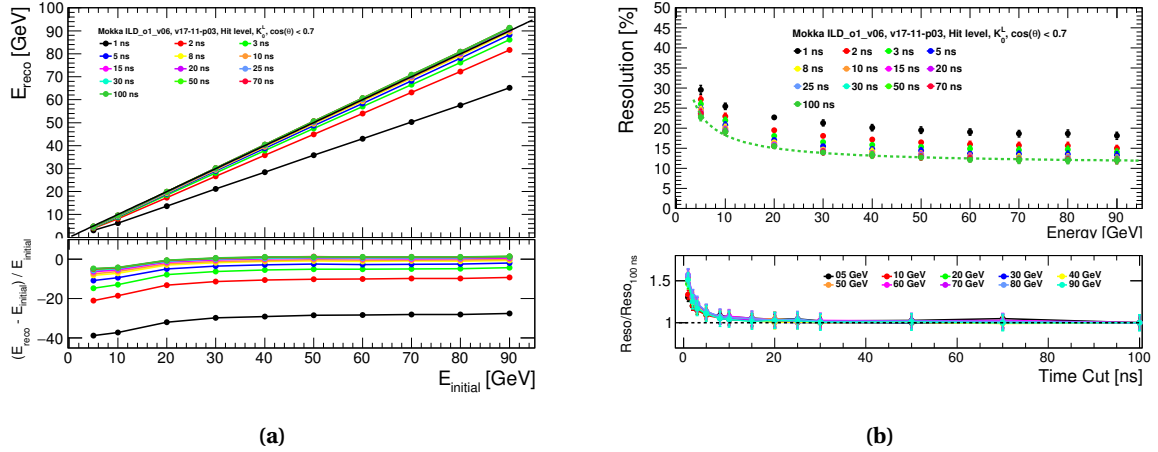


Figure 12.15 – a) The top plot shows the reconstructed energy E_{reco} as a function of the initial particle energy $E_{initial}$ for different timing cuts assuming a time resolution of 1 ns. The bottom plot represent the relative deviation to the line $x = y$ for the different time cuts. b) Energy resolution curves for 1 ns time resolution. The plot represents the relative energy resolution $\frac{\sigma_E}{E}$ for kaons from 5 to 90 GeV for each timing cut. The green line is a fit applied to 100 ns timing cut of the typical form $\frac{\sigma_E}{E} = \frac{a}{\sqrt{E}} \oplus b$.

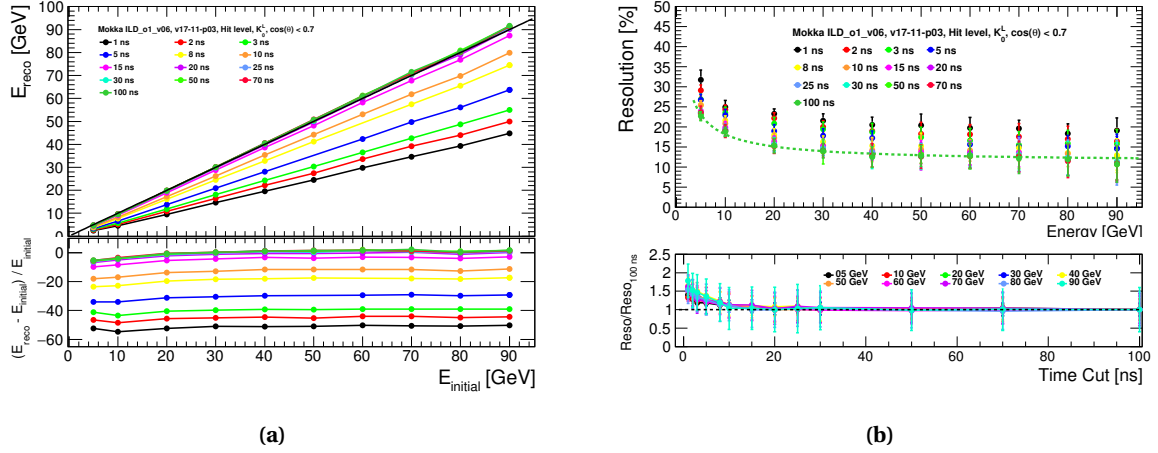
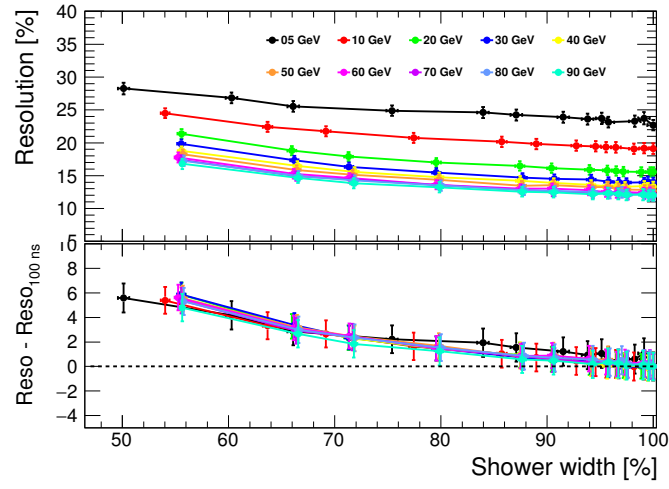


Figure 12.16 – a) The top plot shows the reconstructed energy E_{reco} as a function of the initial particle energy $E_{initial}$ for different timing cuts assuming a time resolution of 8 ns. The bottom plot represent the relative deviation to the line $x = y$ for the different time cuts. b) Energy resolution curves for 8 ns time resolution. The plot represents the relative energy resolution $\frac{\sigma_E}{E}$ for kaons from 5 to 90 GeV for each timing cut. The green line is a fit applied to 100 ns timing cut of the typical form $\frac{\sigma_E}{E} = \frac{a}{\sqrt{E}} \oplus b$.

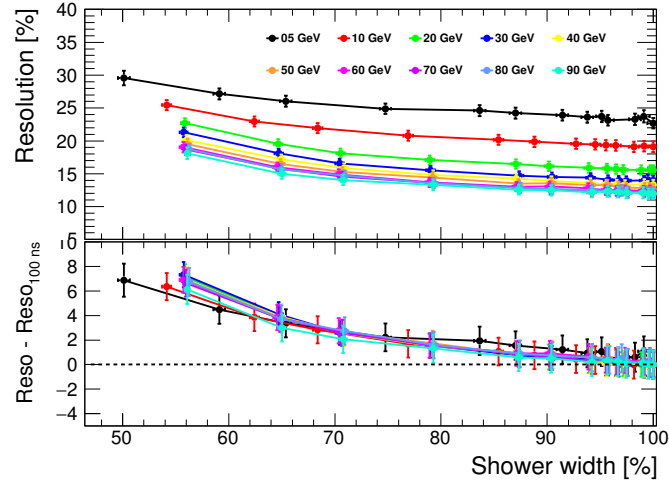
explained because more than 90% of the energy is deposited within 10 ns. This deposited energy can be identified mostly to the core of the shower in a radius of around 10 cm around the main shower axis. Moreover, the shower width gets reduced by around 40-50%. However, for higher timing resolution, the linearity and energy resolution would get much more affected by timing cuts of 5-10 ns. The shower width can still be reduced by around 30% for a loss in resolution of around 6-8% (absolute) and a degradation of the linearity by 20-30% maximum. One could use timing information in order to improve the pattern recognition efficiently. For example, timing could be used to help in the clustering step in Pandora, especially for nearby close showers. Then a re-clustering step taking into account timing information could be done to recover the loss in energy resolution and linearity. In addition, as the electromagnetic core of the shower is related to quasi-instantaneous energy depositions and the hadronic part of the shower is related to late energy depositions, timing information could be used to improve the energy resolution by software compensation [3].

12.5 Understanding the degradation of the energy resolution with timing cuts

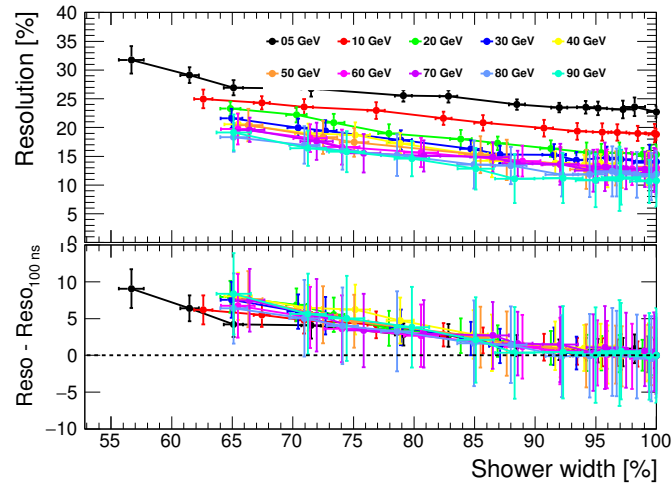
To investigate and understand the degradation of the energy resolution with timing cuts, a simple complementary analysis has been done based on the CAN 028 [161]. The analysis note presents a software compensation method to improve the energy resolution using a correction factor derived from the knowledge of the electromagnetic and hadronic fraction in a shower on an event-by-event basis. It was found that the shape of energy density distributions is correlated with the calorimeter response. The goal of this study is to show that timing cuts favor high electromagnetic fraction events and thus, reduces the correlation.



(a) 0.4 ns time resolution.



(b) 1 ns time resolution.



(c) 8 ns time resolution.

Figure 12.17 – Energy resolution as a function of the shower width assuming different time resolutions. The top plot shows the relative energy resolution $\frac{\sigma_E}{E}$ for kaons from 5 to 90 GeV where each point is representing a timing cut as a function of the shower width. The bottom plot shows the deviation to the nominal resolution at 100 ns as a function of the shower width. The error bars are statistical uncertainties.

12.5.1 Hit Energy spectra in HCAL

Due to the high granularity of the HCAL in the ILD detector, a detailed study of hadronic showers is possible at the single cell level (hits). The hadronic calorimeter in ILD is of a non-compensating nature resulting in a higher response for the electromagnetic component of a hadronic shower than for the hadronic component. The $\frac{e}{\pi}$ ratio is around 1.2 [38]. Because of this, hadron induced showers with a higher electromagnetic fraction will give a higher response and vice-versa. An example is shown in figure 12.19. E_{mean} and σ correspond to the mean of the distribution and RMS, respectively. The blue subsample contains events reconstructed with $E_{reco} < E_{mean} - \sigma$ and the red one with $E_{reco} > E_{mean} + \sigma$. The corresponding hit energy spectrum is shown in figure 12.19a. This shows that the shape of the hit energy spectrum is closely related to the deposited energy. Clusters with a higher reconstructed energy contain hits with larger hit energies which are expected to be mainly caused by the EM component.

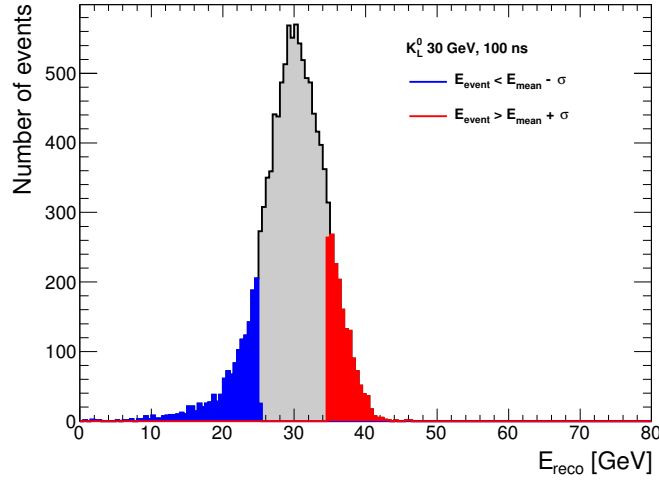


Figure 12.18 – Reconstructed energy distribution for 30 GeV kaons. The blue sample corresponds to events with $E_{reco} < E_{mean} - \sigma$ and the red sample corresponds to events with $E_{reco} > E_{mean} + \sigma$.

Following the CAN 028, a quantitative probability C_i^{lim} of the i -th event was obtained as follows:

$$C_i^{lim} = \frac{N_i(e \leq e^{lim})}{N_i^{HCAL}} \quad (12.2)$$

where $N_i(e \leq e^{lim})$ is the number of hits with energy $e \leq e^{lim}$ and N_i^{HCAL} the number of hits in the HCAL. The value of e^{lim} is between 3 to 5 MIPs, determined by looking at the intersection of hit energy spectra of the red and blue subsamples for kaons between 10 and 80 GeV. The figure 12.19b shows the hit energy spectra between 0 and 14 MIP for 30 GeV.

The distribution of C_i^{lim} for different values of e^{lim} are shown in figure 12.20a for 30 GeV kaons. One can see that the distributions get narrower with increasing e^{lim} . By choosing the right value of e^{lim} , it may be possible to distinguish between the red and blue subsamples by their C_i^{lim} distributions. For this analysis, a value of 3.5 MIP was chosen for e^{lim} . One can observe that events where the reconstructed energy is below $E_{mean} - \sigma$ correspond to a higher value of C_i^{lim} and vice-versa. The blue distribution has a mean of 0.71 and the red distribution has a mean of 0.61, this corresponds to a separation of 14.1%. An inverse correlation is

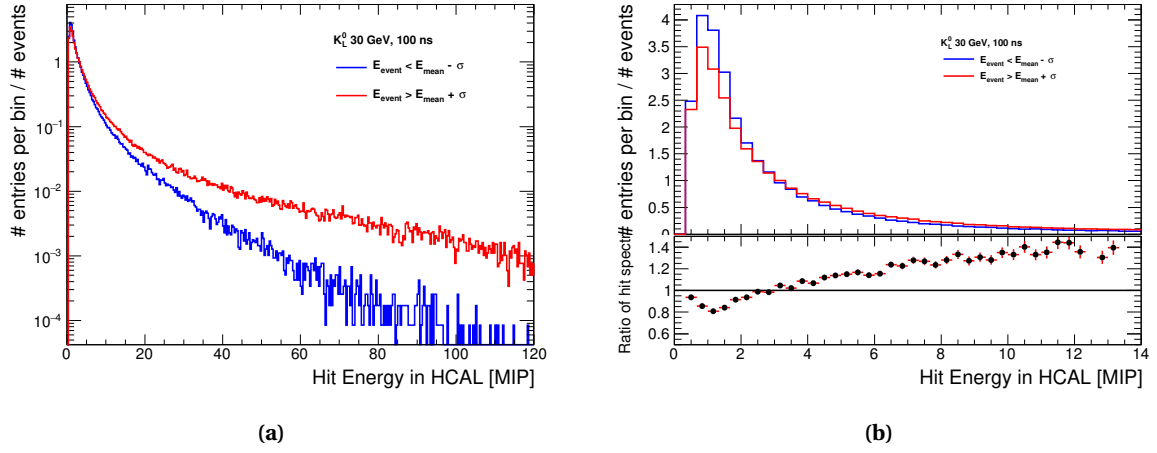


Figure 12.19 – Hit energy spectrum in the HCAL corresponding to subsamples with low (in blue) and high (in red) energy depositions. The left plot is focused in the region between 0 and 14 MIPs. The bottom plot shows the ratio of the red to the blue spectrum that was used to determine the value for e^{lim} .

found between the total energy in the HCAL and C^{lim} as shown in figure 12.20b. The inverse correlation is much stronger for higher kaon energies and becomes weaker with lower energies.

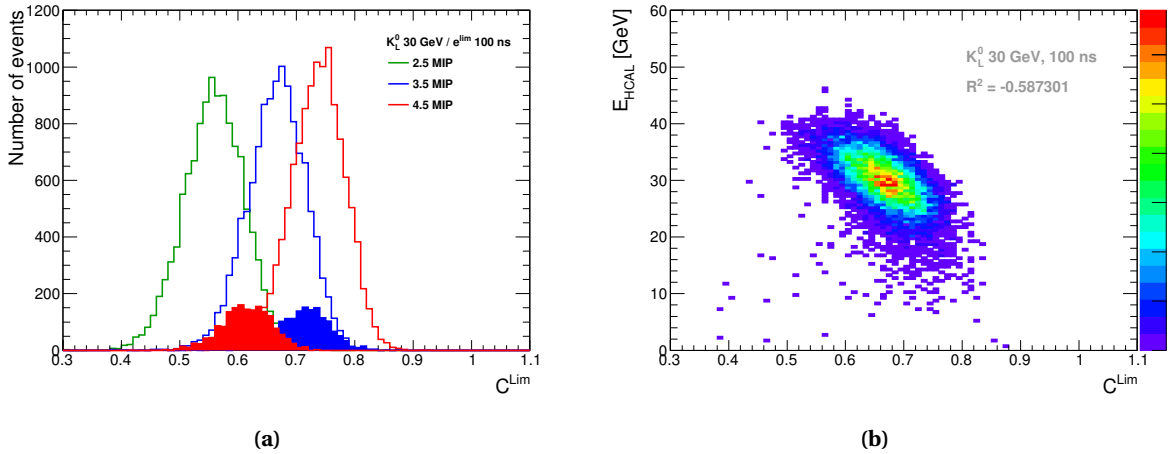


Figure 12.20 – a) Distributions of C^{lim} for different values of e^{lim} for 30 GeV kaons. The red and blue filled histograms corresponds to events that are in the region $E_{mean} \pm \sigma$ respectively for $e^{lim} = 3.5$ MIPs. b) Energy deposited in the HCAL as a function of C^{lim} for $e^{lim} = 3.5$ MIPs for 30 GeV kaons.

In a next step, a timing cut is applied and a comparison with these results is done. It is expected that timing cuts will have an effect of narrowing the C^{lim} distributions, thus bringing the blue C^{lim} distribution (hadronic component) closer to the red C^{lim} distribution (EM component). Therefore reducing the inverse correlation of C^{lim} with the energy deposited. This is due to the fact that fluctuation are cut down by timing cuts, favoring hadronic showers with a higher electromagnetic fraction.

12.5.2 Influence of timing cuts on hit energy spectra in HCAL

A check was performed on the shape of the hit spectra in the HCAL with different timing cuts. The figure 12.21 shows the hit spectra for 30 GeV kaons with a timing cut of 100 and 1 ns. The green line in the bottom plot represents the value of $e^{lim} = 3.5$ MIPs.

One can notice that the shape of the spectra differs with timing cuts. A large reduction of low energy hits (~ 1 MIP) is visible. With a cut of 1 ns, there are around 10% fewer hits over 4 MIPs but up to 60% fewer hits below 1 MIP. With a value of 3.5 MIP for e^{lim} , it seems that there are globally fewer hits below, thus reducing the value of C^{lim} . A lower value of C^{lim} would correspond to a higher energy deposited thus giving a hint that timing cuts enhance the electromagnetic response of the calorimeter making even more non-compensating. This is shown in figure 12.22a.

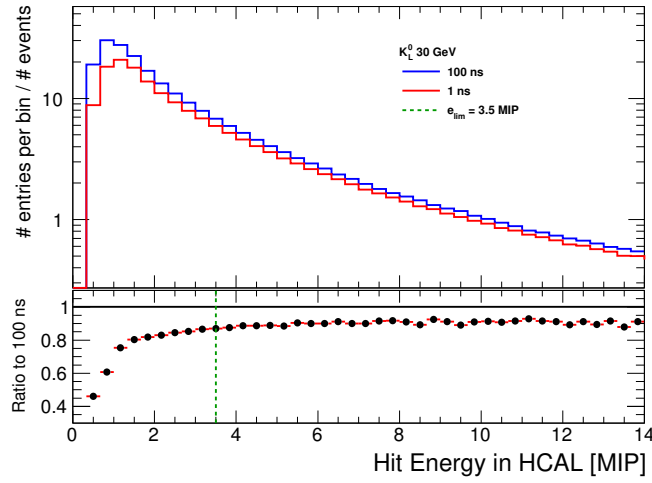


Figure 12.21 – Normalized hit energy spectra in the HCAL for 30 GeV kaons applying a timing cuts of 100 ns in blue and 1 ns in red. The bottom plot shows the ratio of the red spectra to the blue spectra.

The blue C^{lim} distribution has a mean of 0.66 and the red C^{lim} distribution has a mean of 0.58. This corresponds to a separation of 12.1%. The timing cut of 1 ns has the effect of reducing the distance between both distributions by around 2% compared to the nominal 100 ns timing cut. To further confirm this observation, the same correlation plots between the energy deposited in the HCAL and C^{lim} is shown in figure 12.22b for 1 ns timing cut. The anti-correlation is reduced slightly with the correlation coefficient going from -0.58 to -0.48 and the distribution looks more circular. This further confirms that the timing cuts reduce the fluctuations between the electromagnetic and hadronic fractions in hadronic showers by cutting the hadronic response and enhancing the electromagnetic response. This has an effect of non-compensation in the response to hadronic showers, thus degrading the energy resolution furthermore.

12.6 Conclusion and Outlook

In this chapter, a first look at the effect of timing cuts on hadronic showers in the GEANT 4 simulation of the ILD detector has been done. In a first step, a perfect time resolution was assumed. It was shown that timing cuts affect the calorimeter response (up to 20% for 5 GeV kaon) and energy resolution (up to 20-30%

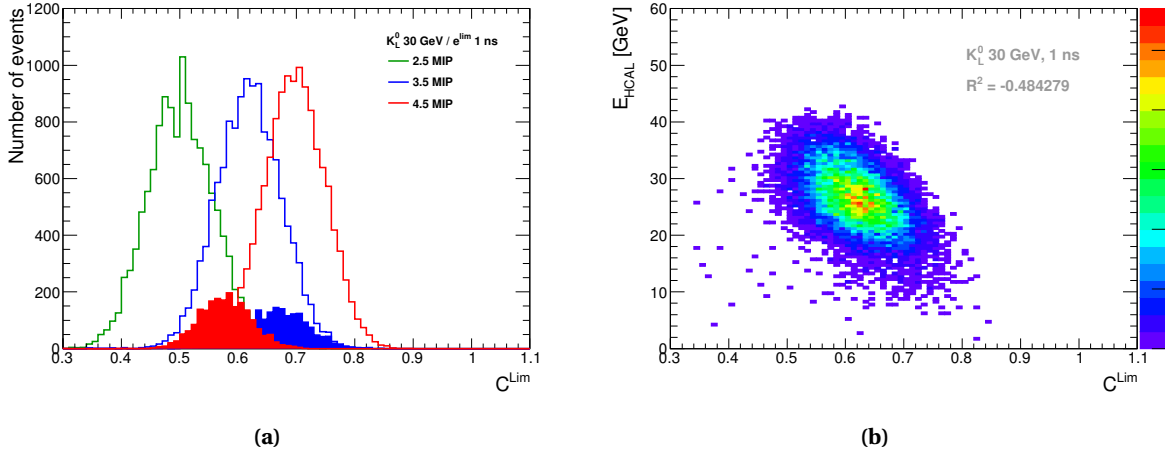


Figure 12.22 – a) Distributions of C^{lim} for different values of e^{lim} for 30 GeV kaons for a 1 ns timing cut. The red and blue filled histograms corresponds to events that are in the region $E_{mean} \pm \sigma$ respectively. b) Energy deposited in the HCAL as a function of C^{lim} for $e^{lim} = 3.5$ MIPs for 30 GeV kaons with a timing cut of 1 ns.

relative to 100 ns for 5 GeV kaon). It has been shown that most of the shower energy is deposited within 10-15 ns and that timing cuts are removing mostly outer hits from the hadronic shower, thus reducing the width of the shower without affecting much the energy resolution. This could be used as a starting point in order to improve clustering and pattern recognition in PandoraPFA. The effect of timing cuts on the energy resolution is mostly an increase of the constant term. This has been investigated and it is understood that the timing cut introduces a bias on hadronic shower by cutting away late hits mostly coming from the hadronic part of the shower, thus reducing the hadronic response and enhancing the electromagnetic response. Timing cuts act as a non-compensation effect in the response to hadronic showers thus degrading the energy resolution.

Finally, a more realistic study has been done, assuming a time resolution of the AHCAL front-end electronics between 0.4 to 8 ns. It shows that a time resolution in the order of 1 ns and below has little impact on the response and resolution of the calorimeter. The energy resolution is degraded up to 6-8% (absolute) for a tight timing cut but can reduce the shower width by 40%. Such reduction of the shower width by applying timing cuts could be used to improve the pattern recognition. As for the currently achieved time resolution of 8 ns, it is not ideal but could still, to a certain level, provide information that could be used to improve shower separation. However, this study shows the effects of different time resolutions but does not give the answer what time resolution is needed as it depends mostly on the aim for the use of timing cuts. A time resolution of 8 ns is perfectly fine if it is only needed to separate bunch-crossings (around 200 ns apart at the ILC). However, a better time resolution would give access to a powerful tool that could be used to separate nearby showers.

In the future, analysis using time information should be performed in order to evaluate the potential of timing and the needed time resolution in order to help in the separation of overlapping nearby hadronic showers, the pattern recognition and as well improve the calorimeter energy resolution by software compensation.

Chapter 13

Summary

The International Linear Collider (ILC) is a future linear electron-positron collider with a center-of-mass energy of 250 GeV, upgradeable to 500 GeV. It will require an unprecedented jet energy resolution to reach the goals in the precision measurement of the Standard Model parameters. In order to achieve the jet energy resolution in the range of 3-4%, the Particle Flow Algorithms (PFAs) concept combines the tracking and calorimeter measurements into the best jet energy measurement, by measurement each individual particle in a jet and using the best sub-detector resolution to measure the energy. PFAs need to correctly associate energy depositions in the calorimeters and tracks. This needs an unprecedented spatial resolution which can be achieved with high granular calorimeters.

The CALICE collaboration develops such high granularity calorimeter prototypes. One of the design, the analog hadron calorimeter (AHCAL), consists of plastic scintillator tiles of $3 \times 3 \text{ cm}^2$ area, read out by Silicon Photomultipliers (SiPMs). Several prototypes have been built and tested in various beams as a proof-of-concept. Nowadays, the focus of such calorimeters is the scalability to a full linear collider detector by integrating the front-end electronics onto the active layers.

This thesis presents the first timing analysis of a large scale analog hadron calorimeter based on scintillator-SiPM technology. In the testbeam campaign at CERN in July 2015, the CALICE AHCAL technological calorimeter prototype was operated in muon, electron and pion beams in an energy range up to 90 GeV. The main challenges in this analysis are the enormous number of channels to be calibrated in energy and time, the understanding of the different features of the front-end electronics and the contamination of beam events with multi-particles of different types and energy.

As part of this thesis work, the commissioning procedure of the AHCAL boards (HBU), that were used in the testbeam at CERN, has been presented. Around 60 SPIROC chips have been tested manually with a yield of 84%. It takes around 10 minutes per chip to be tested and it is expected to be reduced to under few minutes by automatizing the chip testing for the next prototype. In total, 3 EBU and 24 HBU boards have been commissioned. Around 7-8 hours are needed to perform the commissioning for old generation boards due to the high range of LED voltage needed to calibrate the SiPM gain. New generation boards and improvements in SiPM quality reduce the commissioning time under 1 hour per board.

Before comparing the recorded data to simulation, the energy scale calibration of the detector must be performed and validated. Thus, the energy scale calibration of the full testbeam prototype has been presented. A robust method for extracting the most probable value of a MIP has been developed to accommodate

for the high number of channels (3744) to be calibrated in the AHCAL. Around 85% of the channels could be calibrated with a calibration uncertainty between 1% to 3%. The energy scale calibration has been validated on single channel level with simulation. The agreement between data and simulation is satisfactory.

This thesis focuses on the timing development of hadronic shower in a highly granular calorimeter. This has been presented in this thesis with the timing analysis of testbeam data recorded in July 2015 at CERN. Firstly, the timing calibration of a full scale hadron calorimeter prototype has been shown. After calibration, a time resolution of around 5 ns for muons and 8 ns for electron was achieved. The increase in the time resolution for electron showers is mainly due to a feature of the front-end electronic that induces a shift of the timing measurement as a function of the number of hits within a SPIROC2b ASIC. A detailed validation of the simulation is performed with muons and electromagnetic interactions, yielding an agreement between data and simulation within 10-20%.

The analysis of the pion data recorded with the AHCAL technological prototype aims to improve our understanding of the time development of hadronic showers. First, the correlation between the hit energy and the hit time has been investigated. The data showed that late depositions are concentrated at low hit energies below 1.5 MIPs in iron absorber. Secondly, the hit time as a function of the hit distance to the shower axis has been looked at. It showed that mostly delayed timing hits are at a great distance from the shower axis. Finally, the calorimeter testbeam setup allows for the investigation of time correlations between modules. The results showed that time correlations are visible at short distance range ($\sim 18\%$) as well as long distance range in smaller proportions ($\sim 3\%$).

A detailed comparison has been performed with several physics lists in GEANT 4. Overall, a good agreement is present between data and simulations within statistical and systematical uncertainties. The tracking of low energy neutrons in the HP package or other implementations like in QBBC show that they are needed to reproduce well the tail of the data which is otherwise generally over-estimated. Time correlations are reproduced in simulation but the proportion of hits in data and simulation differ quite significantly. This may be due to the selection of the data that does not reject efficiently multi-particle events. More data and investigations are needed to understand furthermore the time development of hadron shower in a full calorimeter.

At last, as part of this thesis, the application of timing cuts on the full ILD detector simulation was performed. This analysis aims to understand the effect of timing cuts on calorimeter energy response and energy resolution and the development of hadron shower through the calorimeter. The results showed that, assuming a perfect timing resolution, timing cuts worsen the calorimeter response (up to 10-20% relative to 100 ns) and energy resolution to a few percent level (up to 6% absolute). The radial development of a hadron shower showed that timing cuts are removing mostly outer hits from the shower. Timing cuts reduce the width of the shower, up to 40% for a timing cut of 1 ns and corresponding to a decrease of the shower width by around 60 mm, without affecting much the energy resolution. This is quite significant and could help greatly in the case of overlapping nearby showers. The effect of timing cuts on the energy resolution is described by an increase of the constant term. This effect has been investigated and it is understood that the timing cut has a bias effect on hadronic shower by decreasing the hadronic response of a shower, such that the EM fraction becomes more important. Timing cuts act as a non-compensation effect in the response to hadronic showers thus degrading the energy resolution. Finally, different timing resolutions were assumed and showed that ideally timing cuts with timing resolution around 1 ns would help to greatly reduce the shower width, by around 50%, without affecting much the energy resolution (up to 6% in absolute compared to 100 ns). Timing cuts could be used to improve separation of overlapping showers and as well it could improve the energy

resolution with software compensation using time information. However, more studies should be done using timing information in order to provide an idea of the required time resolution.

Some of the difficulties encountered in this analysis come from the fact that only a small part of the prototype was equipped with active layers and using various generations of SiPMs and readout electronics. However, a new prototype has been build in April 2018 and consists of 40 active layers using homogenous electronics. The new prototype is currently being tested at the CERN SPS facility in various beams. Such prototype provides very detailed images of events that can be used to provide a very good selection. Moreover, highly granular calorimeters are now interesting also in the context of LHC, where high granularity is mainly used to suppress pile-up events. In this case, a very good timing resolution, in the order of few picoseconds, could help to improve the pile-up rejection.

Acknowledgments

Everything leading up to this thesis would not have been possible without the continuous support of many people. Here, I would like to thank these people and I may have forgot some.

First, I would like to thank Dr. Roman Poeschl and Dr. Thibault Frisson who made me start in this research area. It was such a great experience and gave the will to pursue my studies in particle physics and detector development. Moreover, they gave me the opportunity to go to CERN and advised me to go to DESY.

I would like to thank Dr. Mark Terwort who supervised my work during the DESY summer school and without whom I may not have started a thesis at DESY. I would like to thank Dr. Felix Sefkow who has his door always open for questions and advices. I profited so much from your guidance and knowledge about calorimetry, physics and politics. I would like to give a special thank to Prof. Dr. Erika Garutti who endorsed me as her student and gave me advices through my thesis.

I would like to give a special thanks to Dr. Katja Krüger, this thesis would not have been finished without your enormous efforts in proof-reading presentations, abstracts, papers and this thesis. I am thankful for all the ideas, the questions, the guidance and the discussions we had through all my thesis. Your tremendous knowledge about physics and past experiments (especially about H1) gave me more interest in particle physics and shaped me as a young scientist. I would like to give an exceptional thank to Dr. Marcel Stanitzki who proof-read my thesis twice and give me wonderful comments and advices about it. I am also greatly thankful for the talks we had and the joy that you bring with you.

I would like to thank many other people from the FLC group for their advices, teaching and administrative help over these years: Ties Behnke, Karsten Büsser, Mathias Reinecke, Shaojun Li, Remi Été, Andrea Schröder, Karsten Gadow, Jenny List, Moritz and many others that may have left in the meantime.

The AHCAL group people, especially Jiri, Ambra, Lan, Oskar, Ali, Ambra, Coralie, Benjamin and Yuan made my work in this group unforgettable and very entertaining some time, especially during shifts at DESY or CERN.

I would like to thank Alex, Alexey, Hayk, Sergey and Volodymyr who sparked in me the interest for bouldering which help me to stay in shape and keep my head cool most of the time. I would like to thank many other friends: Ksenia, Artur L., Artur T., Ali H., Natali, Nataliia K., Nataliia Z., Olga, Miro, that made my work during the last 4 years a wonderful experience.

Last but not least, I would like to especially thank my girlfriend, Mengqing Wu, who supported me through the last hard month of my thesis. You are the best thing that happened in my life. I am deeply grateful for all your advices and the strength you gave me. I love you. Finally, to my grandparents that unfortunately past away before this thesis and to my aunt, who always supported me in every way for the last 27 years and I would not have achieved my goals without your support.

Appendix A

Event selection

Table A.1 – Selection cuts for the muon runs.

Name	Beam Energy	Cut
Preselection	All	$0\text{ mm} < cog_z < 800\text{ mm}$
	All	$0 < n_{hits} < 20$
Track Selection (Modules 1 to 10)	All	n_{hits} in tower > 7
	All	n_{hits} in layer < 3
Track Selection (Modules 11 to 14)	All	n_{hits} in tower > 2
	All	n_{hits} in layer < 3

Table A.2 – Selection cuts for each electron runs.

Name	Beam Energy	Cut
Event Quality	All	Cherenkov ON
	All	Energy in the first 3 layers of AHCAL $> 10\text{ MIP}$
Electron Selection	10 GeV	$25 < n_{hits} < 75$
	15 GeV	$30 < n_{hits} < 90$
	20 GeV	$40 < n_{hits} < 100$
	30 GeV	$50 < n_{hits} < 110$
	40 GeV	$60 < n_{hits} < 120$
	50 GeV	$70 < n_{hits} < 140$
	All	$cog_z < 250\text{ mm}$
	All	$-90\text{ mm} < cog_{x,y} < 90\text{ mm}$
	All	Energy in last two layers $< 1\% E_{sum}$

Table A.3 – Selection cuts for the pions runs.

Name	Beam Energy	Cut
Event Quality	All	Cherenkov OFF
Pion Selection	All	$n_{hits} > 20$
	All	n_{hits} in the first 2 AHCAL layers < 5
	All	Energy in last two layers $> 1\% E_{sum}$
Multi Particle Rejection	All	n_{hits} in time window > 5
	All	$n_{Cluster} > 0$

Table A.4 – Selection cuts for the time reference channels.

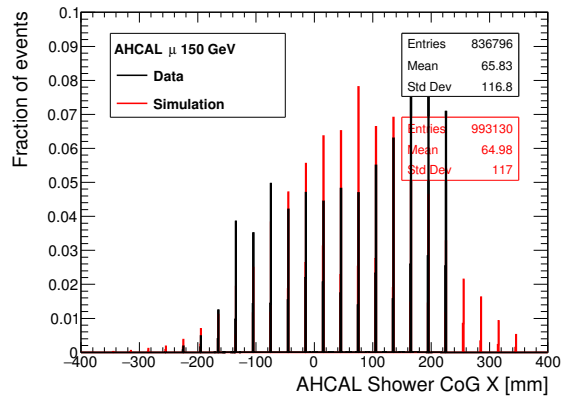
Name	Selection cut
T_{11}	$3 < E[MIP] < 4.5$ TDC > 0
T_{12}	$114 < E[MIP] < 145$ TDC > 0
T_{13}	$2.6 < E[MIP] < 3.8$ TDC > 0
T_{14}	$6.8 < E[MIP] < 8.3$ TDC > 0

Table A.5 – Selection cuts for the extraction of noise hits from muon runs.

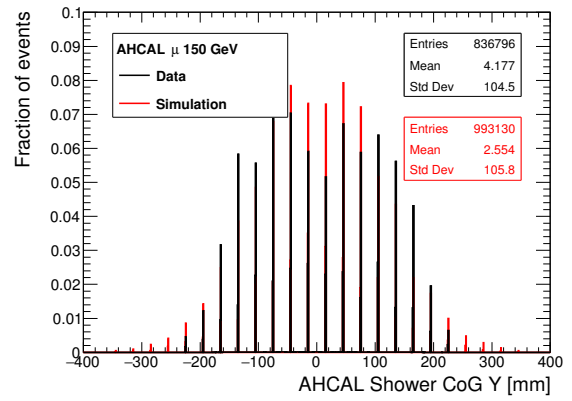
Name	Beam Energy	Cut
Noise selection	All	n_{hits} in a tower > 7
	All	$0 < n_{hits} < 30$
	All	n_{hits} in layer < 3

Appendix B

Validation: Additional Plots

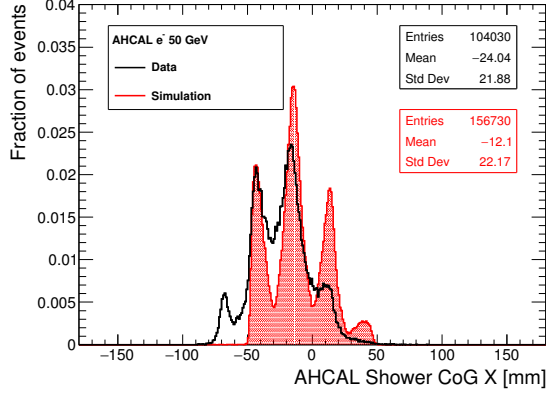


(a) Beam profile X.

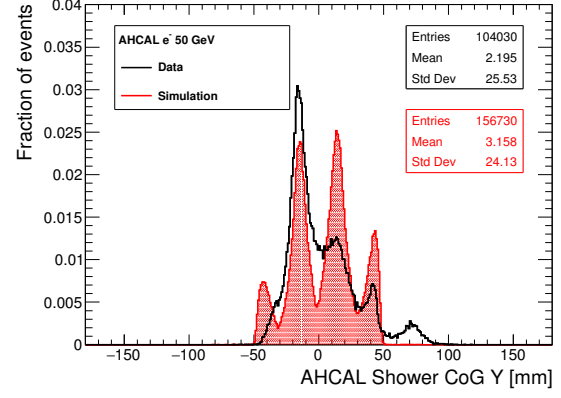


(b) Beam profile Y.

Figure B.1 – Beam profiles for 150 GeV muons in data and simulation. Simulated with QGSP_BERT_HP using GEANT 4 v10.1.

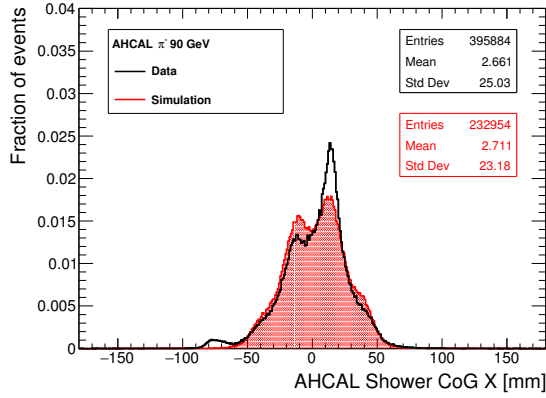


(a) Beam profile X.

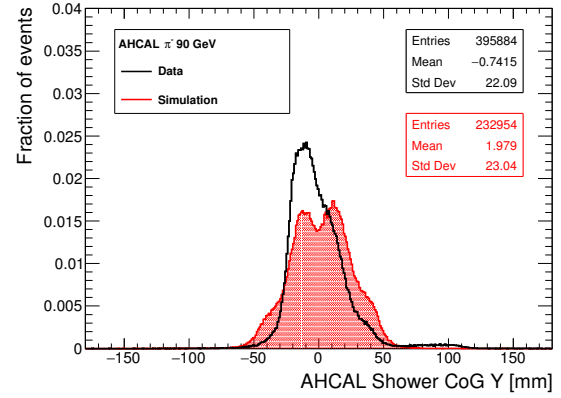


(b) Beam profile Y.

Figure B.2 – Beam profiles for 50 GeV electrons in data and simulation. Simulated with QGSP_BERT_HP using GEANT 4 v10.1.



(a) 90 GeV.



(b) 90 GeV.

Figure B.3 – Beam profiles for 90 GeV pions in data and simulation. Simulated with QGSP_BERT_HP using GEANT 4 v10.1.

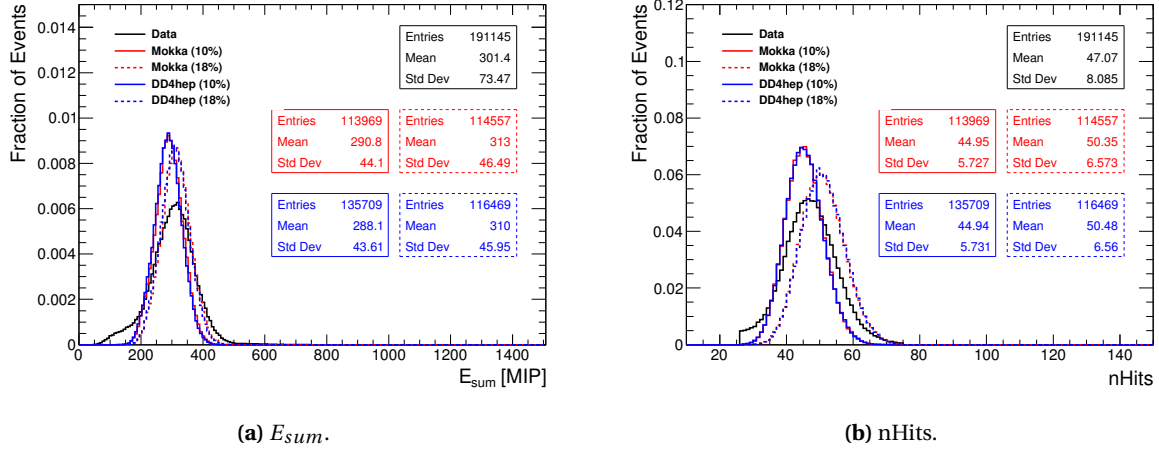


Figure B.4 – a) The energy sum in the AHCAL for 10 GeV electrons for data and simulations with a cross-talk value of 10% and 18%. b) The number of hits in the AHCAL for 10 GeV electrons for data and simulations with a cross-talk value of 10% and 18%.

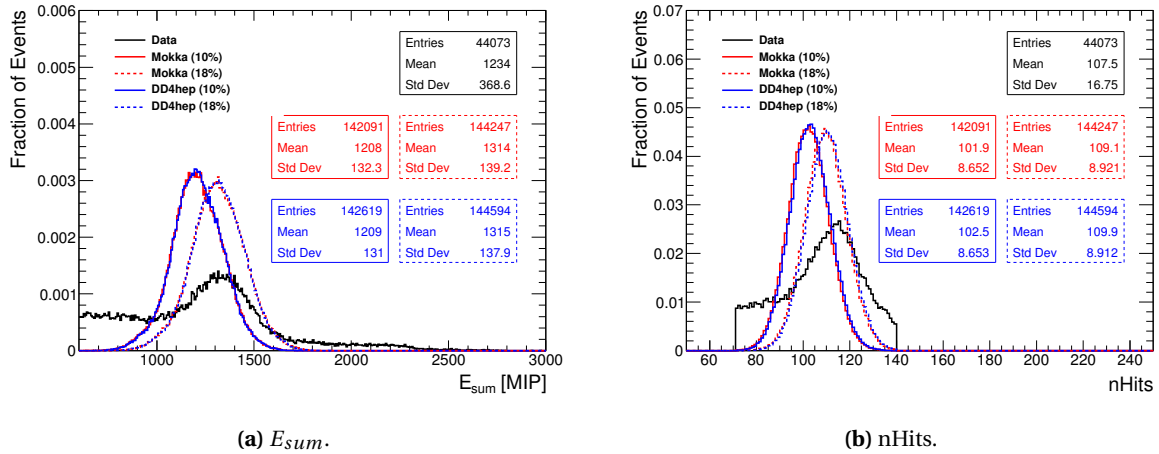
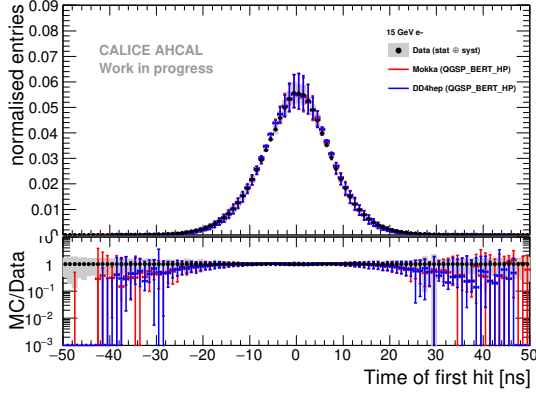


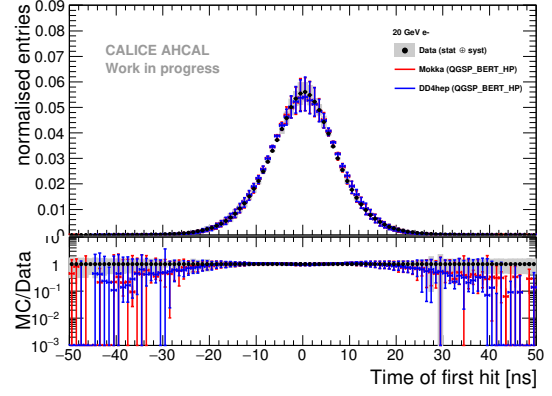
Figure B.5 – a) The energy sum in the AHCAL for 50 GeV electrons for data and simulations with a cross-talk value of 10% and 18%. b) The number of hits in the AHCAL for 50 GeV electrons for data and simulations with a cross-talk value of 10% and 18%.

Appendix C

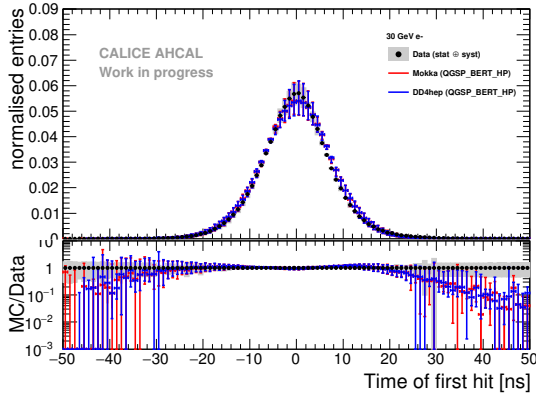
Timing: Additional Plots



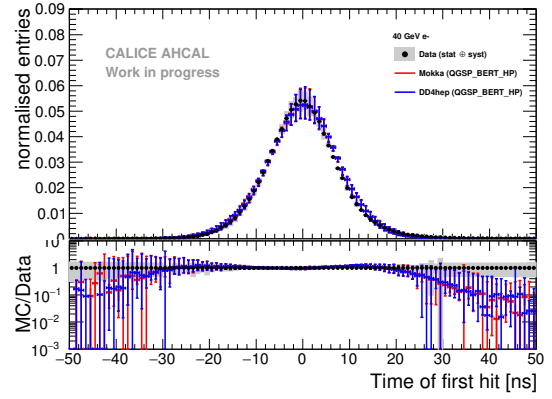
(a) 15 GeV.



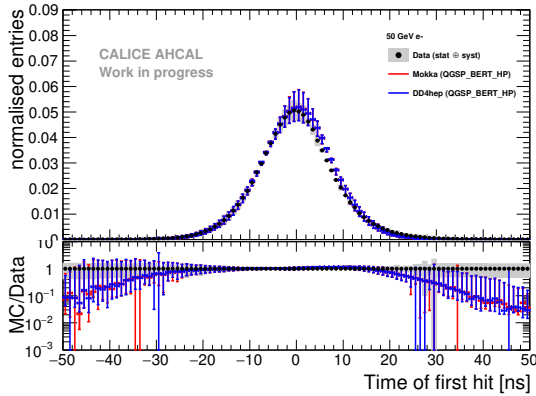
(b) 20 GeV.



(c) 30 GeV.

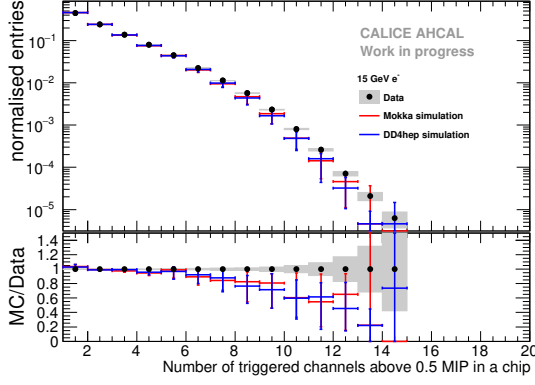


(d) 40 GeV.

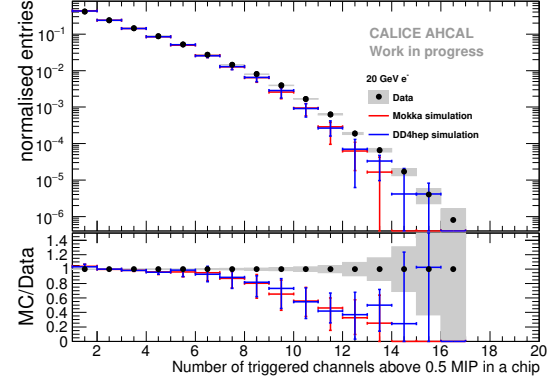


(e) 50 GeV.

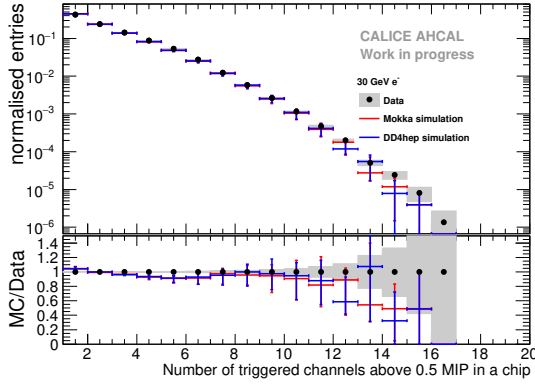
Figure C.1 – Comparison between electron data and MC for all energies of the time of first hit. The grey area represents the statistical and systematical error of the data. Error bars in simulation are obtained by varying the cross-talk parameter and with the uncertainty from the number of hits parametrization.



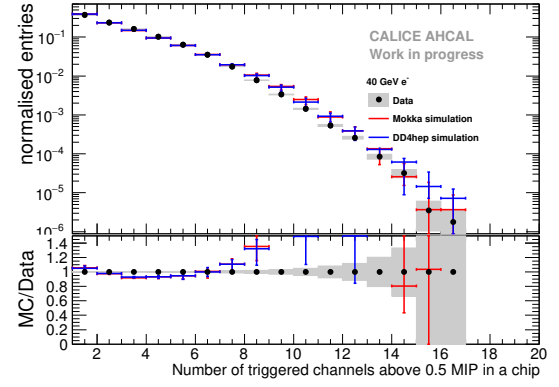
(a) 15 GeV.



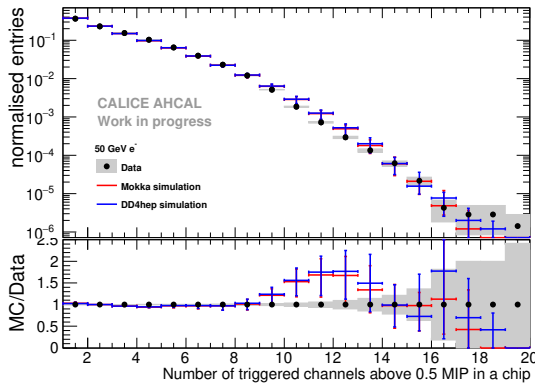
(b) 20 GeV.



(c) 30 GeV.

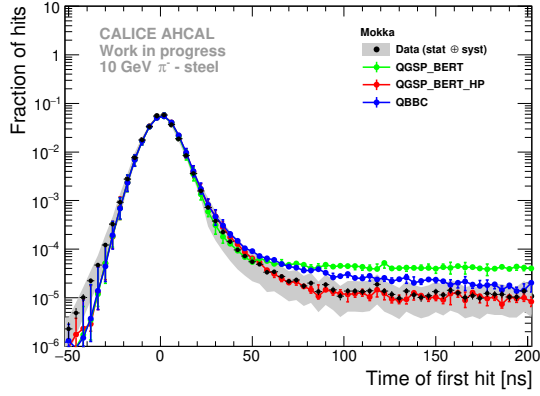


(d) 40 GeV.

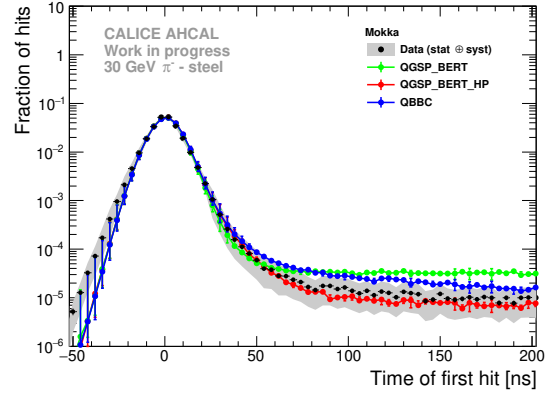


(e) 50 GeV.

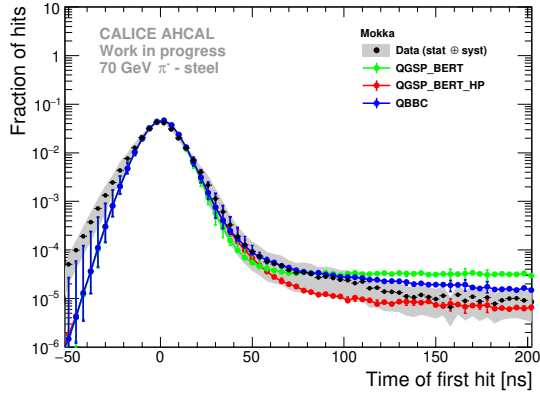
Figure C.2 – Comparison between electron data and MC for all energies of the number of triggered channels per chip. The grey area represents the statistical error of the data. Error bars in simulation are obtained by varying the cross-talk parameter between 10% and 18%.



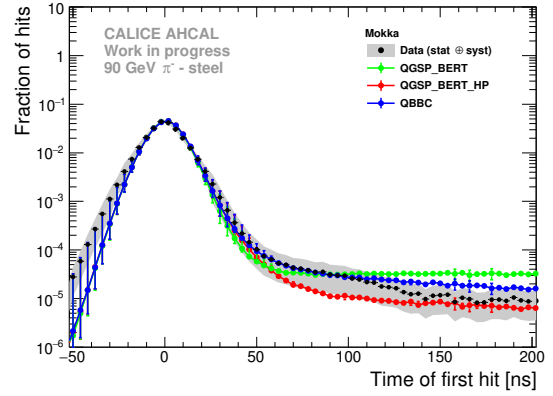
(a) 10 GeV.



(b) 30 GeV.



(c) 70 GeV.



(d) 90 GeV.

Figure C.3 – Comparison between data and the MOKKA simulation for pions between 10 and 90 GeV of the time of first hit. The grey box represents the statistic and systematic uncertainty of the data. The error bars are the uncertainty on the MOKKA simulation obtained by varying the cross-talk parameter and the uncertainty on the time smearing.

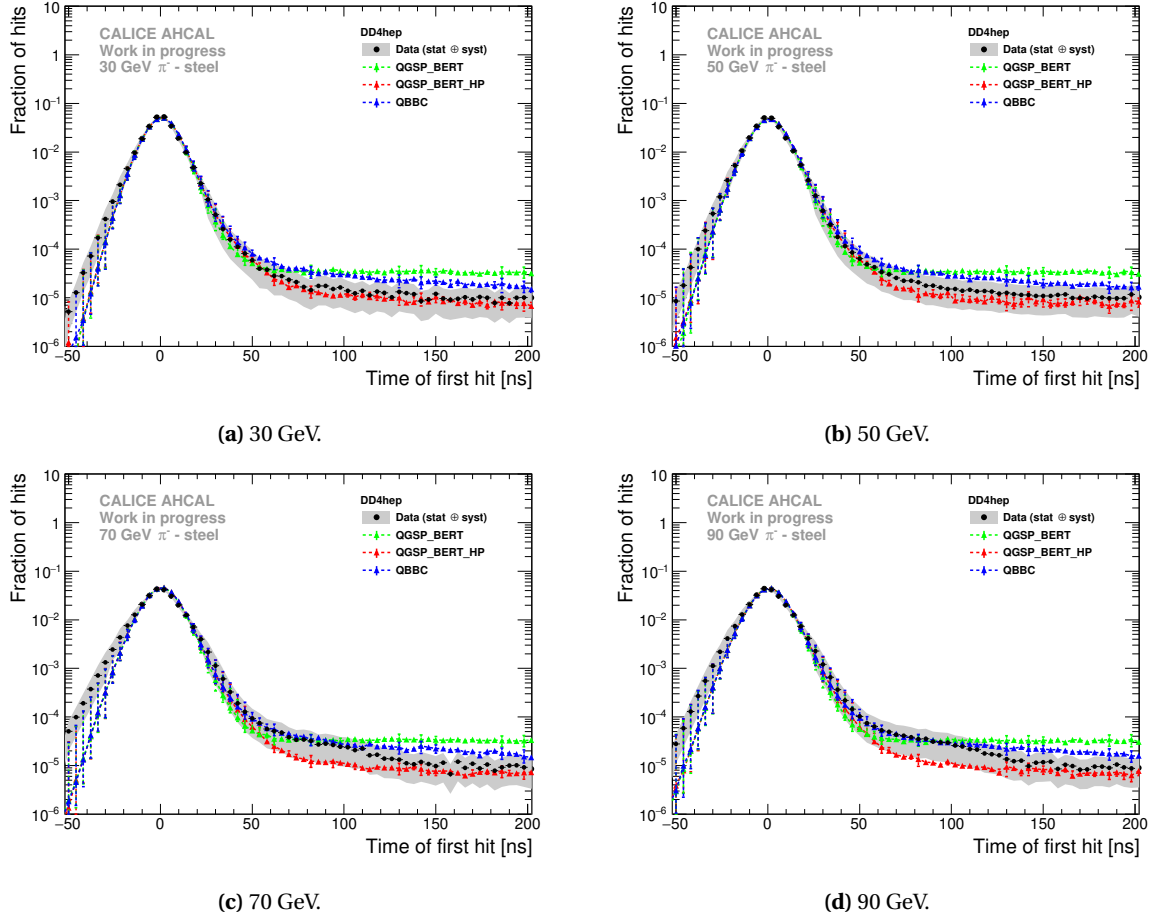
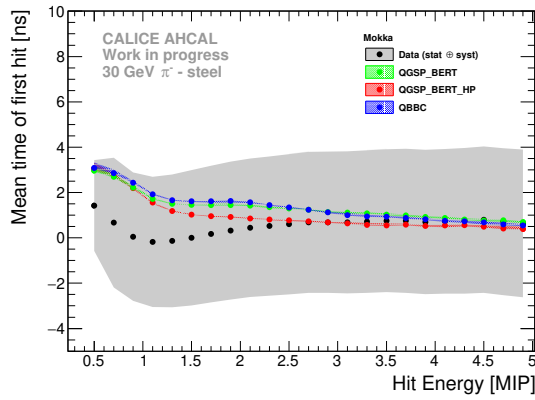
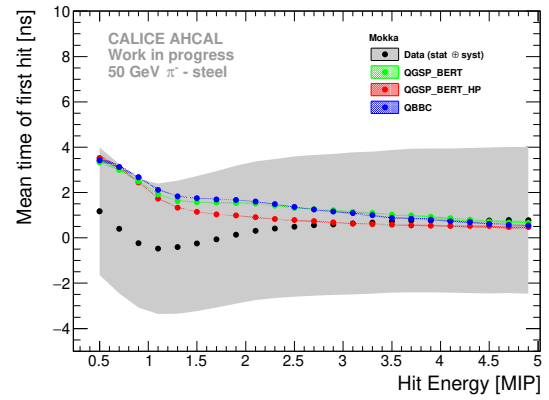


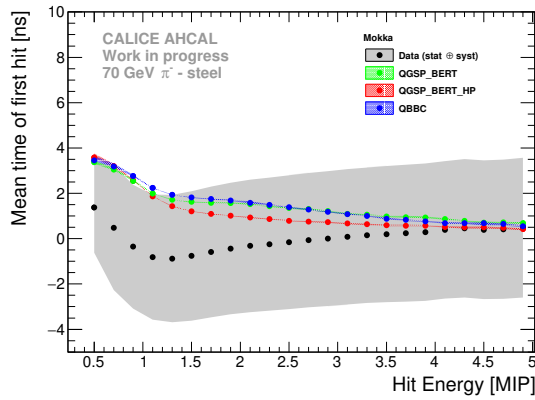
Figure C.4 – Comparison between data and the DD4HEP simulation for pions between 30 and 90 GeV of the time of first hit. The grey box represents the statistic and systematic uncertainty of the data. The error bars are the uncertainty on the DD4HEP simulation obtained by varying the cross-talk parameter and the uncertainty on the time smearing.



(a) 30 GeV.



(b) 50 GeV.



(c) 70 GeV.

Figure C.5 – Comparison between the MOKKA simulation and data of the time of first hit as a function of the hit energy for pion beams between 30 GeV and 70 GeV. The grey and color bands shows the systematics.

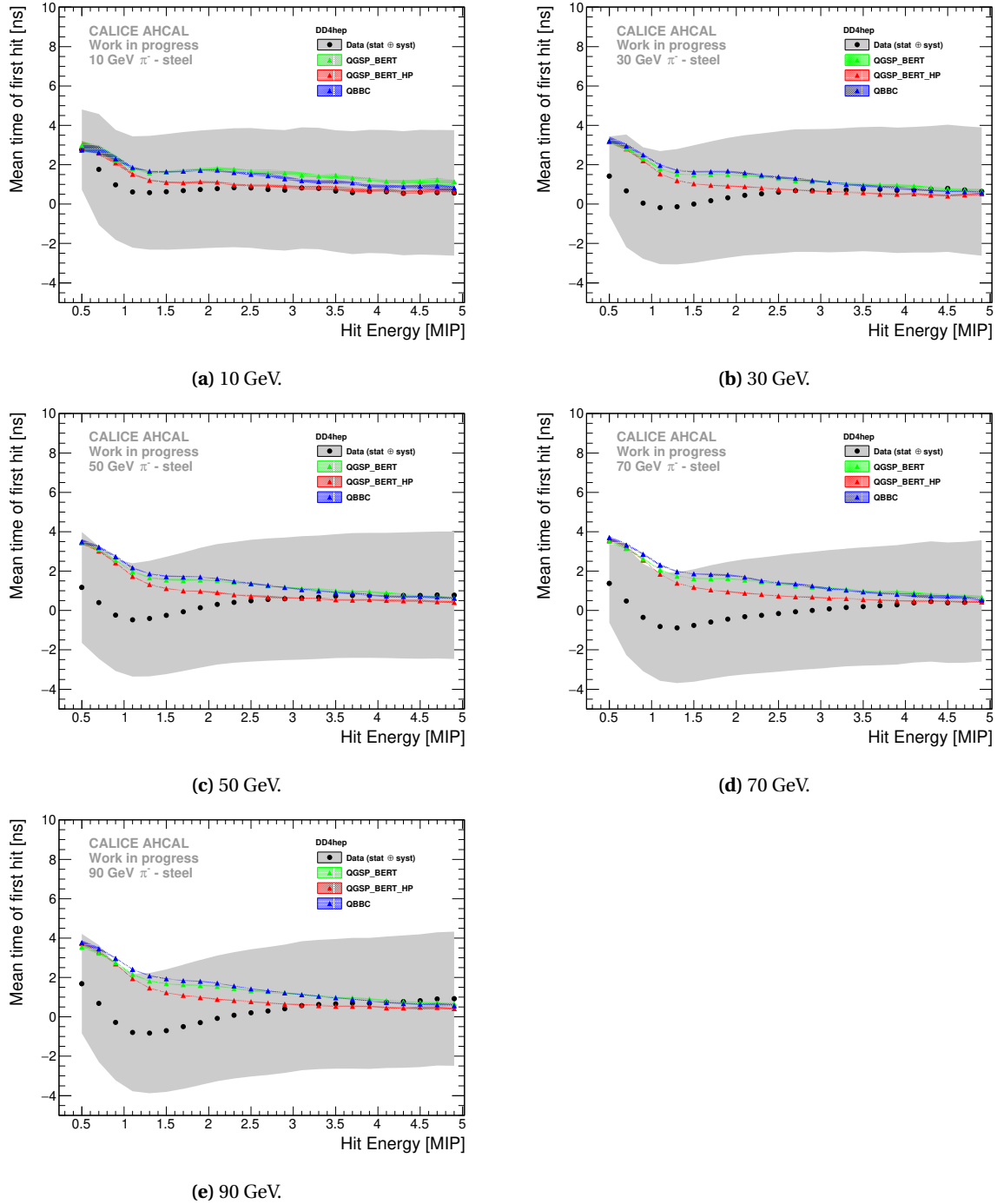
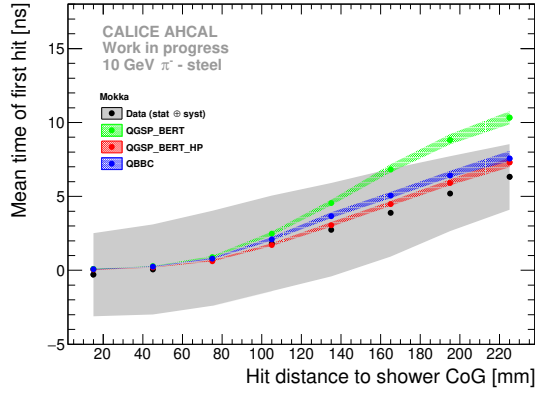
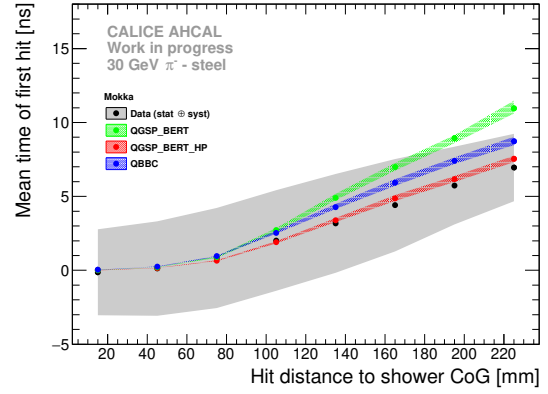


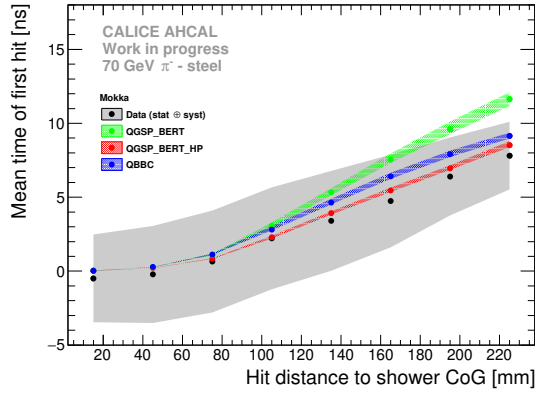
Figure C.6 – Comparison between the DD4HEP simulation and data of the time of first hit as a function of the hit energy for pion beams between 10 GeV and 90 GeV. The grey and color bands shows the systematics.



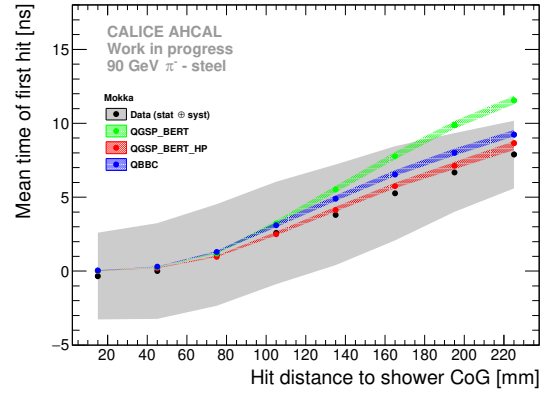
(a) 10 GeV.



(b) 50 GeV.

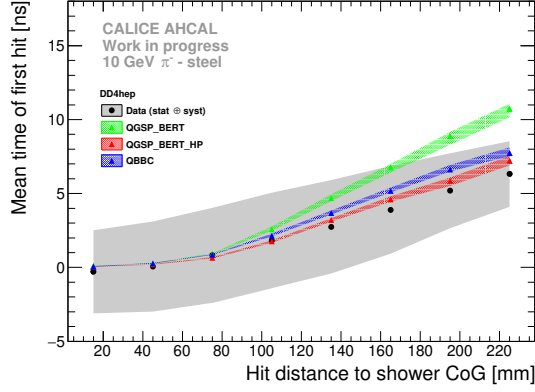


(c) 70 GeV.

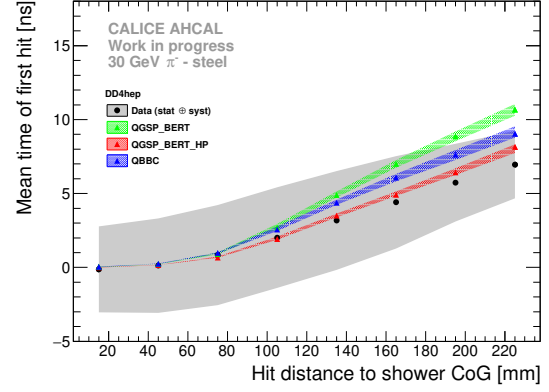


(d) 90 GeV.

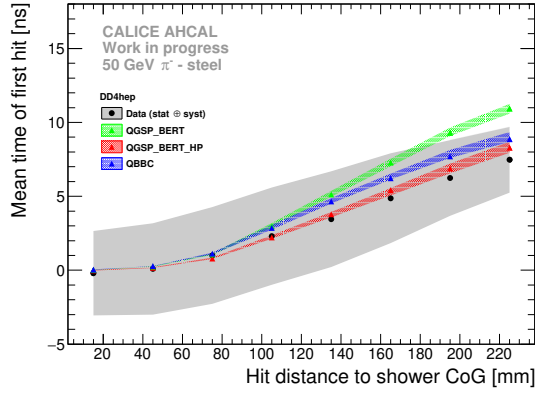
Figure C.7 – Comparison of the time of first hit as a function of the hit distance to the shower axis in data and the Mokka simulation for pion beam energies between 10 GeV and 90 GeV for modules 3 to 10. The grey and color bands shows the systematics.



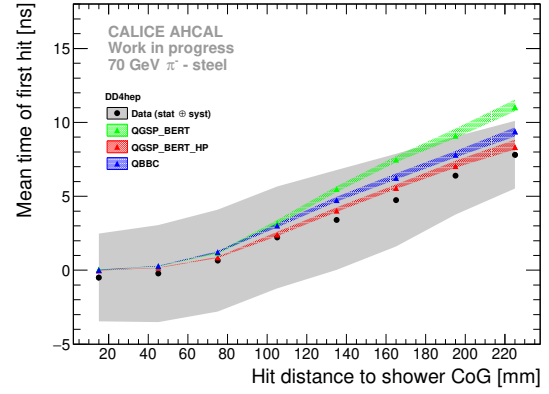
(a) 10 GeV.



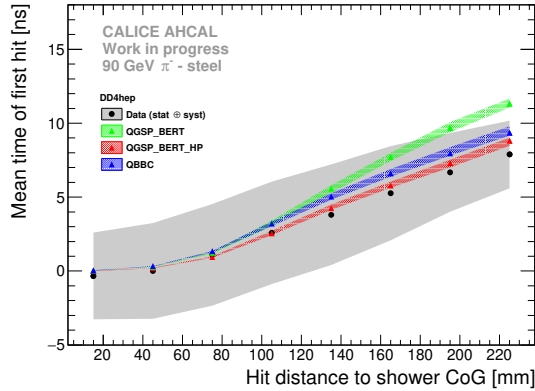
(b) 30 GeV.



(c) 50 GeV.

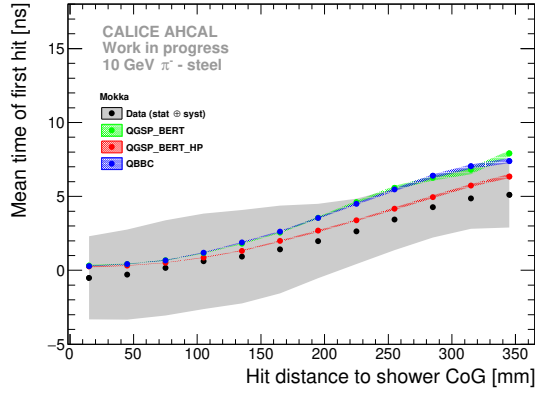


(d) 70 GeV.

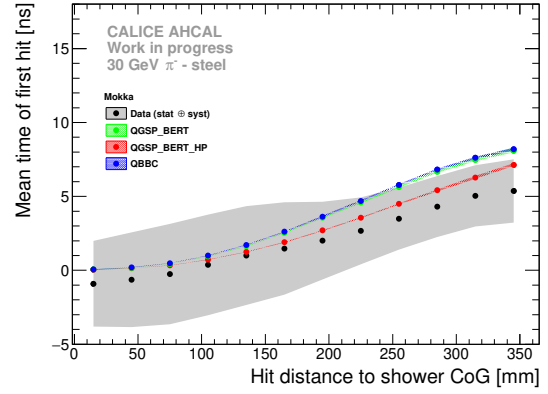


(e) 90 GeV.

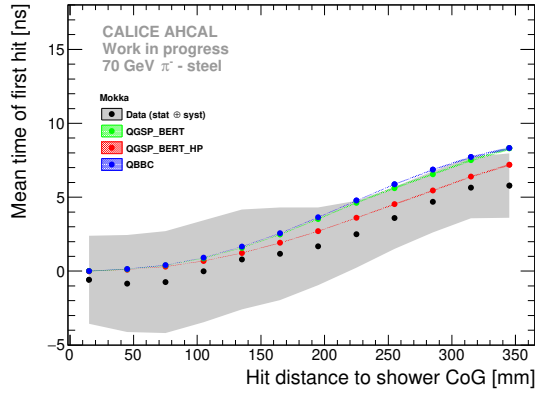
Figure C.8 – Comparison of the time of first hit as a function of the hit distance to the shower axis in data and the DD4HEP simulation for pion beam energies between 10 GeV and 90 GeV for modules 3 to 10. The grey and color bands shows the systematics.



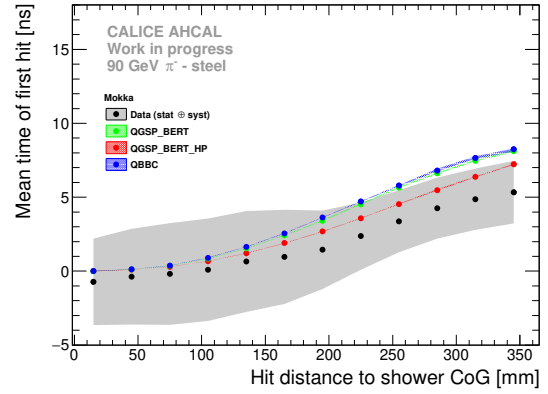
(a) 10 GeV.



(b) 30 GeV.

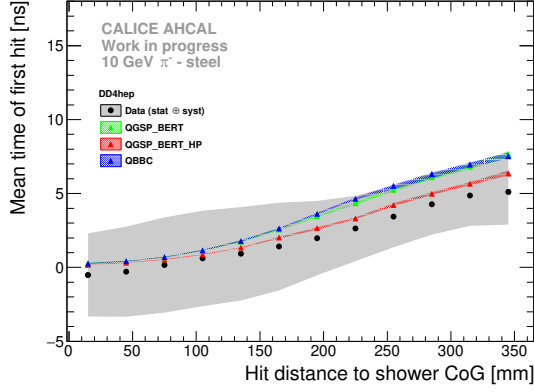


(c) 70 GeV.

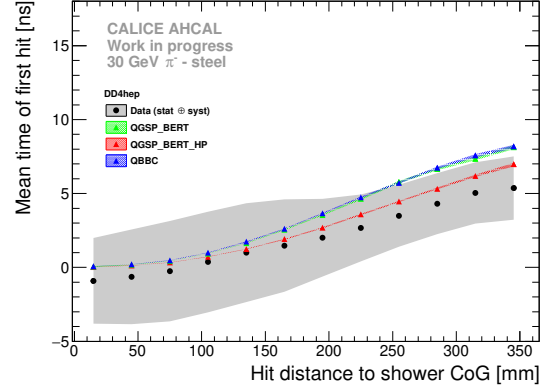


(d) 90 GeV.

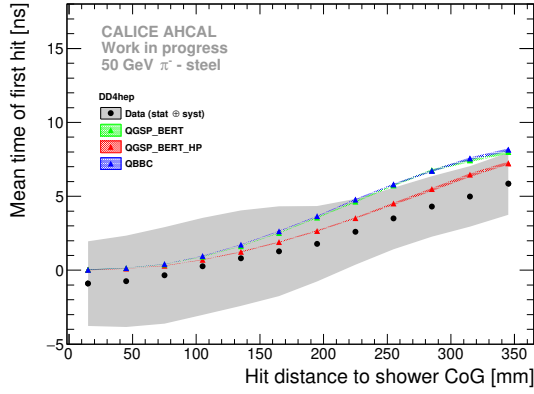
Figure C.9 – Comparison of the time of first hit as a function of the hit distance to the shower axis in data and the MOKKA simulation for pion beam energies between 10 GeV and 90 GeV for modules 11 to 14. The grey and color bands shows the systematics.



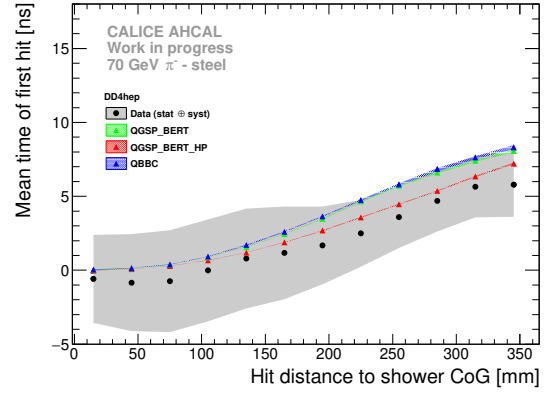
(a) 10 GeV.



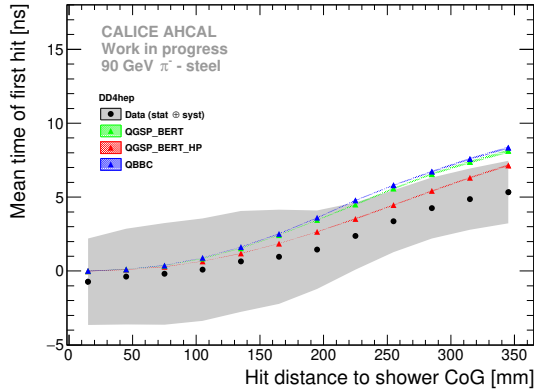
(b) 30 GeV.



(c) 50 GeV.



(d) 70 GeV.



(e) 90 GeV.

Figure C.10 – Comparison of the time of first hit as a function of the hit distance to the shower axis in data and the DD4HEP simulation for pion beam energies between 10 GeV and 90 GeV for modules 11 to 14. The grey and color bands shows the systematics.

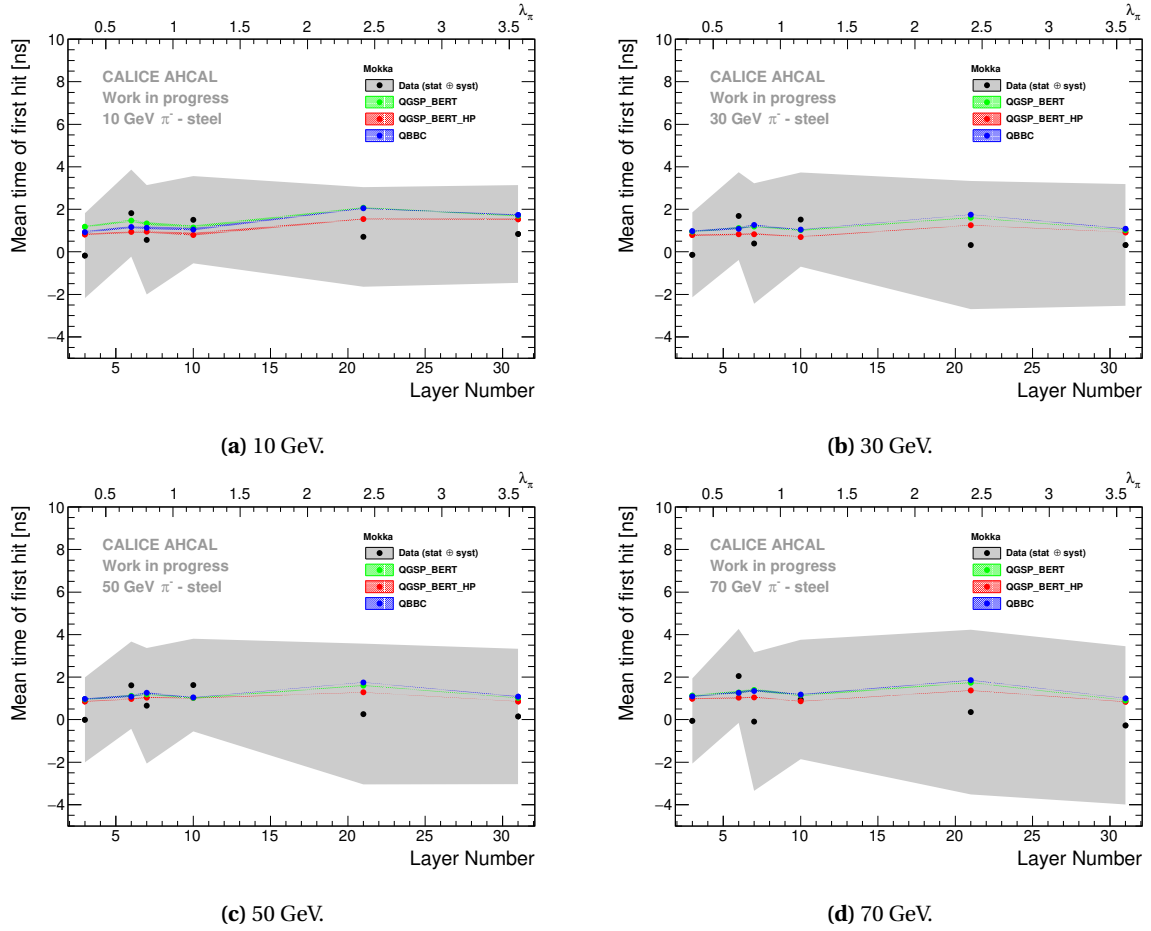


Figure C.11 – Comparison of the time of first hit as a function of the layer position in data and the Mokka simulation for pion beams between 10 GeV and 70 GeV. The grey and color bands shows the systematics.

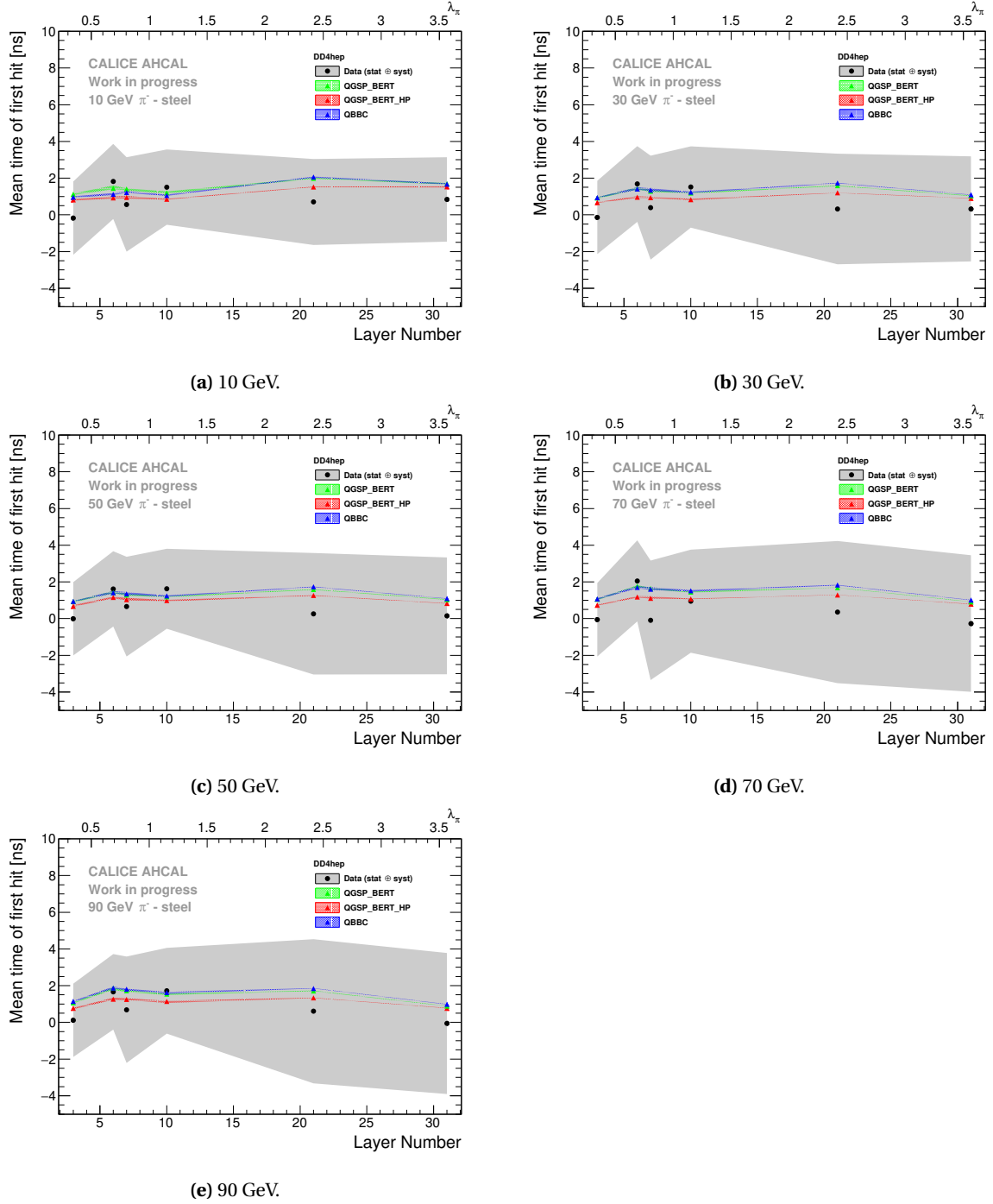


Figure C.12 – Comparison of the time of first hit as a function of the layer position in data and the DD4HEP simulation for pion beams between 10 GeV and 90 GeV. The grey and color bands shows the systematics.

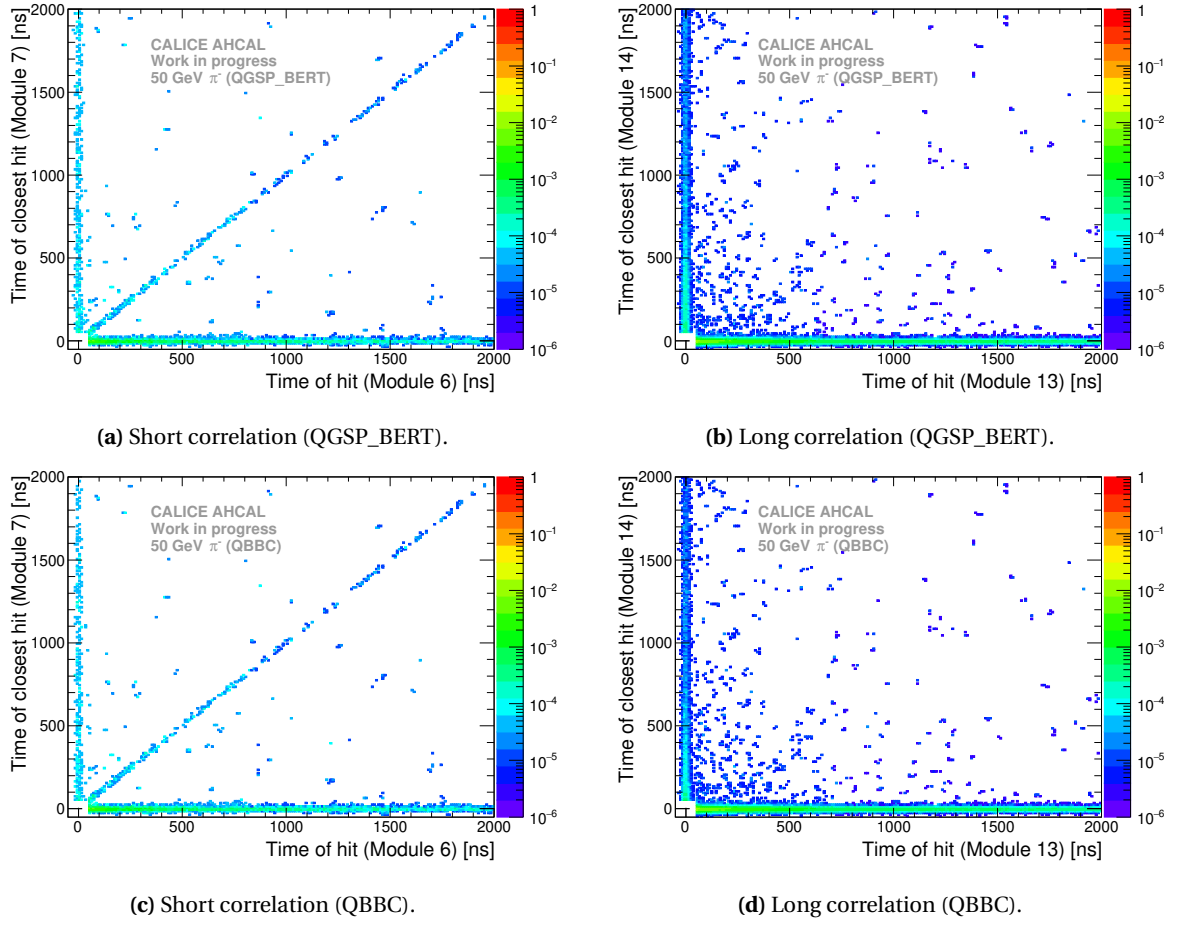
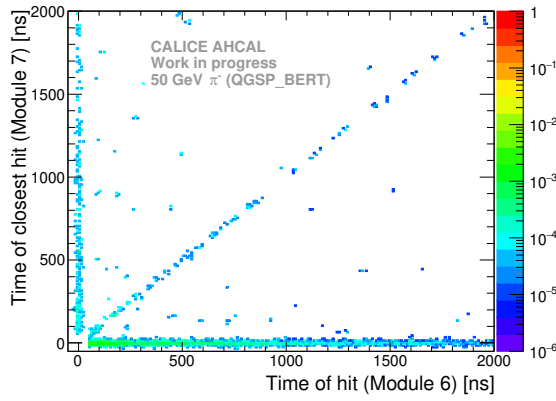
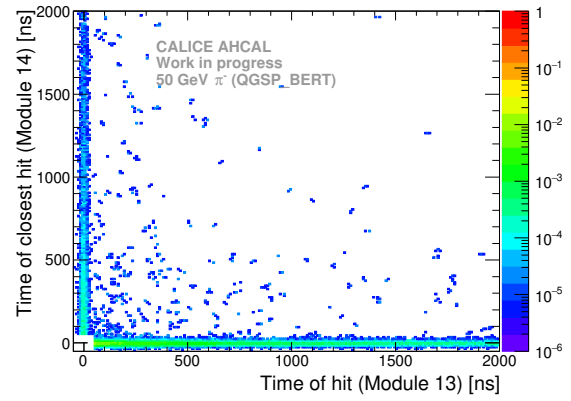


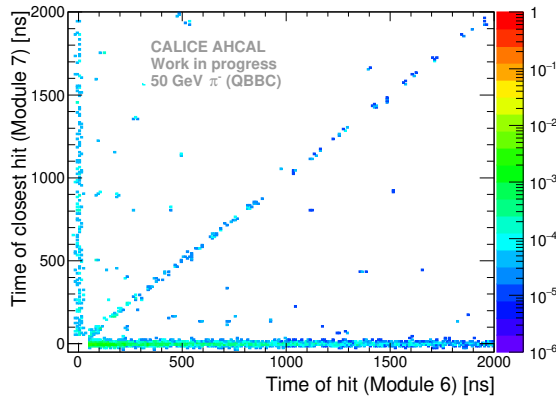
Figure C.13 – Timing correlations between modules 6 and 7 and modules 13 and 14 in MOKKA simulations for different physics lists in 50 GeV pion beam. Each bins are normalized to the number of entries in the 2D histogram.



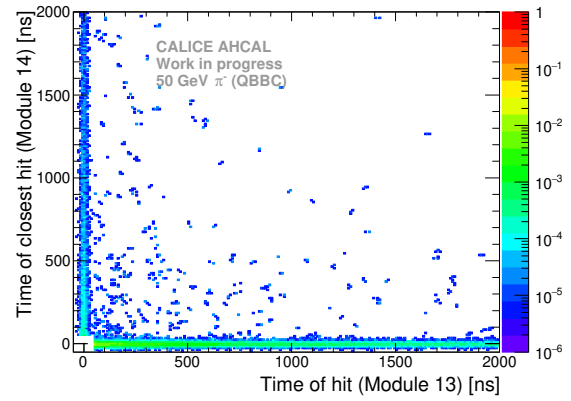
(a) Short correlation (QGSP_BERT).



(b) Long correlation (QGSP_BERT).



(c) Short correlation (QBBC).



(d) Long correlation (QBBC).

Figure C.14 – Timing correlations between modules 6 and 7 and modules 13 and 14 in DD4HEP simulations for different physics lists in 50 GeV pion beam. Each bins are normalized to the number of entries in the 2D histogram.

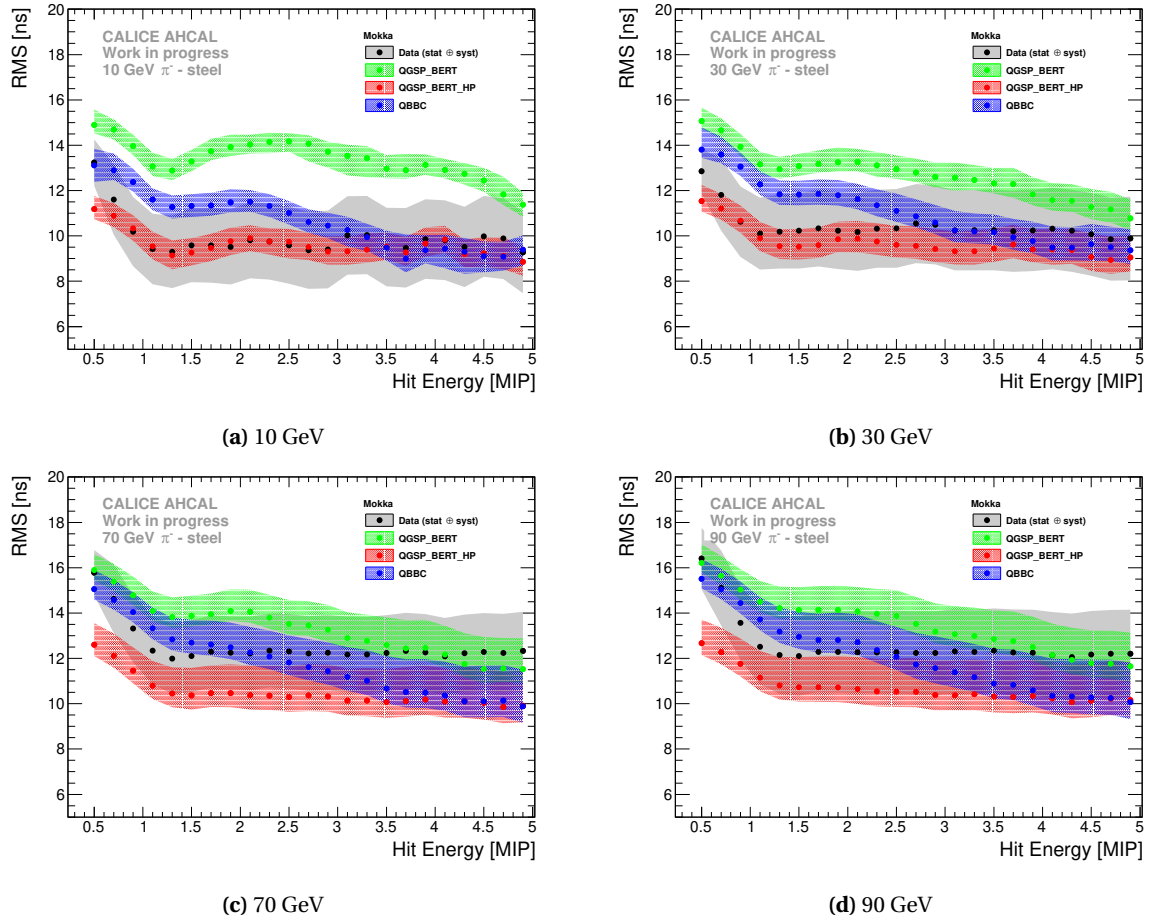


Figure C.15 – Comparison of the RMS of the hit time distribution as a function of the hit energy in data and the Mokka simulation for pion beam energies between 10 GeV and 90 GeV. The grey and color bands shows the systematics.

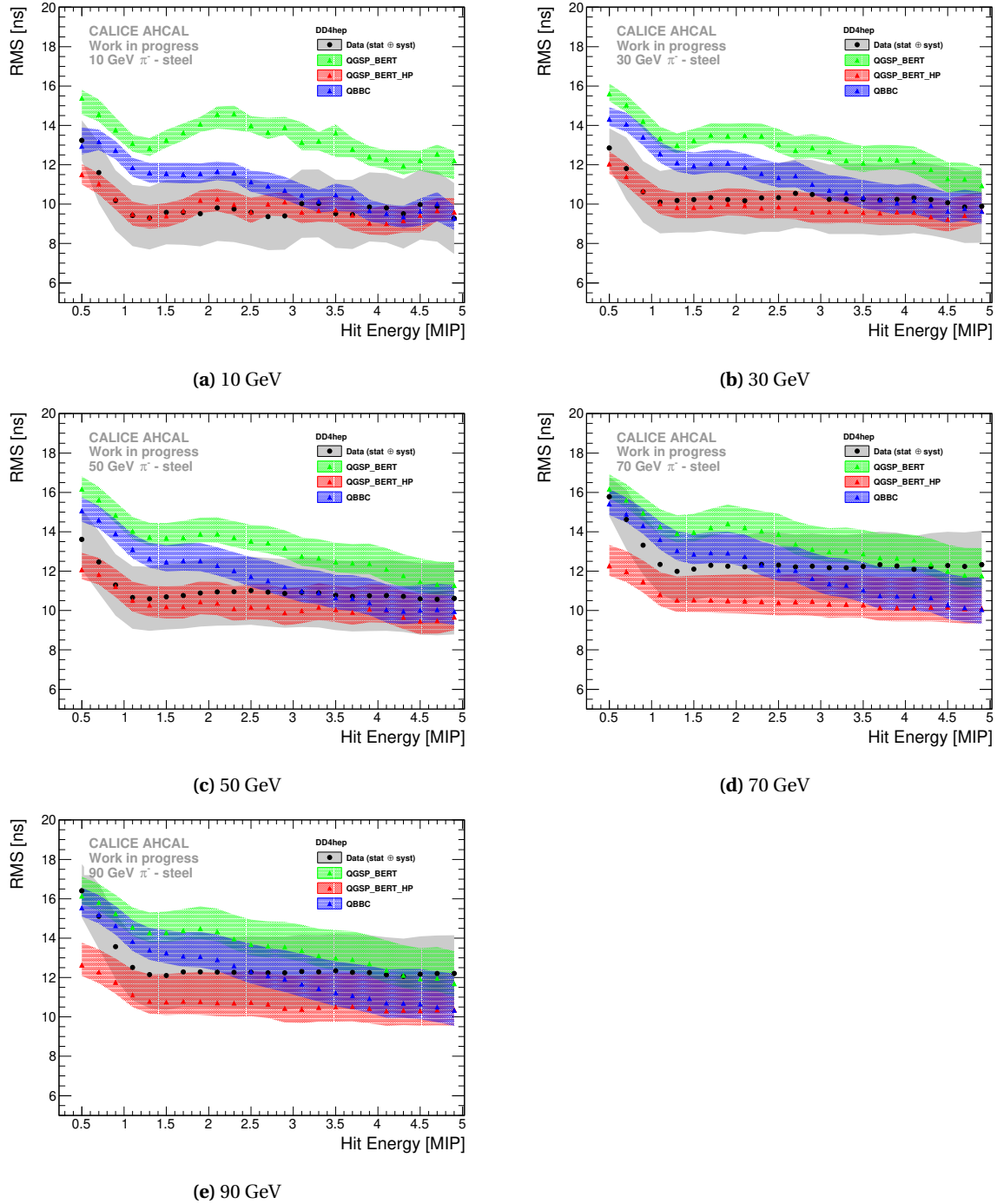
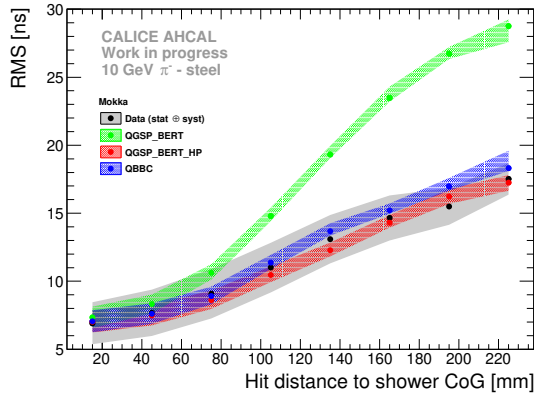
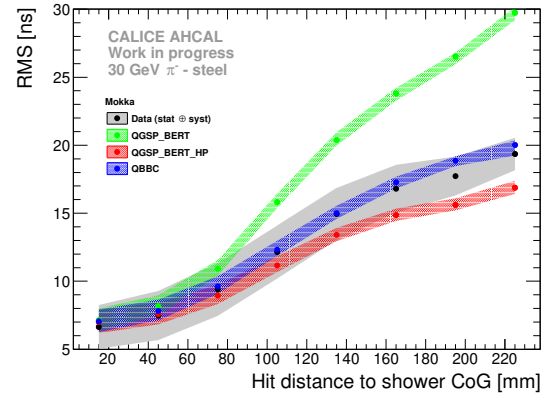


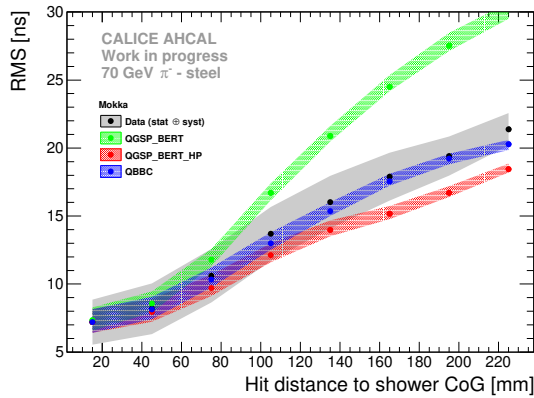
Figure C.16 – Comparison of the RMS of the hit time distribution as a function of the hit energy in data and the DD4HEP simulation for pion beam energies between 10 GeV and 90 GeV. The grey and color bands shows the systematics.



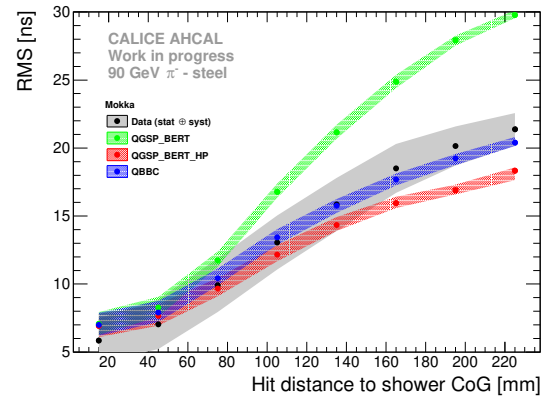
(a) 10 GeV



(b) 30 GeV

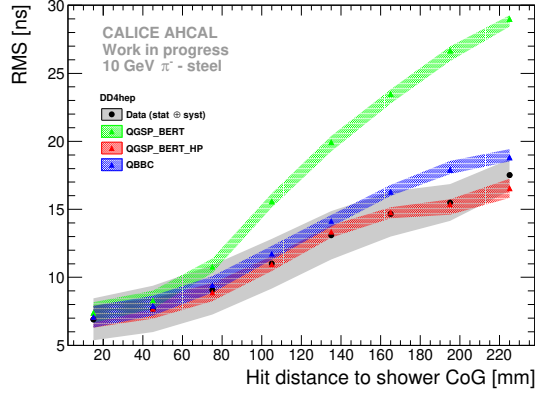


(c) 70 GeV

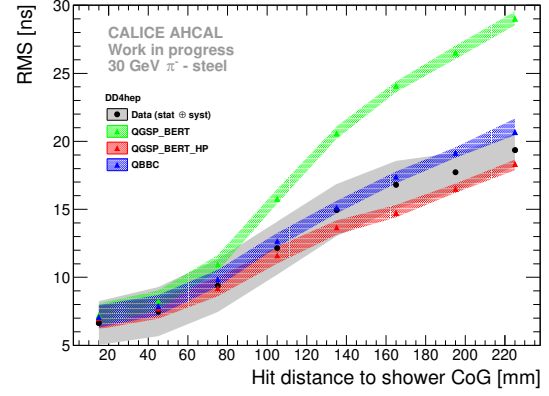


(d) 90 GeV

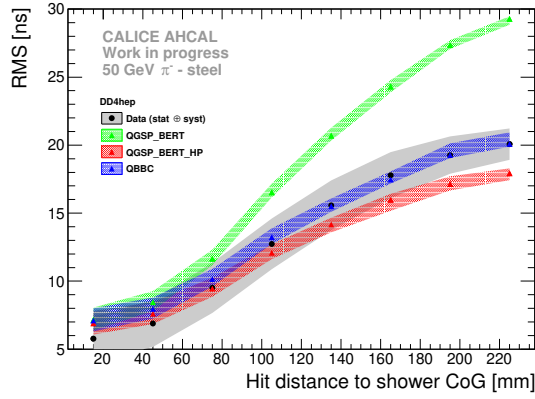
Figure C.17 – Comparison of the RMS of the hit time distribution as a function of the hit distance to the shower center of gravity in data and the Mokka simulation for pion beam energies between 10 GeV and 90 GeV for modules 3 to 10. The grey and color bands shows the systematics.



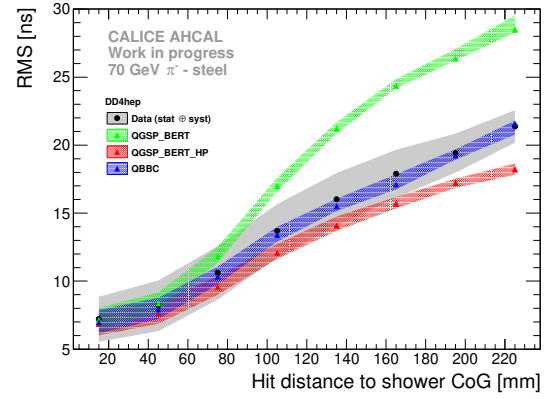
(a) 10 GeV



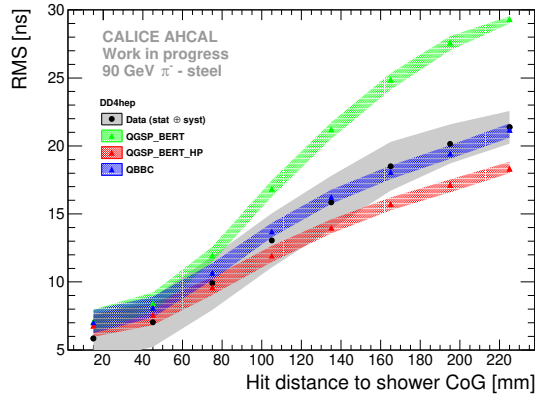
(b) 30 GeV



(c) 50 GeV

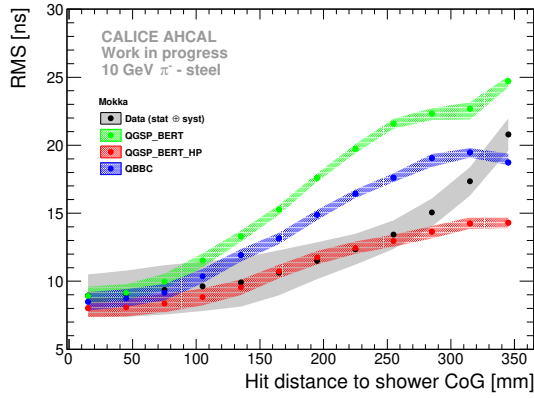


(d) 70 GeV

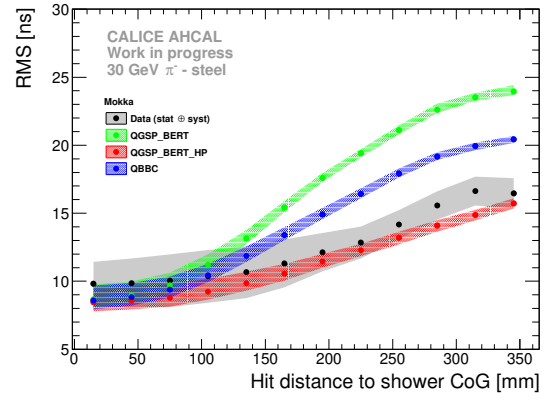


(e) 90 GeV

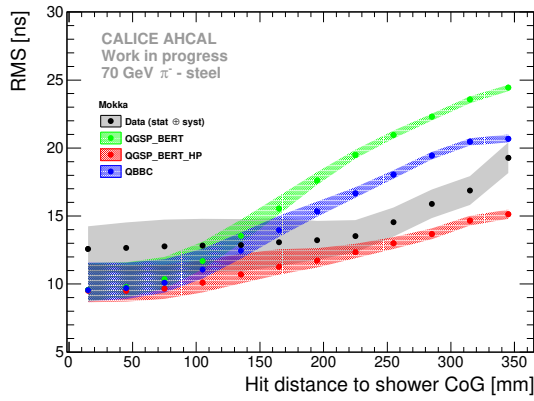
Figure C.18 – Comparison of the RMS of the hit time distribution as a function of the hit distance to the shower center of gravity in data and the DD4HEP simulation for pion beam energies between 10 GeV and 90 GeV for modules 3 to 10. The grey and color bands shows the systematics.



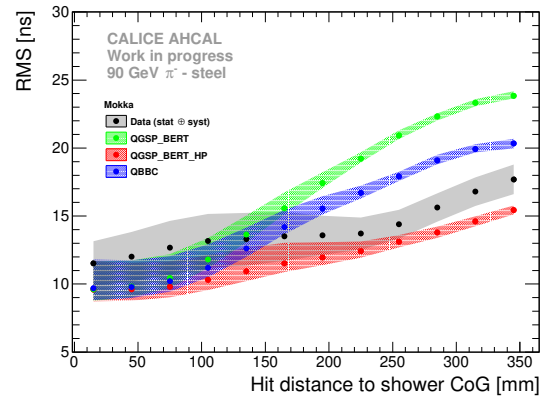
(a) 10 GeV



(b) 30 GeV



(c) 70 GeV



(d) 90 GeV

Figure C.19 – Comparison of the RMS of the hit time distribution as a function of the hit distance to the shower center of gravity in data and the Mokka simulation for pion beam energies between 10 GeV and 90 GeV for modules 11 to 14. The grey and color bands shows the systematics.

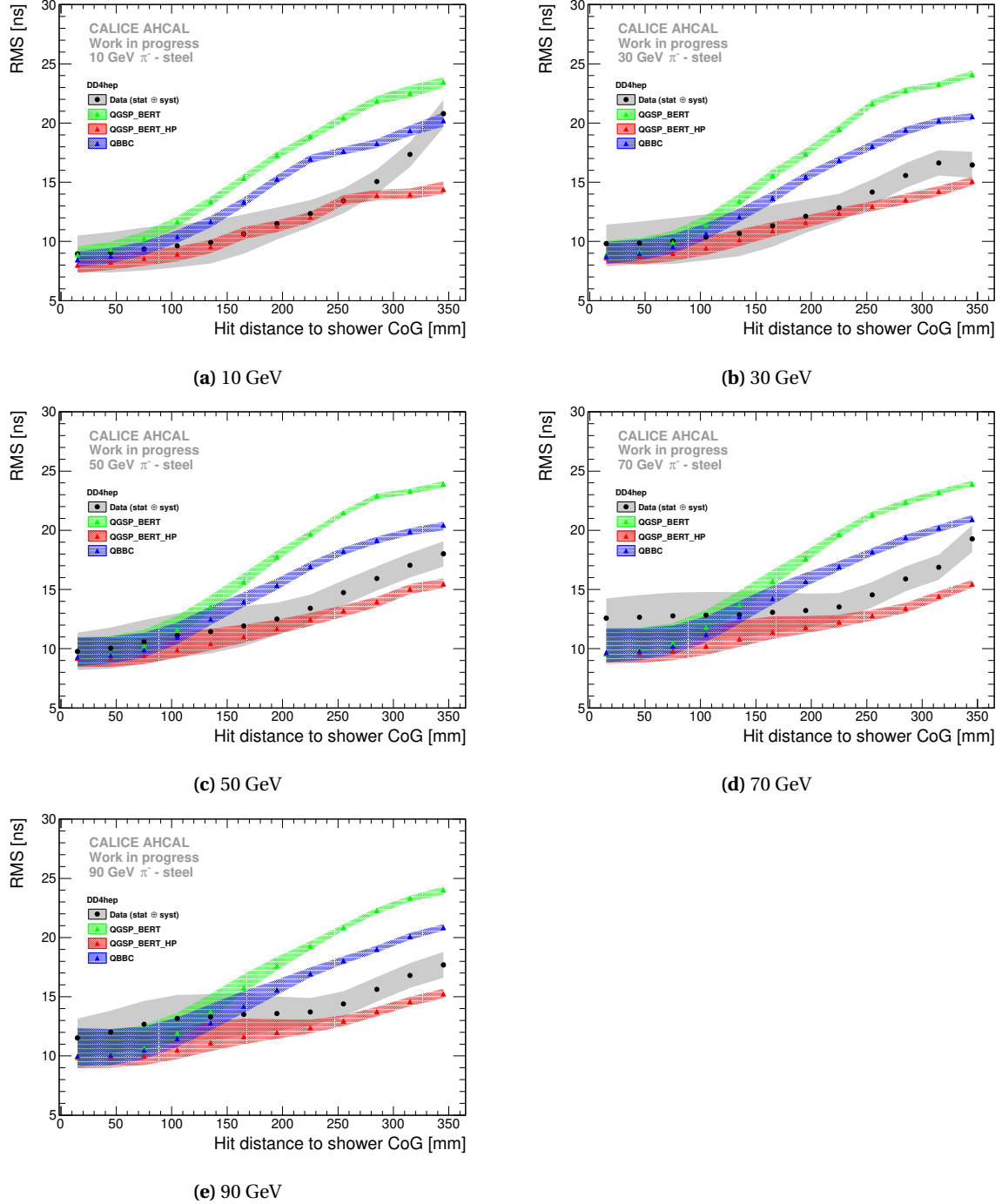


Figure C.20 – Comparison of the RMS of the hit time distribution as a function of the hit distance to the shower center of gravity in data and the DD4HEP simulation for pion beam energies between 10 GeV and 90 GeV for modules 11 to 14. The grey and color bands shows the systematics.

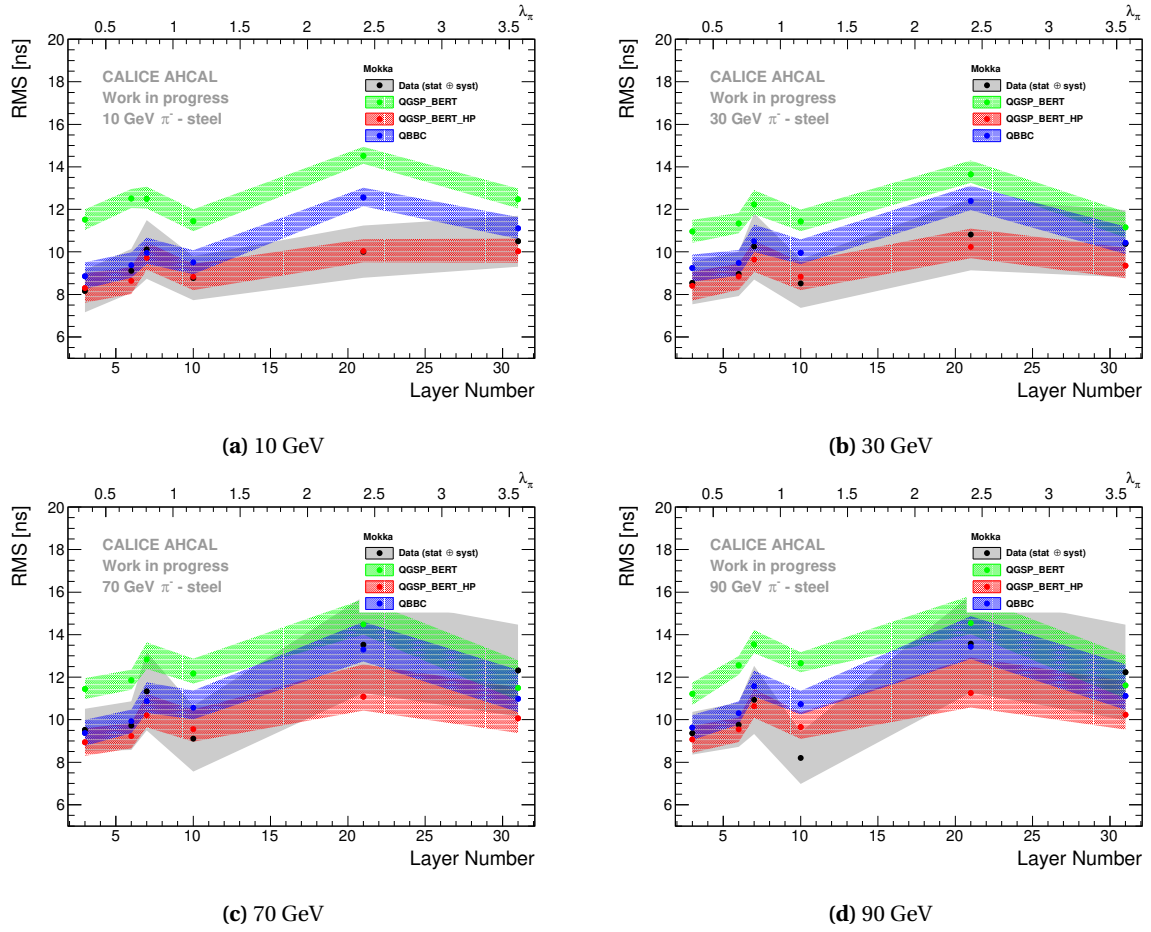


Figure C.21 – Comparison of the RMS of the hit time distribution as a function of layer in data and the Mokka simulation for pion beam energies between 10 GeV and 90 GeV. The grey and color bands shows the systematics.

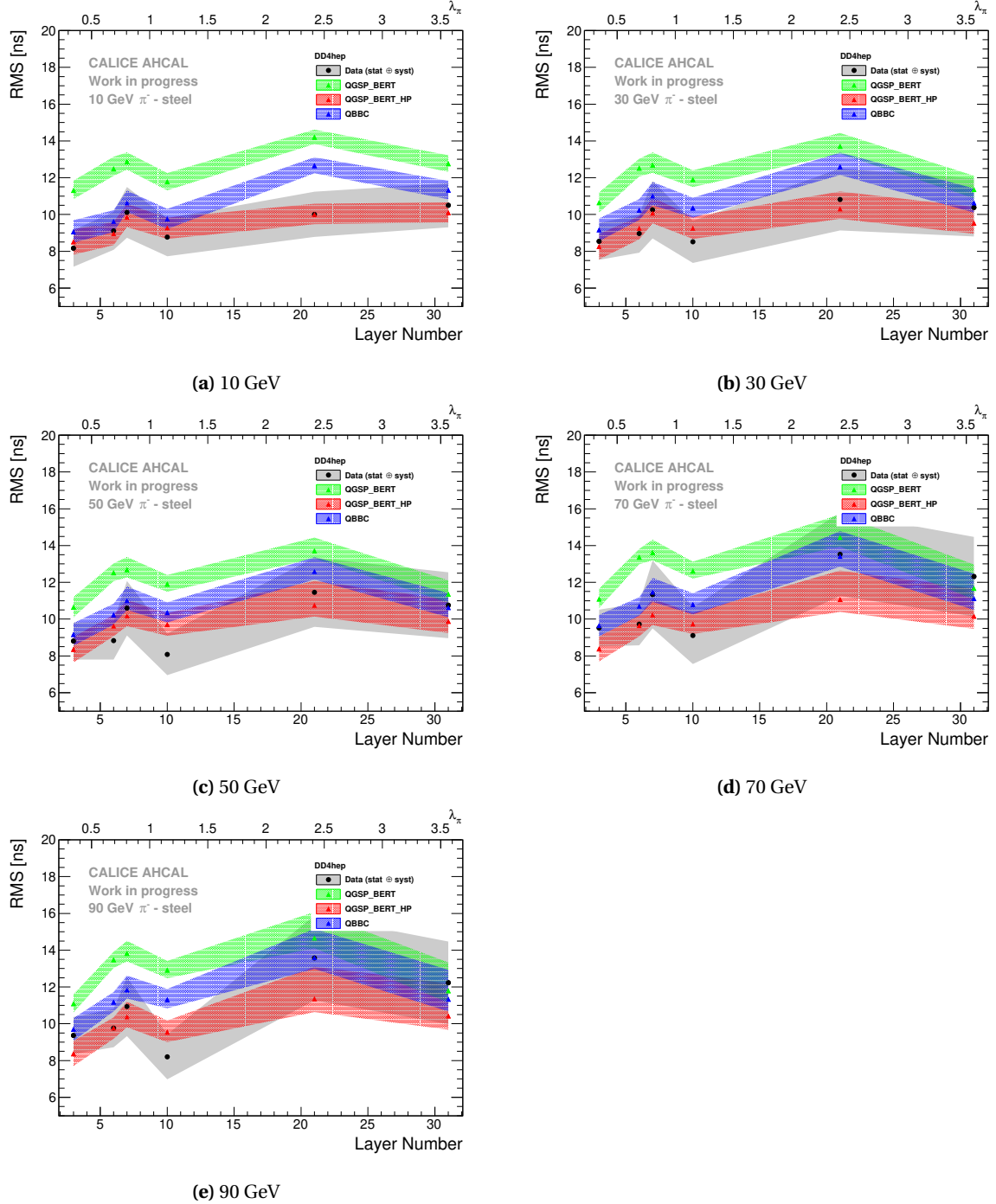


Figure C.22 – Comparison of the RMS of the hit time distribution as a function of layer in data and the DD4HEP simulation for pion beam energies between 10 GeV and 90 GeV. The grey and color bands shows the systematics.

Appendix D

Extraction of noise hits for simulation.

The AHCAL operates in auto-trigger during data taking. Due to this feature, noise hits can't be extracted like the previous CALICE physics prototypes which were extracted by sending external triggers to the detector between beam spills. Moreover, if no validation signal is provided by the trigger scintillators to the chip, hits that are stored in the chip are removed.

One solution to this problem is to use real data events to extract noise hits. It is can be efficiently done using muon runs because a track is present in the calorimeter due to the muon. By removing the identified muon track and keeping remaining hits, noise hits can be extracted. Muon runs from 24647 to 24656 are used for the extraction of noise hits. The table [A.5](#) shows the cuts applied for event selection.

The track found in the selected event is removed and the remaining hits are considered as noise hits. Initially, the time of the noise hits is in TDC unit. To get an approximation time distribution of noise hits, the time of a noise hit is randomly shifted by a flat distribution between 500 and 3500 ns. This acts as a time reference for these hits to give a good description of the noise time distribution. The figures [D.1](#) and [D.2](#) show the energy and time distribution of noise hits.

Most of the fraction of noise hits have an energy under 2 MIPs. Higher hit energies can be seen and they may be due to delta electrons from muon tracks. However, it is not expected to have a great impact on timing. The introduction of noise for timing is very important to compare data and simulation especially for pions where a late tail is present.

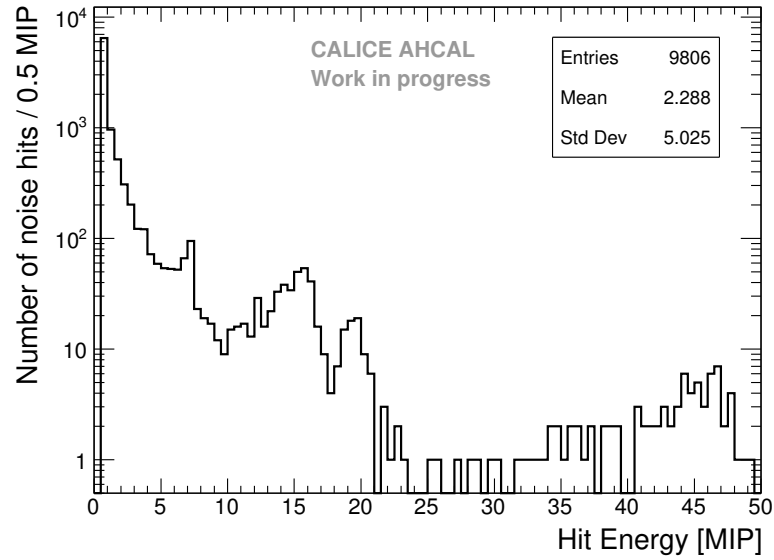


Figure D.1 – Hit energy distribution of the extracted noise hits. Most of the hits have an energy below 2 MIPs although a tail is visible to high energies.

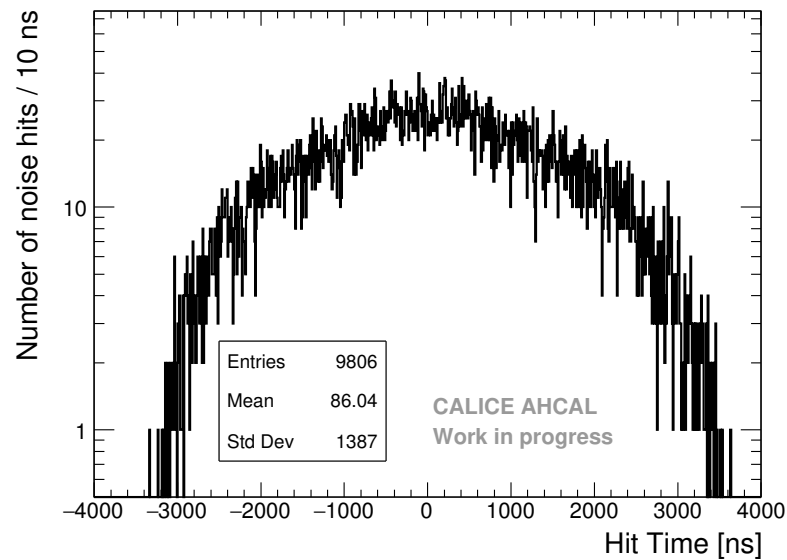


Figure D.2 – Time distribution of the extracted noise hits. The description of the shape of the time distribution is important for the simulation.

Appendix E

Estimation of the uncertainty of the time calibration.

In this appendix, a small study of the uncertainty made on the calibration from TDC to nanoseconds is done. By simple calculation, the conversion is done in the following way:

$$\begin{aligned} T [\text{ns}] &= (\text{TDC} - \text{Ped}) * \text{slope} \\ &= (\text{TDC} - \text{Ped}) * \frac{A}{(\text{Max} - \text{Ped})} \quad \text{with } A = 3920 \text{ ns} \end{aligned}$$

To avoid correlations between the slope and the pedestal, the uncertainty is obtained by differentiating w.r.t Max and Ped. The uncertainty is then obtained via:

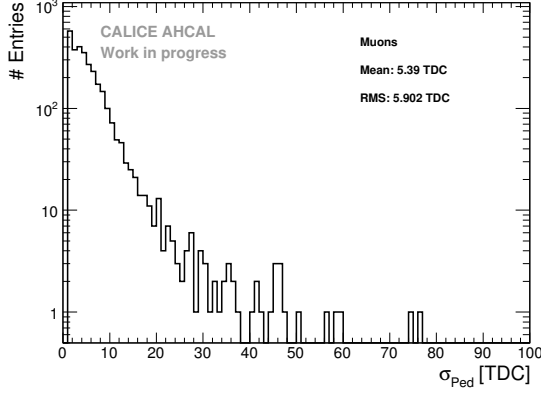
$$\partial t^2 = \left(\frac{\partial t}{\partial \text{Ped}} \right)^2 \times \sigma_{\text{Ped}}^2 + \left(\frac{\partial t}{\partial \text{Max}} \right)^2 \times \sigma_{\text{Max}}^2 + \left(\frac{\partial t}{\partial A} \right)^2 \times \sigma_A^2$$

Assuming that σ_A is null, we get the following formula:

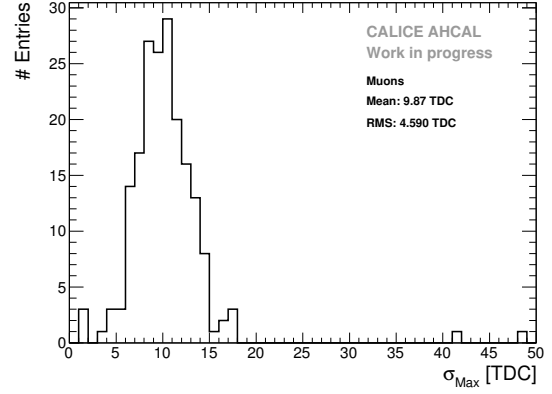
$$\partial t^2 = \frac{1}{(\text{Max} - \text{Ped})^2} \left[\left(\frac{A(\text{TDC} - \text{Max})}{(\text{Max} - \text{Ped})} \right)^2 \times \sigma_{\text{Ped}}^2 + \left(\frac{A(\text{TDC} - \text{Ped})}{(\text{Max} - \text{Ped})} \right)^2 \times \sigma_{\text{Max}}^2 \right]$$

As expected, the formula is symmetric and should be minimum in the middle of the ramp as long as σ_{Max} and σ_{Ped} are similar. However, the uncertainty will be greater on one side or the other depending on the σ being the biggest. The uncertainties estimations σ_{Max} and σ_{Ped} are described in section 9.3. Distributions of the uncertainties extracted are shown in figures E.1a and E.1b. These uncertainties are likely to be over-estimated as they are not reflected in the final timing distribution. Moreover, the shift of the distribution to zero is correcting any uncertainty made on the pedestal for each channels thus σ_{Ped} is likely very small.

The figure E.2b represent the uncertainty made for one channel selected in a single chip for a single memory cell and BXID. It shows the symmetric behavior of the error and present a minimum around the middle of the ramp. This is not a typical channel as mostly the maximum has an error higher than the pedestal due to the difficulty to pick perfectly the maximum of the ramp with the sharp falling edge. A more typical channel can be seen in figure E.2a.

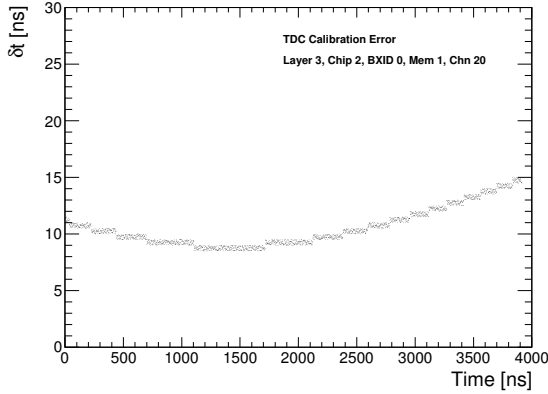


(a) Uncertainty extracted from the edge detection for the pedestal for each chip, channel, memory-cell and BXID.

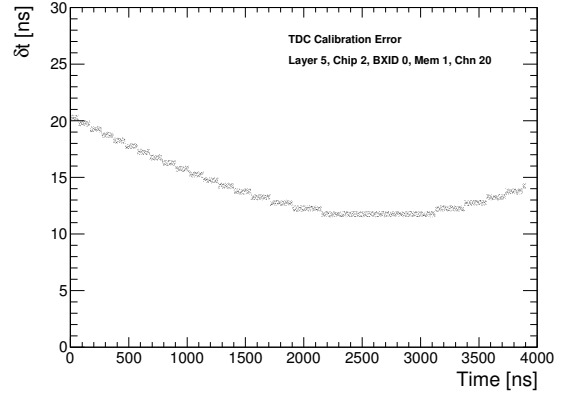


(b) Uncertainty extracted from the edge detection for the maximum of the ramp for each chip and BXID.

Figure E.1 – a) Pedestal uncertainty distribution extracted for all channels in the detector, most of the errors made are small with a high tail certainly due to the limited statistics for some channels. $\mu = 5.37$ TDC, $RMS = 5.82$ TDC **b)** Maximum uncertainty distribution extracted from the edge detection method for each chip and BXID. The error is a bit higher than for the pedestal in general due to the difficulty to detect perfectly the end of the ramp. $\mu = 9.85$ TDC, $RMS = 4.60$ TDC.



(a) Uncertainties extracted from the edge detection for the pedestal for each chip, channel, memory-cell and BXID.



(b) Calibration uncertainty made on the conversion to nanosecond for a channel on layer 5.

Figure E.2 – a) Uncertainty distribution made for a single channel on layer 3. The error is varying between 9 and 14 ns but is likely to be over-estimated and not valid for the final time distribution **b)** Uncertainty distribution made for a single channel on layer 5. The uncertainty is between 12 and 20 ns but is likely to be over-estimated and not valid for the final time distribution.

Appendix F

Influence of the number of triggered channels and parametrization in simulation.

The correction applied function of the number of hits above 0.5 MIPs in a chip is only a global correction shifting the mean of the time distribution. However, it does not correct for the increase of the width of the time distribution. The increase of the width can be clearly seen in figure F.1a. This increase has to be implemented in the simulation in order to match the timing distribution of electrons without also influencing the time distribution for muons. A parametrization extracted from data is therefore implemented in the simulation. This parametrization assumes the following, the effect is additional to the seen muon resolution giving then:

$$\text{RMS}_{\text{obs}}^2 = \text{RMS}_{\mu}^2 + \text{RMS}_{\text{effect}}^2$$

The $\text{RMS}_{\text{effect}}$ is extracted from data by fitting with a function of the following form:

$$f(t) = A \times e^{-\frac{(t-\mu_1)^2}{2(\sigma_1^2 + \sigma_{\text{effect}}^2)}} + B \times e^{-\frac{(t-\mu_2)^2}{2(\sigma_2^2 + \sigma_{\text{effect}}^2)}} + C$$

The parameters μ_1 , σ_1 , μ_2 and σ_2 are fixed from table 10.2. By plotting σ_{effect} extracted as a function of the number of triggered channels in a chip, one can extract a parametrization. This is done for each electron energy point as shown in figure F.1b. One can observe that each parametrization curve is slightly different for each energy. This may be due to the fact that each energy affects not exactly the same part of the detector. Moreover, the 50 GeV parametrization looks very different than the others. All time distributions for all chips and layers have been investigated manually in order to understand the different but no clear reason has been found.

To accommodate this, a mean parametrization is used in simulation with an envelope used as uncertainty as shown in figure F.2. Only points up to 10-11 number of channels are extracted from data. Above this, the value of σ_{effect} is extrapolated. This should in principle have relatively a small effect for electrons as mainly 6-10 hits are expected per chip. However, the effect may be relevant for pions.

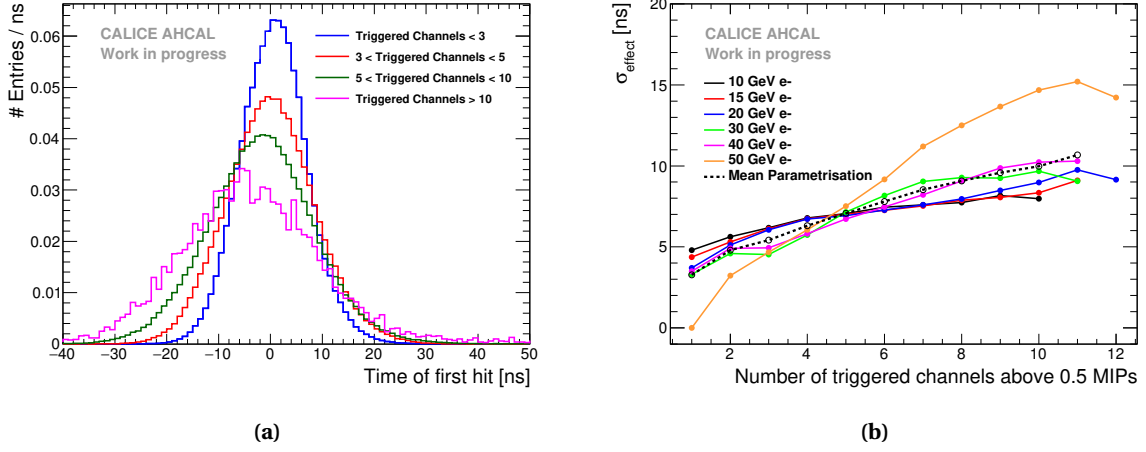


Figure E.1 – a) Time of the first hit distribution for 20 GeV electrons for different binning of number of triggered channels in a chip. The distribution width is increasing with the number of triggered channels in a chip. b) σ_{effect} extracted function of the number of triggered channels in a chip for each energies. σ_{effect} increases up to 12-15 ns with the number of triggered channels in a chip.

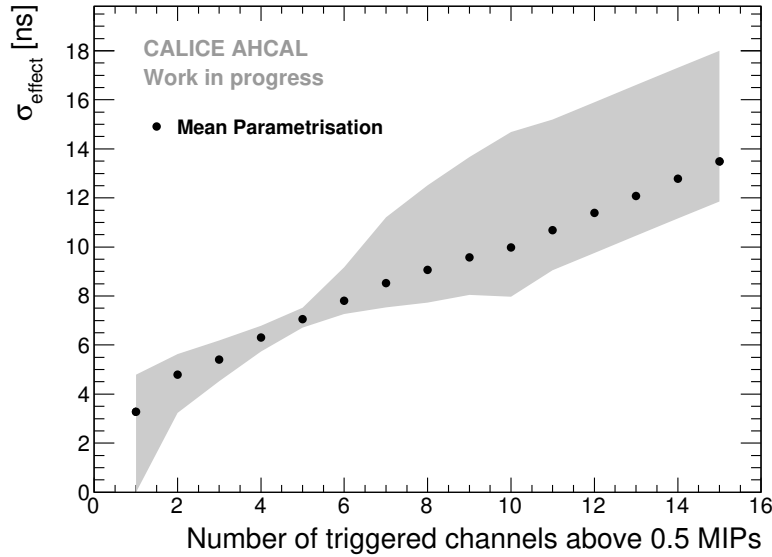


Figure E.2 – Mean parametrization of σ_{effect} as a function of number of triggered channels. The grey area represents the uncertainty on the parametrization.

Appendix G

Tables of rejected chips.

The procedure to reject chips is explained in section [7.2.5](#).

Table G.1 – Table of chips rejected for muon runs.

Name	Beam Energy	Chips
Muon Runs	All	157, 169-184

Table G.2 – Table of chips rejected for electron and pion runs.

Name	Beam Energy	Chips
Electron Runs	All	145, 149-151, 153, 157, 161-168, 172, 175, 187-189, 191
Pion Runs	All	145-152, 185-200 + Electron chips

Appendix H

List of dead channels.

This appendix contains the list of channels that are considered dead or noisy for the testbeam at CERN in July 2015. This list contains channels that presented no calibration value such as pedestal, gain or MIP value. An additional cross-check was performed manually [\[145\]](#) using the muon and electron data. The total of dead and noisy channels accounts for 15% of the whole detector (3744 channels).

Table H.1 – Table containing the list of dead and noisy channels.

Layer #	Chip	Chn
1	0	0, 1, 4, 6, 13, 17, 26, 27, 29, 30-35
	1	0, 1-6, 8, 11, 12, 15, 18-20, 22-28, 30-35
	2	0-8, 13, 16, 17, 20, 28, 32, 35
	3	0, 3, 7, 18, 19, 22, 27, 29, 30-35
2	0	0-6, 8
	1	1, 5, 17, 18, 27, 29-35
	2	15, 17, 18, 22, 23, 27, 29-35
	3	0-8, 16, 17, 25
3	3	0, 14
4	1	8
	2	24, 34
	3	0, 12, 19, 24, 26
5	0	9, 19, 23, 26, 31, 32
	1	1, 8, 17
	2	9, 29
	3	0, 6, 15, 33
6	0	0-5, 6, 8-35
	1	1, 5, 6, 10-12, 13-16, 18, 22-28, 31-35
	2	0-6, 8, 9, 12, 14, 18, 21-23, 24, 27-29, 31-34
	3	0, 1-6, 8, 10-12, 15-18, 22-25, 27, 34, 35
7	0	3, 12, 17, 29, 35
	1	1, 2, 5, 14, 15, 21, 31
	2	0, 3, 4, 7, 9, 12, 13
	3	0, 14, 17, 20, 21
8	0	6, 9, 13, 21, 27, 28, 32, 35
	1	0, 6, 9, 21, 24, 25, 26
	2	5-35
	3	0, 4, 8, 10, 11, 22, 27
9	0	0, 5, 14, 22, 24, 29, 34, 35
	1	3, 5, 6, 10, 14, 19, 29, 30, 31, 35
	2	5, 13, 20-24, 29
	3	0, 1, 4, 5
10	0	0-12, 14-18, 20-24, 26, 27, 29, 30, 32, 35
	1	0, 1-4, 6, 10-17, 19, 20, 22-25, 28-30, 32
	2	0, 3, 4, 6, 8, 10-21, 23, 24, 26, 29, 32-35
	3	0, 2, 4, 5, 7-12, 17, 18, 22-24, 26, 28, 35

Table H.2 – Table containing the list of dead and noisy channels.

Layer #	Chip	Chn
11	0	0-3, 16, 18, 23, 28, 32-35
	1	7, 17, 30, 31
	2	1, 3, 18, 22, 28-30
	3	1, 3, 11
	4	2, 16, 22, 34, 35
	5	7, 12, 17, 19-21, 29, 30, 34
	7	0, 30, 32
	8	0, 23
	10	0, 6, 35
	11	1, 5
	12	3-5
	13	17, 29, 30
	14	1, 8
	15	0, 1, 6, 10, 20, 25, 29, 30
12	0	0, 23, 34
	1	0, 17
	3	0
	5	17
	6	34
	8	17
	9	34
	10	0, 6, 12, 17, 28
	12	5
	13	0, 17
13	0	23, 34, 35
	1	17
	3	1
	5	17, 19
	6	14, 21
	7	31
	8	23, 34
	9	28, 29
	10	0, 6, 12, 34
	12	5, 34
	13	12, 13, 15, 17
	14	20
14	0	17
	1	17
	5	17
	7	7, 8
	9	17
	10	0, 5, 6, 12, 35
	11	12, 31
	12	5
	13	17, 28, 32

Appendix I

Calibration database

This appendix contains tables [I.1](#) and [I.2](#) of the folder and tags names in the geometry and calibration database used for the timing analysis.

Table I.1 – The CALICE geometry database folder names of the 2015 CERN testbeam campaign. Tags are given in brackets.

Calibration set	Database folder/tag
Ahc2ModuleDescription	/cd_calice_cernSPS2015/TestbeamJuly2015/ModuleDescription (HEAD)
Ahc2ModuleConnection	/cd_calice_cernSPS2015/TestbeamJuly2015/ModuleConnection (HEAD)
Ahc2ModuleLocationReference	/cd_calice_cernSPS2015/TestbeamJuly2015/ModuleLocationReference (HEAD)
Ahc2DetectorTransformation	/cd_calice_cernSPS2015/TestbeamJuly2015/DetectorTransformation (HEAD)
Ahc2HardwareConnection	/cd_calice_cernSPS2015/TestbeamJuly2015/Ahc2HardwareConnection (HEAD)

Table I.2 – The CALICE calibration database folder names of the 2015 CERN testbeam campaign. Tags are given in brackets.

Calibration set	Database folder/tag
E4DPedestal	/cd_calice_cernSPS2015/TestbeamJuly2015/Pedestal (ahc2_pedestal_010)
E4DGainConstants	/cd_calice_cernSPS2015/TestbeamJuly2015/gain_constants (ahc2_gain_constants_004)
E4DGainSlopes	/cd_calice_cernSPS2015/TestbeamJuly2015/gain_slopes (ahc2_gain_slopes_003)
E4DMipConstants	/cd_calice_cernSPS2015/TestbeamJuly2015/mip_constants (ahc2_mip_constants_008)
E4DMipSlopes	/cd_calice_cernSPS2015/TestbeamJuly2015/mip_slopes (ahc2_mip_slopes_006)
E4DDeadCellMap	/cd_calice_cernSPS2015/TestbeamJuly2015/DeadCellMap (ahc2_DeadCells_017)
E4DSaturationParameters	/cd_calice_cernSPS2015/TestbeamJuly2015/SaturationParameters (ahc2_Sat_001)
E4DIntercalibration	/cd_calice_cernSPS2015/TestbeamJuly2015/Intercalibration (ahc2_IC_008)
E4DPhysicsCalibIntercalibration	/cd_calice_cernSPS2015/TestbeamJuly2015/PhysicsCalibIntercalibration (ahc2_PhysicsCalibIC_002)
E4DTimeSlopes	/cd_calice_cernSPS2015/TestbeamJuly2015/TimeSlopes (ahc2_time_slopes_001)
E4DTimePedestal	/cd_calice_cernSPS2015/TestbeamJuly2015/TimePedestal (ahc2_time_Ped_001)

List of tables

1.1	Elementary fermions and their properties in the Standard Model. The masses are from [8]. The quark masses depend on the calculation scheme.	4
1.2	Bosons in the Standard Model. The masses are from [8]. The photon and gluon are assumed to be massless. Gravitation is not considered.	5
2.1	Decay modes of the Higgs boson and the branching ratio for a SM Higgs boson at $m_H = 125$ GeV []. Others represents $\mu\mu$, $\gamma\gamma$, $Z\gamma$ and invisible.	17
5.1	Material description in MOKKA and DD4HEP simulations of the testbeam setup at CERN in July 2015. The X_0 and λ_n numbers are obtained by the command-line <i>materialScan</i> in the DD4HEP framework.	61
5.2	Number of single particle events simulated in MOKKA and DD4HEP for each particle type and energy.	61
6.1	List of the different SiPMs used in the CALICE AHCAL in July 2015.	66
6.2	List of breakdown and operating voltages applied to each SiPM types. V_{op} represents $V_{Br} + V_{overvoltage}$. V_{PB} is the voltage applied to the power board.	67
6.3	List of the targeted gains for each module type.	69
7.1	List of AHCAL channels used as time reference for this analysis.	80
7.2	List of runs taken at SPS in July 2015. The number of event specified in the table are including single noise hit events.	81
7.3	Efficiency of the electron selection for simulated electrons, muons and pions for energies between 10 and 50 GeV. The efficiency is defined as the number of events after selection divided by the number of events before selection. It is estimated from Monte-Carlo and does not included the Cherenkov efficiency.	85
7.4	Efficiency of the pion selection for beam energies between 10 and 90 GeV. The efficiency is defined as the number of events after selection divided by the number of events before selection. It is estimated from Monte-Carlo and does not included the Cherenkov efficiency.	85
8.1	Table containing the results of the extraction of the MIP calibration constants. The results are regrouped by SiPM type. $\langle \text{MIP} \rangle$ is the mean of the MIP calibration constant distribution per SiPM type. RMS is the standard deviation of MIP calibration constant distribution per SiPM type. Dead and noisy channels are rejected.	95

8.2 Settings of the particle gun in simulation used to reproduce the beam profile of the data runs used in this thesis.	98
9.1 Table with the number of events selected for the muon and electron data for the timing calibration.	104
10.1 Summary of systematic uncertainties.	123
10.2 Timing resolution extracted with a double Gaussian fit from muon data used for simulation. . .	123
11.1 Table with the number of events selected in the pion dataset for the timing study.	127
11.2 Summary of the fit results in figure 11.1.	129
11.3 Table with fraction of entries in the red box region as calculated with equation 11.2. The top is for MOKKA simulations, the bottom is for DD4HEP simulations. The quoted errors are only statistical errors.	141
12.1 Assumption on the time resolution of the front-end electronics for different scenarios.	158
A.1 Selection cuts for the muon runs.	173
A.2 Selection cuts for each electron runs.	173
A.3 Selection cuts for the pions runs.	174
A.4 Selection cuts for the time reference channels.	174
A.5 Selection cuts for the extraction of noise hits from muon runs.	174
G.1 Table of chips rejected for muon runs.	209
G.2 Table of chips rejected for electron and pion runs.	209
H.1 Table containing the list of dead and noisy channels.	212
H.2 Table containing the list of dead and noisy channels.	213
I.1 The CALICE geometry database folder names of the 2015 CERN testbeam campaign. Tags are given in brackets.	215
I.2 The CALICE calibration database folder names of the 2015 CERN testbeam campaign. Tags are given in brackets.	216

List of figures

2.1	Feymann diagrams for the Higgs production at the ILC at tree level. [20]	16
2.2	The recoil mass distribution for $Zh \rightarrow \mu^+ \mu^- X$ at $\sqrt{s} = 250$ GeV for 250 fb^{-1} integrated luminosity and beam polarisation of (+80%, -30%). Simulated with $m_h = 125$ GeV. [42]	17
2.3	Relative precision of the Higgs couplings extracted for the ILC in a model-dependent analysis. Projections of the achievable precision on the Higgs couplings for the HL-LHC are shown as well in a pessimistic (CMS-1) and optimistic (CMS-2) case on the systematic uncertainties [39].	19
2.4	Schematic of the International Linear Collider (not to scale). [1].	21
2.5	Schematic of beam structure of the ILC operated a design parameters.	21
2.6	Picture of a nine-cell 1.3 GHz superconducting RF niobium cavity developed for the ILC. [36].	22
2.7	Schematic view of the International Large Detector. [38]	23
2.8	Schematic view of the Silicon Detector. The different sub-detector are shown: tracking (red), ECAL (green), HCAL (violet) and flux return yoke (blue). [38]	26
2.9	a) Schematic view of the CLIC accelerator at $\sqrt{s} = 3$ TeV [64]. b) Schematic overview of the CLIC detector concepts [65].	26
3.1	a) Energy loss for electrons in lead as a function of the energy. All the different processes contributing to the electron energy loss are represented. b) Photon total cross-section as function of the photon energy in lead. $\sigma_{p.e.}$ is the photo-electric cross-section, $\sigma_{g.d.r.}$ is the photonuclear cross-section (Giant Dipole Resonance [67]) where the target nucleus is broken up, κ_e is the pair production cross-section in an electron field and κ_{nuc} is the pair production cross-section in a nuclear field [8].	30
3.2	Simple model illustrating the development of an electromagnetic shower. The x-axis represents the depth of the shower in radiation length X_0 . The y-axis represents the lateral development of the shower in Molière radius ρ_M .	31
3.3	Mean energy loss of muons in copper as a function of particle momentum. Vertical bands indicate boundaries between model transitions [8].	32
3.4	Schematic of a hadronic shower. The different "types" of energy are represented in colors. Electromagnetic energy: decay of π^0 s and η s to γ s. Non-EM energy: ionization by charged hadrons, spallation. Escaped energy: neutrinos from hadron decays. Invisible energy: nuclear binding energy, neutron scattering and capture [68].	33

3.5	Schematic of the Particle Flow Concept. On the left: Traditional calorimetry, The ECAL and HCAL measure the energy deposited by all particles in a jet (charged particles, photons and neutral particles). The tracker information is not used. On the right: Particle flow approach, The tracker measures all charged particles and the calorimeter information is removed, the ECAL measures the photons and the HCAL measures only neutral particles [76].	37
3.6	Empirical jet energy resolution as function of the jet energy for PandoraPFA and the ILD detector. The estimated contribution of confusion is represented by the back dotted line. The dotted-dashed blue curve shows the jet energy resolution only from the calorimetric depositions. Moreover, a parametrization of a typical jet energy resolution ($\frac{60\%}{\sqrt{E}} \oplus 2\%$) is shown in red using the traditional calorimetry approach [80].	39
4.1	a) The schematics of the SiW-ECAL physics prototype. b) Picture of a layer of the SiW-ECAL technological prototype.	43
4.2	a) Photo of the ScECAL physics prototype with the Fe-AHCAL at FNAL. b) Photo of the top side of a layer of the technological ScECAL prototype.	44
4.3	Cross-section of an active RPC layer in the DHCAL prototype. Taken from [87].	45
4.4	Photo of SDHCAL at CERN in 2012.	46
4.5	Picture of a surface-mounted SiPM. The picture shows the SiPM package as well the grid of pixels.	47
4.6	Schematic of the TDC ramps in the SPIROC2B [104].	49
4.7	Schematic of the analog signal path of the SPIROC2 for a single channel [104].	50
4.8	a) Photo of the active layer of the AHCAL physics prototype showing the layout of the differently sized tiles. b) Photo of the AHCAL physics prototype at CERN.	50
4.9	a) Top view of the HBU2 with SPIROC2b. b) Picture of the AHCAL technological prototype in 2015 with several layers inserted.	51
4.10	The two different tiles used in the AHCAL technological prototype. The tile on the left is an older version with a WLS fiber and the tile on the right is a new design invented by MPI Munich and adapted by University of Hamburg which is wrapped in reflective foil and has no WLS fiber.	52
4.11	Photo of the top view of the HBU5 with SPIROC2e used for the new AHCAL prototype.	52
5.1	Schematic of the cascade model. The incoming projectile and all secondaries inside the nucleus are tracked and their interaction is calculated until their energy is under a certain threshold or leave the nucleus [76].	56
5.2	a) The sketch shows the formation of a string between the projectile and one of the quarks inside the nucleus. b) Representation of the fragmentation of the strings via the generation of quark-antiquark pairs into hadrons [76].	57
5.3	Schematic of the physics list used in GEANT 4 v10.1 for this thesis. The validity range extends above 30 GeV. The diagonal regions represent the overlap region between the different models. The probability to select each model varies linearly between 0 and 100% in the overlap region.	58

5.4	a) DD4hep geometry model of the 2015 testbeam prototype. The dark blue represents the steel absorber structure, the light blue represents the active scintillator layers and the beam instrumentation in front and back of the calorimeter and the dark grey represents the additional lead material to account for missing upstream material. b) Material description of one layer in the MOKKA and DD4HEP simulations of the AHCAL. Dimensions are not to scale.	60
5.5	The energy deposited in the AHCAL cells from the raw simulation without any detector effects for 8 GeV muons. The spectrum has been fitted with a Landau distribution and the MPV is extracted as the MIP_{toGeV} factor.	62
6.1	a) Testboard used to test the SPIROC2B chip standalone. The red square represents the 36 input channels of the SPIROC ASIC, the purple square represents the input signals for the ALTERA such as clocks. In yellow and blue squares represent the output signals, analog and digital, of the SPIROC. The green square, above the blue and yellow one, represents the input and output DACs that can be measured automatically via a Keithley multimeter with the Labview software. b) Example of an analog signal outputted by the slow shaper of the SPIROC2B. The signal is represented in yellow. The trigger is represented in red.	64
6.2	a) Reconstructed input DAC curves of the 36 channels for the Chip 16 of the tested batch. b) Reconstructed output DAC curve for same tested chip.	65
6.3	a) Reconstructed signal shape for several channels of Chip 174 on HBU_2_15 (Module 11). Only channels where the integral of the holdscan curve is over 6000 are shown. The dotted red line represent the hold time chosen for this board. b) Single pixel spectrum of a single channel. The fit is done by a multi-Gaussian where the distance between the 1 st and 2 nd peaks is the fitted SiPM gain.	67
6.4	a) Generic dependence of the gain as function of the pre-amplifier capacitance used to determine the value of the pre-amplifier feedback capacitor to use. b) Results of the gain fit for the same channel as shown above after adjustment of the pre-amplifier feedback capacitor from 100 fF to 675 fF.	69
6.5	ET reference spectrum and AT spectra of a single channel for different trigger threshold values of 300, 350 and 400. One can notice a clear dependence of the trigger position as a function of the threshold value.	70
6.6	a) Trigger efficiency S-Curve fit for a typical channel at a trigger threshold of 400. $\mu = 403.542 \pm 4.04538$. b) Extracted trigger threshold positions as a function of the trigger threshold value. One can observe a linear behavior.	71
6.7	a) Observed histogram of the number of memory cells filled per cycle for a typical chip with a trigger threshold of 210 and a time window T of 3 ms. $\lambda_{mem} = 1.5 \pm 0.1$. b) Extracted noise rate as a function of the trigger threshold setting for a full board.	72
7.1	Sketch view of the beamline setup at the CERN SPS H2 beamline in July 2015.	78
7.2	Photo of the AHCAL detector during the installation in the testbeam area.	79
7.3	Simplified view of the detector layout used in July 2015.	79
7.4	Event distribution in $cog_Z : n_{Hits}$ plane. The size of each box represents the number of events in each bin. The black box represents the space-phase covered by the pre-selection.	82

7.5	a) Distribution of number of hits in a layer normalized to the number of events for simulated muons at 150 GeV, electrons and pions at 50 GeV. The black line represents the cut of the maximum allowed number of hits in a layer applied for the MIP selection. b) Distribution of the number of hits in a track normalized to the number of events for simulated muons at 150 GeV, electrons and pions at 50 GeV. A AHCAL tower size cut of 7 hits for the inner 12×12 tiles and a AHCAL tower size of 2 hits for the modules 11 to 14 on the outer tiles (Outer BL) were chosen. .	83
7.6	Distribution of the variables used in the electron selection of simulated electron and pion beams between 10 and 50 GeV. The muons are simulated at 150 GeV. These plots were used to determine the best selection criteria for electrons.	84
7.7	Multi-particle event in the 50 GeV pion data sample. The colors represent the time of the hit: green < 5 ns, blue 5 ns to 15 ns, yellow 15 ns to 35, orange 35 ns to 50 ns and red > 50 ns. One can observe an additional late muon going through the detector.	86
7.8	Distribution of the variables used in the pion selection for simulated muon, electron and pion beams between 10 and 90 GeV. These plots were used to determine the best selection criteria for pions.	87
7.9	a) Distribution of the variable R_{chip} for 50 GeV electrons for all chips. Each entry corresponds to a chip. The red line represent the cut applied to reject bad chips. b) Example of a typical bad chip that is rejected with this method (Chip 149).	88
8.1	Typical pedestal distribution of a channel in auto-trigger mode. The different colored boxed represent the iterative procedure to extract the pedestal value marked with the red line. The upper x-axis shows the corresponding ADC value in terms of MIP and pixels.	92
8.2	Distribution of the difference between the mean pedestal to the memory-cell wise pedestal per channel.	93
8.3	Typical energy distribution in a single channel of the AHCAL with the data collected in July 2015 at CERN. The convoluted function is represented in red with the extracted MIP constant for this channel showed by the vertical red line.	94
8.4	Relative error $\frac{\Delta MIP_i}{MIP_i}$ for the 3171 detector channels in the AHCAL. The right tail comes from the layers 1 and 2 where difficulties are met for the determination of the MIP constant.	95
8.5	MPV fitted value in MIP for the two muon sub-samples. Even runs are in blue, odd runs are in red.	96
8.6	Beam profiles for 10 GeV electrons in data and simulation. Simulated with QGSP_BERT_HP using GEANT 4 v10.1.	97
8.7	Beam profiles for 10 GeV pions in data and simulation. Simulated with QGSP_BERT_HP using GEANT 4 v10.1	97
8.8	a) Hit Energy Spectra for the complete AHCAL for muon like-track hits for both data and simulation. b) Longitudinal mean energy profile for muon like-track hits in data and simulations.	99
8.9	Distribution of the fitted MIP value in single channels of the AHCAL for data and simulation.	99
8.10	Electron hit energy spectra for data and simulation for 10 and 50 GeV beam energies. The different colors corresponds to the variation of the cross-talk parameter in the simulations between 10% and 18%.	100

- 8.11 **a)** Comparison of the mean energy sum in the AHCAL as function of the beam energy for electron data and simulations with different cross-talk parameters. Simulated with QGSP_BERT_HP in GEANT 4 v10.1. **b)** Comparison of the mean number of hits in the AHCAL as function of the beam energy for electron data and simulations with different cross-talk parameters. Simulated with QGSP_BERT_HP in GEANT 4 v10.1. 101
- 9.1 Schematic of the TDC ramp in the SPIROC used in testbeam with a slow clock of 250 kHz. The slope of the ramp is $s = (Max - Ped)/\Delta_t$. The time of the hit is then calculated as the following: $t_{Hit} = 1/s \times (TDC_{Hit} - Ped)$ 103
- 9.2 **a)** TDC spectrum of a typical chip (all channels). The black lines indicate the fitted Max and Pedestal parameters for this chip. The extracted parameters are $1/s = 1.44 \pm 0.01$ ns/TDC, $a = 888 \pm 5$ TDC and $b = 3613 \pm 8$ TDC. **b)** TDC spectrum of a bad chip on module 11. The chip 175 on this module is presenting a long tail to high TDC values. The reason is not understood but present on all chips on that module. 105
- 9.3 Distribution of the inverse of the slope for even and odd bunch-crossing IDs. $\mu_{odd} = 1.564$ ns/TDC, $RMS_{odd} = 0.121$, $\mu_{even} = 1.556$ ns/TDC, $RMS_{even} = 0.113$. In total, 208 TDC slopes were extracted. 106
- 9.4 **a)** Time difference between the trigger channels before and after correction for T_{12} and T_{14} . $\mu = 10.6$ ns, $RMS = 11.6$ ns, $\mu_{corrected} = 0.9$ ns, $RMS_{corrected} = 4.8$ ns. The two visible peaks in blue are due to pedestal values being different dependent of the bunch-crossing parity. **b)** Distribution of the uncertainty σ_{ref} . The red line represents the cut of 4 ns. 107
- 9.5 **a)** Time of first hit distribution for a single channel (Chip 236, Chn 21, Mem 01, BXID 1). An offset of -165.3 ns is determined for this channel. **b)** Distribution of the difference of offsets extracted for even and odd BXID for each channel and memory-cell. A mean time offset difference of 12 ns is visible between even and odd BXID. 108
- 9.6 **a)** Time of the first hit distribution of the AHCAL after the time calibration. $\mu = -0.06$ ns, $RMS = 5.65$ ns. The distribution is asymmetric to the left. **b)** Time resolution for all layers in the AHCAL. The mean RMS time resolution is represented by the blue line. The sigma resolution of each layer is obtained from a Gaussian fit. Mean $\sigma = 5.65$ ns, Mean $RMS = 5.82$ ns. 109
- 9.7 **a)** Distribution of the time of arrival of the 5th photon for a light yield of 15 pixels per MIP. **b)** RMS/Mean of the time of arrival of the 5th photon as a function of the number of fired pixels. As expected, the RMS/Mean decreases with a higher number of fired pixels. 109
- 9.8 **a)** Quadratic fit of chip 146 (BXID even) on layer 9. The graph is slightly curved showing that this chip presents a non-linear TDC ramp. **b)** Profile for chip 146 on layer 9 after the non-linearity correction of the ramp. The correction parameters are applied on the data to cross-check the quality of the correction. The curve flattens with the non-linearity correction applied. 110
- 9.9 **a)** Time of the first hit distribution of the AHCAL before the non-linearity correction in black and after in blue. The non-linearity correction improves the time resolution by around 5.1%. **b)** Time resolution for all layers in the AHCAL. A comparison of the RMS after the simple calibration is shown with the black dashed line. 111

9.10	a) Time of first hit as a function of the hit energy. A difference up to 6 ns is seen between small and large amplitudes. Time-walk correction extracted from data. The fit function is of the form $A \times e^{-\lambda x} + B$. b) Time of first hit as a function of the hit energy after correction showing a spread of less than 1 ns.	111
9.11	a) Time of the first hit for muons after the simple calibration in blue, after the non-linearity correction in red and after all corrections in black. Each correction improves the time resolution. b) Time resolution obtained for each layer in the AHCAL. A comparison of the RMS after the simple calibration and the non-linearity correction is shown with the black and green dashed lines.	112
10.1	Time of the first hit distribution for 20 GeV electrons after applying the calibration constants extracted from the muon data. The blue distribution represents the time of first hit distribution obtained with muons.	116
10.2	a) Mean time of the first hit as a function of the number of triggered channels above 0.5 MIP in a chip. The mean time shifts upwards with the increase of triggered channels leading to large tails in the time distribution. A second order polynomial fit is done for the time correction shown by the red dashed line. b) The RMS of the time of first hit distribution as a function of the number of triggered channels above 0.5 MIP in a chip for 20 GeV electrons. The RMS of the time distribution can increase up to 10-15 ns for a high number of triggered channels in a chip.	116
10.3	Residuals of the mean time of the first hit as a function of the number of triggered channels above 0.5 MIP in a chip after correction. The correction has been applied to all electron samples separately to evaluate the systematic uncertainty. The vertical red lines delimit the three sections used for the systematic uncertainty.	117
10.4	a) Time of the first hit distribution for 20 GeV electrons after the number of triggered channel in a chip correction. b) Comparison of time distribution of 20 GeV electrons and muons. The electron time distribution is very similar to the muon time distribution when only a single channel triggers in a chip.	118
10.5	Comparison of the time of first hit distribution for electron beam energies between 10 GeV and 50 GeV. The bottom plots shows the relative difference to the 20 GeV electron time distribution.	119
10.6	Time of the first hit distribution for 3 GeV electron showers at the DESY II testbeam in May 2016 combining layers 12 to 14 in black. The blue distribution is the time of first hit in the case of events in which only single hits in a chip are taken. The red distribution is the time of first hit for the same layers in 10 GeV electrons collected at the CERN SPS in July 2015.	120
10.7	Time of the first hit distribution for events where the center of gravity of the shower is in the four center tiles for 10 GeV electrons on the left and 50 GeV electrons on the right. Under each figure, the deviation of each time distribution to the top left tile is shown. The mean deviation of the time distributions is shown in a black line. The dashed black line represents a 30% deviation relative to the top left tile time distribution.	121
10.8	Time of first hit distribution for muons in data and simulation between -50 and 50 ns. The grey area represents the statistical uncertainty of the data. The error bars of the simulation are obtained by varying the cross-talk parameter between 10% and 18% and taking into account the error of a global time smearing parametrization.	124

- 10.9 a) Comparison of the time of first hit between data and simulations for 10 GeV electrons. The grey area represents the statistical and systematical error of the data. Error bars in simulation are obtained by varying the cross-talk parameter between 10% and 18% and with the uncertainty on parametrization of the width of the time distribution as a function of the number of triggered channels in a chip. b) Comparison of the number of triggered channels per chip between data and MC for 10 GeV electrons. The grey area represents the statistical error of the data. Error bars in simulation are obtained by varying the cross-talk parameter between 10% and 18%. 124
- 11.1 Time of first hit for muons, electrons and pions in steel absorber in a range of -100 to 250 ns. The histograms are normalized to the number of events where at least one hit was identified. The errors bars are statistical and systematic uncertainties. The lines represent the fit to the data as explained in the text. 128
- 11.2 Comparison of the time of first hit distribution for 50 GeV pions in data and three different physics list for MOKKA (left) and DD4HEP (right) simulations. The grey and color bands shows the statistical and systematic uncertainties. 129
- 11.3 On the left, the mean time of first hit as a function of the hit energy for muons, electrons and pions in steel absorber taken in a range of -50 to 200 ns. The bands represent the systematic uncertainty. On the right, the time distribution for 90 GeV pions for different hit energy ranges. 130
- 11.4 Comparison of the mean time of the first hit as a function of the hit energy in data and MOKKA simulation for 10 GeV and 90 GeV pions. The grey and color bands show the statistical and systematic uncertainties. 131
- 11.5 a) The RMS of the time distribution as a function of the hit energy for muons, electrons and pions in steel absorber taken in a range of -50 to 200 ns. The systematics are shown by the color bands. b) Comparison between data and simulation of the RMS of the time distribution as a function of the hit energy. The color bands show the statistical and systematic uncertainty. . . 131
- 11.6 The mean time of first hit for muon, electron and pion beams. The left plot shows the mean time dependency for the modules 3 to 10 and the right for the modules 11 to 14. The reason for the separation is described in the text. The systematics are shown by the color bands. . . . 132
- 11.7 Comparison of the mean time of first hit as a function of the hit distance to the shower axis in data and MOKKA simulation for 50 GeV pion for the modules 3 to 10 on the left and for modules 11 to 14 on the right. The grey and color bands shows the systematics. 133
- 11.8 Dependency of the RMS as a function of the hit distance to the shower axis in data for muons, electrons and pions. On the left for the modules 3 to 10. On the right, for modules 11 to 14. The systematics are shown by the color bands. 134
- 11.9 Comparison of the RMS as a function of the hit distance to the shower axis in MOKKA simulation for 50 GeV pion for the modules 3 to 10 on the left and for modules 11 to 14 on the right. The color bands show the statistical and systematic uncertainty. 134
- 11.10 Mean time of first hit as a function of the hit distance to the center of gravity for 50 GeV pions for different modules. On the left, it is shown for data. On the right, it is shown for simulation using the QGSP_BERT_HP physics list. Both figures shows the same behavior with a decrease of the curve slope for deeper layers in the calorimeter. 135

- 11.11 Performance of the FHI algorithm in the AHCAL detector. The left plot shows the difference between the reconstructed FHI layer and the MC truth. The distribution is slightly de-centered at -0.81 with a RMS of 1.87. The right plot shows the correlation between the reconstructed FHI layer and the MC truth. The black line represent a guide for a perfect correlation. 136
- 11.12 Mean time of first hit as a function of the hit distance to the shower axis for 50 GeV pions for a fixed distance of 4 between the reconstructed FHI layer and a layer. The left plot shows the radial timing profile of modules 7 and 10 in data. The right plots shows the radial timing profile for the same layers in simulation with the QGSP_BERT_HP physics list. 137
- 11.13 Mean time of the first hit as a function of the hit distance to the shower axis for 50 GeV pions for different reconstructed FHI layers. In data on the left and in simulation with the QGSP_BERT_HP physics list on the right. 137
- 11.14 The left plot shows the mean time of the first hit as a function of the layer for muon, electron and pion beams. The right plot shows the mean time of the first hit as a function of the distance to the reconstructed FHI layer for 50 GeV pions. 138
- 11.15 On the left, comparison of the mean time of first hit as a function of the layer in data and MOKKA simulation for 90 GeV pions. The grey and color bands shows the systematics. On the right, mean time of first hit as a function of the layer for 50 GeV pions in simulation with the QGSP_BERT_HP physics list with no time smearing. 139
- 11.16 a) The RMS of the time distribution as a function of the layer for muons and pions in steel absorber taken in a range of -50 to 200 ns. b) Comparison between data and simulation of the RMS of the time distribution as a function of the layer. The color bands show the statistical and systematic uncertainty. 139
- 11.17 The left plot shows the time correlation between modules 6 and 7 separated by $1 X_0$. The right plot shows the time correlation for modules 13 and 14 separated by $1 \lambda_\pi$. Each bin is normalized to the number of entries in the 2D histogram. The red box represent the region of interest. Both plots show a visible time correlation. 140
- 11.18 Hit timing correlations between modules 6 and 7 and modules 13 and 14 in the MOKKA simulation with QGSP_BERT_HP for 50 GeV pions. Each bin is normalized to the total number of entries in the 2D histogram. 141
- 12.1 Mean reconstructed energy E_{reco} for 5 to 90 GeV K_L^0 as a function of the simulated energy $E_{initial}$. The reconstructed energy is the sum of all calibrated hit energies. The bottom plot shows the relative deviation from linearity. Error bars represent the statistical uncertainty. The black and blue curves represent the cases where software compensation or energy truncation reconstruction scheme is used and are the same. The red and green curve are the same, representing the case where the energy truncation and the non-linearity correction reconstruction scheme are used after a recalibration of the PandoraPFA calibration constants has been performed. 149
- 12.2 Relative energy resolution $RMS_{90}/Mean_{90}$ as a function of the energy. Error bars represent the statistical uncertainty. The black and blue curves are the same and the red and green curve are the same. 149

- 12.3 Mean PFO reconstructed energy E_{reco} for 5 to 90 GeV K_L^0 as a function of the simulated energy $E_{initial}$ for different energy reconstruction schemes. The bottom plot shows the relative deviation from linearity. Error bars represent the statistical uncertainty. 150
- 12.4 Relative PFO energy resolution $RMS_{90}/Mean_{90}$ as a function of the energy for different energy reconstruction schemes. Error bars represent the statistical uncertainty. 150
- 12.5 a) Momentum distribution for charged particles in simulated $e^+e^- \rightarrow Z/\gamma \rightarrow q\bar{q}$ with $q = u, d, s$ at $\sqrt{s} = 91$ GeV and $e^+e^- \rightarrow W^+W^- \rightarrow q\bar{q}q\bar{q}$ where q is a quark at $\sqrt{s} = 500$ GeV. b) Distribution of distances to the closest charged track for neutral particles produced in $Z/\gamma \rightarrow q\bar{q}$ and $W^+W^- \rightarrow q\bar{q}q\bar{q}$ processes measured at the front face of the electromagnetic calorimeter in the ILD detector. 151
- 12.6 a) Distribution of the number of PFO reconstructed per event for 50 GeV K_L^0 in the ILD barrel for different timing cuts. It shows that timing cuts indeed improves the number of events reconstructed with a single PFO but as well a large tail is present. The use of timing cuts reduces slightly the tail of the distribution. b) Number of events reconstructed with only a single PFO normalized to the number of events in the case of 100 ns. It shows a relative increase with a lower timing cut, up to 10-25% more events are reconstructed with a single PFO using a 1 ns timing cut. 152
- 12.7 a) Normalized energy distribution of 2^{nd} most energetic cluster. One can see that most of the entries are below few percents. b) Normalized distance to main PFO of 2^{nd} most energetic cluster. The distribution peaks in the region 25-30 cm. 153
- 12.8 The top plot shows the reconstructed energy E_{reco} as a function of the initial particle energy $E_{initial}$ for different timing cuts assuming a perfect time resolution. The bottom plot represent the relative deviation to the line $x = y$ for the different time cuts. 154
- 12.9 The top plot illustrates the relative energy resolution ($\frac{\sigma_E}{E}$) at single particle level for different timing cuts. The green line is a fit performed at 100 ns of the form $\frac{\sigma_E}{E} = \frac{a}{\sqrt{E}} \oplus b$ where a is the stochastic term ($46.73\% \pm 2.03$) and b the constant term ($10.99\% \pm 0.41$). The bottom plot shows the relative change of the energy resolution compared to 100 ns as a function of the timing cut for each particle energy. The error bars represent the statistical uncertainty. 155
- 12.10 Fraction of the total shower energy as a function of the timing cut. The fraction is defined such as the shower energy at a 100 ns timing cut is 100%. 155
- 12.11 The top plot shows the radial profile of a 50 GeV hadronic shower overlaid for different timing cuts. The bottom plot shows the ratio of the histograms to 100 ns radial profile. 156
- 12.12 a) Mean shower width as a function of the timing cut for different K_L^0 energies between 5 GeV and 90 GeV. The y-axis has been normalized to the shower width at 100 ns. The shower width decreases steadily as a function of the timing cut, indicating that the shower gets narrower. b) Mean shower width in mm as a function of the timing cut for different K_L^0 energies between 5 GeV and 90 GeV. Under 20 ns, the shower width is very similar indicating the core of the shower is fairly identical for all energies. 157
- 12.13 The top plot shows the energy resolution as a function of the relative shower width for different particle energies. Each point represents a timing cut from 1 ns to 100 ns from left to right. The bottom plot shows the absolute loss of resolution as a function of the relative shower width. 157

- 12.14 **a)** The top plot shows the reconstructed energy E_{reco} as a function of the initial particle energy $E_{initial}$ for different timing cuts assuming a time resolution of 0.4 ns. The bottom plot represent the relative deviation to the line $x = y$ for the different time cuts. **b)** Energy resolution curves for 0.4 ns time resolution. The plot represents the relative energy resolution $\frac{\sigma_E}{E}$ for kaons from 5 to 90 GeV for each timing cut. The green line is a fit applied to 100 ns timing cut of the typical form $\frac{\sigma_E}{E} = \frac{a}{\sqrt{E}} \oplus b$ 159
- 12.15 **a)** The top plot shows the reconstructed energy E_{reco} as a function of the initial particle energy $E_{initial}$ for different timing cuts assuming a time resolution of 1 ns. The bottom plot represent the relative deviation to the line $x = y$ for the different time cuts. **b)** Energy resolution curves for 1 ns time resolution. The plot represents the relative energy resolution $\frac{\sigma_E}{E}$ for kaons from 5 to 90 GeV for each timing cut. The green line is a fit applied to 100 ns timing cut of the typical form $\frac{\sigma_E}{E} = \frac{a}{\sqrt{E}} \oplus b$ 159
- 12.16 **a)** The top plot shows the reconstructed energy E_{reco} as a function of the initial particle energy $E_{initial}$ for different timing cuts assuming a time resolution of 8 ns. The bottom plot represent the relative deviation to the line $x = y$ for the different time cuts. **b)** Energy resolution curves for 8 ns time resolution. The plot represents the relative energy resolution $\frac{\sigma_E}{E}$ for kaons from 5 to 90 GeV for each timing cut. The green line is a fit applied to 100 ns timing cut of the typical form $\frac{\sigma_E}{E} = \frac{a}{\sqrt{E}} \oplus b$ 160
- 12.17 Energy resolution as a function of the shower width assuming different time resolutions. The top plot shows the relative energy resolution $\frac{\sigma_E}{E}$ for kaons from 5 to 90 GeV where each point is representing a timing cut as a function of the shower width. The bottom plot shows the deviation to the nominal resolution at 100 ns as a function of the shower width. The error bars are statistical uncertainties. 161
- 12.18 Reconstructed energy distribution for 30 GeV kaons. The blue sample corresponds to events with $E_{reco} < E_{mean} - \sigma$ and the red sample corresponds to events with $E_{reco} > E_{mean} + \sigma$ 162
- 12.19 Hit energy spectrum in the HCAL corresponding to subsamples with low (in blue) and high (in red) energy depositions. The left plot is focused in the region between 0 and 14 MIPs. The bottom plot shows the ratio of the red to the blue spectrum that was used to determine the value for e^{lim} 163
- 12.20 **a)** Distributions of C^{lim} for different values of e^{lim} for 30 GeV kaons. The red and blue filled histograms corresponds to events that are in the region $E_{mean} \pm \sigma$ respectively for $e^{lim} = 3.5$ MIPs. **b)** Energy deposited in the HCAL as a function of C^{lim} for $e^{lim} = 3.5$ MIPs for 30 GeV kaons. 163
- 12.21 Normalized hit energy spectra in the HCAL for 30 GeV kaons applying a timing cuts of 100 ns in blue and 1 ns in red. The bottom plot shows the ratio of the red spectra to the blue spectra. . 164
- 12.22 **a)** Distributions of C^{lim} for different values of e^{lim} for 30 GeV kaons for a 1 ns timing cut. The red and blue filled histograms corresponds to events that are in the region $E_{mean} \pm \sigma$ respectively. **b)** Energy deposited in the HCAL as a function of C^{lim} for $e^{lim} = 3.5$ MIPs for 30 GeV kaons with a timing cut of 1 ns. 165
- B.1 Beam profiles for 150 GeV muons in data and simulation. Simulated with QGSP_BERT_HP using GEANT 4 v10.1. 175

B.2	Beam profiles for 50 GeV electrons in data and simulation. Simulated with QGSP_BERT_HP using GEANT 4 v10.1.	176
B.3	Beam profiles for 90 GeV pions in data and simulation. Simulated with QGSP_BERT_HP using GEANT 4 v10.1.	176
B.4	a) The energy sum in the AHCAL for 10 GeV electrons for data and simulations with a cross-talk value of 10% and 18%. b) The number of hits in the AHCAL for 10 GeV electrons for data and simulations with a cross-talk value of 10% and 18%.	177
B.5	a) The energy sum in the AHCAL for 50 GeV electrons for data and simulations with a cross-talk value of 10% and 18%. b) The number of hits in the AHCAL for 50 GeV electrons for data and simulations with a cross-talk value of 10% and 18%.	177
C.1	Comparison between electron data and MC for all energies of the time of first hit. The grey area represents the statistical and systematical error of the data. Error bars in simulation are obtained by varying the cross-talk parameter and with the uncertainty from the number of hits parametrization.	180
C.2	Comparison between electron data and MC for all energies of the number of triggered channels per chip. The grey area represents the statistical error of the data. Error bars in simulation are obtained by varying the cross-talk parameter between 10% and 18%.	181
C.3	Comparison between data and the MOKKA simulation for pions between 10 and 90 GeV of the time of first hit. The grey box represents the statistic and systematic uncertainty of the data. The error bars are the uncertainty on the MOKKA simulation obtained by varying the cross-talk parameter and the uncertainty on the time smearing.	182
C.4	Comparison between data and the DD4HEP simulation for pions between 30 and 90 GeV of the time of first hit. The grey box represents the statistic and systematic uncertainty of the data. The error bars are the uncertainty on the DD4HEP simulation obtained by varying the cross-talk parameter and the uncertainty on the time smearing.	183
C.5	Comparison between the MOKKA simulation and data of the time of first hit as a function of the hit energy for pion beams between 30 GeV and 70 GeV. The grey and color bands shows the systematics.	184
C.6	Comparison between the DD4HEP simulation and data of the time of first hit as a function of the hit energy for pion beams between 10 GeV and 90 GeV. The grey and color bands shows the systematics.	185
C.7	Comparison of the time of first hit as a function of the hit distance to the shower axis in data and the MOKKA simulation for pion beam energies between 10 GeV and 90 GeV for modules 3 to 10. The grey and color bands shows the systematics.	186
C.8	Comparison of the time of first hit as a function of the hit distance to the shower axis in data and the DD4HEP simulation for pion beam energies between 10 GeV and 90 GeV for modules 3 to 10. The grey and color bands shows the systematics.	187
C.9	Comparison of the time of first hit as a function of the hit distance to the shower axis in data and the MOKKA simulation for pion beam energies between 10 GeV and 90 GeV for modules 11 to 14. The grey and color bands shows the systematics.	188

C.10	Comparison of the time of first hit as a function of the hit distance to the shower axis in data and the DD4HEP simulation for pion beam energies between 10 GeV and 90 GeV for modules 11 to 14. The grey and color bands shows the systematics.	189
C.11	Comparison of the time of first hit as a function of the layer position in data and the MOKKA simulation for pion beams between 10 GeV and 70 GeV. The grey and color bands shows the systematics.	190
C.12	Comparison of the time of first hit as a function of the layer position in data and the DD4HEP simulation for pion beams between 10 GeV and 90 GeV. The grey and color bands shows the systematics.	191
C.13	Timing correlations between modules 6 and 7 and modules 13 and 14 in MOKKA simulations for different physics lists in 50 GeV pion beam. Each bins are normalized to the number of entries in the 2D histogram.	192
C.14	Timing correlations between modules 6 and 7 and modules 13 and 14 in DD4HEP simulations for different physics lists in 50 GeV pion beam. Each bins are normalized to the number of entries in the 2D histogram.	193
C.15	Comparison of the RMS of the hit time distribution as a function of the hit energy in data and the MOKKA simulation for pion beam energies between 10 GeV and 90 GeV. The grey and color bands shows the systematics.	194
C.16	Comparison of the RMS of the hit time distribution as a function of the hit energy in data and the DD4HEP simulation for pion beam energies between 10 GeV and 90 GeV. The grey and color bands shows the systematics.	195
C.17	Comparison of the RMS of the hit time distribution as a function of the hit distance to the shower center of gravity in data and the MOKKA simulation for pion beam energies between 10 GeV and 90 GeV for modules 3 to 10. The grey and color bands shows the systematics.	196
C.18	Comparison of the RMS of the hit time distribution as a function of the hit distance to the shower center of gravity in data and the DD4HEP simulation for pion beam energies between 10 GeV and 90 GeV for modules 3 to 10. The grey and color bands shows the systematics.	197
C.19	Comparison of the RMS of the hit time distribution as a function of the hit distance to the shower center of gravity in data and the MOKKA simulation for pion beam energies between 10 GeV and 90 GeV for modules 11 to 14. The grey and color bands shows the systematics.	198
C.20	Comparison of the RMS of the hit time distribution as a function of the hit distance to the shower center of gravity in data and the DD4HEP simulation for pion beam energies between 10 GeV and 90 GeV for modules 11 to 14. The grey and color bands shows the systematics.	199
C.21	Comparison of the RMS of the hit time distribution as a function of layer in data and the MOKKA simulation for pion beam energies between 10 GeV and 90 GeV. The grey and color bands shows the systematics.	200
C.22	Comparison of the RMS of the hit time distribution as a function of layer in data and the DD4HEP simulation for pion beam energies between 10 GeV and 90 GeV. The grey and color bands shows the systematics.	201
D.1	Hit energy distribution of the extracted noise hits. Most of the hits have an energy below 2 MIPs although a tail is visible to high energies.	204

- D.2 Time distribution of the extracted noise hits. The description of the shape of the time distribution is important for the simulation. 204
- E.1 a) Pedestal uncertainty distribution extracted for all channels in the detector, most of the errors made are small with a high tail certainly due to the limited statistics for some channels. $\mu = 5.37$ TDC, RMS = 5.82 TDC b) Maximum uncertainty distribution extracted from the edge detection method for each chip and BXID. The error is a bit higher than for the pedestal in general due to the difficulty to detect perfectly the end of the ramp. $\mu = 9.85$ TDC, RMS = 4.60 TDC. 206
- E.2 a) Uncertainty distribution made for a single channel on layer 3. The error is varying between 9 and 14 ns but is likely to be over-estimated and not valid for the final time distribution b) Uncertainty distribution made for a single channel on layer 5. The uncertainty is between 12 and 20 ns but is likely to be over-estimated and not valid for the final time distribution. 206
- E.1 a) Time of the first hit distribution for 20 GeV electrons for different binning of number of triggered channels in a chip. The distribution width is increasing with the number of triggered channels in a chip. b) σ_{effect} extracted function of the number of triggered channels in a chip for each energies. σ_{effect} increases up to 12-15 ns with the number of triggered channels in a chip. 208
- E.2 Mean parametrization of σ_{effect} as a function of number of triggered channels. The grey area represents the uncertainty on the parametrization. 208

Acronyms

ADC Analog to Digital Converter

APD Avalanche Photo-diode

ASIC Application Specific Integrated Chip

BDS Beam Delivery System

BGA Ball Grid Array

BXID Bunch Crossing Identification

CALICE Calorimeters for Linear Experiments

CEPC Circular Electron Positron Collider

CLIC Compact Linear Collider

CP Charge Parity

CPS CMOS Pixel Sensor

DAC Digital to Analog Converter

DEPFET Depleted Field Effect Transistor

ECAL Electromagnetic Calorimeter

ETD Endcap Tracking Detector

FCC Future Circular Collider

FHI First Hard Interaction

FPCCD Fine Pixel CCD

FPGA Field Programmable Gate Array

FTD Forward Tracking Detector

GEM Gas Electron Multiplier

HCAL Hadronic Calorimeter

ILC International Linear Collider

ILD International Large Detector

LED Light Emitting Diode

LEP Large Electron-Positron Collider

LHC Large Hadron Collider

Micromegas Micro-Mesh Gaseous Structure

MIP Minimum Ionizing Particle

PDE Photon Detection Efficiency

PFA Particle Flow Algorithm

PFO Particle Flow Object

QCD Quantum Chromo Dynamics

QED Quantum Electro Dynamics

QFT Quantum Field Theory

RPC Resistive Plate Chamber

SCRF Supra Conducting Radio Frequency

SET Silicon External Tracker

SiD Silicon Detector

SiPM Silicon Photo-Multiplier

SIT Silicon Internal Tracker

SKIROC2 Silikon Kalorimeter Read-Out Chip

SM Standard Model

SPIROC2B SiPM Integrated Read-Out Chip

SPS Super Proton Synchrotron

SUSY Supersymmetry

TDC Time to Digital Converter

TPC Time Projection Chamber

VBF Vector-Boson Fusion

VTX Vertex Detector

Bibliography

- [1] T. Behnke, J. E. Brau, B. Foster, J. Fuster, M. Harrison, J. M. Paterson, M. Peskin, M. Stanitzki, N. Walker, and H. Yamamoto, “The International Linear Collider Technical Design Report - Volume 1: Executive Summary,” 2013.
- [2] L. Linssen, A. Miyamoto, M. Stanitzki, and H. Weerts, “Physics and Detectors at CLIC: CLIC Conceptual Design Report,” *ArXiv e-prints*, Feb. 2012.
- [3] A. Benaglia, E. Auffray, P. Lecoq, H. Wenzel, and A. Para, “Space-Time Development of Electromagnetic and Hadronic Showers and Perspectives for Novel Calorimetric Techniques,” vol. 63, pp. 574–579, 04 2016.
- [4] J. Thomson, “Cathode Rays,” *Philos. Mag.* 44(1897), 293, 1897.
- [5] E. Rutherford, “The scattering of α and β particles by matter and the structure of the atom,” *Phil. Mag.* 21(1911) 669, 1911.
- [6] E. Noether, “Invariant variation problems,” *Transport Theory and Statistical Physics*, vol. 1, pp. 186–207, Jan. 1971.
- [7] C.-N. Yang and R. L. Mills, “Conservation of Isotopic Spin and Isotopic Gauge Invariance,” *Phys. Rev.*, vol. 96, pp. 191–195, 1954.
- [8] C. Patrignani *et al.*, “Review of Particle Physics,” *Chin. Phys.*, vol. C40, no. 10, p. 100001, 2016.
- [9] D. Griffiths, *Introduction to elementary particles; 2nd, rev. ed.* Physics textbook, Weinheim: Wiley-VCH, 2008.
- [10] A. Einstein, “On the electrodynamics of moving bodies,” *Annalen Phys.*, vol. 17, pp. 891–921, 1905. [Annalen Phys.14,194(2005)].
- [11] P. W. Higgs, “Broken Symmetries and the Masses of Gauge Bosons,” *Phys. Rev. Lett.*, vol. 13, pp. 508–509, 1964.
- [12] F. Englert and R. Brout, “Broken Symmetry and the Mass of Gauge Vector Mesons,” *Phys. Rev. Lett.*, vol. 13, pp. 321–323, 1964.
- [13] G. Aad *et al.*, “Observation of a new particle in the search for the Standard Model Higgs boson with the ATLAS detector at the LHC,” *Phys. Lett.*, vol. B716, pp. 1–29, 2012.

- [14] S. Chatrchyan *et al.*, “Observation of a new boson at a mass of 125 GeV with the CMS experiment at the LHC,” *Phys. Lett.*, vol. B716, pp. 30–61, 2012.
- [15] M. E. Peskin and D. V. Schroeder, *An Introduction to quantum field theory*. Reading, USA: Addison-Wesley, 1995.
- [16] R. Lakes, “Experimental limits on the photon mass and cosmic magnetic vector potential,” *Phys. Rev. Lett.*, vol. 80, pp. 1826–1829, 1998.
- [17] G. V. Chibisov, “Astrophysical upper limits on the photon rest mass,” *Sov. Phys. Usp.*, vol. 19, pp. 624–626, 1976. [Usp. Fiz. Nauk119,551(1976)].
- [18] E. R. Williams, J. E. Faller, and H. A. Hill, “New experimental test of Coulomb’s law: A Laboratory upper limit on the photon rest mass,” *Phys. Rev. Lett.*, vol. 26, pp. 721–724, 1971.
- [19] C. Rubbia, “Physics Results of the UA1 Collaboration at the CERN Proton-Antiproton Collider,” *NATO Sci. Ser. B*, vol. 122, pp. 1–79, 1985.
- [20] H. Baer, T. Barklow, K. Fujii, Y. Gao, A. Hoang, S. Kanemura, J. List, H. E. Logan, A. Nomerotski, M. Perelstein, *et al.*, “The International Linear Collider Technical Design Report - Volume 2: Physics,” 2013.
- [21] M. Aaboud *et al.*, “Evidence for the $H \rightarrow b\bar{b}$ decay with the ATLAS detector,” *JHEP*, vol. 12, p. 024, 2017.
- [22] X. Artru and M. G. Bowler, “Quantisation of the string fragmentation model,” *Zeitschrift für Physik C Particles and Fields*, vol. 37, pp. 293–304, Jun 1988.
- [23] B. R. Webber, “A QCD Model for Jet Fragmentation Including Soft Gluon Interference,” *Nucl. Phys.*, vol. B238, pp. 492–528, 1984.
- [24] R. P. Feynman, “The behavior of hadron collisions at extreme energies,” *Conf. Proc.*, vol. C690905, pp. 237–258, 1969.
- [25] M. Kobayashi and T. Maskawa, “Cp-violation in the renormalizable theory of weak interaction,” *Progress of Theoretical Physics*, vol. 49, no. 2, pp. 652–657, 1973.
- [26] E. S. Battistelli *et al.*, “Galaxy clusters as probes for cosmology and dark matter,” in *Proceedings, 14th Marcel Grossmann Meeting on Recent Developments in Theoretical and Experimental General Relativity, Astrophysics, and Relativistic Field Theories (MG14) (In 4 Volumes): Rome, Italy, July 12-18, 2015*, vol. 1, pp. 576–601, 2017.
- [27] G. Giesen, J. Lesgourgues, B. Audren, and Y. Ali-Haïmoud, “CMB photons shedding light on dark matter,” *JCAP*, vol. 1212, p. 008, 2012.
- [28] U. Dore and D. Orestano, “Experimental results on neutrino oscillations,” *Rept. Prog. Phys.*, vol. 71, p. 106201, 2008.
- [29] A. R. Vieira, B. Hiller, M. D. R. Sampaio, and M. C. Nemes, “Naturalness and Theoretical Constraints on the Higgs Boson Mass,” *Int. J. Theor. Phys.*, vol. 52, pp. 3494–3503, 2013.
- [30] J. R. Ellis and M. K. Gaillard, “Strong and Weak CP Violation,” *Nucl. Phys.*, vol. B150, pp. 141–162, 1979.

- [31] A. D. Sakharov, "Violation of CP Invariance, c Asymmetry, and Baryon Asymmetry of the Universe," *Pisma Zh. Eksp. Teor. Fiz.*, vol. 5, pp. 32–35, 1967. [*Usp. Fiz. Nauk*161,61(1991)].
- [32] "Projected Performance of an Upgraded CMS Detector at the LHC and HL-LHC: Contribution to the Snowmass Process," in *Proceedings, 2013 Community Summer Study on the Future of U.S. Particle Physics: Snowmass on the Mississippi (CSS2013): Minneapolis, MN, USA, July 29-August 6, 2013*, 2013.
- [33] M. Benedikt and F. Zimmermann, "Future Circular Colliders," *Proc. Int. Sch. Phys. Fermi*, vol. 194, pp. 73–80, 2016.
- [34] C.-S. S. Group, "CEPC-SPPC Preliminary Conceptual Design Report. 1. Physics and Detector," 2015.
- [35] C.-S. S. Group, "CEPC-SPPC Preliminary Conceptual Design Report. 2. Accelerator," 2015.
- [36] C. Adolphsen, M. Barone, B. Barish, K. Buesser, P. Burrows, J. Carwardine, J. Clark, H. Mainaud Durand, G. Dugan, E. Elsen, *et al.*, "The International Linear Collider Technical Design Report - Volume 3.I: Accelerator & in the Technical Design Phase," 2013.
- [37] C. Adolphsen, M. Barone, B. Barish, K. Buesser, P. Burrows, J. Carwardine, J. Clark, H. Mainaud Durand, G. Dugan, E. Elsen, *et al.*, "The International Linear Collider Technical Design Report - Volume 3.II: Accelerator Baseline Design," 2013.
- [38] H. Abramowicz *et al.*, "The International Linear Collider Technical Design Report - Volume 4: Detectors," 2013.
- [39] K. Fujii *et al.*, "Physics Case for the International Linear Collider," 2015.
- [40] A. Arbey *et al.*, "Physics at the e^+e^- Linear Collider," *Eur. Phys. J.*, vol. C75, no. 8, p. 371, 2015.
- [41] J. Yan, S. Watanuki, K. Fujii, A. Ishikawa, D. Jeans, J. Strube, J. Tian, and H. Yamamoto, "Measurement of the Higgs boson mass and $e^+e^- \rightarrow ZH$ cross section using $Z \rightarrow \mu^+\mu^-$ and $Z \rightarrow e^+e^-$ at the ILC," *Phys. Rev.*, vol. D94, no. 11, p. 113002, 2016.
- [42] M. A. Thomson, "Model-independent measurement of the e^+e^- to HZ cross section at a future e^+e^- linear collider using hadronic Z decays," *The European Physical Journal C*, vol. 76, p. 72, Feb 2016.
- [43] R. S. Gupta, H. Rzehak, and J. D. Wells, "How well do we need to measure Higgs boson couplings?," *Phys. Rev.*, vol. D86, p. 095001, 2012.
- [44] K. Kajantie, M. Laine, K. Rummukainen, and M. E. Shaposhnikov, "Is there a hot electroweak phase transition at $m(H)$ larger or equal to $m(W)$?," *Phys. Rev. Lett.*, vol. 77, pp. 2887–2890, 1996.
- [45] C. F. Dürig, *Measuring the Higgs Self-coupling at the International Linear Collider*. PhD thesis, Hamburg U., Hamburg, 2016.
- [46] J. Tian, "Study of Higgs self-coupling at the ILC based on the full detector simulation at $\sqrt{s} = 500$ GeV and $\sqrt{s} = 1$ TeV," in *Helmholtz Alliance Linear Collider Forum: Proceedings of the Workshops Hamburg, Munich, Hamburg 2010-2012, Germany*, (Hamburg), pp. 224–247, DESY, DESY, 2013.

- [47] A. Alboteanu, W. Kilian, and J. Reuter, “Resonances and Unitarity in Weak Boson Scattering at the LHC,” *JHEP*, vol. 11, p. 010, 2008.
- [48] “First combination of Tevatron and LHC measurements of the top-quark mass,” 2014.
- [49] F. Abe *et al.*, “Observation of top quark production in $\bar{p}p$ collisions,” *Phys. Rev. Lett.*, vol. 74, pp. 2626–2631, 1995.
- [50] S. Abachi *et al.*, “Observation of the top quark,” *Phys. Rev. Lett.*, vol. 74, pp. 2632–2637, 1995.
- [51] G. Gustavino, *Search for New Physics in Mono-jet Final States in pp Collisions at $\sqrt{s} = 13$ TeV with the ATLAS Experiment at the LHC*. PhD thesis, Rome U., 2017.
- [52] M. Habermehl, K. Fujii, J. List, S. Matsumoto, and T. Tanabe, “WIMP Searches at the International Linear Collider,” *PoS*, vol. ICHEP2016, p. 155, 2016.
- [53] H. Baer, V. Barger, and P. Huang, “Hidden SUSY at the LHC: the light higgsino-world scenario and the role of a lepton collider,” *JHEP*, vol. 11, p. 031, 2011.
- [54] J. Reuter, “The BSM Physics Case of the ILC,” in *Proceedings, International Workshop on Future Linear Colliders (LCWS15): Whistler, B.C., Canada, November 02-06, 2015*, 2016.
- [55] K. Fujii *et al.*, “Physics Case for the 250 GeV Stage of the International Linear Collider,” 2017.
- [56] M. Altarelli, R. Brinkmann, M. Chergui, W. Decking, B. Dobson, S. Düsterer, G. Grübel, W. Graeff, H. Graafsma, J. Hajdu, *et al.*, eds., *XFEL: The European X-Ray Free-Electron Laser. Technical design report*. 2006.
- [57] R. Poeschl, K. Buesser, and T. Tauchi, “ILD Conventions and Rules,” 2016.
- [58] M. Winter *et al.*, “Development of CMOS Pixel Sensors fully adapted to the ILD Vertex Detector Requirements,” in *International Workshop on Future Linear Colliders (LCWS12) Arlington, Texas, USA, October 22-26, 2012*, 2012.
- [59] S. Murai, A. Ishikawa, T. Sanuki, A. Miyamoto, Y. Sugimoto, C. Constantino, H. Sato, H. Ikeda, and H. Yamamoto, “Recent status of FPCCD vertex detector R&D,” in *Proceedings, International Workshop on Future Linear Colliders (LCWS15): Whistler, B.C., Canada, November 02-06, 2015*, 2016.
- [60] M. Boronat, “DEPFET pixel detector for future e^-e^+ experiments,” *Nucl. Part. Phys. Proc.*, vol. 273-275, pp. 982–987, 2016.
- [61] F. Sauli, “GEM: A new concept for electron amplification in gas detectors,” *Nucl. Instrum. Meth.*, vol. A386, pp. 531–534, 1997.
- [62] Y. Giomataris, P. Rebougeard, J. P. Robert, and G. Charpak, “MICROMEGAS: A High granularity position sensitive gaseous detector for high particle flux environments,” *Nucl. Instrum. Meth.*, vol. A376, pp. 29–35, 1996.
- [63] F. J. Mueller, *Development of a Triple GEM Readout Module for a Time Projection Chamber & Measurement Accuracies of Hadronic Higgs Branching Fractions in vvH at a 350 GeV ILC*. Dr., Universität Hamburg, Hamburg, 2016. Universität Hamburg, Diss., 2016.

- [64] M. Aicheler, P. Burrows, M. Draper, T. Garvey, P. Lebrun, K. Peach, N. Phinney, H. Schmickler, D. Schulte, and N. Toge, “A Multi-TeV Linear Collider Based on CLIC Technology,” 2012.
- [65] M. J. Boland *et al.*, “Updated baseline for a staged Compact Linear Collider,” 2016.
- [66] R. Wigmans, *Calorimetry: energy measurement in particle physics; 2nd ed.*, vol. 168 of *International series of monographs on physics*. Oxford: Oxford Univ. Pr., 2017.
- [67] B. L. Berman and S. C. Fultz, “Measurements of the giant dipole resonance with monoenergetic photons,” *Rev. Mod. Phys.*, vol. 47, pp. 713–761, 1975.
- [68] K.-J. Grahn, “A Layer Correlation Technique for Pion Energy Calibration at the 2004 ATLAS Combined Beam Test,” in *Proceedings, 2009 IEEE Nuclear Science Symposium and Medical Imaging Conference (NSS/MIC 2009): Orlando, Florida, October 25-31, 2009*, pp. 751–757, 2009.
- [69] C. Biino, “The cms electromagnetic calorimeter: overview, lessons learned during run 1 and future projections,” *Journal of Physics: Conference Series*, vol. 587, no. 1, p. 012001, 2015.
- [70] T. Abe *et al.*, “Belle II Technical Design Report,” 2010.
- [71] A. Henriques, “The ATLAS tile calorimeter,” in *Proceedings, 4th International Conference on Advancements in Nuclear Instrumentation Measurement Methods and their Applications (ANIMMA 2015): Lisbon, Portugal, April 20-24, 2015*, pp. 1–7, 2015.
- [72] R. Blair *et al.*, “The CDF-II detector: Technical design report,” 1996.
- [73] A. Bernstein, T. Bienz, A. Caldwell, L. Chen, M. Derrick, I. Gialas, A. Hamri, R. Imlay, S. Kartik, H. Kim, T. Kinnel, H. Kreutzmann, C. Li, J. Lim, R. Loveless, B. Lu, U. Mallik, K. McLean, R. McNeil, W. Metcalf, B. Musgrave, B. Oh, S. Park, J. Parsons, D. Reeder, J. Repond, S. Ritz, M. Roco, P. Sandler, F. Sciulli, W. Smith, R. Talaga, G. Tzanakos, L. Wai, M. Wang, J. Whitmore, J. Wu, and S. Yang, “Beam tests of the ZEUS barrel calorimeter,” *Nuclear Instruments and Methods in Physics Research Section A: Accelerators, Spectrometers, Detectors and Associated Equipment*, vol. 336, no. 1, pp. 23 – 52, 1993.
- [74] N. Akchurin *et al.*, “Dual-readout Calorimetry,” 2013.
- [75] P. Schacht, “Software compensation for single particles and jets in the H1 calorimeter,” in *ECFA Large Hadron Collider Workshop, Aachen, Germany, 4-9 Oct 1990: Proceedings.3.*, 1990.
- [76] N. Feege, *Low-energetic hadron interactions in a highly granular calorimeter*. PhD thesis, Hamburg U., 2011.
- [77] A. Ebrahimi, *Jet Energy Measurements at ILC: Calorimeter DAQ Requirements and Application in Higgs Boson Mass Measurements*. Dissertation, Universität Hamburg, Hamburg, 2017. Dissertation, Universität Hamburg, 2017.
- [78] I. Abt *et al.*, “Energy flow and charged particle spectrum in deep inelastic scattering at HERA,” *Z. Phys.*, vol. C63, pp. 377–390, 1994.
- [79] A. M. Sirunyan *et al.*, “Particle-flow reconstruction and global event description with the CMS detector,” *JINST*, vol. 12, no. 10, p. P10003, 2017.

- [80] M. A. Thomson, “Particle Flow Calorimetry and the PandoraPFA Algorithm,” *Nucl. Instrum. Meth.*, vol. A611, pp. 25–40, 2009.
- [81] J. S. Marshall and M. A. Thomson, “The Pandora Particle Flow Algorithm,”
- [82] A.-M. Magnan, “HGCAL: a High-Granularity Calorimeter for the endcaps of CMS at HL-LHC,” *Journal of Instrumentation*, vol. 12, no. 01, p. C01042, 2017.
- [83] The CALICE collaboration, “Design and electronics commissioning of the physics prototype of a Si-W electromagnetic calorimeter for the International Linear Collider,” *Journal of Instrumentation*, vol. 3, no. 08, p. P08001, 2008.
- [84] The CALICE collaboration, “Construction and commissioning of the CALICE analog hadron calorimeter prototype,” *Journal of Instrumentation*, vol. 5, no. 05, p. P05004, 2010.
- [85] The CALICE collaboration, “Construction and Response of a Highly Granular Scintillator-based Electromagnetic Calorimeter,” *arXiv*, 2017.
- [86] G. Baulieu and al., “Construction and commissioning of a technological prototype of a high-granularity semi-digital hadronic calorimeter,” *Journal of Instrumentation*, vol. 10, no. 10, p. P10039, 2015.
- [87] B. Bilki and al., “Calibration of a digital hadron calorimeter with muons,” *Journal of Instrumentation*, vol. 3, no. 05, p. P05001, 2008.
- [88] The CALICE Collaboration, “Response of the CALICE Si-W electromagnetic calorimeter physics prototype to electrons,” *Nuclear Instruments and Methods in Physics Research Section A: Accelerators, Spectrometers, Detectors and Associated Equipment*, vol. 608, no. 3, pp. 372 – 383, 2009.
- [89] S. Callier, F. Dulucq, C. de La Taille, G. Martin-Chassard, and N. Seguin-Moreau, “SKIROC2, front end chip designed to readout the Electromagnetic CALorimeter at the ILC,” *Journal of Instrumentation*, vol. 6, no. 12, p. C12040, 2011.
- [90] K. Kotera, D. Jeans, A. Miyamoto, and T. Takeshita, “A novel strip energy splitting algorithm for the fine granular readout of a scintillator strip electromagnetic calorimeter,” *Nucl. Instrum. Meth.*, vol. A789, pp. 158–164, 2015. [Erratum: *Nucl. Instrum. Meth.*A797,330(2015)].
- [91] C. Neubueser, *Comparison of Two Highly Granular Hadronic Calorimeter Concepts*. Dr., Universitat Hamburg, Hamburg, 2016. Universitat Hamburg, Diss., 2016.
- [92] B. Bilki, “Construction and Testing of the CALICE Digital Hadron Calorimeter,” in *Proceedings, International Conference on Calorimetry for the High Energy Frontier (CHEF 2013): Paris, France, April 22-25, 2013*, pp. 168–174, 2013.
- [93] M. Bedjidian, J.-P. Ianigro, R. Kieffer, I. Laktineh, N. Lumb, and S. Vanzetto, “Glass resistive plate chambers for a semi-digital HCAL,” *Nuclear Instruments and Methods in Physics Research Section A: Accelerators, Spectrometers, Detectors and Associated Equipment*, vol. 623, no. 1, pp. 120 – 122, 2010. 1st International Conference on Technology and Instrumentation in Particle Physics.
- [94] B. Bilki and the CALICE Collaboration, “The calice digital hadron calorimeter: calibration and response to pions and positrons,” *Journal of Physics: Conference Series*, vol. 587, no. 1, p. 012038, 2015.

- [95] F. D. et al., “HARDROC: Readout chip for CALICE/EUDET Digital Hadronic Calorimeter,”
- [96] V. Buridon *et al.*, “First results of the CALICE SDHCAL technological prototype,” *JINST*, vol. 11, no. 04, p. P04001, 2016.
- [97] D. Renker and E. Lorenz, “Advances in solid state photon detectors,” *Journal of Instrumentation*, vol. 4, no. 04, p. P04004, 2009.
- [98] E. Garutti, “Silicon Photomultipliers for High Energy Physics Detectors,” *JINST*, vol. 6, p. C10003, 2011.
- [99] E. Garutti, R. Klanner, D. Lomidze, J. Schwandt, and M. Zvolsky, “Characterisation of highly radiation-damaged SiPMs using current measurements,” 2017.
- [100] K. Kotera, W. Choi, and T. Takeshita, “Describing the response of saturated SiPMs,” 2015.
- [101] Y. Liu, V. Büscher, J. Caudron, P. Chau, S. Krause, L. Masetti, U. Schäfer, R. Spreckels, S. Tapprogge, and R. Wanke, “A Design of Scintillator Tiles Read Out by Surface-Mounted SiPMs for a Future Hadron Calorimeter,” in *Proceedings, 21st Symposium on Room-Temperature Semiconductor X-ray and Gamma-ray Detectors (RTSD 2014): Seattle, WA, USA, November 8-15, 2014*, p. 7431118, 2016.
- [102] S. Callier, F. Dulucq, R. Fabbri, C. de La Taille, B. Lutz, G. Martin-Chassard, L. Raux, and W. Shen, “Silicon photomultiplier integrated readout chip (spiroc) for the ilc: Measurements and possible further development,” in *2009 IEEE Nuclear Science Symposium Conference Record (NSS/MIC)*, pp. 42–46, Oct 2009.
- [103] “Omega LAL/IN2P3 Website.”
- [104] Omega Group, “SPIROC2 User Guide,” 2009.
- [105] The CALICE Collaboration, “Analysis of low-energetic electron and pion data collected with the AHCAL prototype at Fermilab,” *CALICE Analysis Note*, vol. 34, 2011.
- [106] The CALICE Collaboration, “Hadronic energy resolution of a highly granular scintillator-steel hadron calorimeter using software compensation techniques,” *Journal of Instrumentation*, vol. 7, no. 09, p. P09017, 2012.
- [107] F. Sefkow, “Prototype tests for a highly granular scintillator-based hadron calorimeter,” *CHEF 2017*, 2017.
- [108] J. Kvasnicka and I. Polak, “Led calibration systems for calice hadron calorimeter,” *Physics Procedia*, vol. 37, pp. 402 – 409, 2012. Proceedings of the 2nd International Conference on Technology and Instrumentation in Particle Physics (TIPP 2011).
- [109] Kvasnicka, Jiri, “A Scalable Data Acquisition System for the CALICE Tile Hadron Calorimeter,” *Conference Record IEEE*, 2016.
- [110] J. Kvasnicka, “Data Acquisition System for the CALICE AHCAL Calorimeter,” *JINST*, vol. 12, no. 03, p. C03043, 2017.
- [111] M. Wing, R. Ete, Y. Liu, and J. Kvasnicka, “Data acquisition software,” Dec 2017.

- [112] Christian Graf for the CALICE Collaboration, "Performance of a Highly Granular Scintillator-SiPM Based Hadron Calorimeter Prototype in Strong Magnetic Fields," *Conference Record IEEE*, 2017.
- [113] F. Sefkow, "CMS scintillator HGCal," Dec 2017.
- [114] P. Chau, "HBU tile assembly & integrated performance test setup," Dec 2017.
- [115] F. Sefkow, "Welcome and overview," Dec 2017.
- [116] S. Agostinelli and al., "Geant4 – a simulation toolkit," *Nuclear Instruments and Methods in Physics Research Section A: Accelerators, Spectrometers, Detectors and Associated Equipment*, vol. 506, no. 3, pp. 250 – 303, 2003.
- [117] H. V. P. Mora de Freitas, "Detector Simulation with MOKKA/GEANT4 : Present and Future," software, Laboratoire Leprince Ringuet CNRS/IN2P3 - Ecole Polytechnique 91128 Palaiseau, France, 2003.
- [118] M. Frank, F. Gaede, C. Grefe, and P. Mato, "DD4hep: A Detector Description Toolkit for High Energy Physics Experiments," *Journal of Physics: Conference Series*, vol. 513, no. 2, p. 022010, 2014.
- [119] V. Ivanchenko and al., "Recent Improvements in Geant4 Electromagnetic Physics Models and Interfaces," in *3th Monte Carlo Conference MC2010*, vol. 2, (Tokyo, Japan), pp. 898–903, Oct. 2010.
- [120] J. Apostolakis and al., "Progress in Geant4 electromagnetic physics modeling and validation," in *CHEP2015*, 2015.
- [121] The CALICE Collaboration, "Validation of GEANT4 Monte Carlo Models with a Highly Granular Scintillator-Steel Hadron Calorimeter,"
- [122] The CALICE Collaboration, "Pion and proton showers in the CALICE scintillator-steel analogue hadron calorimeter," *Journal of Instrumentation*, vol. 10, no. 04, p. P04014, 2015.
- [123] A. Heikkinen, N. Stepanov, and J. P. Wellisch, "Bertini intra-nuclear cascade implementation in Geant4,"
- [124] G. Folger, V. N. Ivanchenko, and J. P. Wellisch, "The Binary Cascade," *The European Physical Journal A - Hadrons and Nuclei*, vol. 21, pp. 407–417, Sep 2004.
- [125] G. Folger and J. P. Wellisch, "String Parton Models in Geant4,"
- [126] J. A. et al., "GEANT4 Physics Lists for HEP,"
- [127] "ILCSOFT web portal."
- [128] F. Gaede, T. Behnke, N. Graf, and T. Johnson, "LCIO: A Persistency framework for linear collider simulation studies," *eConf*, vol. C0303241, p. TUKT001, 2003.
- [129] F. Gaede, "Marlin and LCCD: Software tools for the ILC," *Nucl. Instrum. Meth.*, vol. A559, pp. 177–180, 2006.
- [130] <https://svnsrv.desy.de/websvn/wsvn/General.calice?>
- [131] M. Terwort and A. Lucaci-Timoce, "The calice software framework and operational experience," in *IEEE Nuclear Science Symposium Medical Imaging Conference*, pp. 1–4, Oct 2010.

- [132] P. Mora de Freitas and H. Videau, “Detector simulation with MOKKA / GEANT4: Present and future,” in *Linear colliders. Proceedings, International Workshop on physics and experiments with future electron-positron linear colliders, LCWS 2002, Seogwipo, Jeju Island, Korea, August 26-30, 2002*, pp. 623–627, 2002.
- [133] M. Frank, F. Gaede, C. Grefe, and P. Mato, “DD4hep: A Detector Description Toolkit for High Energy Physics Experiments,” *J. Phys. Conf. Ser.*, vol. 513, p. 022010, 2014.
- [134] M. et al., “Precise measurement of Birks kB parameter in plastic scintillators,”
- [135] “CERN North Area H2 beamline.”
- [136] The CALICE collaboration, “Electromagnetic response of a highly granular hadronic calorimeter,” *Journal of Instrumentation*, vol. 6, no. 04, p. P04003, 2011.
- [137] O. Hartbrich, *Scintillator Calorimeters for a Future Linear Collider Experiment*. PhD thesis, Hasylab, DESY, Hamburg, 2016.
- [138] O. Hartbrich, “Commissioning and LED system tests of the engineering prototype of the analog hadronic calorimeter of the CALICE collaboration,” Master’s thesis, Wuppertal U., Dept. Math., 2012.
- [139] A. Elkhali, “Design of new test-board for the SPIROC2E BGA package,” *AHCAL Main Meeting, December 2016*, 2016.
- [140] L. T. T. Tong, “Trigger Threshold Verification for the Hadronic Calorimeter Prototype for the ILC,” *Summer Student Report*, 2014.
- [141] B. Hermberg, *Measuring Hadronic Jets at the ILC - From Particle Flow Calorimetry to the Higgs Self-Coupling*. PhD thesis, U. Hamburg, Dept. Phys., Hamburg, 2015.
- [142] The CALICE Collaboration, “Timing of hadron showers in the CALICE Analog Hadronic Calorimeter prototype using steel absorber,” *CALICE Analysis Note*, vol. 61, 2018.
- [143] B. Govorkov, “Cherenkov detectors in Cherenkov’s laboratory,” *Nuclear Instruments and Methods in Physics Research Section A: Accelerators, Spectrometers, Detectors and Associated Equipment*, vol. 553, no. 1, pp. 9 – 17, 2005. Proceedings of the fifth International Workshop on Ring Imaging Detectors.
- [144] K. Gadow, E. Garutti, P. Gottlicher, M. Reinecke, F. Sefkow, M. Terwort, “Concept, Realization and Results of the Mechanical and Electronics Integration Efforts for an Analog Hadronic Calorimeter,” *EUDET Report*, 2010.
- [145] A. Provenza, *Calibration and analysis of data taken with the technological prototype of the Analog Hadron Calorimeter (AHCAL) for a detector at the International Linear Collider*. PhD thesis, 2018, ongoing.
- [146] A. Provenza, “Analysis of July 2015 CERN test beam electron data,” *CALICE Collaboration Meeting, Tokyo*, 2017.
- [147] S. Schroeder, “Commissioning of a prototype hadronic calorimeter,” *Master Thesis*, 2015.

- [148] F. Lenzen, “Channel by Channel MIP-Calibration of the Analogue Hadronic Calice-Calorimeter,” *Bachelor Thesis, Bergische Universitat Wuppertal*, 2014.
- [149] E. Brienne, “Studies of the front-end electronics of the Analog HCAL.” DESY summer student report, 2012.
- [150] S. Laurien, “Private communication,” 2016.
- [151] O. Hartbrich, “Investigation of the time measurement capabilities of the SPIROC2b ASIC.” DESY summer student report, 2011.
- [152] C. Günter, *Comparison of Iron and Tungsten Absorber Structures for an Analog Hadron Calorimeter*. PhD thesis, U. Hamburg, Dept. Phys., Hamburg, 2015.
- [153] F. Simon, C. Soldner, and L. Weuste, “T3B - an experiment to measure the time structure of hadronic showers,” *Journal of Instrumentation*, vol. 8, no. 12, p. P12001, 2013.
- [154] R. Ellsworth, J. Goodman, A. Ito, J. Macfall, F. Siohan, R. Streitmatter, S. Tonwar, P. Viswanath, and G. Yodh, “A study of albedo from hadronic calorimeter for energies $\sim 100\text{--}2000$ GeV,” *Nuclear Instruments and Methods in Physics Research*, vol. 203, no. 1, pp. 167 – 177, 1982.
- [155] The CALICE Collaboration, “Pion Showers in the CALICE AHCAL Prototype,” *CALICE Analysis Note 026*, 2010.
- [156] B. Li, K. Fujii, and Y. Gao, “Kalman-filter-based track fitting in non-uniform magnetic field with segment-wise helical track model,”
- [157] R. Fruhwirth, “Application of Kalman filtering to track and vertex fitting,” *Nucl. Instrum. Meth.*, vol. A262, pp. 444–450, 1987.
- [158] D. Jeans and O. Hartbrich, “Realistic calorimeter hit digitisation in the ILDCaloDigi processor,” 2015.
- [159] Tran, Huong Lan and Krüger, Katja and Sefkow, Felix and Green, Steven and Marshall, John and Thomson, Mark and Simon, Frank, “Software compensation in Particle Flow reconstruction,” *Eur. Phys. J.*, vol. C77, no. 10, p. 698, 2017.
- [160] S. Green, “Pandora Analysis Calibration Executables,”
- [161] The CALICE Collaboration, “A new approach to software compensation for the CALICE AHCAL,” *CALICE Analysis Note 028*, 2010.

Eidesstattliche Versicherung

Hiermit versichere ich an Eides statt, die vorliegende Dissertationsschrift selbst verfasst und keine anderen als die angegebenen Hilfsmittel und Quellen benutzt zu haben.

Die eingereichte schriftliche Fassung entspricht der auf dem elektronischen Speichermedium.

Die Dissertation wurde in der vorgelegten oder einer ähnlichen Form nicht schon einmal in einem früheren Promotionsverfahren angenommen oder als ungenügend beurteilt.

Declaration on oath

I hereby declare, on oath, that I have written the present dissertation by my own and have not used other than the acknowledged resources and aids.

Hamburg, den 06/08/2018

A handwritten signature in black ink, appearing to be 'Eldwan Brianne', written over a horizontal line.

Eldwan Brianne